MODELING AND SIMULATION OF TOPOLOGICAL INSULATORS, TOPOLOGICAL SEMI-METALS AND FERRIMAGNETS FOR TIME AND ENERGY EFFICIENT SWITCHING OF MAGNETIC TUNNEL JUNCTION

by

Ahmed Kamal Reza

A Dissertation

Submitted to the Faculty of Purdue University

In Partial Fulfillment of the Requirements for the degree of

Doctor of Philosophy

Department of Electrical and Computer Engineering

West Lafayette, Indiana

December 2019

THE PURDUE UNIVERSITY GRADUATE SCHOOL
STATEMENT OF DISSERTATION APPROVAL

Dr. Kaushik Roy, Chair

Department of Electrical and Computer Engineering

Dr. Anand Raghunathan

Department of Electrical and Computer Engineering

Dr. Zhihong Chen

Department of Electrical and Computer Engineering

Dr. Shreyas Sen

Department of Electrical and Computer Engineering

Approved by:

Dr. Dimitrios Peroulis

Head of the Departmental Graduate Program

Dedicated to my parents and wife for their unconditional love and support

ACKNOWLEDGMENTS

First, I want to thank my PhD supervisor, Prof. Kaushik Roy, who has guided me in every possible way to make me a better researcher. I am very thankful for his patience and understanding to guide me through tough periods with my research. I am always astonished by how quickly and clearly he can address the key issues his students are facing and give appropriate advice. I will always remember the conversations with him that made me approach a problem in a more scientific way and find out logical solutions to that problem.

I would also like to thank my PhD advisory committee members, Prof. Anand Raghunathan, Prof. Zhihong Chen and Prof. Shreyas Sen for their insightful advice regarding my research. I also want to thank all the members of our research group, Nanoelectronics Research Laboratory, for helping in every possible way. I definitely had plenty of fun interacting with such a lively group of people.

I would like to take this opportunity to thank my family, and in particular, my parents and my wife for their unconditional love and support. My parents have always guided me throughout my life through their invaluable advice. They have always encouraged me to dream bigger and work harder. My wife has been a constant inspiration throughout my doctoral study. She always inspires me to push myself harder to achieve something extraordinary. They were always by my side in hard time. Without their constant support, this work would never have been possible.

This thesis has been possible due to the help and support of numerous people and I want to apologize for not being able to list everyone here. I just want to express my gratitude to everyone who has helped me in pursuing my dream and try to be a better human being through my contribution to science.

TABLE OF CONTENTS

LIST OF TABLES

LIST OF FIGURES

ABSTRACT

Magnetic Tunnel Junction (MTJ) sits at the very heart of all spintronic devices with possible applications in on/off-chip memories, sensors etc. The most significant step in the operation cycle of MTJ is the switching of the magnetization direction of the free magnetic layer (write operation). Fast and energy-efficient switching of MTJ is a big challenge and has been investigated by researchers. MTJ switching is mainly of two types – spin-transfer torque based switching (STT-MTJ) and spin-orbit torque based switching (SOT-MTJ). SOT-MTJ has fewer reliability issues than STT-MTJ because of separate read and write paths. In SOT-MTJ, switching is executed by injecting spin-polarized current in the MTJ free layer. Spin-polarized current can be generated by passing charge current through heavy metals (HM) like Pt, β-W etc. Nevertheless, the charge to spin current conversion efficiency is low (3%-10%) in HMs. On the other hand, topological insulator (TI) has excellent charge current to spin current conversion efficiency (~37% in Bi_2Se_3, a 3D TI), far better than HMs. We proposed a simulation framework for TI/Ferromagnet (FM) heterostructures that can capture the 'inverted' surface electronic band structure of 3D TI and calculate the spin transport properties at TI/FM interface using non-equilibrium Green's function (NEGF) formalism. The magnetization dynamics of the FM layer, due to the transfer of spin angular momentum, is simulated using Landau–Lifshitz–Gilbert–Slonczewski (LLGS) formalism. Finally, we evaluated the performance of three different TI/FM memory structures and showed that TI based memories are not energy efficient because of the shunting current through the FM layer. In order to solve the shunting current issue, we explored newly discovered Topological semi-metals (TM). We found that TM like Na_3Bi has higher charge current to spin current conversion efficiency (~30%) than HMs and higher electrical conductivity (~12.5x more) than TIs. Therefore, Na_3Bi provides us a trade-off point between HM and TI as a non-magnetic spin injector. We modeled the MTJ with Na_3Bi as spin injector. Our simulation showed that a CoFeB-MgO-CoFeB-Na_3Bi MTJ consumes almost 10x and 728x less electrical power during iso-speed write operation compared with CoFeB-MgO-CoFeB-Pt and CoFeB-MgO-CoFeB-Bi_2Se_3 MTJs, respectively.

Slow switching speed due to long precession time is another major drawback of a ferromagnet (FM) based MTJ as compared with traditional CMOS technology. Ferrimagnet (FiM) can offer faster switching speed because of 'bulk torque' generation. Our *ab-initio* analysis of ferrimagnet CoTb based ferrimagnet MTJ (FMTJ) showed that a thick (~10-12nm) CoTb layer is necessary to fully utilize the advantage of bulk torque generation inside CoTb. We developed a model to simulate the FiM magnetization dynamics incorporating Dzyaloshinskii-Moriya interaction (DMI) at FiM/HM interface. Our simulation exhibited that for picosecond range switching speed, CoTb based FMTJ is ~25 times more energy efficient and

more immune to thermal noise than CoFeB based MTJ. Nevertheless, FMTJ has lower TMR and higher critical switching current.

Finally, we analyzed the MTJ reliability issues. The major reliability concern in an MTJ is the time-dependent dielectric breakdown (TDDB) in the thin MgO tunneling barrier layer. We simulated the lifetime of MTJ with 1nm thick MgO layer using Weibull plot analysis. We found that at an operating voltage of 0.6V and room temperature, 1% of the MTJs (in a sample of 1000 MTJs) will have 3rd soft-dielectric breakdown in the MgO layer in almost 24 years.

1. INTRODUCTION

Technology scaling has been driving the evolution of the modern semiconductor industry over the past few decades. In the 1980s, the density of on-chip transistors was ~700 transistors per mm^2 [1]. Aggressive technology scaling now enables us to incorporate ~6 million transistors per nm^2 in state-of-the-art microprocessors of today as shown in fig. 1.1 [1-5]. Due to technology scaling, the microprocessor performance improved more than 100x over the last couple of decades [1-7] due to faster switching speed of the transistors. Processor performance increased faster than memory performance making memory a bottleneck in the system. In order to keep up with the fast processor speed and to reduce the data transfer latency, the on-chip cache was introduced in computers in the 1980s [8-10]. On-chip caches (mainly made of 6T static random-access memory cells) allow keeping data close to the processor cores which enhances overall chip performance. Smaller transistor size allows chip designers to increase the size of on-chip caches (Fig. 1.2).

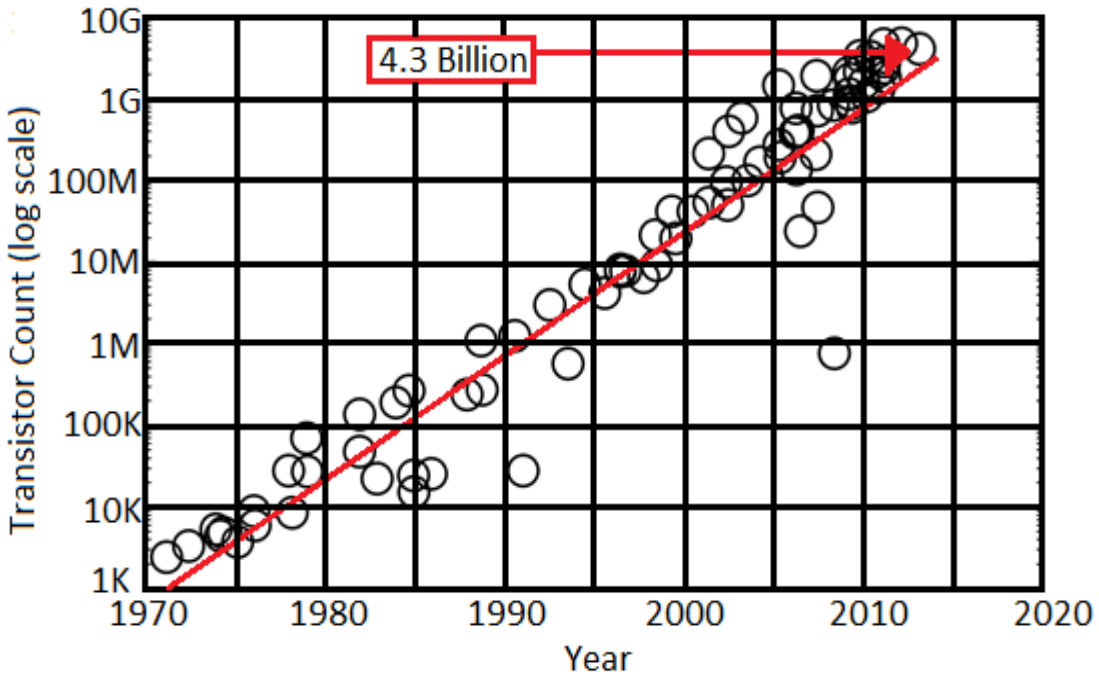

Fig. 1.1. CMOS scaling trends in terms of transistor count (reproduced from [6]).

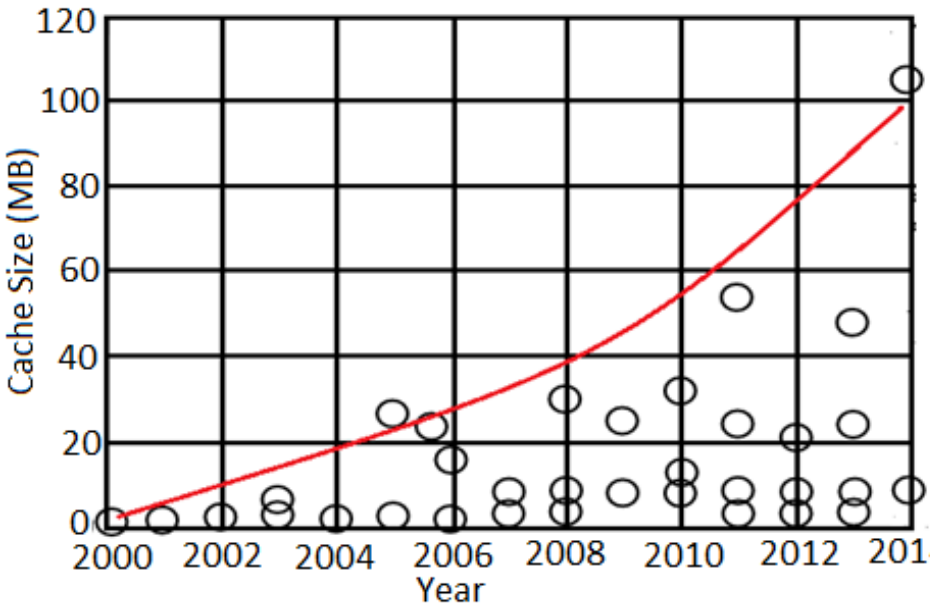

Fig. 1.2. Scaling trend of on-chip caches (reproduced from [6]).

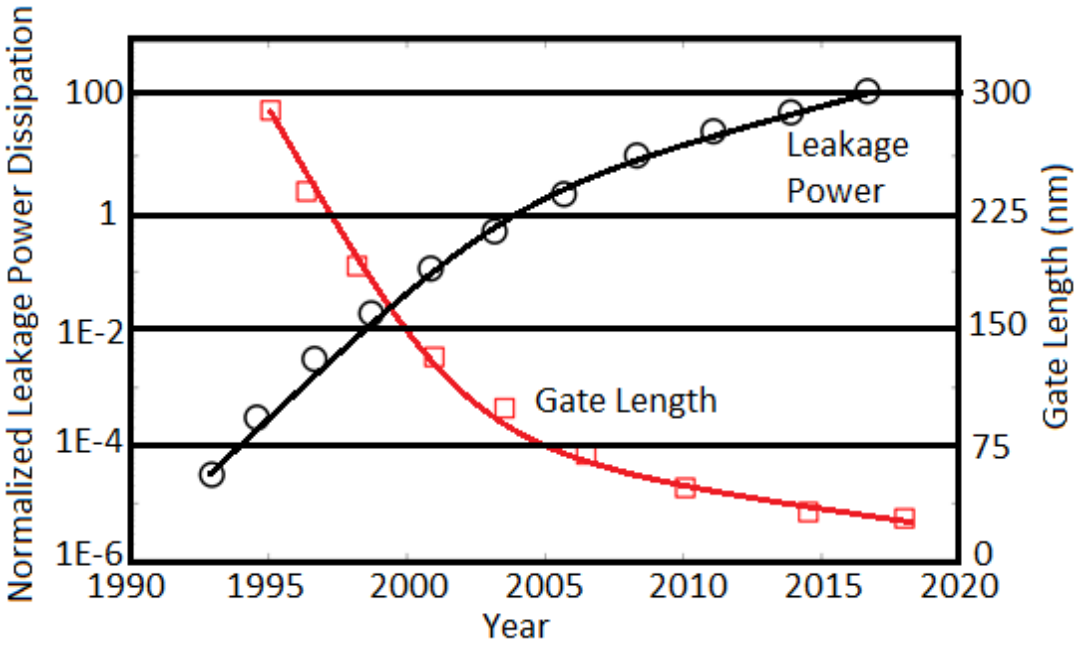

Fig. 1.3. Increase of sub-threshold leakage power in 6T SRAM cell with decreasing gate length (reproduced from [7]).

State-of-the-art 6T static random-access memory (SRAM) can occupy as much as ~70% of the core area in microprocessors [2]. Memory subsystems based on the 6T SRAM cells are volatile. Therefore, the power supply of 6T SRAM cells cannot be turned off to save power when

the processor is idle [1]. The idle mode of 6T SRAM cells is a big concern due to leakage power dissipation (mainly sub-threshold leakage) which is rising with technology scaling (fig. 1.3) [6]. Hence, power dissipation in modern microprocessors is increasingly dominated by idle-mode leakage power of the memory subsystems [6]. Therefore, low power, low leakage, high density and high speed non-volatile 'universal' memory technologies compatible with current CMOS technology are needed to mitigate the large power dissipation while increasing the on-chip cache size.

In recent years, several non-volatile memory technologies have been proposed and are intensively researched [11]. The most attractive non-volatile memory technologies include phase-change memory (PCM), ferroelectric RAM (FeRAM), magnetic RAM (MRAM) and resistive RAM (RRAM). However, MRAM has emerged as one of the leading candidates for future universal memory because of its potential for high-density, reasonable write speed (< 10 ns) and extremely good endurance (> 10^{14} write cycles) compared to other non-volatile memory technologies [11]. MRAMs are also compatible with the CMOS fabrication process, requiring minimal changes to the back-end-of-line (BEOL) fabrication process (addition of 2 mask steps) [11]. The basic storage device in MRAMs is the magnetic tunnel junction (MTJ). MRAMs are inherently compatible with digital logic because the MTJ has only two stable states [12].

1.1 Computer Memories and Universal Memory

Modern computers contain a hierarchy of memory types for retrieving and storing different types of information. Computer memories have a wide range of types, speed and size depending on the requirement. The fastest memories are the CPU registers (fig. 1.4) with a latency of ~0.3 ns. The second fastest memory in the computer is the cache memory. The processor contains three tiers of cache made of SRAM. The level one cache, the smallest and the fastest one, is reserved for a particular core [13]. Level three cache is the slowest and the largest one and is shared between multiple cores [13]. Another low cost primary active memory is the dynamic random-access memory (DRAM) (latency ~10 ns) which is cheaper but slower than SRAM [13]. Registers, SRAM and DRAM are volatile memories and require a constant power supply to maintain their information. On the other hand, solid state drive (latency ~100 ns) [14] and hard disk drive are non-volatile memories but they are roughly 30,000-50,000 times slower than the CPU registers [14].

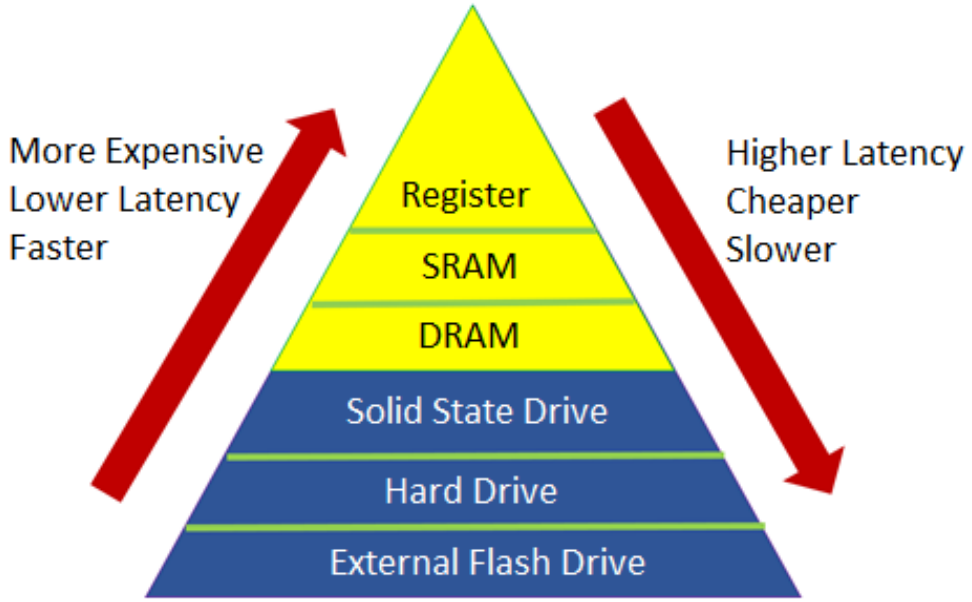

Fig. 1.4. The "pyramid" of memory in modern computers [15]. Most information is stored in slower nonvolatile memories (blue). Volatile memories (yellow) are mainly active during processing. The pyramid is not scaled.

To date, there is no single type of memory that satisfies every requirement simultaneously. Different memory types need different hardware and software implantations for proper functioning. Merging different memory types in a single system is a costly and complicated process. It also degrades the overall system performance. Therefore, the search for 'universal memory' with the high storage density and the non-volatility of solid state drives and hard drives, the low latency of SRAM, the unlimited read/write cycles like DRAM and SRAM is going on with great interest. Many alternative memory technologies have been proposed in the last couple of decades as potential universal memories. A few of the most notable alternative memories are phase change memory, resistive random-access memory, racetrack memory and magnetoresistance random-access memory (MRAM). MRAM is the solid state analog of a hard disk drive. It stores information in the magnetization state of a nanometer-scale magnet. The reading and writing operations are done electronically, without any moving parts. The storage element in an MRAM is the magnetic tunnel junction (MTJ).

1.2 The Magnetic Tunnel Junction

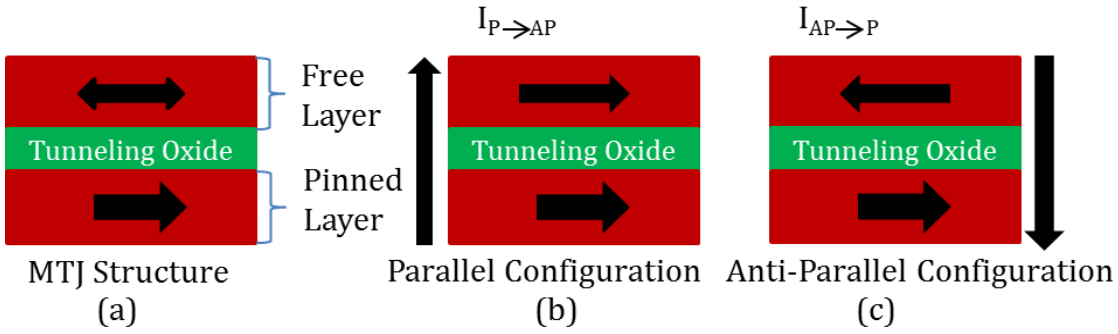

Fig. 1.5. (a) Structure of a magnetic tunnel junction, (b and c) Charge current directions to induce spin-transfer torque switching from parallel (p) to anti-parallel (AP) and AP to P.

The magnetic tunneling junction (MTJ) is the heart of MRAMs. The structure of an MTJ is illustrated in Fig. 1.5. It consists of a tunneling oxide layer sandwiched between two ferromagnetic electrodes. One of the ferromagnetic electrodes is magnetically fixed (called the pinned layer or PL). It works as a reference layer. The magnetization of another ferromagnetic electrode (called the free layer or FL) can be modified so that its magnetization direction can be either parallel (P) or antiparallel (AP) to that of the PL. The energy barrier between P and AP configurations is small enough so that the MTJ can be switched between different configurations with a minimum amount of energy but large enough (~40kT) to ensure thermal stability [13–16]. MTJ resistance, $R_{MTJ,}$ is different for different magnetic configurations of the MTJ and binary data is represented accordingly. R_{MTJ} depends on the tunneling barrier material and thickness, the cross-sectional area of the MTJ, quality of the interface between tunneling oxide and ferromagnet. MgO is a popular choice as the tunneling oxide barrier because its crystalline structure enhances the tunneling magnetoresistance ratio of the MTJ. The complex spin-polarized $\Delta_1$band of MgO helps the tunneling of majority spin and works as a spin filter [12] (fig. 1.6). The spin-polarized $\Delta_1$band is not available for minority career tunneling (fig. 1.6) and hence, the resistance is high in antiparallel configuration. Since the mechanism for electron transport is direct tunneling, at a same cross-sectional area, R_{MTJ} depends exponentially on the tunneling oxide thickness, t_{MgO}. At iso-t_{MgO}, R_{MTJ} depends linearly on the cross-sectional area of the MTJ. The difference in MTJ electrical resistances for parallel and anti-parallel configurations can be explained with the help of the band diagram.

Fig. 1.7 illustrates an example band structure of the MTJ when it is in the P configuration (fig. a) and in the AP configuration (fig. b). Electrons flowing between the electrodes carry either up-spin (majority spin) or down-spin (minority spin). Majority (up-spin) electrons will tunnel into the spin-up energy bands and minority (down-spin) electrons will tunnel into the spin-down energy bands. Assuming that spin scattering is negligible, the flow of minority and majority spins can be thought of as two decoupled paths and the total charge current flow is the scalar addition of the two spin currents.

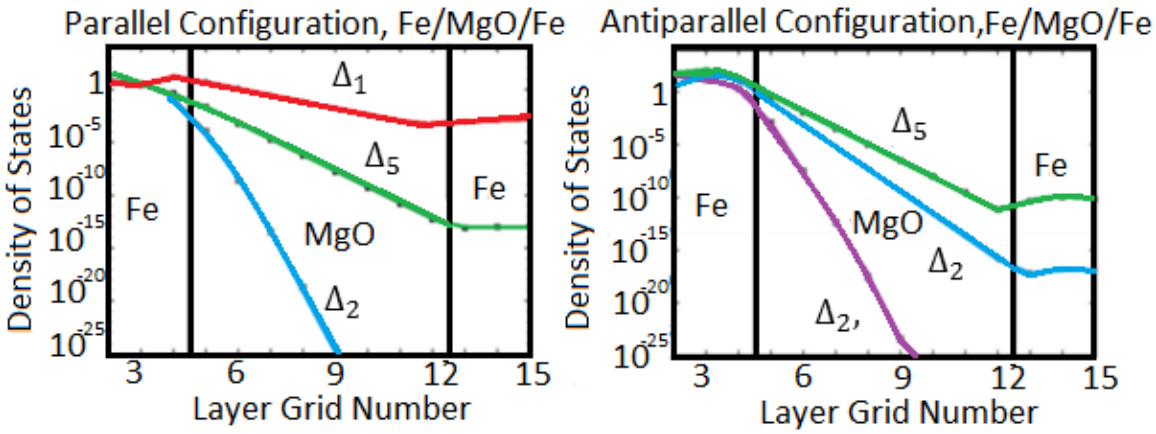

Fig. 1.6. Tunneling density of states in Fe/MgO/Fe MTJ (reproduced from [12])

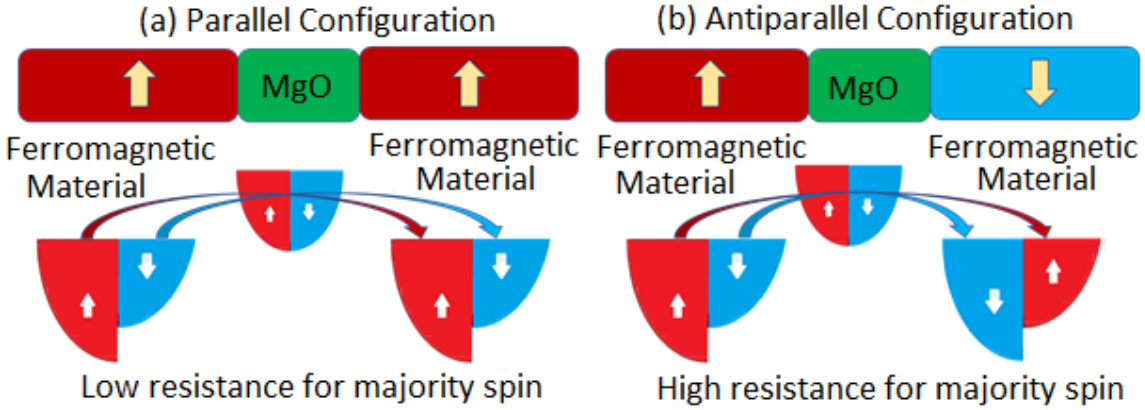

Fig. 1.7. Band diagrams for up and down spins when MTJ is in (a) P configuration and in (b) AP configuration, to illustrate the effect of tunneling magneto-resistance (TMR). The relative magnetization direction of the FL with respect to the PL gives rise to the TMR effect. The TMR effect arises due to the difference in density of states of majority and minority spins around the Fermi energy (E_F) of the FM contacts [17].

Let us consider the MTJ in the P configuration first. Fig. 1.7(a) illustrates the band diagram for the electron transport direction of an MTJ in the P configuration. The density of states (DOS) for up-spins in the FL and PL is high and DOS for down-spin in FL and PL is low. When a small voltage, V_D, is applied, there are sufficient states to accommodate all the up-spin electrons to tunnel between FL and PL. On the other hand, there is little room for down-spin election to tunnel between FL and PL. Therefore, the up-spin current is higher than the down-spin current. Furthermore, as the majority electrons are spin-up, the overall electrical resistance (R_p) of the conduction path is low.

Now, let us consider the MTJ in AP configuration. Fig. 1.7(b) illustrates the band diagram along the electron transport direction of an MTJ in the AP configuration. Note, there is a mismatch between the DOS of iso-spins in the left and right magnetic electrodes. The majority electron spin is the up-spin in the left ferromagnet while in the right ferromagnet, the majority spin is the down-spin. Therefore, in the left electrode, the up-spin DOS is higher than down-spin DOS while in the right electrode, the scenario regarding spin-dependent DOS is exactly opposite. When a small voltage, V_D, is applied, an energy gap of qV_D is created between the Fermi levels of the two electrodes creating an energy channel of conduction. Majority up-spin electrons from left contact want to tunnel through the MgO barrier into the right contact. But there are few up-spin energy bands available in the right contact to accommodate a large number of up-spin electrons. On the other hand, few minority down-spin electrons can easily tunnel from the left contact to the right contact. As a result, the overall electrical current is low and AP configuration has high electrical resistance (R_{AP}) path. The difference in MTJ resistance between P and AP configurations is measured by the Tunneling Magneto-resistance Ratio (TMR) = $(\frac{R_{AP}-R_P}{R_P} \times 100)\%$. TMR is an important MTJ performance metric. MTJ with high TMR (>50%) is necessary for reliable MRAM read operation [10].

1.3 MRAM: Types, Comparison, Issues and Solutions

Different categories of magnetoresistance random-access memory (MRAM) have been developed during the gradual progress in spintronic research. All of the MRAMs use MTJ as the elementary storage unit. Fig. 1.8 shows different types of MRAMs. Reading the state of an MRAM bit is identical in all MRAMs. The read line of MRAM is connected to the MTJ fixed

layer as shown in fig. 1.8. When charge current is allowed to flow through the read line, it tunnels through tunneling MgO layer into the MTJ free layer due to a bias voltage of 0.1-0.2V across the MTJ. The electrical resistance of the current path depends on the orientation of the magnetic layers as discussed above. With carefully-chosen magnetic materials and a good spin-filtering tunnel barrier such as MgO, the resistance can change by more than 5× between the two magnetic states at room temperature [10].

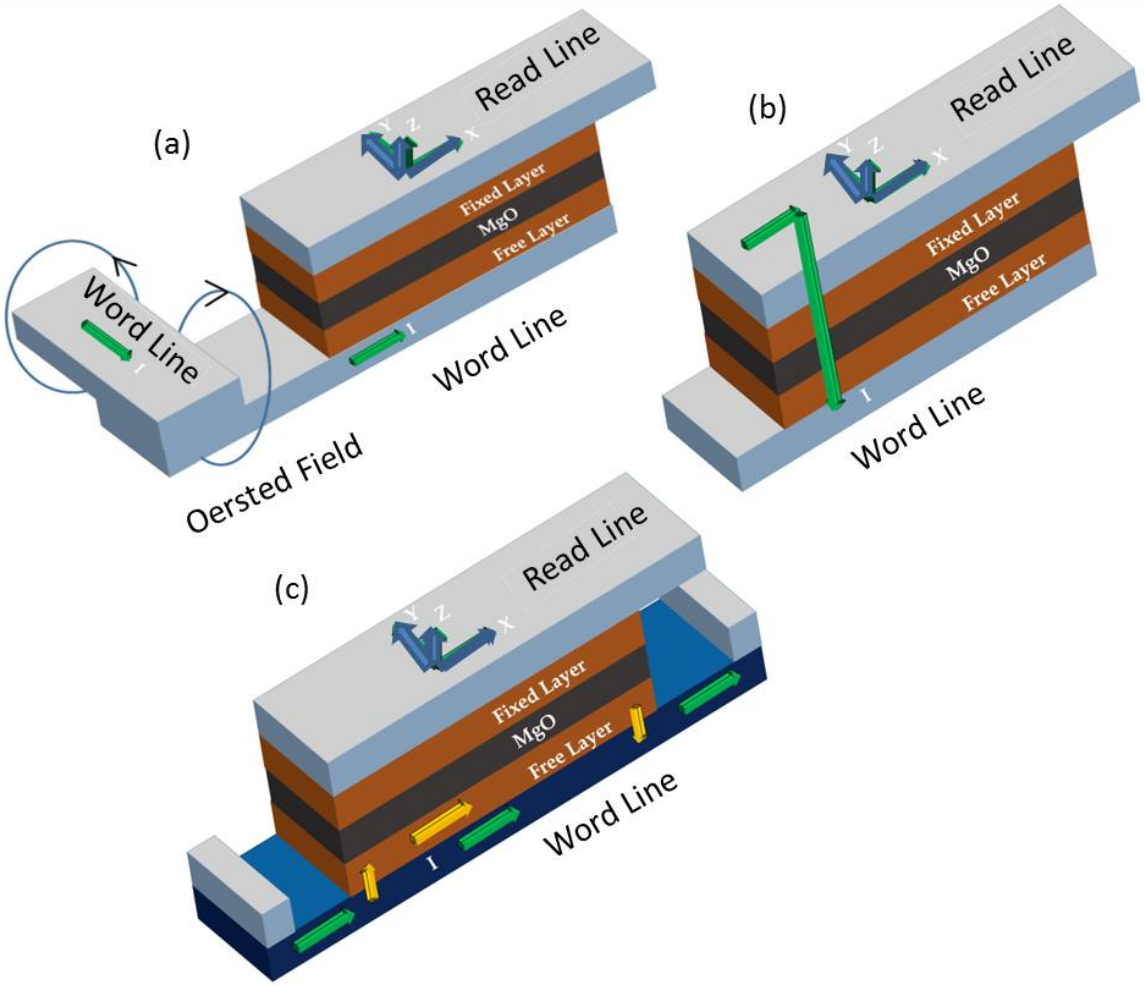

Fig. 1.8. Different types of MRAMs (a) field-driven MRAM (b) STT-MRAM (c) SOT-MRAM (yellow arrows show the spin diffusion current from spin injector flowing into the MTJ free layer magnet while green arrows show the charge current direction).

Changing the state of an MTJ i.e., conducting a write operation is significantly different in different categories of MRAMs. Early MRAM designs (field-driven MRAM) switched bits using magnetic fields (fig. 1.8 (a)), analogous to writing heads in hard drives. In field-driven MRAM,

charge current is flown through two perpendicular lines (fig. 1.8 (a)), creating large enough magnetic fields to flip the MTJ free layer magnet [19]. Field-driven MRAM operation is straightforward to implement. Nevertheless, there are some problems associated with it. A magnetic field cannot be confined to a particular bit cell and can accidentally switch the neighboring bit cells. Generation of the magnetic field is a power-hungry operation as well. It is also difficult to scale down the word lines. Implementation of larger arrays greatly increases the power required to flip each bit [20,21]. Utilization of spin current and spin-transfer torque for switching the MTJ free layer provides a more reliable and energy efficient way to write MRAM.

1.3.1 Spin-Transfer Torque Based MRAM (STT-MRAM): Operating Principle and Issues

In 1989, J. C. Slonczewski published a theoretical study of two magnetic layers separated by an insulating barrier. He predicted that for a non-zero external bias, spin angular momentum would flow from one magnetic layer to the other. Transferring enough amount of spin angular momentum can generate magnetic oscillations [22], even switch it. Later, the concept of MTJ is extended by replacing the tunnel junction by a metallic spacer between the two magnetic layers [24,25]. Several research groups reported switching of nanometer-range magnets with metallic spacers in 2000 [26]. Switching of STT-MTJ (fig. 1.8(b)) with Al_2O_3 tunneling barrier was also demonstrated in 2004 [27,28]. Since then, much progress has been made on the development of STT-MRAM. In 2012, Everspin released the first commercial STT-MRAM module, [29] while Samsung announced commercial launching of 1GB STT-MRAM product last year. Due to the high cost, low density, high-power consumption and slow speed [30], STT-MRAMs are currently limited to applications where the memory reliability is more important (typically in the harsh environment applications like motor vehicles).

The mechanism used to switch the magnetic layer in STT-MTJ is based on *spin-transfer torque (STT)*. Electrons in charge current have a random spin orientation. When charge current flows through a thick magnetic layer (fig. 1.9(a)), electron spin magnetic field and magnetic moments of the magnetic layer (ferromagnet 1 in fig. 1.9(a)) exert torque on each other. All the magnetic moments inside a ferromagnet are pointing in the same direction. The magnetization direction ($\overrightarrow{M_1}$) of the thick ferromagnet 1 remains unaffected by the STT due to random electron spin orientation in charge current. Rather, most of the electrons in charge current become spin-polarized ($\vec{m}$) to the magnetization direction of ferromagnet 1 (fig. 1.9(a)). The spin-polarized

current flows through a second thin magnetic layer (ferromagnet 2 in fig. 1.9(a)) with a different magnetic alignment ($\overrightarrow{M_2}$). The electron spins, which are misaligned with the magnetization of the second magnetic layer, will apply spin-transfer torques on the magnetic moments of ferromagnet 2. The torque ($\overrightarrow{M_{STT}}$) is proportional to $-\overrightarrow{M_2} \times (\overrightarrow{M_2} \times \overrightarrow{M_1})$ (fig. 1.9(b)).

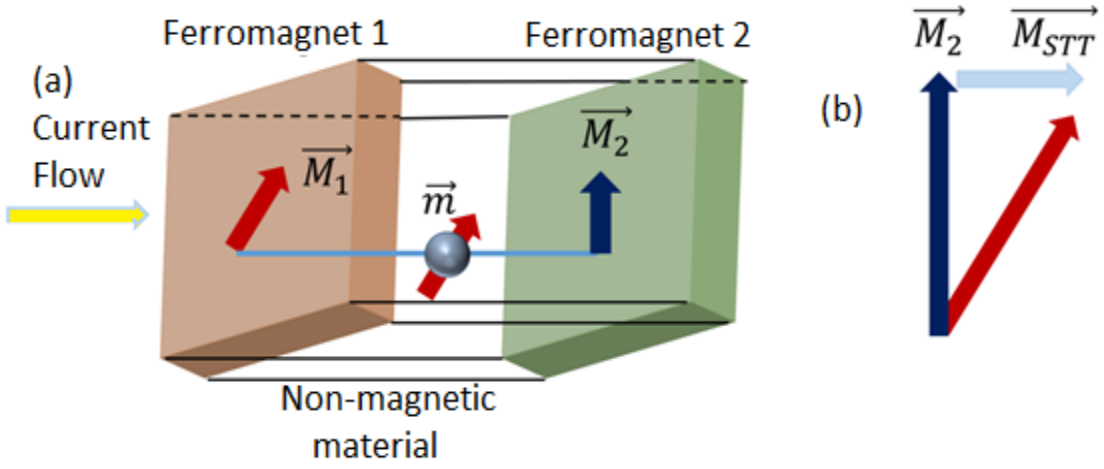

Fig. 1.9. (a) Concept of in-plane spin transfer torque in ferromagnet-1/non-magnetic-material/ ferromagnet-2 system. Electron (silver color) flows through ferromagnet 1, gets spin polarized (red arrow) and exerts spin transfer torque on magnetic moments of ferromagnet 2. (b) Direction of torque $\overrightarrow{M_{STT}}$ (light blue arrow) applied on magnetic moments of ferromagnet 2.

For a charge current of I_c, the maximum STT per unit moment (τ_{max}) is written as,

$$\tau_{max} = PI_c \frac{\hbar}{2e} \frac{\gamma}{M_s V_{mag}}$$

P is the fraction of charge current which become spin-polarized, γ is the gyromagnetic ratio, V_{mag} is the volume of the free magnetic layer and M_s is the saturation magnetization of the free magnetic layer.

STT-MTJ has demonstrated high spin-torque efficiency. Nevertheless, in two-terminal STT-MRAM devices where the write and the read paths are the same, reliability issues may arise. During a read operation, there is a probability that the free layer might switch. Therefore, in order to ensure stability, the volume of the free layer is kept large making the scaling of the device extremely difficult. Moreover, large volume free layer requires lots of switching current. Another significant drawback of the STT-MRAM is the large writing current injected through the tunneling barrier. In order to inject the required amount of writing current, a voltage pulse of 0.5-0.6V is applied across the MTJ. As a result, the tunneling barrier becomes exposed to a high

electric field (~10^9 V/m) which can cause a dielectric breakdown. In addition, the ballistic tunneling of electrons across the tunneling barrier into the receiving electrode causes inelastic relaxation of hot writing electrons. Therefore, large writing current also causes self-heating in the STT-MTJ. Separation of read and write paths in MTJ solves most the issues of STT-MTJ. In order to have separate read and write paths in MTJ, several researchers [31-34] proposed the three terminal MRAM cell (fig 1.8 (c)).

1.3.2 Spin-Orbit Torque Based Three Terminal MRAM (SOT-MRAM)

In a three terminal device, a spin injector (heavy spin Hall metals (SHM) like Pt, β-W, topological insulators) is attached to the MTJ free layer (fig. 1.10). The charge current

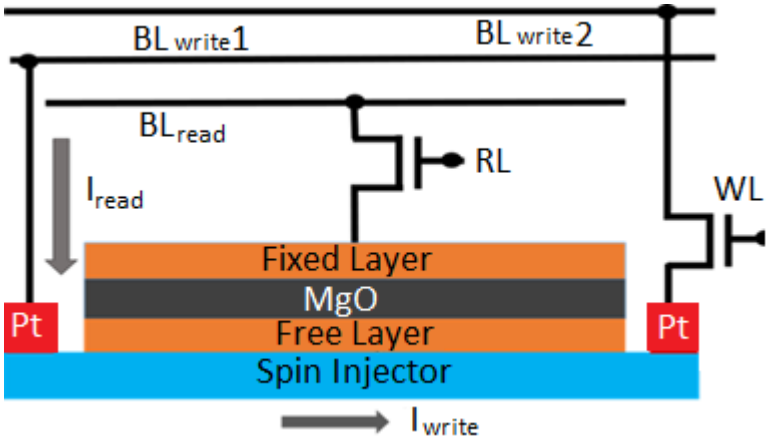

Fig. 1.10. Schematic diagram of three terminal SOT-MRAM cell

gets converted to spin current while flowing through the spin injector (I_{write} in fig. 1.10), due to spin Hall effect. Spin current gets accumulated in the spin injector, diffuses into the MTJ free layer (fig. 1.8(c), yellow arrows), applies torque on the magnetic moments and switches the magnetization direction. The direction of the read current (I_{read}) is the same as STT-MRAM. Read and write operations are controlled by access transistors (fig. 1.10). Separation of read and write paths not only improves the reliability of the device but also provides a better scaling opportunity. More details on the operation principle, modeling and analysis of SOT-MTJ can be found in the subsequent chapters.

1.4 Contribution and organization of the thesis

In the thesis, first, we show the modeling of current-driven SOT-MRAM where the spin-polarized current is injected by a topological insulator (TI). We discuss and compare the TI-based memory structure with spin Hall metal-based memory structures and CMOS memory structures. We find that due to the low electrical conductance of TI, the shunting current loss is a significant issue in TI based MTJ. We try to find a solution in topological semi-metal based SOT-MTJ where topological semi-metal Na_3Bi acts as the spin injector. We show that Na_3Bi can be an efficient spin injector by reducing the writing power consumption in ferromagnet based SOT-MTJ since Na_3Bi has higher conductivity than TI and higher charge current to spin current conversion efficiency than SHMs.

Ferromagnet (FM) based MTJ is relatively slower because of long ferromagnet precession time. We model ferrimagnet (FiM) based memory structures because FiM has strong exchange coupling resulting in bulk torque generation and lowering the switching time. We developed a magnetization simulation framework of FiM considering Dzyaloshinskii-Moriya interaction (DMI). Then we modeled FiM CoTb based FMTJ and analyzed the performance with respect to FM based MTJ. We show that CoTb based FMTJ is more energy efficient for picosecond range switching and thermally more robust than FM based MTJ. The tunneling barrier in MTJ is exposed to a high electric field and hence, the dielectric breakdown can be a significant MTJ reliability issue. We model the time-dependent dielectric breakdown (TDDB) in MTJ tunneling barrier using Büttiker probe based NEGF formalism and analyze the reliability, performance degradation with time and lifetime of the MTJ.

2. MODELING AND EVALUATION OF TOPOLOGICAL INSULATOR/FERROMAGNET HETEROSTRUCTURE BASED MEMORY

2.1 Topological Insulator as Spin Injector in Spin-Orbit Torque Based MTJ

In a spin-transfer torque based MTJ (STT-MTJ), the current for read and one of the write operations flow in the same direction through the MTJ, leading to reliability concerns (discussed in section 1.3.1) [32-34]. As a solution to the issues, the use of Spin Hall Metal (SHM) for write operation has been proposed in three terminal spin-orbit torque (SOT) based MTJ. In SHMs, when the charge current is injected, spin-orbit coupling (SOC) causes electrons with different spins to deflect in different directions. The iso-spin electrons accumulate at opposite surfaces of SHM and produce a spin current, transverse to the applied charge current (Spin Hall Effect (SHE) [32]). The efficiency of generating spin currents in these devices is represented by the spin Hall angle, which is the ratio of the spin current to the supplied charge current. However, the efficiency is rather low and typical SHMs such as Ta, β-W and other heavy metals show spin Hall angles less than 0.3 [35]. On the other hand, experimental evidence shows very high spin Hall angle for Topological Insulators (TI) (~1.1) [36], making them a potential candidate for spin-based memories. TIs are characterized by unique quantum-mechanical properties due to their unusual surface states. Although the bulk of a TI is insulating, the surface is conducting due to band inversion at the surface [37,38]. The band inversion is a consequence of the high SOC in TIs. Inside the bulk of 3D TI, SOC is insignificant due to crystal symmetry [38] and a bulk band-gap of 0.3eV has been experimentally observed [35]. Nevertheless, in the 3D TI surface, strong SOC pushes the conduction band down and pulls the valence band up (detail in ref. [35]). Therefore, the valence band and the conduction band touch each other at the interface [35] and spin-polarized surface states are observed. The strong SOC also enables a TI to manipulate the magnetization of an adjacent ferromagnet (FM) layer by generating a high SOT through the Rashba-Edelstein effect [35, 39, 40]. Strong Rashba-Edelstein effect enables the helical locking of the relative orientation of spin and momentum at the conducting 3D TI surface states [35-37], resulting in a high charge to spin current conversion ratio.

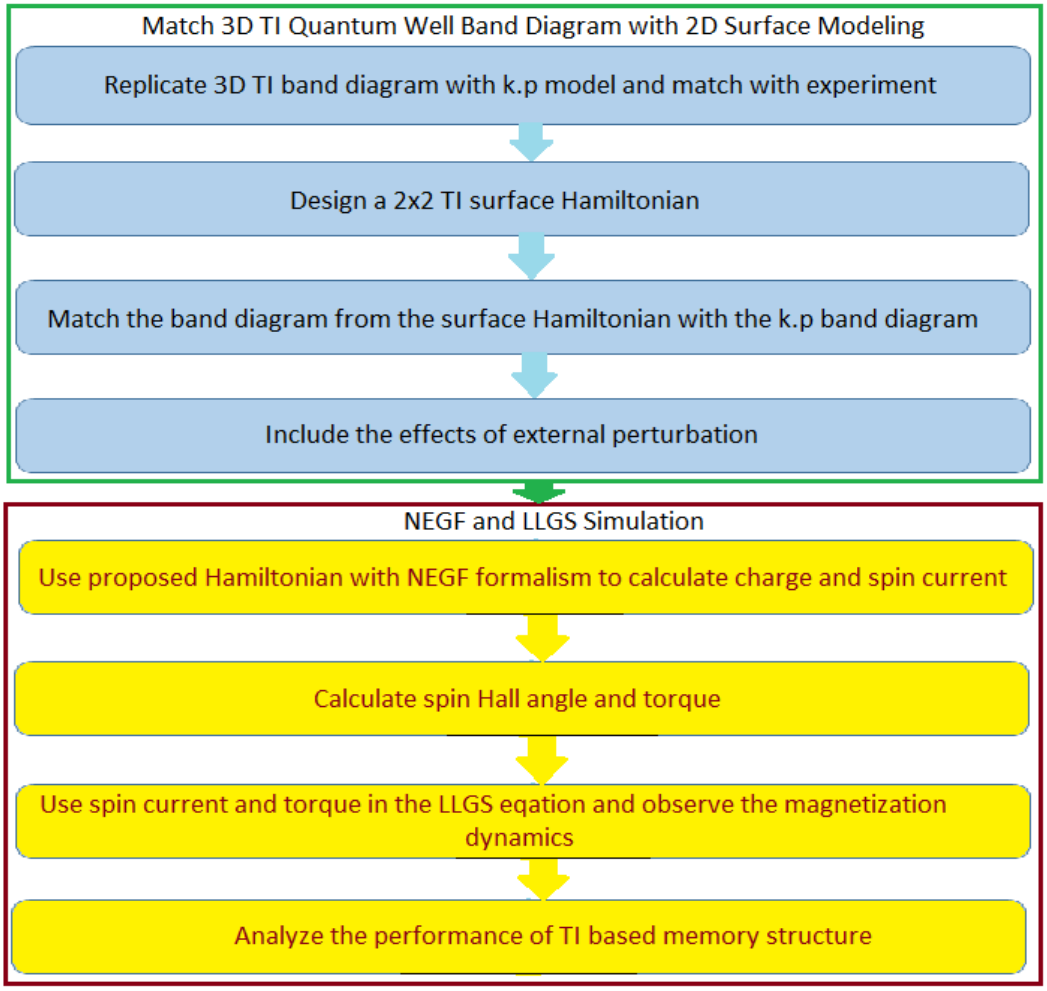

Fig. 2.1: Flow diagram of the modeling details

Recent experiments [35, 40] have clearly demonstrated the strong SOT in 3D TI acting on the FM layer in a TI/FM heterostructures and unusually high spin Hall angle [35]. The efficiency in generating the required FM switching spin currents with lower charge current injection is a top priority for having energy efficient SOT-MTJ write operation. Consequently, a lot of effort has been made to model the behavior of a TI/FM heterostructure [35,41,42]. However, none of the existing models consider the overall simulation framework for calculating the spin transport and the magnetization dynamics of the FM layer.

In this chapter, for analyzing the performance of new TI based memory devices, we propose a complete simulation framework that is computationally inexpensive, yet shows an excellent match with the experimental results. Fig. 2.1 shows the modeling framework. We first design a Hamiltonian which includes the important aspects of a TI/FM heterostructure that affect the

charge and spin transport properties. We formulate a 2D surface Hamiltonian for a TI structure by considering the quantum confinement effect, the position of the Fermi level, Dirac cone, Rashba effect, exchange coupling energy with the adjacent FM layer and the effect of external magnetic field on the band structure. We compare the band structure resulting from our proposed Hamiltonian with the band diagram from a standard 4x4 k.p [43] Hamiltonian of TI and find an excellent match. Next, we calculate the electrical transport characteristics by applying our Hamiltonian to standard Non-Equilibrium Green's Functions (NEGF) formalism of quantum transport [33]. We determine the charge current, the spin current, the charge conductivity and the in-plane and out-of-plane spin conductivity through self-consistent NEGF simulations. From the ratio of the obtained charge current and spin current, we calculate the spin Hall angle and find a good match with experimental data. Finally, we analyze the magnetization dynamics of the TI/FM heterostructure (Fig. 2.2) by incorporating the NEGF calculations into the Landau–Lifshitz–Gilbert–Slonczewski (LLGS) [39] magnetization dynamics model. We then apply our model on potential memory structures based on three different TI/FM heterostructures to analyze their performance. We also show that due to the higher spin Hall angles, the critical current required for operation is lower in TI based memories compared to SHE based memories. It may be lead to energy-efficient memories, although the high amount of shunting current through the FM layer in TI/FM heterostructures can be a bottleneck for memory efficiency.

The rest of the chapter is organized as follows. In section 2.2, we show the 4 band k.p model of 3D TI to produce the band-diagram of TI quantum well, considering quantum confinement. We present the details of our proposed simulation framework, including 2D TI surface Hamiltonian, the NEGF transport method and LLGS magnetization dynamics. In section 2.3, we present TI/FM heterostructure based memory device and then evaluate three such structures (Cr doped $(Bi_{0.5}Sb_{0.5})_2Te_3/(Bi_{0.5}Sb_{0.5})_2Te_3$, Permalloy $(Ni_{0.81}Fe_{0.19})/Bi_2Se_3$ and Yttrium Iron Garnet/Bi_2Se_3) for memory applications. We check the consistency of our results with experimental observations [35, 36, 40] and also discuss the prospects and challenges of TI based memory for real-world applications. Section 2.4 concludes the chapter.

2.2 Proposed Model for TI/FM Heterostructure

2.2.1 4 Band k.p Model and Band Structure of 3D TI

The first step in developing our numerical model is to replicate the band structure of a 3D TI using a simple k.p model [43]. We use the k.p model for two reasons. First, the k.p method exhibits excellent agreement with experimental results (shown later) for predicting the quantum confinement gap opening in TI quantum well band structure. Second, we can benchmark the band diagram from our proposed Hamiltonian with the k.p method since k.p method produces a band structure that is already benchmarked with *ab-initio* calculations [37]. The band structure of a TI is unique because the bulk is insulating but the surface is conducting due to band inversion at the surface. TIs have high spin-orbit coupling (SOC) and it causes the conduction and valence bands to touch each other in the surface at the Γ point (center of the Brillouin zone in reciprocal lattice),

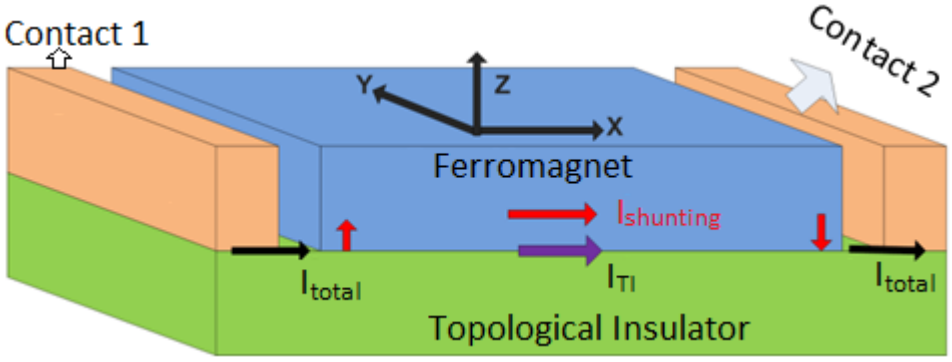

Fig. 2.2: Schematic drawing of a TI/FM heterostructure where the total charge current (black arrow) is flowing through the TI surface along the x-axis from Contact 1 to Contact 2. One part of the charge current will shunt through (red arrow) the top FM layer and the rest (purple arrow) will flow through the TI surface. Charge current is spin-polarized in perpendicular directions i.e., along y and z-axis.

thereby creating the band inversion. Electrical current primarily flows at the surface of a TI due to the band inversion at the Γ point. Therefore, the band diagram and transport properties of a TI can be characterized by the physics near the Γ point. We first develop a simple 2×2 Hamiltonian to model the TI surface by considering the important physical properties of the surface. Next, we apply the Hamiltonian to extract the band structure and compare it with the band diagram from a standard k.p Hamiltonian of TI [37, 38]. The k.p model we consider here is a 4x4 k.p model for 3D TI [37] which includes important symmetry properties such as time-reversal symmetry, inversion symmetry and three-fold rotation symmetry along the z-axis. The k.p dispersion

relation in 3D TI is computed by considering the four low lying states: $|P1_z^+ \uparrow\rangle$, $|P1_z^+ \downarrow\rangle$, $|P2_z^- \uparrow\rangle$ and $|P2_z^- \downarrow\rangle$ which are closest to the Fermi level [38]. The dispersion relation for a finite wave vector **k** is expressed by the following Hamiltonian [38],

$$H(\mathrm{k}) = \epsilon_0(\mathrm{k})\mathrm{I}_{4\times4} + \begin{pmatrix} M(k) & A_1k_z & 0 & A_2k_- \\ A_1k_z & -M(k) & A_2k_- & 0 \\ 0 & A_2k_+ & M(k) & -A_1k_z \\ A_2k_+ & 0 & -A_1k_z & -M(k) \end{pmatrix} \quad (2.1)$$

Here, $k_\pm = k_x \pm ik_y$, $\epsilon_0(\mathrm{k}) = C + D_1k_z^2 + D_2(k_x^2 + k_y^2)$ and $\mathrm{M(k)} = M - B_1k_z^2 - B_2(k_x^2 + k_y^2)$ [8]. With the parameters given in ref. [37], the band structure of Bi_2Se_3 obtained from the model matches well with the *ab initio* calculations. The Quantum Well (QW) bandgap opening shows good agreement with experimental observations [44]. However, we observe the inadequacies of the model when we apply the parameters to Bi_2Te_3 and Sb_2Te_3. In Fig. 2.3, we show the comparison of the bulk E-k dispersion diagram using the parameters in ref. [37] with *ab initio* calculations around the Γ point.

Table 2.1. Parameters for Bi_2Te_3 and Sb_2Te_3

Parameters	Bi_2Te_3 parameters ref [37]	Tuned parameters for Bi_2Te_3	Sb_2Te_3 parameters ref [37]	Tuned parameters for Sb_2Te_3
M (eV)	-0.3	-0.3	-0.22	-0.22
A1 (eV- Å)	0.3	0.3	0.84	0.84
A2 (eV- Å)	2.87	2.303	3.4	3.4
B1(eV- Å²)	-2.79	- 3.79	-19.64	- 19.64
B2 (eV- Å²)	-57.38	-57.38	-48.51	-48.51
C (eV)	-0.18	-0.18	0.001	0.001
D1 (eV - Å²)	6.55	0.3	-12.39	-15.39
D2 (eV - Å²)	49.68	49.68	-10.78	-10.78

We notice that the k.p band structures of Bi_2Te_3 and Sb_2Te_3 do not sufficiently match with the ab initio calculations. In addition, when we construct a z-confined thin quantum well band structure, we observe that the conduction and valence bands overlap, which is incorrect. It could be a direct consequence of the inaccurate parameters. We also vary the quantum well thickness from 1 nm to 6 nm and measure the bandgap opening up at the Γ point and find that it does not show

sufficient match with the experimental data [45][46]. Therefore, we tuned the parameter set of ref. [37] in a trial and error method until we achieved a better match with the ab initio calculations for Bi_2Te_3 and Sb_2Te_3. The tuned parameters are listed in Table 2.1.

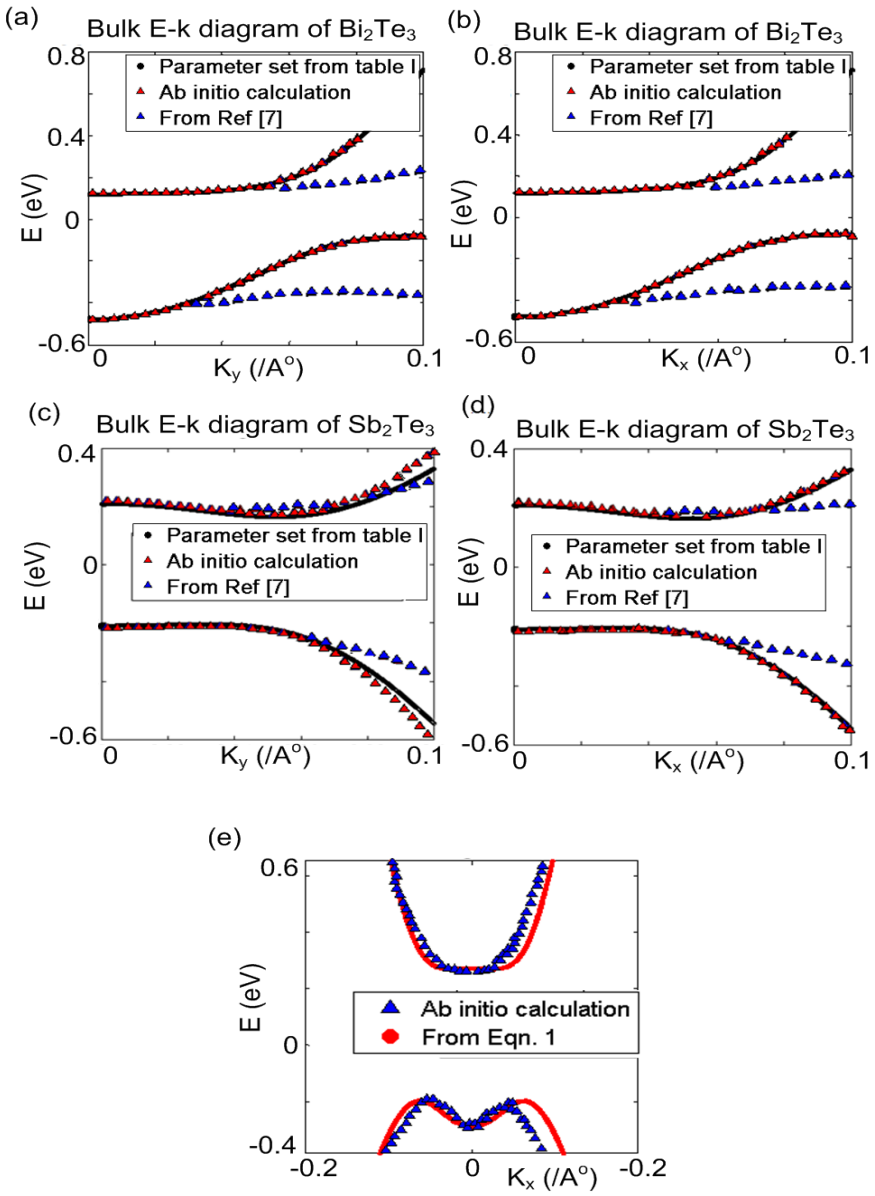

Fig. 2.3: Bulk band diagram comparison of (a) Bi_2Te_3 along k_y (b) Bi_2Te_3 along k_x (c) Sb_2Te_3 along k_y (d) Sb_2Te_3 along k_x and (e) Bi_2Se_3 along k_x. (*Ab initio* calculations are shown in reference [37]).

2.2.2 Surface Hamiltonian Modeling Including External Perturbations

As discussed earlier, for electrical transport calculations, it is sufficient to model the Hamiltonian at the surface in the vicinity of the Γ point [38][47]. We first discuss the Hamiltonian for modeling the TI surface without any perturbations. The top and bottom surfaces of a TI are modeled by a simple Hamiltonian (small 4x4 Hamiltonian with all diagonal elements as zero) as [48],

$$H_D(\mathbf{k}) = \begin{pmatrix} 0 & iv_F k_- & m_k^* & 0 \\ -iv_F k_+ & 0 & 0 & m_k^* \\ m_k & 0 & 0 & -iv_F k_- \\ 0 & m_k & iv_F k_+ & 0 \end{pmatrix} \tag{2.2}$$

v_F is the Fermi velocity at the TI surface. The basis of the Hamiltonian are $|t\uparrow\rangle, |t\downarrow\rangle, |b\uparrow\rangle$ and $|b\downarrow\rangle$ where t and b denote the top and the bottom surfaces respectively, and m_k is the tunneling effect between the top and the bottom surfaces.

It can be seen from Fig. 2.2 that the spin-transfer torque (STT) acting on the FM layer arises due to the current flow through the top surface. Therefore, only the Hamiltonian for the top surface is required for transport calculations and the tunneling between the top and bottom surfaces can be ignored. Hence, the effective Hamiltonian can be written as,

$$H_D^{eff}(k) = \begin{pmatrix} 0 & iv_F k_- \\ -iv_F k_+ & 0 \end{pmatrix} \tag{2.3}$$

Note that, it is a Dirac Hamiltonian of the form, $H = v_F(\hat{z} \times \vec{\sigma}).\vec{k}$ ($\vec{\sigma}$ is the Pauli spin matrix, and $k = k_x + k_y$), and only the Dirac type surface states are modeled. Consequently, the Hamiltonian captures the Dirac cone at the Γ point of the TI. The Hamiltonian is then modified in the following way to include the Fermi level.

$$H_D^{eff}(k) = \begin{pmatrix} \mu & iv_F k_- \\ -iv_F k_+ & \mu \end{pmatrix} \tag{2.4}$$

μ denotes the position of the Fermi level. Quantum confinement in the z-direction opens up a bandgap at the Dirac point [35] which is represented as Δ_{conf}. When an FM is placed on top of a TI surface, the exchange coupling energy needs to be considered as well. The exchange coupling arises as the spin of the TI surface state is coupled with the FM moment [49]. It results in increasing the bandgap opening at the Dirac point and is represented by Δ_{ex}. The bandgap opening is present when the top FM layer has an out-of-plane i.e., z-directed magnetization.

However, for in-plane magnetization, though strong exchange coupling may exist at the surface, no bandgap opening has been observed [50]. The combined bandgap opening is represented as: $\Delta_{gap} = \Delta_{conf} + \Delta_{ex}$. It can be included in the Hamiltonian as follows.

$$H_D^{eff}(k) = \begin{pmatrix} \mu + \Delta_{gap} & iv_F k_- \\ -iv_F k_+ & \mu - \Delta_{gap} \end{pmatrix} \quad (2.5)$$

There will be some effects in the interface due to the orbital overlapping between the TI and the FM layers. Therefore, a 20 band $sp^3d^5s^*$-SO tight-binding model will give more precise results. However, it is computationally very expensive. Therefore, we have only modeled the major effects that impact the surface transport properties (Dirac cone, Rashba effect, exchange coupling, Fermi velocity, external magnetic field, surface scattering etc.). Moreover, since the transport takes place through the surface of the TI, our 2D surface Hamiltonian is adequate to account for the 3D effects.

When electrical current flows through the surface of a TI, two types of spin-orbit torques (SOT) work on the FM layer – the field like SOT and the spin-transfer like SOT [40]. The field-like SOT is proportional to the exchange coupling [49]. Since the surface Hamiltonian of eqn. (2.5) includes the effect of exchange coupling energy, it can be used to calculate the field like SOT. It has been experimentally observed that the field-like torque is usually several orders of magnitude lower than the Slonczewski STT [10]. The Slonczewski STT arises due to the Rashba Spin-Orbit coupling (SOC) in a two-dimensional electron gas. Rashba SOC can be modeled as, $H_{Rashba} = \frac{p^2}{2m} - \frac{\lambda}{\hbar}\vec{S}.(\hat{z} \times \vec{p})$ [51] where p is the momentum, m is the effective mass, λ is the Rashba coupling parameter and $\vec{S}$ is the Pauli spin matrix. In our model, the perturbed surface state Hamiltonian is used to capture the Rashba SOC as shown below.

$$H_{surface}^{eff}(k) = \begin{pmatrix} B_1\left(k_x^2 + k_y^2\right) + \mu + \Delta_{gap} & i(v_F k_- - \lambda k_-) \\ -i(v_F k_- - \lambda k_-) & -B_2\left(k_x^2 + k_y^2\right) + \mu - \Delta_{gap} \end{pmatrix} \quad (2.6)$$

B_1 and B_2 are two fitting parameters for modeling the Rashba splitting of 2D surface electron gas with the unit of eV-Ang^2. Exact values of B_1 and B_2 are determined by matching the surface band diagram with the z-confined 3D Quantum Well (QW) band structure. Additionally, the interfacial states between the TI and FM affect the conductivity and the total spin current at the TI surface. For example, in a Permalloy/Bi_2Se_3 heterostructure, Permalloy is a face-centered

cubic structure (lattice constant ~0.355 nm) [52] whereas Bi_2Se_3 is a rhombohedral crystal with hexagonal supercell (lattice constants: a = 0.4318 nm and c = 2.864 nm) [38]. Including Rashba effect and the changed Fermi velocity at the surface due to the mismatch in lattice constants, the Hamiltonian can be modified in the following way.

$$H_{surface}^{eff}(k) = \begin{pmatrix} B_1\left(k_x^2 + k_y^2\right) + \mu + \Delta_{gap} & Ak_- \\ Ak_+ & -B_2\left(k_x^2 + k_y^2\right) + \mu - \Delta_{gap} \end{pmatrix} \quad (2.7)$$

A is another fitting constant with a unit of eV-Ang. A includes the off-diagonal Rashba effect and the modified Fermi velocity. External magnetic fields can also act as a strong external perturbation on the TI surface states. Therefore, it is important to include the effect of it. The applied external magnetic field in any arbitrary direction can be represented by: $\overrightarrow{B_{ext}} = B$ (sin θ cos φ$\hat{x}$ + sin θ sin φ$\hat{y}$ + cos θ $\hat{z}$). If $\vec{A}$ is the vector potential of the magnetic field defined such that, $\overrightarrow{B_{ext}} = \nabla \times \vec{A}$, then the effect of the magnetic field can be included in the Hamiltonian by Peierls phase substitution, $k_{new} = k - \frac{e}{\hbar c} A$ [53]. Now, if the external constant magnetic field (B) is in-plane i.e. in the x-y plane (fig. 2.2) having an angle of φ with the x-axis, the vector magnetic potential or the Landau Gauge [53] can be expressed as $\vec{A}$ = (Bz sin φ, -Bz cos φ, 0) where z is the confined length along the z-axis. The wave vectors k_x and $k_y$are then transformed to: $k_{x,new} = k_x - \frac{e}{\hbar} Bz\, sin\varphi$ and $k_{y,new} = k_y + \frac{e}{\hbar} Bz\, cos\varphi$. For a particular confinement length (z) and constant magnetic field (B), Bz is a constant. Hence, the Landau Gauge depends only on the angle φ. Again, if the external magnetic field is in the x-direction then, $\vec{A} = (0, -\mathrm{Bz}, 0)$ and the wave vector k_x remains unchanged while, $k_{y,new} = k_y + \frac{e}{\hbar} Bz$. Similarly, for y-directed magnetic fields, the Landau gauge becomes: $\vec{A} = (\mathrm{Bz}, 0, 0)$, k_y remains unchanged while, $k_{x,new} = k_x - \frac{e}{\hbar} Bz$. Therefore, for an in-plane magnetic field, the Hamiltonian can be written as,

$$H_{surface}^{eff}(k) = \begin{pmatrix} B_1\left(k_{x,new}^2 + k_{y,new}^2\right) + \mu + \Delta_{gap} & Ak_- \\ Ak_+ & -B_2\left(k_{x,new}^2 + k_{y,new}^2\right) + \mu - \Delta_{gap} \end{pmatrix} \quad (2.8)$$

Here, $k_\pm = k_{x,new} \pm ik_{y,new}$. The out of plane i.e. the z-directed magnetic field gives rise to a

Landau Gauge, $\vec{A} = (-\mathrm{By}, 0, 0)$. In this case, the wave vector k_y remains unchanged and $k_{x,new} = k_x + \frac{e}{\hbar} By$. The choice of Landau gauge may vary for any magnetic field. Here we have used the simplest form of Landau gauge for computational simplicity.

2.2.3 Electrical Transport and Magnetization Dynamics

In general, the TI/FM bilayer heterostructures are small enough for applying the NEGF formalism of quantum transport [54]. We use the standard self-consistent 2D NEGF method [54] to determine the total current and the spin current at the TI surface. Using our proposed Hamiltonian from the previous section, we first calculate the retarded Green's function defined as,

$$G^R = [EI - H^{eff}_{surface}(k) - \sum_{c1} - \sum_{c2}]^{-1} \tag{2.9}$$

$\sum_{c1}$ and $\sum_{c2}$ are the self-energy matrices for the contacts. Using the retarded Green's function, the non-equilibrium Green's function can be written as,

$$G^n = G^R \sum^{in} G^A \tag{2.10}$$

G^A is the complex conjugate of G^R and $\sum^{in}$ is the strength of the contacts defined as: $\sum^{in} = [\Gamma_1]f_1 + [\Gamma_2]f_2$, where f_1, f_2 are the Fermi levels of the contacts and Γ_1, Γ_2 are defined as $\Gamma_1 = \mathrm{i}[\sum_{c1} - \sum_{c1}^{\dagger}]$ and $\Gamma_2 = \mathrm{i}[\sum_{c2} - \sum_{c2}^{\dagger}]$. Using these quantities, we finally calculate the charge current density.

$$J = \frac{2\pi}{ih} \int Real[Trace\,(H^{eff}_{surface} G^n - G^n H^{eff}_{surface})]\; dE \tag{2.11}$$

Next, the spin current flowing in the TI surface [55] is,

$$J_{s0} = \frac{2\pi}{ih} \int Real[Trace\,(S.(H^{eff}_{surface} G^n - G^n H^{eff}_{surface}))]\, dE \tag{2.12}$$

Spin current diffuses from the interface into the FM layer exerting a torque on it [35]. We then apply the charge and spin currents to the LLG equation with Slonczewski STT term. The magnetization dynamics can be represented as [56],

$$\frac{\partial \hat{m}}{\partial t} = -|\gamma| \hat{m} \times \overrightarrow{H_{eff}} + \alpha \hat{m} \times \frac{\partial \hat{m}}{\partial t} + \overrightarrow{Torque} \tag{2.13}$$

$\overrightarrow{H_{eff}}$ is the effective magnetic field acting on the ferromagnet, $\hat{m}$ is the unit vector pointing in the direction of magnetization of the FM layer, α is the damping constant, γ is the gyromagnetic

ratio, and $\overrightarrow{Torque}$ is the sum of the field-like torque and spin-transfer like SOT [40] acting on the FM. The field-like SOT can be calculated as $\vec{\tau}_{FL} = \Delta_{ex}\hat{m} \times \vec{n}_s$ [49], where $\vec{n}_s$ is the non-equilibrium spin density. $\vec{n}_s$ can be easily related to spin current density in the ferromagnetic layer as, $J_s = -\mathcal{D}\vec{\nabla}.\vec{n}_s$ [57] where $\mathcal{D}$ is the diffusion coefficient of spin inside the FM layer. On the other hand, spin-transfer like SOT is defined as the spatial change of the spin current. It can be expressed as [57]:

$$\vec{\tau}_{ST} = \frac{1}{V}\iiint\left(-\vec{\nabla}J_s - \frac{1}{\tau_{sf}}\vec{n}_s\right)dV \tag{2.14}$$

V is the volume of the ferromagnet and τ_{sf} is the spin relaxation time. As shown in Fig. 2.2, spin current diffuses in the z-direction into the FM layer. Therefore eqn. (2.14) can be simplified to:

$$\vec{\tau}_{ST} = \frac{1}{d}\int_0^d\left(-\overrightarrow{\nabla_z}J_s - \frac{1}{\tau_{sf}}\vec{n}_s\right)dz \tag{2.15}$$

d is the thickness of the FM layer. Here, torque consists of both in-plane and out-of-plane components. In order to solve the equation, we first derive an expression for $\vec{n}_s$. If we consider the diffusion equation for the spin diffusion into the FM layer we can write during steady-state [58]:

$$\overrightarrow{\nabla}J_s = -\frac{1}{\tau_j}\vec{n}_s \times \hat{m} - \frac{1}{\tau_\phi}\hat{m} \times (\vec{n}_s \times \hat{m}) - \frac{1}{\tau_{sf}}\vec{n}_s \tag{2.16}$$

τ_j is the spin precession time and τ_φ is the spin decoherence time. The boundary conditions for solving the equation are: $J_s(0) = pJ_{s0}$ (p is the spin injection efficiency from the interface into the FM layer) and $J_s(d) = 0$. Moreover, as we have stated earlier, spin diffuses in the z-direction; hence, we can assume that the spin variation only exists along the z-axis. Spin current at the interface has both the in-plane and out-of-plane components i.e. $J_s(0) = J_{s,II}(0) + iJ_{s,\perp}(0)$. Using these conditions, we solve eqn. (2.16) and get the following solution for the non-equilibrium spin density.

$$n_{s,II} + in_{s,\perp} = \left(C_1 exp\left(-\frac{z}{L}\right) + C_2 exp\left(\frac{z}{L}\right)\right) \tag{2.17}$$

L is defined as, $\frac{1}{L^2} = \frac{1}{\lambda_{sf}^2} + \frac{1}{\lambda_\phi^2} - \frac{i}{\lambda_j^2}$ [57]. λ_{sf}, λ_j and λ_φ are spin relaxation, spin precession and spin decoherence length inside the FM layer, respectively. Using the boundary conditions we get $C_1 = -\frac{n_{s0}\exp(\frac{d}{L})}{\exp(\frac{-d}{L})-\exp(\frac{d}{L})}$ and $C_2 = \frac{n_{s0}\exp(\frac{d}{L})}{\exp(\frac{-d}{L})-\exp(\frac{d}{L})}$. Here n_{s0} is the non-equilibrium spin density at

the bottom of the FM layer (where it touches the TI). n_{s0} can be related to spin current density at the interface by the equation, $n_{s0} = \frac{pLJ_{s0}}{D}$ [57]. Therefore eqn. (2.17) can be written as,

$$n_{s,II} + in_{s,\perp} = n_{s0}\left(\frac{\sinh\left(\frac{d-z}{L}\right)}{\sinh\left(\frac{d}{L}\right)}\right) = \frac{pJ_{s0}L}{D}\left(\frac{\sinh\left(\frac{d-z}{L}\right)}{\sinh\left(\frac{d}{L}\right)}\right) \quad (2.18)$$

Now, the spin-transfer torque can be written as,

$$\tau_{ST} = \frac{1}{d}\int_0^d \left(-\frac{n_{s0}D}{L^2}\frac{\sinh(\frac{d-z}{L})}{\sinh(\frac{d}{L})} - \frac{n_{s0}}{\tau_{sf}}\frac{\sinh(\frac{d-z}{L})}{\sinh(\frac{d}{L})}\right)dz \quad (2.19)$$

The diffusion coefficient is related to spin relaxation length by the Einstein-Smoluchowski equation [57] as, $D\tau_{sf} = \lambda_{sf}^2$. Therefore, the torque can be rewritten as,

$$\tau_{sT,II} + i\tau_{sT,\perp} = \frac{pJ_{s0}L^2}{d}\left(\frac{1}{\lambda_\phi^2} - \frac{i}{\lambda_j^2}\right)\frac{\cosh\left(\frac{d}{L}\right)-1}{\sinh(\frac{d}{L})} \quad (2.20)$$

For the TI/FM heterostructure, besides the field-like and the spin-transfer like spin-orbit torque, there is another important torque working at the heterostructure interface. It is called the anti-damping torque which arises due to the Berry curvature [58]. It appears because the carrier spins experience two effective magnetic fields due to the FM layer magnetization and the applied electric field. As a result of these two effective B-fields, carrier spins become inclined towards the z-axis and produce an anti-damping torque. The torque can be incorporated in LLGS equation via the Gilbert damping constant, α. When the applied electric field and FM layer magnetization is perpendicular to each other there will be no anti-damping torque [62] and α is large as shown in our first simulated structure (Sec. III).

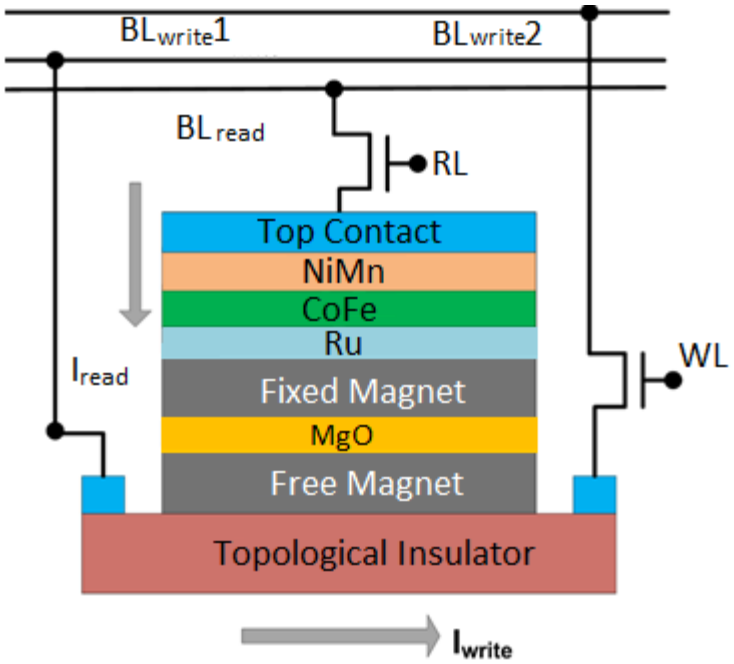

Fig. 2.4: Diagram of the proposed memory cell.

On the contrary, when the FM layer magnetization is not perpendicular to the applied electric field, α is small as calculated in our second simulated structure. Our calculation of α for both the cases agrees well with experimental observations [35][40].

2.3 Exploring Memory Bit Cells and Devices

2.3.1 Memory Bit Cell Structure

In Fig. 2.4, we propose a memory cell using TI/FM bilayer heterostructure. The memory cell has three layers. The first layer is an MTJ with TI at the bottom for switching the free magnetic layer. The write current flows through the TI, and depending on the direction of the current, the free layer is expected to switch, leading to a change in the tunneling magnetoresistance (TMR), which can be interpreted as binary '1' or '0', accordingly. The second layer is the antiferromagnetic (AFM) layer (Ni-Mn) which stabilizes the magnetization of the fixed magnet. The third layer comprising of Ruthenium (Ru) and CoFe is called the synthetic antiferromagnetic (SAF) layer and it fixes the magnetization of the fixed magnetic layer by canceling the stray fields around it [59]. In the proposed device, the CoFe, through nonmagnetic material Ru, is exchange coupled to the free magnetic layer [59]. In Fig. 2.4, we also show the read-write circuitry. The top terminal is connected to read bit line BL_{read} via an access transistor controlled

by a read line (RL). Read operation is performed by making the RL and BL_{read} high and BL_{write1} low to pass a read current through the MTJ. Two terminals at the two ends of the TI are connected to two write lines via pass transistor for allowing current flow in both directions to get the alternate magnetization switching. The pass transistor is controlled via the word line (WL). Let us now explore and analyze three different TI/FM combinations for this structure.

2.3.2 Cr Doped $(Bi_{0.5}Sb_{0.5})_2Te_3$/$(Bi_{0.5}Sb_{0.5})_2Te_3$ Based Memory

We first validate our model with the experiment from ref. [10]. Here a magnetically doped (Cr doped $(Bi_{0.5}Sb_{0.5})_2Te_3$) TI is used as the FM layer at very low temperature (1.9 K) since the magnetically doped TI's Curie temperature is well below the room temperature. In the experiment, a 6 nm thick Cr doped $(Bi_{0.5}Sb_{0.5})_2Te_3$ is stacked over a 3 nm thick $(Bi_{0.5}Sb_{0.5})_2Te_3$ [40]. In a 3nm thick $(Bi_{0.5}Sb_{0.5})_2Te_3$, due to surface state delocalization, Bi_2Te_3 and Sb_2Te_3 quantum wells have larger bandgap opening (Δ_{conf}) than Bi_2Se_3 [44]-[46].Using the parameters in Table 2.1, we have calculated the bandgap opening of Bi_2Te_3 and Sb_2Te_3 quantum wells separately for different confinement lengths and compared with the experimental results [45][46] (Fig. 2.5). We find that 3 nm quantum wells of Bi_2Te_3 and Sb_2Te_3 have bandgap openings of 85 meV and 35 meV, respectively. Using a mole fraction of 0.5, we can assume that the gap opening of 3 nm thick $(Bi_{0.5}Sb_{0.5})_2Te_3$ quantum well is ~60 meV (0.5*85 + 0.5*35). We have also plotted the band diagram of a 3 nm thick $(Bi_{0.5}Sb_{0.5})_2Te_3$ quantum well (Fig. 2.6) using Eqn. (2.1). The quantum confinement gap is ~$\mathbf{55}\,\boldsymbol{meV}$ near the Dirac cone which is very close to the above-calculated value. In order to model this experiment, we use, $\Delta_{conf} = \mathbf{30}\,\boldsymbol{meV}$ in eqn. (2.8) because this not only pulls up the conduction band by the amount of Δ_{conf} but also pulls the valence band down by the same amount. Again in eqn. (2.8), for this structure, parameter A can be represented as, $\boldsymbol{A} = \hbar(\boldsymbol{v_F} - \boldsymbol{\lambda})$ where $\boldsymbol{v_F}$ is the Fermi velocity and $\boldsymbol{\lambda}$ is the Rashba coupling parameter. Fermi velocity in Bi_2Te_3 and Sb_2Te_3 are measured as ~$\mathbf{3.5 \times 10^5}\,\boldsymbol{ms^{-1}}$ [11] and ~$\mathbf{4.3 \times 10^5}\,\boldsymbol{ms^{-1}}$ [60], respectively. Therefore, in $(Bi_{0.5}Sb_{0.5})_2Te_3$, the Fermi velocity can be written as, $\mathbf{0.5} \times (\mathbf{3.5 \times 10^5 + 4.3 \times 10^5}) = \mathbf{3.9 \times 10^5}\,\boldsymbol{ms^{-1}}$ resulting in $\hbar v_F$ = 2.57 eV-Å. Tuning $\boldsymbol{\lambda}$ we get A = 3.2 eV-Å. To match the band diagrams, we have determined the fitting parameters, $B_1 = B_2$ = 0.01 eV-$Å^2$, and the Fermi level, $\boldsymbol{\mu} = \mathbf{-0.247}\,\boldsymbol{eV}$.

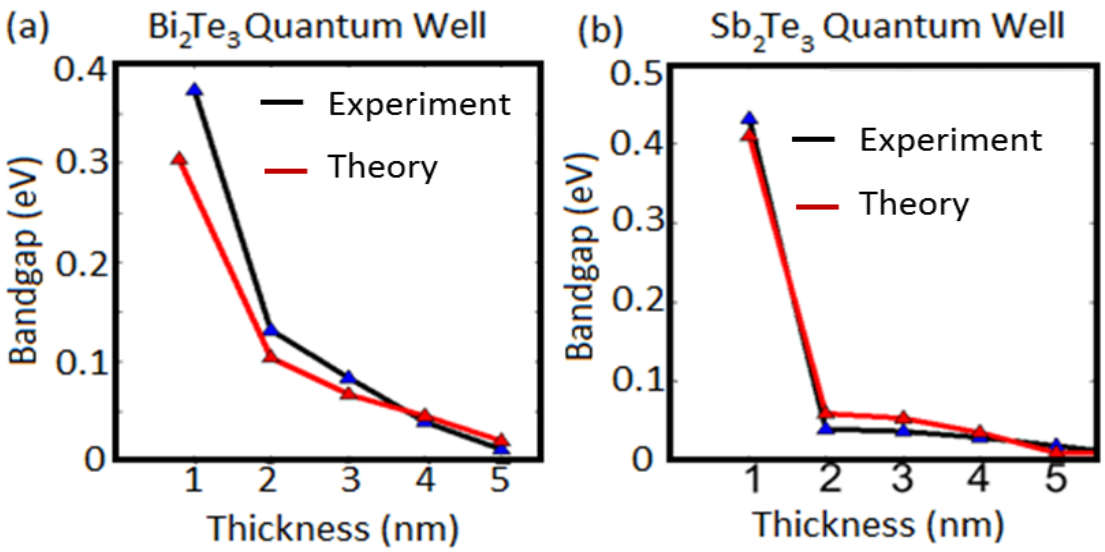

Fig. 2.5: Comparison of bandgap vs $(Bi_{0.5}Sb_{0.5})_2Te_3$ quantum well thickness between theoretical model using table 2.1 and experimental values [11] [12].

Using these parameters, we have plotted and matched the 3D band diagram of a 3 nm thick z-confined $(Bi_{0.5}Sb_{0.5})_2Te_3$ quantum well and the corresponding surface band diagram as shown in Fig. 2.6. Next, we use a 100 nm × 100 nm surface dimension of $(Bi_{0.5}Sb_{0.5})_2Te_3$ for the NEGF and LLGS modeling. This dimension ensures that the quantum confinement along the x and the y-axis do not create any noticeable effects on the band diagram. Using the 2D surface Hamiltonian, Δ_{ex} is tuned to match the conductivity ($\Delta_{ex} = \mathbf{170\ meV}$) and without considering the external magnetic field, we get a conductivity of $\sim\mathbf{225\ S\ cm^{-1}}$ (experimental value $\sim 219\ S\ cm^{-1}$). We also observe a high out of plane spin Hall angle of 0.91. For this structure, almost half of the current shunts through the top magnetic layer. So, for our device simulations, to reduce the conductivity of the FM layer, the thickness of the FM layer is reduced to 3 nm. Similarly, for increasing the conductivity, the thickness of the bottom $(Bi_{0.5}Sb_{0.5})_2Te_3$ layer is increased to 20 nm so that, $\Delta_{conf} = 0\ eV$. For such a structure, the amount of shunting current is only 5%-6% of the total current. Only 0.2 V DC applied to the contacts (Fig. 2.2) is sufficient for switching this structure consuming ~120 fJ/bit energy and it takes ~6 ns to switch. The timing diagram and magnetization diagram is shown in Fig. 2.7. The main drawback of this memory structure is that it only operates at very low temperatures.

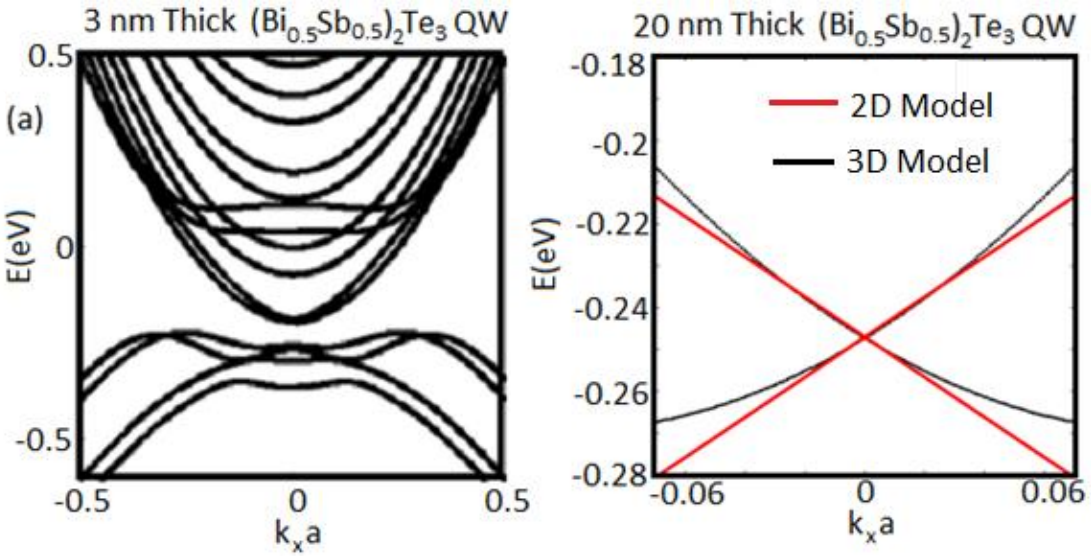

Fig. 2.6: (Left) E-k diagram of a 3nm thick $(Bi_{0.5}Sb_{0.5})_2Te_3$ quantum well. The well is confined in the z-direction. (Right) Band diagram matching of 3D $(Bi_{0.5}Sb_{0.5})_2Te_3$ quantum well and 2D surface modeling for 20nm QW ('a' = lattice constant).

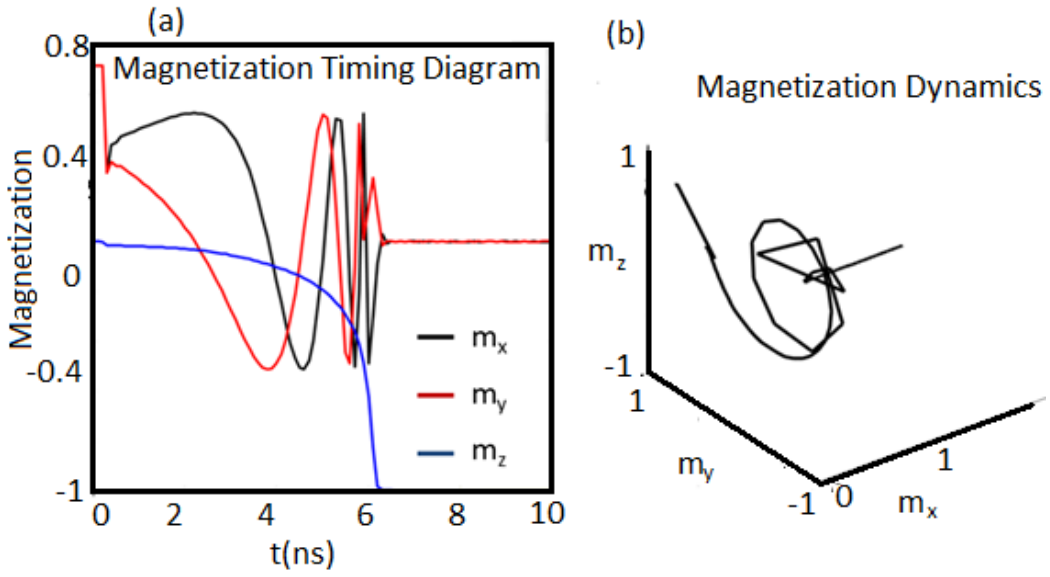

Fig. 2.7: (a) Magnetization Timing diagram, and (b) magnetization dynamics of Cr doped $(Bi_{0.5}Sb_{0.5})_2Te_3/(Bi_{0.5}Sb_{0.5})_2Te_3$ heterostructure based memory.

2.3.3 Permalloy/Bi_2Se_3 Based Memory Structure

For room temperature operation, we here validate our model with an experiment where a Permalloy is coupled with Bi_2Se_3 which gives rise to a high spin Hall angle [35][36]. In the experiment, 8 nm and 16 nm thick quantum wells of Bi_2Se_3 were used [35]. If we consider the

quantum confinement effect, the bandgap at Dirac point is negligible (~0.3 meV for 8 nm thick well and ~0.7 μeV for 16 nm thick well).

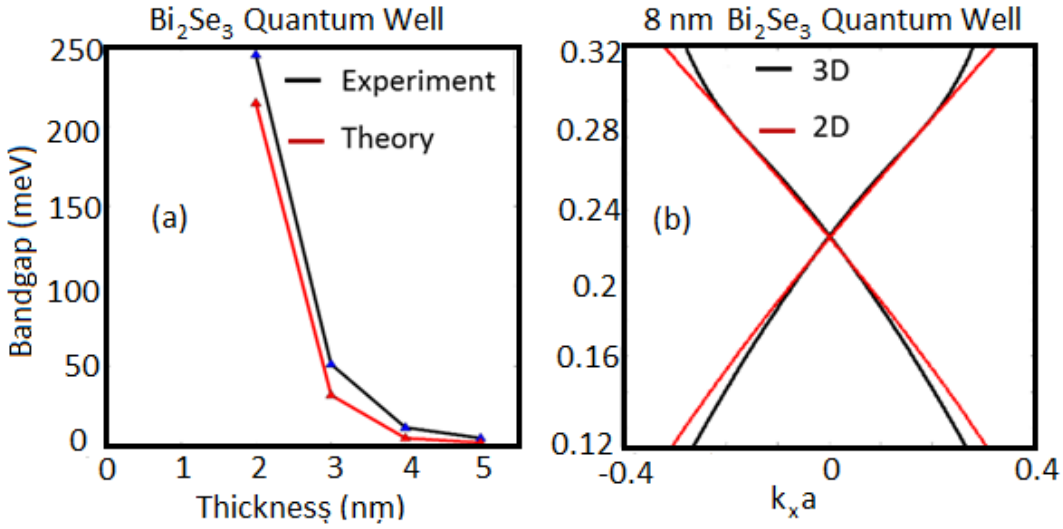

Fig. 2.8: (a) Comparison of Bi_2Se_3 quantum well thickness between the theoretical model and experimental values [44], (b) Band diagram matching of 3D Bi_2Se_3 and 2D surface modeling.

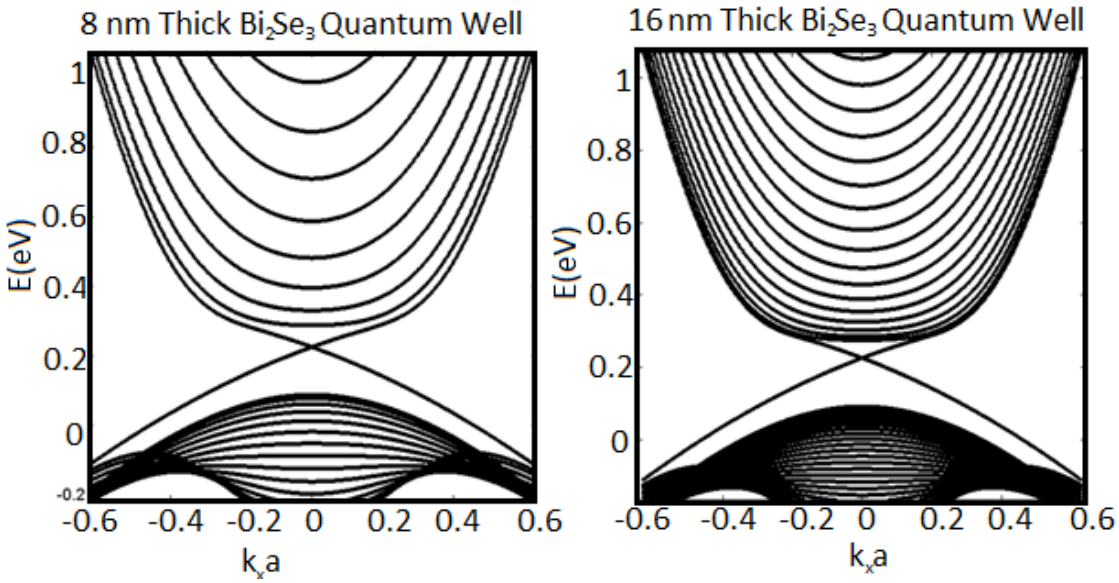

Fig. 2.9: E-k diagrams of 8nm (left) and 16nm (right) thick Bi_2Se_3 quantum wells.

In fig. 2.8, we have shown the effect of quantum confinement in Bi_2Se_3 for different quantum well thicknesses and it is evident that the confinement effect is prominent for thicknesses less than or equal to 6 nm [14]. Therefore, for these cases, we take, $\Delta_{conf} = 0$. From eqn. (2.1), the E-

k diagrams of 8 nm and 16 nm quantum wells of Bi_2Se_3 are calculated and shown in Fig. 2.9. For matching the band structure we have calculated the fitting parameter A to be 1.69 eV-Å in eqn (2.8).

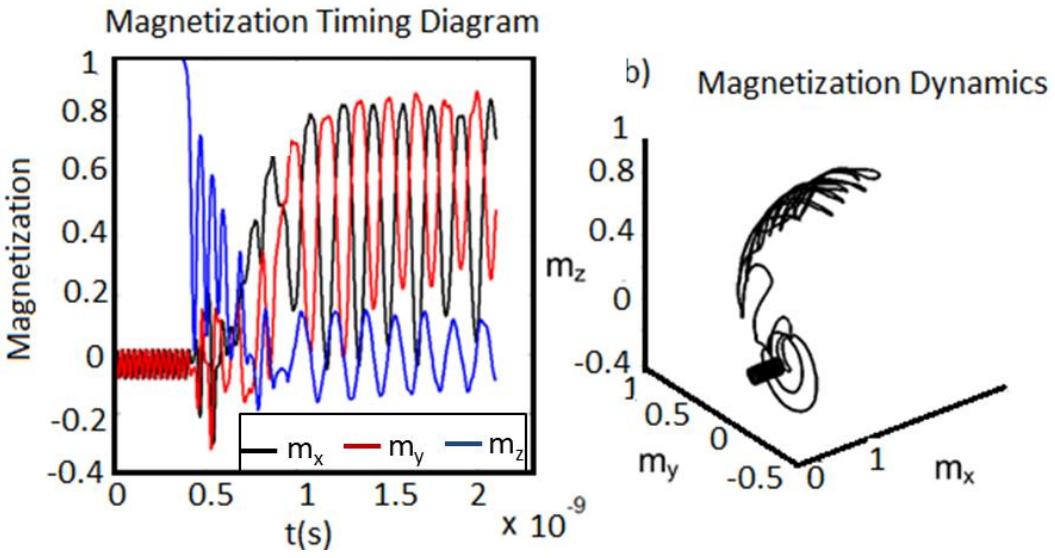

Fig. 2.10: (Left) Magnetization Timing diagram and (right) magnetization dynamics of Permalloy/Bi_2Se_3 heterostructure and matching with ref [35].

Here the conduction and valence bands are not symmetric. Therefore, the other fitting parameters, B1 and B2 are different. We have calculated B_1 = 5 eV-Å^2 and B_2 = 9 eV-Å^2 for matching with the 3D band diagram. The Fermi level, $\mu = -0.225\ eV$. Using these parameters, the comparison of 3D quantum well and 2D surface band diagram is shown in fig. 2.8(b). In order to make the band structure free from quantum confinement in the x and the y directions, we have considered a large enough (60 nm × 60 nm) surface dimension for the NEGF and LLGS modeling. We observe high in-plane and out of plane spin Hall angles of 1.1 and 1.03 respectively for 16 nm thick Bi_2Se_3, matching well with experimentally observed values of ~1.00 and 1.1 respectively [36]. Another important factor is the spin-transfer torque acting on the FM layer. Let us consider the spin efficiency at the interface, p = 1. In Permalloy, considering the spin diffusion length, λ_{sf} = 5nm [35], spin decoherence length, $\lambda_{\varphi} = 1nm$ [35] and spin precession length, $\lambda_j = 1nm$ [35], we have calculated the in-plane and out-of-plane torque to be 5.9×10^{-4} T and 1.2×10^{-5} T, respectively from eqn. (2.20) (experimental values of 2.7 $\times 10^{-5}$ T and 3.7×10^{-5} T).

Table 2.2. Parameters for LLG simulation (simulated in MuMax3 [61])

Parameter	Cr doped $(Bi_{0.5}Sb_{0.5})_2Te_3$ /$(Bi_{0.5}Sb_{0.5})_2Te_3$	Py / Bi_2Se_3	YIG / Bi_2Se_3
Sat. Mag. (Ms, A/m)	1.6×10^6 [40]	0.86×10^6 [62]	0.1418×10^6 [50]
Exchange Cons. (A_{ex}, J/m)	1.9×10^{-12}	1.3×10^{-11} [63]	1.92×10^{-12} [65]
Easy axis	z-axis [40]	45^0 with x-axis in X-Y plane [35]	z-axis
Anis. Cons. Ku (J/m^3)	7200 [40]	500 [64]	-2746 [50]
External Mag. Field	None	0.05 T to 0.09 T along easy axis	None
In-plane Spin Hall angle	0.85	1.1	0.71
Table 2.2 continued			
Out-of-plane Spin Hall angle	0.91	1.03	0.57
Gyromagnetic Ratio (rad/sT)	1.8×10^{11} [40]	1.71×10^{11} [64]	1.79×10^{11} [66]
Damping constant (α)	0.1 [40]	5.4×10^{-4}	3×10^{-4}

Using parameters in TABLE 2.2, we obtain the magnetization dynamics and observe oscillations in magnetization which is consistent with the experiments (fig. 2.10) for RF current. The main issue of the structure is the large amount of current shunting through the adjacent Permalloy (25 times higher than the current flowing through Bi_2Se_3 surface [35]). Applying the NEGF equation at a dc voltage of 0.25 V, the energy consumption is ~9.24 pJ/bit, which is orders of magnitude higher than current memory structures.

2.3.4 Yttrium Iron Garnet (YIG)/Bi_2Se_3 Based Memory

We analyze another structure for room temperature application with TI based memory by using YIG as the top FM layer. YIG is a Ferromagnetic Insulator (FI) with a Curie temperature of 550 K and a bandgap of 2.85 eV [50]. In spite of the fact that the YIG/Bi_2Se_3 interface is rather rough, which suppresses the Spin Hall angle, this structure can still be operated at a very low voltage. We first match the charge transport with a recent experiment on YIG/Bi_2Se_3 heterostructure [50] and then we apply our model to calculate the spin transport, spin-transfer torque and the magnetization dynamics. In order to avoid a significant modification of the transport properties in Bi_2Se_3 due to quantum confinement effect, we have chosen a 60 nm × 60 nm × 8 nm slab of Bi_2Se_3. On top of this layer, a 60 nm × 60 nm × 1.5 nm layer of YIG is placed. Due to the rough interface, the Fermi velocity is suppressed and in eqn. 2.7, A is reduced to 1.23 eV-Å, while the other two fitting parameters are, B_1 = 4.5 eV-Å^2 and B_2 = 13 eV-Å^2. The out-of-plane magnetization of YIG results in a strong exchange coupling which opens up a bandgap of 89 meV. The sheet resistance of Bi_2Se_3 interface is measured to be 606 ohm/sq, which is close to the experimentally observed value of 625 ohm/sq [50]. Now, for applying the LLGS equation, we first determine the STT from eqn. (2.20) and we find the in-plane torque to be 1.9485×10^{-5} T and out-of-plane torque to be 1.6511×10^{-5} T (YIG spin diffusion length, λ_{sf} = 35nm [67], spin decoherence length, λ_{φ} = 9nm [67] and spin precession length, λ_j = 3.4nm [67]). Using the parameters in Table 2.2 and applying a 0.2 V DC on the contacts, we solve the LLGS eqn. and find the YIG switches at ~1.1ns (Fig. 2.11). The critical current density (J_{c0}) of this structure can be expressed as [62]:

$$|J_{c0}| = \frac{2eM_s t_{free}\alpha\mu_0}{\hbar\theta_{SH}}\left(H_c + H_{demag}^{eff}\right) \qquad (2.21)$$

$\boldsymbol{M_s}$ is the saturation magnetization of the YIG layer, $\boldsymbol{t_{free}}$ is the YIG layer thickness, $\boldsymbol{H_c}$ is the critical magnetic field for switching the magnet and $\boldsymbol{H_{demag}^{eff}}$ is the effective demagnetization field. From eqn. (2.21), the critical current is determined to be ~1.742 x 10^9 Amp/m^2 which is quite low. This is primarily because of the high spin hall angle, low damping and low saturation magnetization. In Fig. 2.12(a) and 2.12(b), we have shown the charge current and spin currents, respectively with an applied voltage which show similar trends as reported in ref. [68]. It can be seen that the spin current is very small along the x-axis since the charge current is flowing along

the x-axis and the spin polarization is perpendicular to it. This memory structure consumes ~118.8 fJ/bit of energy at 0.2 V DC operating voltage, which can be further reduced for lower operating voltage at the cost of switching speed.

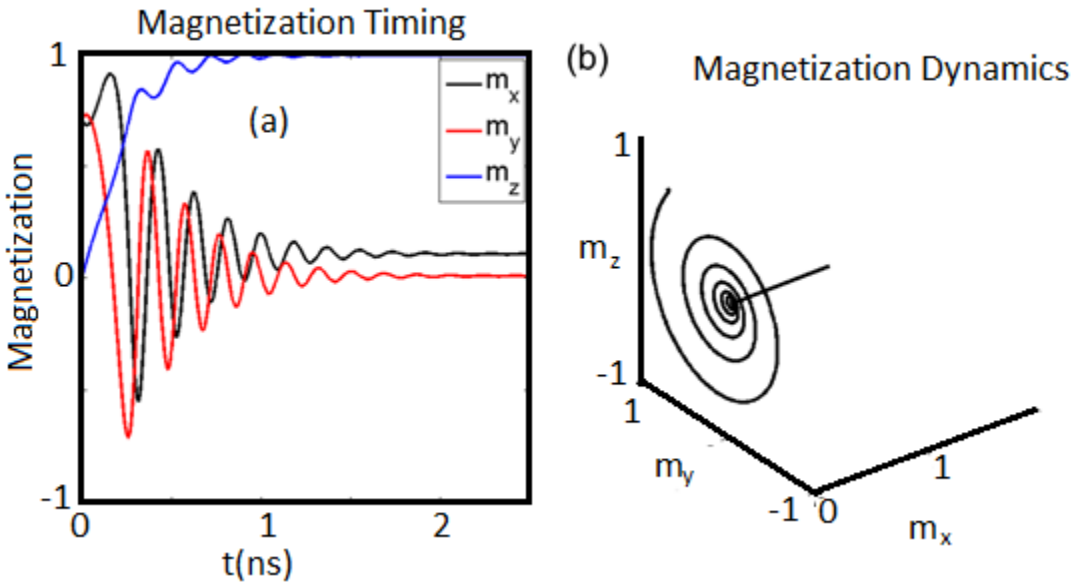

Fig. 2.11: (a) Magnetization Timing diagram and (b) magnetization dynamics of YIG/Bi_2Se_3 heterostructure based memory as shown in fig.2.4.

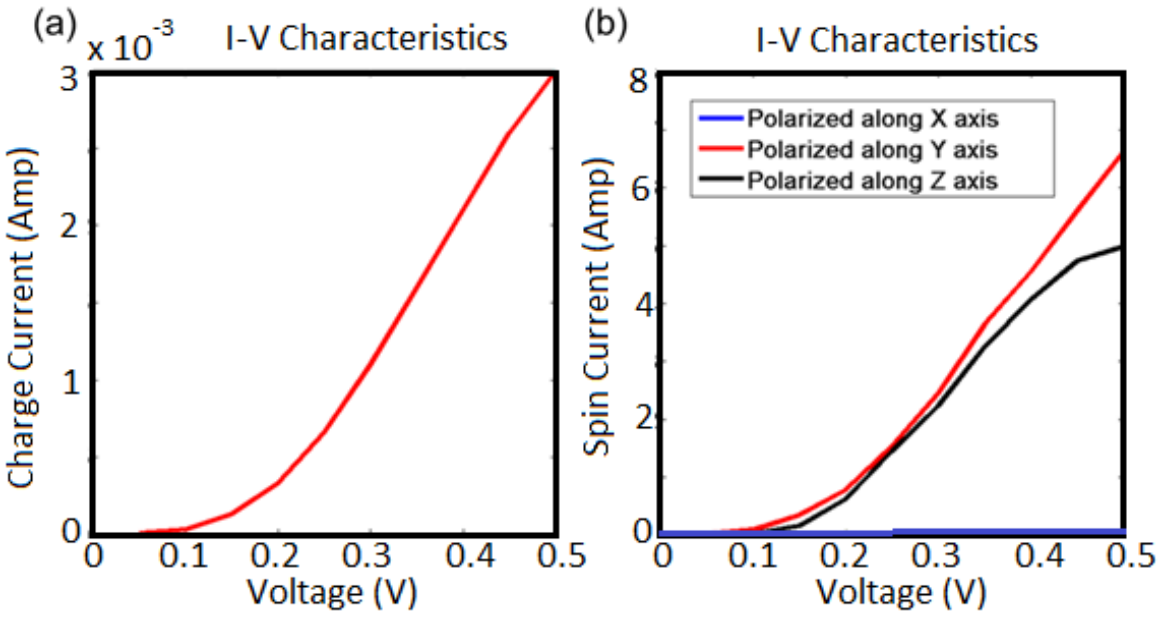

Fig. 2.12: (a) Charge current and (b) Spin current profile with voltage

2.3.5 Prospects and Challenges of TI Based Memory

The primary obstacles for real-world applications of TI based memory device are the current shunting through the FM layer and the functional capability of the structure to work at room temperature. As we have shown, the YIG based memory structure has the potential to solve both of these issues. Additionally, the expected critical current for switching YIG/ Bi_2Se_3 structure (~10^9 Amp/m^2) is found to be lower compared to the current required for SHM based switching (10^{10}-10^{11} Amp/m^2) [32]. Therefore, with the lower critical current density and the higher spin Hall angle, YIG based structure has the potential to be more energy-efficient than existing SHM based structures [32]. However, reducing the surface roughness will be the key challenge.

2.4 Conclusion

We proposed and analyzed TI/FM heterostructure based memory cell using three different TI/FM combinations. To do the analysis, we developed a simulation framework for TI/FM heterostructures and validated our model by benchmarking against experimental results. Our proposed model is computationally efficient because of using a 2×2 surface Hamiltonian and yet it produces good results. Our simulation results on YIG/ Bi_2Se_3 structure indicate that TI based memory devices can be energy efficient. Hence the YIG/ Bi_2Se_3 structure shows good promise and further experiments are needed to make the structure a viable one.

2.5 Summary

Topological Insulators (TI) are unique materials that have insulating bulk but conducting surface states. In this chapter, we propose a simulation framework for TI/Ferromagnet (FM) heterostructures that can capture the electronic band structure of a TI while calculating the transport properties. Our model differs from TI/FM models proposed in the literature in that it can account for the 3D band structure of TIs and the effects of exchange coupling and external magnetic field on the band structure. The proposed approach uses 2D surface Hamiltonian for TIs that includes quantum confinement effect calculated from 3D band diagram. We use the Hamiltonian with self-consistent non-equilibrium Green's functions (NEGF) formalism to determine the charge and spin transport in TI/FM heterostructures. Our calculations agree well

with experimental data and capture the unique features of a TI/FM heterostructure such as the spin Hall angle, spin conductivity etc. Next, we incorporate the results into Landau–Lifshitz–Gilbert–Slonczewski formulation to simulate the magnetization dynamics of an FM layer sitting on top of a TI. Finally, we evaluate the performance of three different TI/FM memory structures and show that TI based memories can be energy efficient if the shunting current through the FM layer is reduced.

3. TOPOLOGICAL SEMI-METAL SODIUM BISMUTH AS EFFICIENT SPIN INJECTOR IN CURRENT DRIVEN MAGNETIC TUNNEL

3.1 Comparison Between Spin-Hall Metal, Topological Insulator and Topological Semi-Metal

An integral part of SOT-MTJ is a non-magnetic spin injector that converts the charge current to spin current which diffuses from the spin injector into the MTJ free layer (fig. 3.1). The spin current applies spin-transfer torque on the MTJ free layer magnetic moments and thus, switches the magnetization direction [69,70]. Inefficiency in charge to spin current conversion is one of the major bottlenecks in SOT-MTJ.

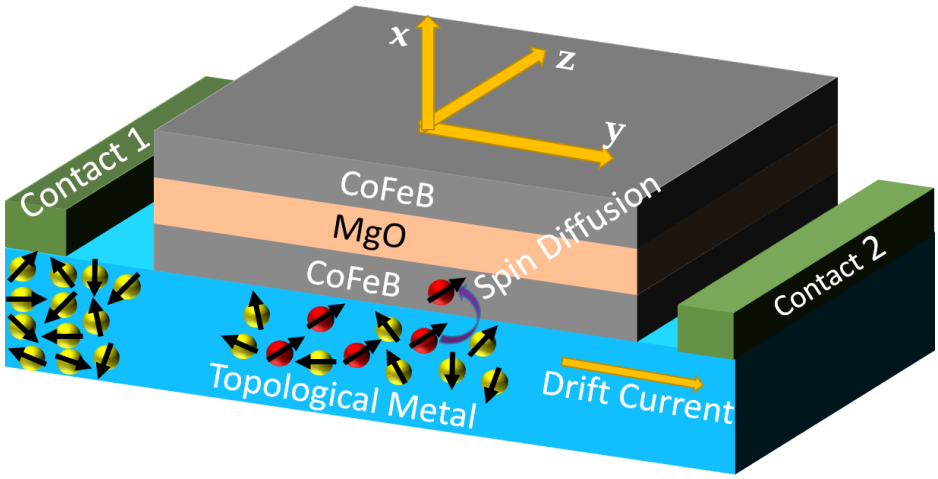

Fig. 3.1: Schematic diagram of a topological metal as a spin injector, injecting spin-polarized current to MTJ free layer.

Heavy spin Hall metals (HM) like Pt, β-W etc are the most popular choices as spin injectors in SOT-MTJs. One of the major drawbacks of HMs is the low charge current to spin current conversion ratio. Spin hall angle, the figure of merit that measures the charge current to spin current conversion efficiency in a spin injector, is defined as, $\theta_{SH} = \frac{2qJ_s}{\hbar J_c}$ [71]. J_s is the spin current density, J_c is the charge current density, q is the electron charge and $\hbar$ is the reduced Plank's constant. The spin Hall angle of Pt is 0.08 [72] which indicates that only 2.7% of the charge current is converted to spin current in Pt. Among the HMs, β-W exhibits the highest spin hall angle of 0.3 [72] which means around 9.9% of the charge current is converted to spin current

in β-W. Rest of the charge current has no contribution in MTJ switching operation and hence, is wasted.

Discovery of high charge current to spin current conversion efficiency in the topological insulator (TI) [72] opened up a new possibility of using TI as an efficient spin injector. Bi_2Se_3, a 3D TI, has a spin Hall angle of 1.1 [72] which means about 36.3% of the charge current is converted to spin current. Nevertheless, TI has low conductivity. The conductivity of TI is almost 25 times lower than that of Permalloy, a widely used MTJ free layer magnet [71]. Moreover, if the MTJ free layer magnet has perpendicular magnetic anisotropy, a gap opens up at the Dirac point of TI band structure further decreasing the TI conductivity [71,73]. Therefore, when TI is used as a spin injector, most of the charge current shunts through the adjacent MTJ free layer. The shunting current does not contribute to MTJ switching and hence, the use of TI as spin injector does not show any significant improvement in power consumption [71] as shown in the previous chapter. Use of ferromagnetic insulators like Yittrium Iron Garnett (YIG) as MTJ free layer reduces the shunting current but the topological insulator forms a very rough surface with YIG [71,74]. In 3D TI, bulk is insulating [39] and current only flows through the surface. A rough interface significantly reduces the spin Hall angle of TI [71].

In TIs, the charge current is converted to spin current due to strong spin-orbit coupling [71,75]. The recent discovery of topological semi-metal Na_3Bi [76,77,78] has also exhibited the property of having a significant amount of spin-orbit coupling leading to the presence of spin-polarized Fermi-arc [78]. Due to the spin polarization of the surface and bulk states, the application of an external electric field is expected to induce a macroscopic spin polarization at the surface and in the bulk of Na_3Bi [78] – a phenomenon known as the Edelstein effect. The presence of Fermi arcs in Dirac semimetals indicates that large Edelstein effect is expected in Na_3Bi. The Edelstein effect in Na_3Bi results in an efficient charge to spin current conversion. Our simulation shows that 15nm thick Na_3Bi quantum well, which is confined along the +x axis, exhibits a spin Hall angle of 0.9228. It signifies that Na_3Bi can convert 30.37% of charge current to spin current which is more efficient than heavy metals. Moreover, our simulation also exhibits that the room temperature resistivity of Na_3Bi (1.4×10^{-6} Ω-m) is 12.5 times lower than the resistivity of Bi_2Se_3 (room temperature resistivity of Bi_2Se_3 is 1.75×10^{-5} Ω-m [72]).

Ref [79] first predicted and modeled the topological gapless phase in topological semi-metal Na_3Bi with 4 band k.p Hamiltonian. In order to better capture the presence of spin-polarized

Fermi arc, we proposed and modeled an 8 band k.p Hamiltonian for Na_3Bi. We benchmarked the near Fermi level band diagram from our proposed Hamiltonian with DFT band structure considering spin-orbit coupling.

In this chapter, we extracted the Na_3Bi bandstructure via density functional theory (DFT). We used the spin-orbit generalized gradient approximations (SO-GGA) [80] method to calculate the spin-dependent band structure of Na_3Bi. We modeled and matched the SO-GGA band structure of Na_3Bi near the Fermi level with 8 band k.p model. The k.p Hamiltonian was used to calculate the charge and spin transport using quantum transport formalism. We applied the non-equilibrium Green's function method [81] of calculating spin current to determine the charge current to spin current conversion efficiency of Na_3Bi. Finally, we showed the comparison of iso-speed power consumption and iso-voltage switching speed during the write operation between Na_3Bi based MTJ and Pt and Na_3Bi based MTJs.

3.2 Modeling of Na_3Bi as Spin Injector

The charge current, while flowing through the Na_3Bi, becomes spin polarized due to strong spin-orbit coupling [78]. Spin current accumulates in the spin injector Na_3Bi layer, diffuses in the SOT-MTJ free layer and exerts two types of torque – field-like spin transfer torque and spin-transfer-like spin-orbit torque. The quantum transport calculation of charge and spin current through the spin injector layer involves a Hamiltonian that can generate the Fermi arc and topological gapless phase in Na_3Bi band structure [78]. Since electrical conduction only involves the near Fermi level energy bands, an 8 band k.p model can capture the topological semi-metal's rotation symmetry and time-reversal symmetry [78,79]. The near Fermi level band diagram of Na_3Bi is benchmarked with the bulk band structure of Na_3Bi which is constructed using DFT (SO-GGA) calculation. Na_3Bi has a hexagonal crystal structure and is a member of p63/mmc space group [78] as shown in figure 3.2a. Being a member of space group number 194, the lattice constants are a=5.448A^o, b=5.448A^o and c=9.655A^o [78].

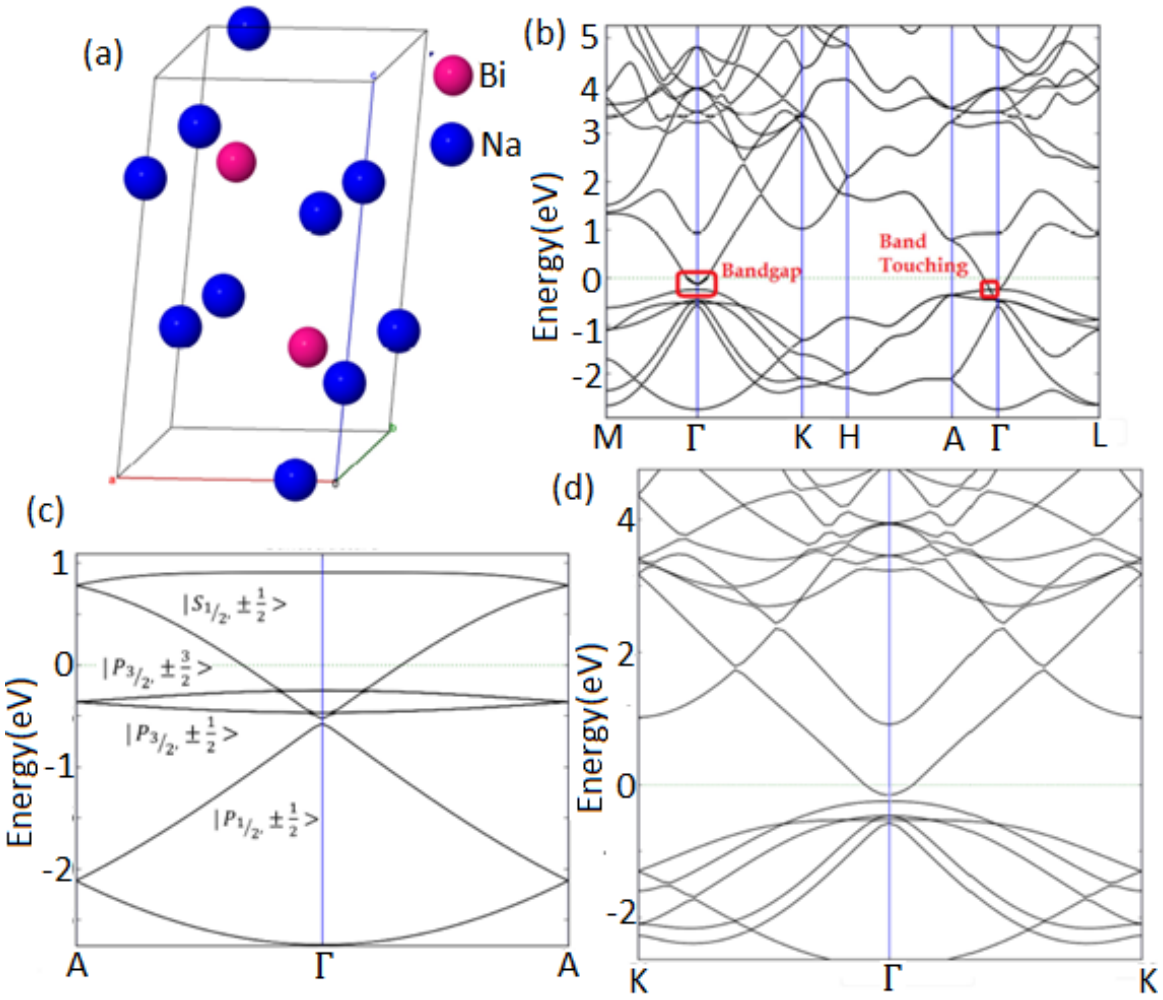

Fig. 3.2: (a) Schematic diagram of Na_3Bi crystal structure. (b) GGA band structure of Na_3Bi considering spin-orbit coupling. Note, projecting the band structure along M-Γ-K shows a small bandgap and there is no band inversion. Nevertheless, band diagram along A-Γ-L shows band inversion and hence, there is no bandgap i.e., conduction and valence band touch each other on both sides of Γ point. (c) Zoomed-in band diagram along A-Γ-A line to show the conduction and valence band crossing on both sides of Γ point when the band diagram is projected on [100] plane. The orbitals near the Fermi label are conduction band $|S_{12}, \pm\frac{1}{2}\rangle$, heavy hole band $|P_{32}, \pm\frac{3}{2}\rangle$, light hole band $|P_{32}, \pm\frac{1}{2}\rangle$ and split-off band $|P_{12}, \pm\frac{1}{2}\rangle$ (d) Zoomed-in band diagram along K-Γ-K line to show the bandgap when projected on [001] plane.

The SO-GGA calculation of Na_3Bi bulk band-structure is executed by creating a k-mesh of size $15 \times 15 \times 8$. K point sampling is done by Monkhorst Pack Grid [82]. The double Zeta polarized basis set [83] is used for SO-GGA calculation of both Sodium and Bismuth atoms. The simulation is done using full potential projected wave method as implemented in the Quantumwise package [84] and spin-orbit coupling is considered.

The SO-GGA band-structure of Na_3Bi is shown in figure 3.2b. The band-structure of Na_3Bi exhibits some interesting properties. Exploring the band structure projected on [100] plane along the +z-axis shows two Dirac points. The zoomed-in band-diagram along A-Γ-A is shown in figure 3.2c. The two Dirac points appear at two Γ′ points on both sides of Γ points along the z-axis. If we explore the band-diagram projected on [001] plane along the +x-axis, we can observe that the conduction band and the valence band do not touch each other. Na_3Bi band structure projection on the [001] plane shows no band structure inversion. It implies that the topological metal shows different conductivity and spin polarization property for different quantum well confinement. To extract the maximum benefit out of the Na_3Bi, we only considered a Na_3Bi slab confined along the x-axis while it is considered to be periodic along the y-axis and the z-axis.

$$\begin{vmatrix} \epsilon_0(k) + M(k) & A_1k_z & 0 & A_2k_- & 0 & 0 & \alpha & 0 \\ A_1k_z & \epsilon_0(k) - M(k & A_2k_- & 0 & 0 & 0 & 0 & \beta \\ 0 & A_2k_+ & \epsilon_0(k) + M(k & -A_1k_z & -\alpha & 0 & 0 & 0 \\ A_2k_+ & 0 & -A_1k_z & \epsilon_0(k) - M(k & 0 & -\beta & 0 & 0 \\ 0 & 0 & -\alpha^\dagger & 0 & -\epsilon_0(k) - M(k) & A_1k_z & & A_2k_- \\ 0 & 0 & 0 & -\beta^\dagger & A_1k_z & -\epsilon_0(k) + M(k & A_2k_- & 0 \\ \alpha^\dagger & 0 & 0 & 0 & 0 & A_2k_+ & -\epsilon_0(k) - M(k & -A_1k_z \\ 0 & \beta^\dagger & 0 & 0 & A_2k_+ & 0 & -A_1k_z & -\epsilon_0(k) + M(k \end{vmatrix}$$

Fig. 3.3: Proposed 8 band k.p model of Na_3Bi

In order to explore the charge to spin current conversion efficiency in Na_3Bi crystal slab cut along [100] plane, the band-diagram near the Fermi level is modeled by a simple 8×8 Hamiltonian. The eight basis sets for the 8×8 Hamiltonian are conduction s states $|S_{12}, \frac{1}{2}\rangle$ and $|S_{12}, -\frac{1}{2}\rangle$, heavy hole states $|P_{32}, \frac{3}{2}\rangle$ and $|P_{32}, -\frac{3}{2}\rangle$, light hole states $|P_{32}, \frac{1}{2}\rangle$ and $|P_{32}, -\frac{1}{2}\rangle$, split-off states $|P_{12}, \frac{1}{2}\rangle$ and $|P_{12}, -\frac{1}{2}\rangle$. The k.p Hamiltonian is written around the Γ point along A-Γ-A line. The resulting Hamiltonian can be written as shown in fig. 3.3 where $\epsilon_0(\boldsymbol{k})$, M($\boldsymbol{k}$), k_+ and k_-

are different wave vector dependent Hamiltonian terms expressed as, $\epsilon_0(k) = C + D_1k_z^2 + D_2k_\perp^2$, $M(k) = M_0 - B_1k_z^2 - B_2k_\perp^2$ and $k_\pm = k_x \pm ik_y$. The Hamiltonian is constructed assuming the relative Fermi energy level to be at 0eV. The fitting of the 8 band k.p Hamiltonian with the DFT band structure projected on [100] surface along the +z-axis near the Fermi level yields the value of Hamiltonian fitting parameters. Our fitting agrees well with ref [79]. Our simulation leads to C = -0.06379 eV, D_1 = 8.7497 eV-Ang^2, D_2 = -8.4011 eV-Ang^2, M = -0.0869 eV, B_1= -10.6513 eV-Ang^2, B_2 = -10.363 eV-Ang^2, A_1 = 2.7564 eV-Ang and A_2=2.46003 eV-Ang. The value of M, B_1 and B_2 is negative which creates the band inversion in 8 band k.p band structure. α and β are the zero-momentum fermion coupling pair parameters defined as $\alpha = \int \psi_{1\uparrow}\psi_{1\downarrow}dk$ and $\beta = \int \psi_{2\uparrow}\psi_{2\downarrow}dk$.. $\psi_{1\uparrow}$ and $\psi_{2\uparrow}$ are the up-spin wave functions of the inverted bands while $\psi_{1\downarrow}$ and $\psi_{2\downarrow}$ are the downspin wave functions of the inverted bands [85]. In our simulation, we have assumed that the coupling between fermions in Na_3Bi and fermions in the adjacent MTJ free layer magnet is negligible.

The Hamiltonian for the confinement of Na_3Bi slab along the x-axis (as shown in fig.3.1) can be modeled using finite difference method. The band diagram of 15nm thick Na_3Bi slab is shown in figure 3.4. The band diagram shows that the band inversion and conduction band - valence band crossing on both sides of the Γ point can be observed from figure 3.2. Moreover, the similarities can be observed between Na_3Bi bulk band diagram along A-Γ-A line and the band diagram of Na_3Bi slab confined along the x-axis (fig. 3.4). The little differences stem from quantum confinement of the Na_3Bi slab.

The 8 band Hamiltonian is used in self-consistent non-equilibrium Green's function (NEGF) [81] formalism to calculate the charge current to spin current conversion efficiency in Na_3Bi. The NEGF formalism is constructed considering both the elastic and the inelastic scattering processes in the Na_3Bi slab. The SO-GGA band structure of Na_3Bi is constructed using the Hartree approximation correction and thus, the electron-electron interaction is taken into account while constructing the Hamiltonian [86]. The elastic scattering of transport electrons due to scattering potential in the channel and the inelastic scattering due to electron-phonon interaction is modeled by inserting virtual probes in the channel. The self-energy matrix of the virtual probe depends on the type of scattering process. The virtual probes are placed in the channel according to the mean free path of the transport medium. The mean free path in Na_3Bi depends on the

electron Fermi velocity and carrier lifetime. The Fermi velocity (v_F) of Na_3Bi is 8.05×10^5 m/s [87] and the quantum lifetime (τ_Q) is 8.16×10^{-14}s [87]. Therefore, the mean free path in Na_3Bi is $\lambda = v_F \times \tau_Q$ = 65.688 nm. We assumed a 100nm long Na_3Bi slab along transport direction (y-axis). Consequently, we assumed one elastic scattering (election scattering due to random potential) and one inelastic scatterer (phonon scattering) in the channel so that we can calculate and match the experimentally measured electron mobility in Na_3Bi (6000 cm^2/Vs [88]) from our current-voltage characteristics. The charge current and spin current-voltage characteristics are derived from the NEGF formalism with scattering.

The retarded Green's function with scattering in NEGF formalism is written as [81],

$$G^R = [EI - H_{TM}(k) - \sum_{c1} - \sum_{c2} - \sum_{0e} - \sum_{0i}]^{-1} \quad (3.1)$$

$\sum_{c1}$ and $\sum_{c2}$ are the self-energy matrices of contact 1 and contact 2 (fig. 3.1). $\sum_{0e}$ and $\sum_{0i}$ are the self-energy matrices of elastic and inelastic scatterers respectively[50]. The Fermi levels of contact 1 and contact 2 are assumed to be f_1 and f_2 and energy level broadening due to contacts, Γ_1 and Γ_2, are defined as $\Gamma_1 = i[\sum_{c1} - \sum_{c1}^{\dagger}]$ and $\Gamma_2 = i[\sum_{c2} - \sum_{c2}^{\dagger}]$. The strength of contacts, $\sum^{in}$, can then be defined as,

$$\sum^{in} = [\Gamma_1]f_1 + [\Gamma_2]f_2 + \sum_{0s}^{in} \quad (3.2)$$

The term $\sum_{0s}^{in}$, defined as $\sum_{0s}^{in} = D_{ij}^{elastic} G^m + D_{mn}^{phonon}(\hbar\omega) \times [G^m(E + \hbar\omega)]_{mn}$, [86] appears due to virtual probes representing the scatterers. $D_{ij}^{elastic}$ is the matrix representing the correlation potential at position i and j, expressed as $D_{ij}^{elastic} = < U_{Ri}|U_{Rj}|U_{Ri}|U_{Rj} >$ where U_{Ri} and U_{Rj} are scattering potentials at position i and j [86]. D_{mn}^{phonon} is the matrix representation of scattering phonon potentials, defined as, $D_{mn}^{phonon} = < U_{Si}|U_{Sj}|U_{Si}|U_{Sj} >$ [86]. Bracket symbol represents the ensemble-averaged value of potential U_s. G^n represents the non-equilibrium Green's function.

The broadening of the energy levels due to the elastic scattering inducing virtual contact is defined as $\Gamma_{ij}^{elastic} = D_{ij}^{elastic} A$ [86]. A is the spectral function matrix defined as, $A = G^R \Gamma G^A$ where G^A is the complex conjugate of G^R. Γ is the overall broadening of the energy levels due to real and virtual contacts. Γ is defined as, $\Gamma = \Gamma_1 + \Gamma_2 + \Gamma_{ij}^{elastic} + \Gamma_{mn}^{Phonon}$ [86]. Γ_{mn}^{Phonon}, broadening of energy level due to the virtual probe of phonon scattering, is defined as, $\Gamma_{mn}^{Phonon} = D_{mn}^{phonon}(\hbar\omega) \times [G_{mn}^n(E + \hbar\omega) + G_{mn}^p(E - \hbar\omega)]$. Note, G_{mn}^p is the hole Green's

function which appears in the expression of Γ_{mn}^{Phonon} because electron-phonon scattering is proportional to the number of empty holes at $E - \hbar\omega$ [86]. G^n is written as [81],

$$G^n = G^R \sum^{in} G^A \tag{3.3}$$

The steady-state electron density in the transport channel can be calculated as trace $[G^n]/2\pi$. G^n and $\sum^{in}$ are solved self-consistently. Using these quantities, the charge current trough topological metal between two points i and i$\pm$1 can be calculated as [81],

$$J_{i,i\pm1} = \frac{i}{h}\int Real[Trace\left(H_{TM,i,i\pm1}G^n_{i\pm1,i} - G^n_{i\pm1,i}H_{TM,i,i\pm1}\right)]\,dE \tag{3.4}$$

The spin current density between i and i$\pm$1 can be written as [81],

$$J_{i,i\pm1} = \frac{i}{h}\int Real[Trace(\vec{S}.\left(H_{TM,i,i\pm1}G^n_{i\pm1,i} - G^n_{i\pm1,i}H_{TM,i,i\pm1}\right)]\,dE \tag{3.5}$$

$\vec{S}$ is the Pauli spin matrix. Pauli spin matrix for three spin system can be written as (derivation can be found in Appendix E),

$$S_x = \begin{bmatrix} 0 & 1 & 1 & 1 & 0 & 0 & 0 & 0 \\ 1 & 0 & 0 & 0 & 1 & 1 & 0 & 0 \\ 1 & 0 & 0 & 0 & 1 & 0 & 1 & 0 \\ 1 & 0 & 0 & 0 & 0 & 1 & 1 & 0 \\ 0 & 1 & 1 & 0 & 0 & 0 & 0 & 1 \\ 0 & 1 & 0 & 1 & 0 & 0 & 0 & 1 \\ 0 & 0 & 1 & 1 & 0 & 0 & 0 & 1 \\ 0 & 0 & 0 & 0 & 1 & 1 & 1 & 0 \end{bmatrix}$$

$$S_y = \begin{bmatrix} 0 & -i & -i & -i & 0 & 0 & 0 & 0 \\ i & 0 & 0 & 0 & -i & -i & 0 & 0 \\ i & 0 & 0 & 0 & -i & 0 & -i & 0 \\ i & 0 & 0 & 0 & 0 & -i & -i & 0 \\ 0 & i & i & 0 & 0 & 0 & 0 & -i \\ 0 & i & 0 & i & 0 & 0 & 0 & -i \\ 0 & 0 & i & i & 0 & 0 & 0 & -i \\ 0 & 0 & 0 & 0 & i & i & i & 0 \end{bmatrix}$$

$$S_z = \begin{bmatrix} 3 & 0 & 0 & 0 & 0 & 0 & 0 & 0 \\ 0 & 1 & 0 & 0 & 0 & 0 & 0 & 0 \\ 0 & 0 & 1 & 0 & 0 & 0 & 0 & 0 \\ 0 & 0 & 0 & 1 & 0 & 0 & 0 & 0 \\ 0 & 0 & 0 & 0 & -1 & 0 & 0 & 0 \\ 0 & 0 & 0 & 0 & 0 & -1 & 0 & 0 \\ 0 & 0 & 0 & 0 & 0 & 0 & -1 & 0 \\ 0 & 0 & 0 & 0 & 0 & 0 & 0 & -3 \end{bmatrix}$$

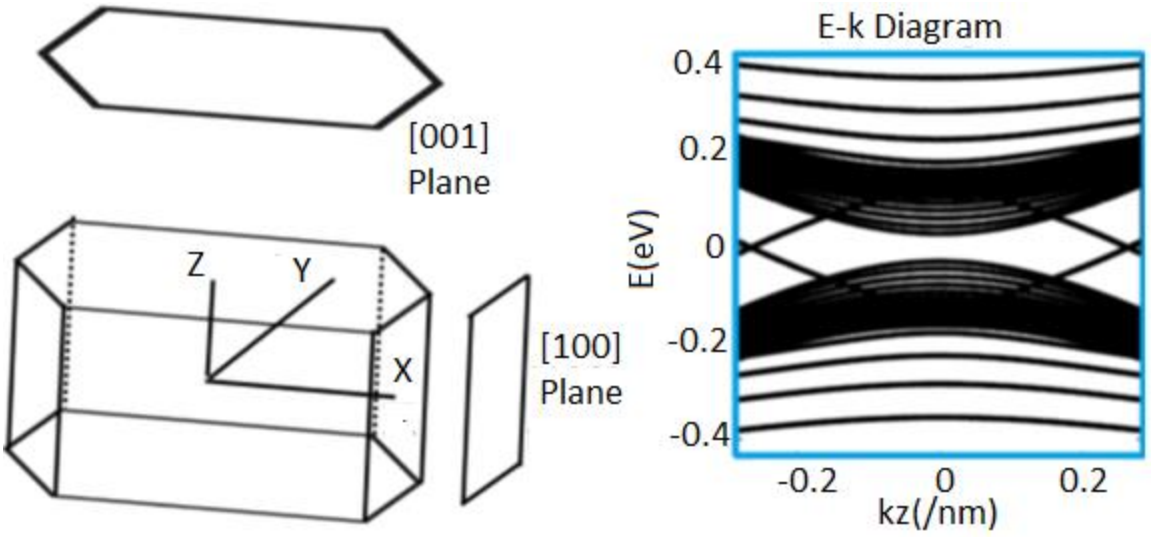

Fig. 3.4: (left) A schematic diagram of the Na_3Bi crystal structure Brillouin zone with [100] and [001] plane projection direction. (right) 8 band k.p band structure of 15nm thick Na_3Bi quantum well. The quantum well is confined along the x-axis.

Spin current diffuses in the MTJ free layer and exerts spin transfer torque on the magnetic moments. The spin-transfer torque can be calculated as shown in ref [71]. The field-like spin-orbit torque can be expressed as [71],

$$\overrightarrow{\tau_{FL}} = \Delta_{ex}\, \hat{m} \times \overrightarrow{n_s} \tag{3.6}$$

Δ_{ex} is the exchange splitting between up spin and down spin states in free layer ferromagnet, $\hat{m}$ is the unit vector pointing along the free layer magnetization and $\overrightarrow{n_s}$ is the non-equilibrium spin density. Assuming 'D' to be the spin diffusion coefficient inside the MTJ free layer, spin diffusion current from the spin injector into SOT-MTJ free layer can be written as the product of D and gradient of $\overrightarrow{n_s}$, i.e., $J_s = -D\vec{\nabla}.\overrightarrow{n_s}$. The spin transfer-like spin-orbit torque can be written as [71],

$$\overrightarrow{\tau_{ST}} = \frac{1}{d}\int_0^d (-\overrightarrow{\nabla_x} J_s - \frac{1}{\tau_{sf}}\overrightarrow{n_s})\, dx \tag{3.7}$$

The term d is the thickness of x-confined MTJ free layer slab and τ_{sf} is the spin relaxation time inside MTJ free layer magnet.

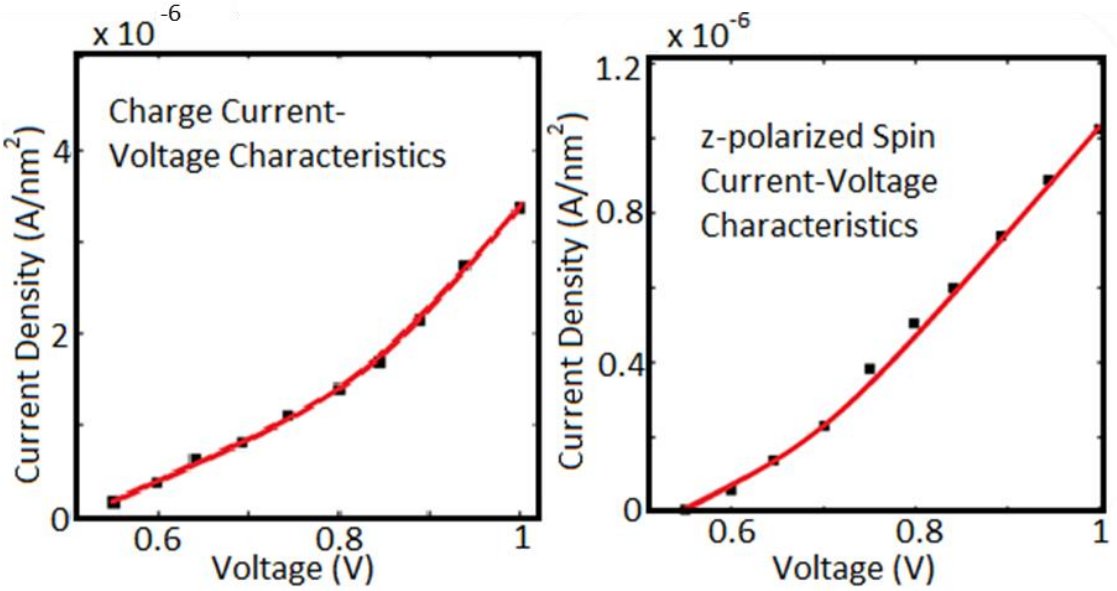

Fig. 3.5: (left) The charge current density variation with applied voltage in Na_3Bi slab. The applied voltage range is 0.55V to 1V. (right) Z-polarized spin current density vs applied voltage in Na_3Bi slab. The charge and spin current calculation are done using non-equilibrium Green's function formalism.

3.3 Result and Discussion

In order to show the advantages of Na_3Bi as an efficient spin injector, we used our model to evaluate the performance (power consumption and switching time) of a CoFeB (fixed layer)-MgO (tunneling barrier)-CoFeB (free layer)-Na_3Bi (spin injector) MTJ. We compared the iso-speed power consumption and iso write voltage switching efficiency of Na_3Bi based MTJ with CoFeB-MgO-CoFeB-Pt and CoFeB-MgO-CoFeB-Bi_2Se_3 MTJs. CoFeB is a popular choice as an MTJ free layer primarily due to excellent Δ_1 spin filtering effect [89] in CoFeB/MgO stack resulting in good tunneling magneto-resistance ratio [90]. The critical switching current of a typical CoFeB free layer having perpendicular magnetic anisotropy is on the order of 10^{-7} Amp/nm^2 [70,91,92]. Applying a voltage difference of 1V across the contacts yields a charge current density of 3.3727×10^{-6} Amp/nm^2 along the y-axis, a +z-polarized spin current density of 1.02431×10^{-6} Amp/nm^2 and +x-polarized spin current density of 4.411×10^{-7} Amp/nm^2. The in-plane (x-y plane) and out-of-plane spin Hall angles are 0.39 and 0.92. Fig 3.5a and 3.5b show the charge current-voltage and z-polarized spin current-voltage characteristics through 15nm thick Na_3Bi slab. We calculated the current-voltage characteristics using benchmarked NEGF formalism. The benchmarking of NEGF formalism is shown in ref [71].

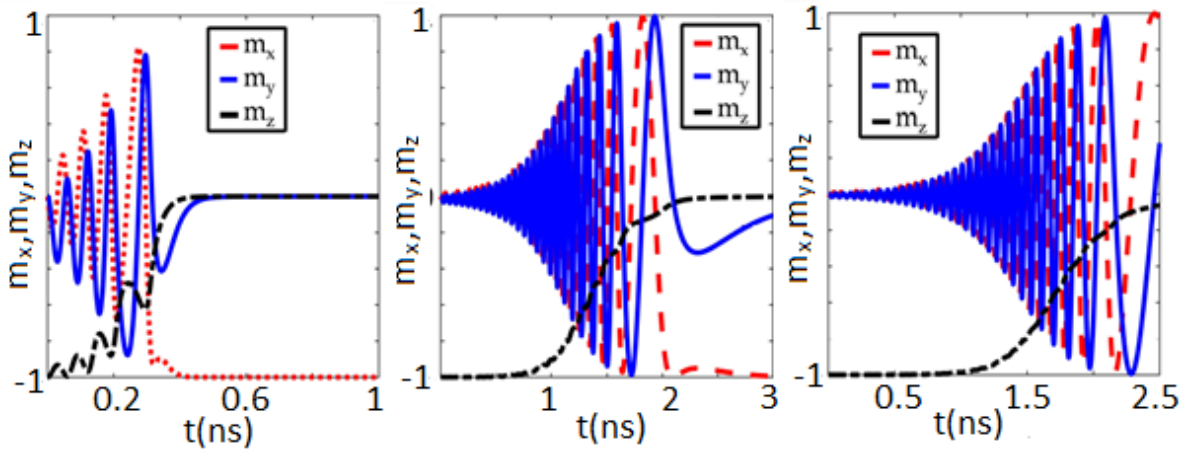

Fig. 3.6: Iso-write voltage-free layer magnetization dynamics comparison of Na_3Bi, Pt and Na_3Bi based MTJs. Magnetization dynamics of CoFeB free layer in (left) CoFeB/MgO/CoFeB/Na_3Bi, (center) CoFeB/MgO/CoFeB/Pt, (right) CoFeB/MgO/CoFeB/ Bi_2Se_3 MTJs when 1v is applied between contact 1 and contact 2 (fig.1)

Na_3Bi provides us with a unique advantage as a spin injector. The charge current to spin current conversion efficiency in Na_3Bi is relatively high compared with the heavy spin Hall metals. In order to generate a spin current density of 1.02431×10^{-6} Amp/nm^2 in Pt, we need a charge current density of 3.9×10^{-5} Amp/nm^2. It is more than ten times higher than the charge current required in Na_3Bi to generate the same amount of spin current. Therefore, the write operation in MTJ becomes more power efficient if Na_3Bi is used as the spin injector rather than Pt.

Table 3.1. Parameters for magnetization dynamics simulation of CoFeB

Parameters	Value
CoFeB dimensions	$100 \times 100 \times 2$ nm^3
Grid Size	$2 \times 2 \times 2$ nm^3
CoFeB Saturation Magnetization, M_s	800 KA/m [93]
Gilbert damping factor, α	0.025 [93]
Exchange correlation constant	3×10^{11} J/m [93]
Perpendicular magnetic anisotropy	6×10^5 J/m^3 [93]

In order to generate a particular amount of spin current to switch an MTJ free layer, Na_3Bi consumes almost 10.1x less electrical power than Pt. On the other hand, a charge current density of 2.83×10^{-6} Amp/nm^2 need to flow through Bi_2Se_3 in order to produce a z-polarized spin current density of 1.02431×10^{-6} Amp/nm^2. Although the required charge current density is 1.4 times lower than that of Na_3Bi, the conductivity of Bi_2Se_3 is relatively low. Therefore, most of the charge current is shunted through the MTJ free layer and gets wasted. For example, if Permalloy (80% Ni and 20%Fe) is used as the free layer of the MTJ and Bi_2Se_3 is used as the spin injector, then 96% of the charge current shunts through the Permalloy free layer [71,72]. Therefore, if Bi_2Se_3 is used as the spin injector, the MTJ write operation becomes power-hungry because of the shunting current loss. Na_3Bi conductivity is 12.5 times higher than that of Bi_2Se_3, eliminating the shunting current loss in MTJ write operation cycle. CoFeB-MgO-CoFeB- Na_3Bi MTJ consumes almost 728.4x less power during write operation than CoFeB-MgO-CoFeB-Bi_2Se_3 MTJ. Note, when charge current flows through Na_3Bi, electron spin get polarized perpendicular to the charge current direction. Here, we assumed the charge current is flowing along the +y-axis. Therefore, charge current can be in-plane polarized (x-polarized) or out-of-plane polarized (z-polarized). In figure 3.5, we only showed the +z-polarized spin current-voltage characteristic. In-plane spin-polarized current also shows similar current-voltage characteristics. However, the in-plane spin-polarized current has a lower magnitude than out-of-plane spin-polarized current as described earlier. Note, we have assumed the spin current injection efficiency from the spin injector to SOT-MTJ free layer to be 1. In reality, there will be loss during the spin current injection.

In figure 3.6, we showed the iso write voltage comparison of the magnetization dynamics of CoFeB free layer in CoFeB-MgO-CoFeB MTJ with different types of spin injectors. The micro-magnetic simulation is done based on the Landau-Lifshitz-Gilbert-Slonczewski (LLGS) [94] magnetization dynamics using the mumax3 [95] package. When Na_3Bi is used as the spin injector, the CoFeB free layer switched its magnetization direction from the -z-axis to the -x-axis in 0.452 ns. On the other hand, CoFeB free layer takes 2.09 ns to switch in case of Pt spin injector while the use of Bi_2Se_3 as spin injector fails to switch the CoFeB free layer for an applied voltage of 1V across the spin injector layer. For a particular write voltage, Na_3Bi based MTJ shows almost 4.3x faster switching speed than Pt-based MTJ. Parameters for CoFeB magnetization dynamics simulation are listed in Table 3.1.

3.4 Conclusion

In conclusion, we proposed and modeled topological metal Na_3Bi with 8 band k.p model and evaluated the power consumption and switching efficiency of Na_3Bi based SOT-MTJ. We also compared the performance parameters (iso-speed switching power and iso- writing voltage switching speed) between Na_3Bi based MTJ and Pt and Bi_2Se_3 based MTJs. Our simulation shows that the topological semi-metal Na_3Bi exhibits excellent charge current to spin current conversion efficiency compared with HM and high conductivity compared with TI to be a potential candidate as a spin injector. Our simulation framework does not consider the interface issues between Na_3Bi and MTJ free layer. Na_3Bi has a hexagonal crystal structure and Co has the same crystal structure [96]. Both of them are members of the same space group. Therefore, magnetic alloys of Co (like CoFeB, CoTb [97]) can be used as the MTJ free layer and would probably form a relatively smooth interface with Na_3Bi. Use of Na_3Bi as spin injector can reduce the power consumption during MTJ write operation by a significant amount. Moreover, Na_3Bi spin injector also enables fast switching of the MTJ and hence, makes the overall MTJ operation cycle more efficient.

3.5 Summary

The free layer in current-driven magnetic tunnel junction (MTJ) can be switched by injecting spin-polarized current from an adjacent spin injector. A non-magnetic efficient spin injector, a converter from the charge current to spin current, has long been and still being quested in the field of spintronic. The first discovered non-magnetic spin injector was the heavy spin hall metal (HM) like Pt and β-W. The HMs can only convert 2% to 10% of the charge current to spin current. Rest of the charge current is wasted and has no contribution in switching the MTJ. The waste of charge current during MTJ switching is one of the major sources of energy loss in MTJ operation. Later, it has been found that topological insulator (TI) like Bi_2Se_3 can convert around 37% charge current to spin current. Nevertheless, the topological insulator has low conductivity compared with the free layer of an MTJ which results in a large amount of shunting charge current loss though the free layer. Topological semi-metal (TM) like Na_3Bi provides us a trade-off point between HM and TI as a non-magnetic spin injector. TMs have higher charge current to spin current conversion efficiency than HMs and higher electrical conductivity than TIs. In this

work, we first calculated the DFT band structure of Na_3Bi, modeled and matched the near-Fermi level band structure with 8 band k.p model. We have used the k.p Hamiltonian in quantum transport (non-equilibrium Green's function - NEGF) formalism to determine the charge current to spin current conversion efficiency in Na_3Bi. We have found that Na_3Bi can convert around 30.37% of charge current to spin current and its conductivity is ~ 12.5 times more than that of Bi_2Se_3. A CoFeB (fixed layer)-MgO (tunneling barrier)-CoFeB(free layer)- Na_3Bi (spin injector) MTJ consumes almost 10.1x and 728.4x less electrical power during iso-speed write operation compared with CoFeB-MgO-CoFeB-Pt and CoFeB-MgO-CoFeB-Bi_2Se_3 MTJs, respectively. Application of iso write voltage of 1V shows that CoFeB-MgO-CoFeB- Na_3Bi MTJ switches 4.3x faster than CoFeB-MgO-CoFeB-Pt MTJ while CoFeB-MgO-CoFeB-Bi_2Se_3 MTJ fails to switch and continues to oscillate.

4. ANALYSIS OF MAGNETIZATION DYNAMICS IN A FERRIMAGNET WITH HEAVY METAL OR TOPOLOGICAL INSULATOR UNDERLAYER

4.1 Significant Factors in Ferrimagnet Magnetization Dynamics

Consumption of high power and slow switching speed due to long precession time [98, 99] are the two major obstacles of a ferromagnet (FM) based spintronic devices as compared with traditional CMOS technology. Antiferromagnet (AFM) and Ferrimagnet (FiM) have some unique advantages over FM. AFM and FiM offer faster switching speed [98], terahertz range oscillation frequency [99] and high domain wall velocity [100]. However, AFM does not have any net magnetization and therefore, it is difficult to sense the switching of the magnetization. In AFM, magnetic moments are compensated in each unit cell. Nevertheless, in FiM devices, magnetic moments do not completely counterbalance each other (fig. 4.1a). Therefore, there is weak ferromagnetism in FiM which can be easily sensed via Magnetic Tunnel Junction. Despite having different net magnetization, AFM and FiM magnetization exhibit respond similarly to an external magnetic perturbation.

Transfer of spin angular momentum via injection of spin-polarized current is a very effective way to introduce magnetic perturbation into FiM devices. In a magnetic tunnel junction, the switching of the magnetization direction of the free layer magnet is accomplished by injecting spin-polarized current [101]. The spin-polarized current can be generated either by certain heavy metals (HM) with spin hall effect (SHE) or topological insulators (TI) [101, 102]. Both the HM and TI have strong spin-orbit coupling [101, 102]. A significant amount of Dzyaloshinskii-Moriya interaction (DMI) is observed in AFM and FiM devices when they come in contact with the materials having high spin-orbit coupling [103-105]. Introduction of DMI modifies the magnetization pattern of FiM, especially near the interface. DMI tilts the magnetic moments which consequently can be used as an aid to switch the magnetization direction. Moreover, DMI plays a significant role in determining the oscillation frequency of FiM and HM hetero-structure. DMI effect is weaker in FM giving the AFM and FiM a unique advantage over FM.

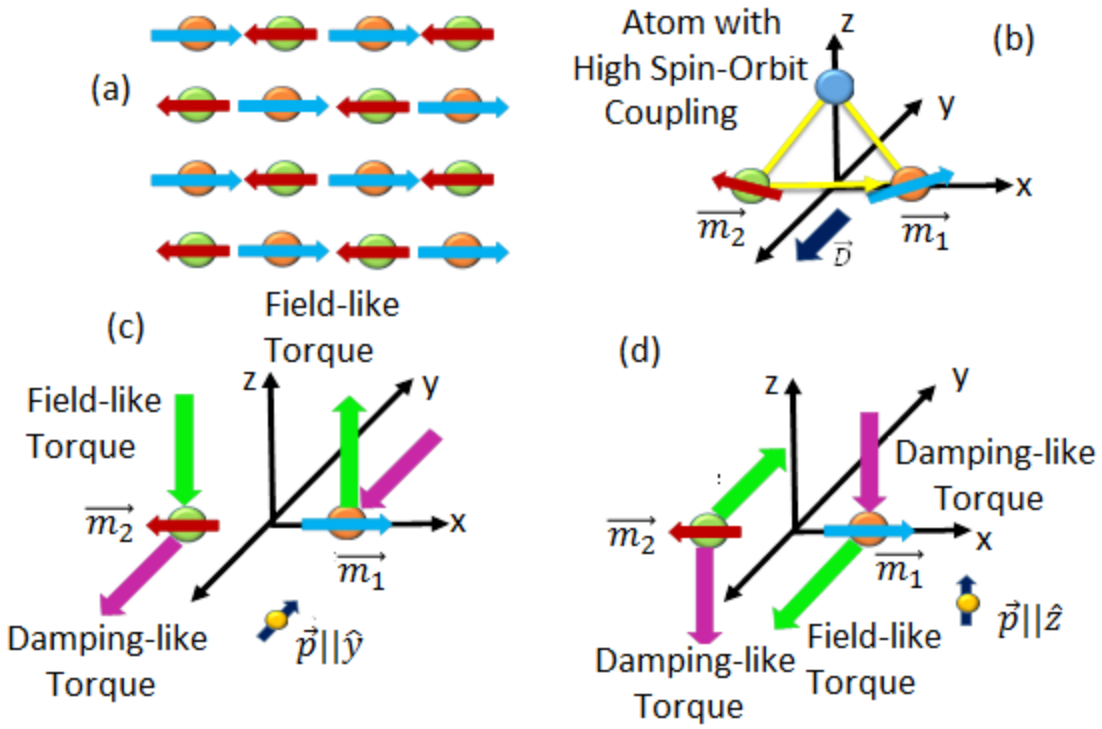

Fig. 4.1: (a) Schematic diagram of a Ferrimagnet sublattice with two magnetic moments (easy axis along the x-axis). (b) Schematic diagram of DMI between FiM sublattice and adjacent atom with high spin-orbit coupling. Due to DMI, magnetic moments inside FiM sublattice are tilted towards +z-axis. (c) Sigma mode when the injected spin polarization is parallel to +y-axis. The direction of torques is shown. (d) Gamma mode when the spin polarization is parallel to +z-axis.

Effect of DMI on magnetization dynamics of AFM and FiM has not been considered in most of the previous works [99, 106]. Ref [103] has included the DMI interaction as a scalar quantity in the vector equation of AFM magnetization. The vector contribution of DMI in magnetization dynamics is derived in this chapter using the method discussed in ref [107, 108]. A detail theoretical analysis reveals the fact that the oscillation frequency in FiM and HM/TI hetero-structure has small or no dependence on injected spin current density (unless spin current torque is comparable with the exchange coupling torque). Rather we claim that the oscillation frequency in FiM mainly depends on the exchange coupling and DMI. Moreover, FiM can have a very complex crystal structure like Yttrium Iron Garnett (YIG) which contains three magnetic moments in a sublattice [109, 110, 111]. Unlike preceding literatures [99, 106], we consider the full crystal sublattice and show how the magnetization dynamic simulation framework is modified with the increasing complexity of FiM sublattice.

In fig.4.1, the magnetic easy axis of the FiM is considered to be parallel to the x-axis. The HM (TI) atoms are along +z-axis with respect to FiM (fig. 4.1b). Consequently, the DMI vector will be parallel to -y-axis [103] (indigo arrow in fig. 4.1b). Note, the DMI will try to align the magnetic moments along the hard axis (+z-axis) (fig. 4.1b) while the exchange coupling will try to keep the magnetization in the energetically favorable x-axis. Hence, the magnetic moments in the sublattices tilt a bit along +z-axis (red and blue arrow in fig. 4.1b). Tilting angle of magnetic moments, due to the combined effect of interaction between DMI and exchange coupling, is low because DMI is weaker compared to exchange coupling.

Injection of large enough spin-polarized current will introduce spin-transfer torque and induce oscillation in FiM magnetic moments. Increasing the amplitude of spin-polarized current will enhance the oscillation amplitude of the FiM magnetic moments. Strong spin transfer torque can even switch the FiM magnetization direction. Spin polarization ($\vec{p}$) can either be parallel to y-axis or z-axis, giving rise to two different oscillation mode - sigma mode ($\vec{p}||\hat{y}$) and gamma mode ($\vec{p}||\hat{z}$) [103] (fig. 4.1c,d). Each oscillation mode can have two different spin-transfer torques - 'field-like (FL) torque' and 'damping-like (DL) torque' [103]. Usually, damping-like torque is the dominant one but the field-like torque can be high for asymmetric AFM and FiM crystal structure.

In this chapter, we demonstrate the magnetization dynamics of FiM devices driven by spin-polarized current from adjacent HM or TI. The solitary effect of interfacial DMI and the independence of oscillation frequency from spin-polarized current are shown by theoretical calculation. The magnetization of the magnetic moments in an FiM sublattice, after being subject to spin-transfer torque, change according to Landau-Lifshitz-Gilbert-Slonczewski (LLGS)[105] equation. In FiM, there can be more than two magnetic moments in a sublattice. FiM magnetism depends on the complexity of the crystal lattice. Initially, we consider an FiM sublattice with two magnetic moments of unequal magnitude pointing opposite to each other (fig. 4.1a) like CoTb [108]. Then, we will expand the theory to more complex FiM crystal structures like $Y_3Fe_5O_{12}$ [109].

4.2 Theory of Ferrimagnet Magnetization Dynamics

In absence of external perturbation, two oppositely polarized magnetic moments, $\overrightarrow{m_1}$ and $\overrightarrow{m_2}$ in a FiM sublattice lies along the +x axis and -x-axis respectively (fig. 4.1). FiM sublattice adjacent to strong spin-orbit coupling will be subject to DMI interaction. DMI will tilt both the magnetic moments to +z-axis (fig. 4.1b). Energy change in the sublattice due to DMI is expressed as, $\epsilon_{DMI} = \vec{D}.(\overrightarrow{m_1} \times \overrightarrow{m_2})$ [111]. Here $\vec{D}$ is the DMI vector which is pointing along -y-axis in this case (fig. 4.1b). Change in magnetization dynamics due to DMI alone is calculated from the derivative of ϵ_{DMI} with respect to the magnetic moment, i.e, $\frac{d\epsilon}{d\overrightarrow{m_1}}$ and $\frac{d\epsilon}{d\overrightarrow{m_2}}$ [107]. Therefore, DMI will try to tilt the magnetic moments along the hard axis.

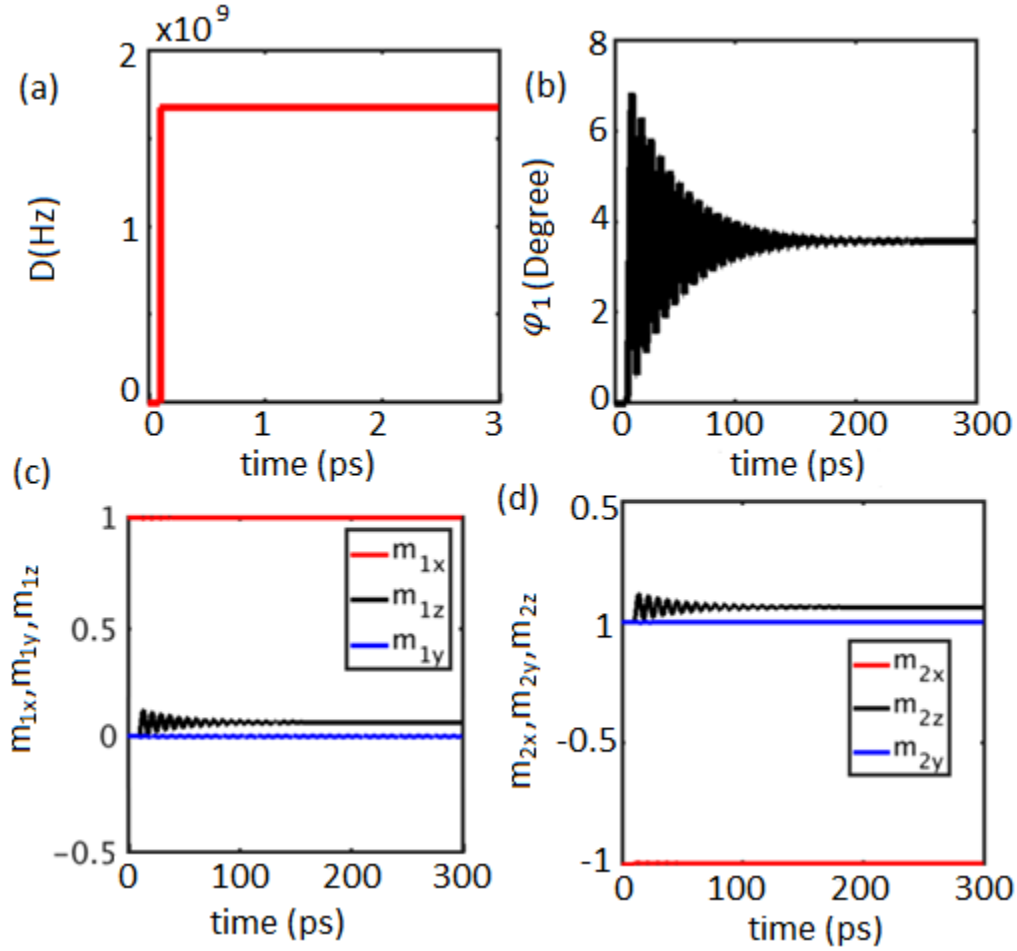

Fig. 4.2: Tilting of $\overrightarrow{m_1}$ and $\overrightarrow{m_2}$ towards +Z-axis due to DMI. The simulation parameters are J=11.749 THz, K_x=26.9228 GHz, K_z=0, α = 0.002, DMI=1.77GHz (~0.0001J), W_s=0 GHz and W_f =0. We can observe that both $\overrightarrow{m_1}$ and $\overrightarrow{m_2}$ tilt around 4o towards +Z-axis.

Fig. 4.2 shows the solitary effect of DMI on magnetic moments. φ_1 measures the out of plane tilting of $\overrightarrow{m_1}$, defined as $\varphi_1 = \frac{m_{1z}}{\sqrt{m_{1x}^2+m_{1y}^2}}$. Increasing the strength of DMI increases the amount of tilting towards +Z-axis. It can be beneficial to the magnetic reorientation of FiM (by effectively reducing the thermal barrier) or can be detrimental especially in case of perpendicular magnetic anisotropy. Reorientation of magnetic moments in FiM is done by injecting spin-polarized current from HM layer.

Therefore, before injecting the spin-polarized current, the magnetization dynamics can be defined by the LLG equation.

$$\frac{d\boldsymbol{m_1}}{dt} = J\boldsymbol{m_1} \times \boldsymbol{m_2} + \boldsymbol{m_2} \times \boldsymbol{D} + K_x m_{1x}\, \hat{\boldsymbol{x}} \times \boldsymbol{m_1} + K_z m_{1z}\, \hat{\boldsymbol{z}} \times \boldsymbol{m_1} + \alpha \boldsymbol{m_1} \times \frac{d\boldsymbol{m_1}}{dt} \quad (4.1)$$

$$\frac{d\boldsymbol{m_2}}{dt} = J\, \boldsymbol{m_2} \times \boldsymbol{m_1} + \boldsymbol{m_1} \times \boldsymbol{D} + K_x m_{2x}\, \hat{\boldsymbol{x}} \times \boldsymbol{m_2} + K_z m_{2z}\, \hat{\boldsymbol{z}} \times \boldsymbol{m_2} + \alpha \boldsymbol{m_2} \times \frac{d\boldsymbol{m_2}}{dt} \quad (4.2)$$

Here J is the symmetric component of exchange coupling constant between $\overrightarrow{m_1}$ and $\overrightarrow{m_2}$, K_x and K_z are the in-plane and out-of-plane anisotropy constants, respectively and α is the Gilbert damping constant. Fig.4.3 and 4.4 exhibit the solitary effect of DMI on FiM magnetization in sigma and gamma mode respectively. Initially, in the absence of DMI, there is no variation in magnetization. After 10ps, the DMI is activated and immediately, the z components of $\overrightarrow{m_1}$ and $\overrightarrow{m_2}$ starts oscillating. This is because the DMI tries to align the magnetization along the +z axis.

Spin angular momentum transfer in FiM introduces the spin transfer torques on magnetic moments in sublattice. Spin polarization can be either parallel to y-axis or z-axis. Fig 4.1 shows the directions of damping-like torque and field-like torque for different spin-polarized current. The damping like torque is defined as $\overrightarrow{\tau_s} = W_s \overrightarrow{m_1} \times (\vec{p} \times \overrightarrow{m_1})$ [98]. $\vec{p}$ is the polarization vector and W_s is the strength of the damping like torque defined as $W_s = \frac{\xi \hbar \gamma J_s}{2 M_0 V e}$ [99]. Here ξ is the scattering efficiency, $\hbar$ is the reduced Plank's constant, γ is the gyromagnetic ratio, $J_s$is the spin-polarized current density. M_0 is defined as the saturation magnetization of the sublattice defined as $M_0 = \sqrt{m_1^2 + m_2^2}$. V refers to the volume of the sublattice and e is the electron charge. Field-like torque is expressed as $\overrightarrow{\tau_f} = W_f \overrightarrow{m_1} \times \vec{p}$ [98]. W_f is the strength of the FL torque defined as $W_f = \beta W_s$. β is the strength of the FL torque relative to DL torque. The value of β depends on the

symmetry of the FiM lattice. For an asymmetric FiM crystal, like Yttrium Iron Garnett, β can be large. Injection of spin-polarized current yields the following LLGS equations for $\overrightarrow{m_1}$ and $\overrightarrow{m_2}$.

$$\frac{d\boldsymbol{m_1}}{dt} = J\boldsymbol{m_1} \times \boldsymbol{m_2} + \boldsymbol{m_2} \times \boldsymbol{D} + K_x m_{1x}\, \hat{\boldsymbol{x}} \times \boldsymbol{m_1} + K_z m_{1z}\, \hat{\boldsymbol{z}} \times \boldsymbol{m_1} + \alpha \boldsymbol{m_1} \times \frac{d\boldsymbol{m_1}}{dt} + W_s\, \boldsymbol{m_1} \times (\boldsymbol{m_1} \times \boldsymbol{p}) + W_f \boldsymbol{m_1} \times \boldsymbol{p} \quad (4.3)$$

$$\frac{d\boldsymbol{m_2}}{dt} = J\, \boldsymbol{m_2} \times \boldsymbol{m_1} + \boldsymbol{m_1} \times \boldsymbol{D} + K_x m_{2x}\, \hat{\boldsymbol{x}} \times \boldsymbol{m_2} + K_z m_{2z}\, \hat{\boldsymbol{z}} \times \boldsymbol{m_2} + \alpha \boldsymbol{m_2} \times \frac{d\boldsymbol{m_2}}{dt} + W_s\, \boldsymbol{m_2} \times (\boldsymbol{m_2} \times \boldsymbol{p}) + W_f \boldsymbol{m_2} \times \boldsymbol{p} \quad (4.4)$$

Algebraic manipulation of the LLGS equations will describe the complete magnetization dynamics of the two magnetic moments $\overrightarrow{m_1}$ and $\overrightarrow{m_2}$ inside FiM sublattice.

$$\begin{aligned}\frac{d\boldsymbol{m_1}}{dt} = {} & \frac{J}{1+\alpha^2}\, \boldsymbol{m_1} \times \boldsymbol{m_2} + \frac{J\alpha}{1+\alpha^2}\, \boldsymbol{m_1} \times (\boldsymbol{m_1} \times \boldsymbol{m_2}) + \frac{1}{1+\alpha^2}\, \boldsymbol{m_2} \times \boldsymbol{D} + \frac{\alpha}{1+\alpha^2}\, \boldsymbol{m_1} \\ & \times (\boldsymbol{m_2} \times \boldsymbol{D}) + \frac{K_x m_{1x}}{1+\alpha^2}\, \hat{\boldsymbol{x}} \times \boldsymbol{m_1} + \frac{\alpha K_x m_{1x}}{1+\alpha^2} (\hat{\boldsymbol{x}} - m_{1x}\boldsymbol{m_1}) + \frac{K_z m_{1z}}{1+\alpha^2}\, \hat{\boldsymbol{z}} \times \boldsymbol{m_1} \\ & + \frac{\alpha K_z m_{1z}}{1+\alpha^2} (\hat{\boldsymbol{z}} - m_{1z}\boldsymbol{m_1}) + \frac{W_s}{1+\alpha^2}\, \boldsymbol{m_1} \times (\boldsymbol{m_1} \times \boldsymbol{p}) - \frac{\alpha W_s}{1+\alpha^2}\, \boldsymbol{m_1} \times \boldsymbol{p} \\ & + \frac{W_f}{1+\alpha^2}\, \boldsymbol{m_1} \times \boldsymbol{p} + \frac{\alpha W_f}{1+\alpha^2}\, \boldsymbol{m_1} \times (\boldsymbol{m_1} \times \boldsymbol{p}) \quad (4.5)\end{aligned}$$

The magnetization dynamics of $\overrightarrow{m_1}$ and $\overrightarrow{m_2}$ in sigma mode and gamma mode are shown in figure 4.3 and 4.4 respectively. In sigma mode of operation, the introduction of DMI creates small oscillation in z components of magnetic moments. As soon as the z component becomes non-zero, the exchange coupling torque (the first and second component of the previous equation) exerts force along the y-direction. Exchange coupling torque, being the largest torque, creates oscillation along the y-direction. Oscillation of y component starts immediately after the start of z-component oscillation. Introduction of spin-transfer torque shows an interesting effect. It increases the oscillation amplitude of y components as expected. But it also increases the oscillation amplitude of the z component as well and $m_{1z}\ and\ m_{2z}$ oscillate in opposite direction. Increase of y component significantly increases the exchange coupling torque along z and exchange coupling torque on $\overrightarrow{m_1}$ and $\overrightarrow{m_2}$ are opposite.

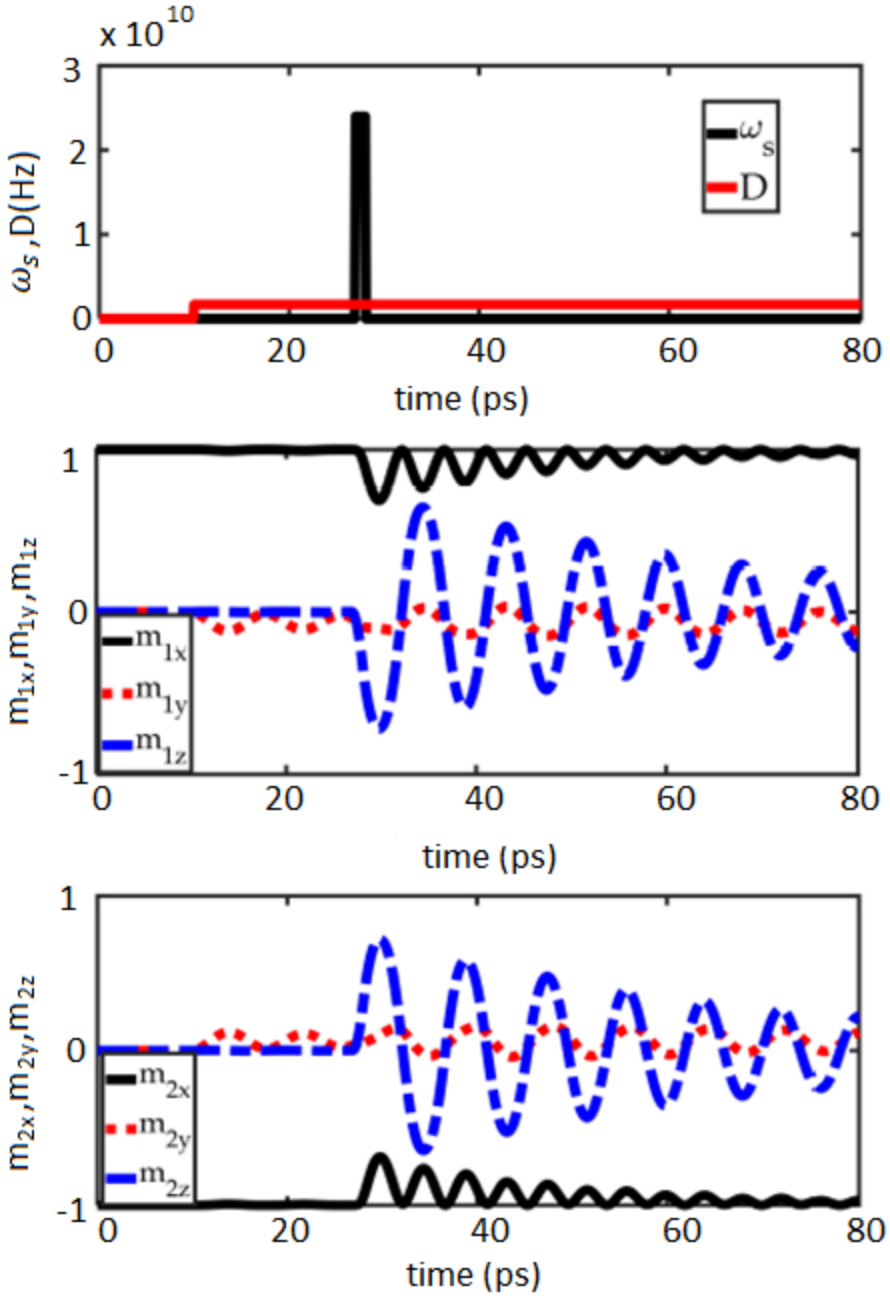

Fig. 4.3.: Sigma mode of magnetization dynamics of $\overrightarrow{m_1}$ and $\overrightarrow{m_2}$ in response to DMI and spin-polarized current ($\vec{p}||\hat{y}$). The first figure shows that DMI becomes active at 10ps while 1ps pulse of spin-polarized current is applied between 27ps and 28ps. The second and third figure shows the different component of $\overrightarrow{m_1}$ and $\overrightarrow{m_2}$. Simulation is done for ferrimagnet CoTb. Simulation parameters are taken from ref [108] (J=11.749 THz, K_x=26.9228 GHz, K_z=0, α=0.002, DMI=1.6784 GHz, W_s=24 GHz and W_f=0). Symmetric ferrimagnet crystal structure (fig.4.1 (a)) yields low field-like torque.

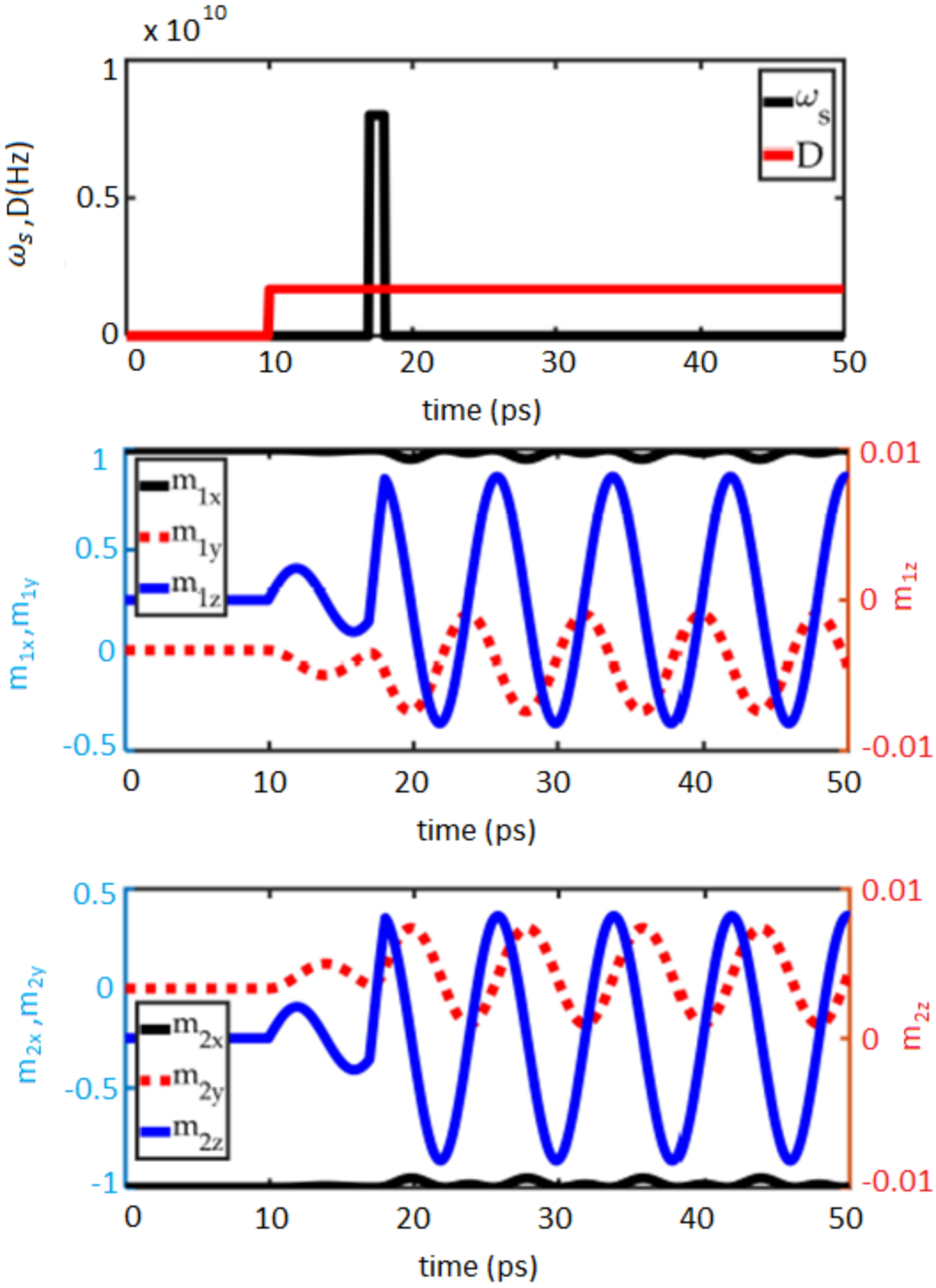

Fig. 4.4.: Gamma mode magnetization dynamics of $\overrightarrow{m_1}$ and $\overrightarrow{m_2}$ in response to DMI and spin-polarized current ($\vec{p}||\hat{z}$). Simulation is done for CoTb, with α =0., W_s=8 GHz and 1ps pulse of spin-polarized current is applied between 17ps and 18ps. Rest of the parameters are the same as in fig. 4.3.

In gamma mode, the oscillation pattern can be explained in a similar way by considering individual torque terms. Note, in gamma mode, the oscillation amplitude of the z component is not as big as it was in sigma mode. Rather y components oscillate with high amplitude and m_{1y} and m_{2y} oscillate in the opposite direction. Also note, the applied spin-polarized current density is lower in gamma mode.

$$\frac{d\boldsymbol{m_2}}{dt} = \frac{J}{1+\alpha^2}\,\boldsymbol{m_2}\times\boldsymbol{m_1} + \frac{J\alpha}{1+\alpha^2}\,\boldsymbol{m_2}\times(\boldsymbol{m_2}\times\boldsymbol{m_1}) + \frac{1}{1+\alpha^2}\,\boldsymbol{D}\times\boldsymbol{m_1} + \frac{\alpha}{1+\alpha^2}\,\boldsymbol{m_2} \times(\boldsymbol{D}\times\boldsymbol{m_1}) + \frac{K_x m_{2x}}{1+\alpha^2}\,\hat{\boldsymbol{x}}\times\boldsymbol{m_2} + \frac{\alpha K_x m_{2x}}{1+\alpha^2}(\hat{\boldsymbol{x}} - m_{2x}\boldsymbol{m_2}) + \frac{K_z m_{2z}}{1+\alpha^2}\,\hat{\boldsymbol{z}}\times\boldsymbol{m_2} + \frac{\alpha K_z m_{2z}}{1+\alpha^2}(\hat{\boldsymbol{z}} - m_{2z}\boldsymbol{m_2}) + \frac{W_s}{1+\alpha^2}\,\boldsymbol{m_2}\times(\boldsymbol{m_2}\times\boldsymbol{p}) - \frac{\alpha W_s}{1+\alpha^2}\,\boldsymbol{m_2}\times\boldsymbol{p} + \frac{W_f}{1+\alpha^2}\,\boldsymbol{m_2}\times\boldsymbol{p} + \frac{\alpha W_f}{1+\alpha^2}\,\boldsymbol{m_2}\times(\boldsymbol{m_2}\times\boldsymbol{p}) \quad (4.6)$$

The weak and staggered magnetization order parameters can be denied as, $\vec{m} = \frac{\vec{m_1}+\vec{m_2}}{2}$ and $\vec{l} = \frac{\vec{m_1}-\vec{m_2}}{2}$ [103] respectively. The staggered magnetization, $\vec{l}$ can be written as,

$$\frac{d\boldsymbol{l}}{dt} = 2J\boldsymbol{l}\times\boldsymbol{m} + \boldsymbol{m}\times\boldsymbol{D} + K_x\,\hat{\boldsymbol{x}}\times(m_x\boldsymbol{l} + l_x\boldsymbol{m}) + K_z\hat{\boldsymbol{z}}\times(m_z\boldsymbol{l} + l_z\boldsymbol{m}) + \alpha\left(\boldsymbol{m}\times\frac{d\boldsymbol{l}}{dt} + \boldsymbol{l}\times\frac{d\boldsymbol{m}}{dt}\right) + W_s\,[\boldsymbol{l}\times(\boldsymbol{m}\times\boldsymbol{p}) + \boldsymbol{m}\times(\boldsymbol{l}\times\boldsymbol{p})] + W_f\boldsymbol{l} \times\boldsymbol{p} \quad (4.7)$$

Similarly, the weak magnetization, $\vec{m}$ is written as

$$\frac{d\boldsymbol{m}}{dt} = 2\boldsymbol{m}\times\boldsymbol{D} + K_x\,\hat{\boldsymbol{x}}\times(m_x\boldsymbol{m} + l_x\boldsymbol{l}) + K_z\hat{\boldsymbol{z}}\times(m_z\boldsymbol{m} + l_z\boldsymbol{l}) + \alpha\left(\boldsymbol{l}\times\frac{d\boldsymbol{l}}{dt} + \boldsymbol{m}\times\frac{d\boldsymbol{m}}{dt}\right) + W_s\,[\boldsymbol{l}\times(\boldsymbol{l}\times\boldsymbol{p}) + \boldsymbol{m}\times(\boldsymbol{m}\times\boldsymbol{p})] + W_f\boldsymbol{m} \times\boldsymbol{p} \quad (4.8)$$

Figure 4.5 and 4.6 shows the magnetization dynamics of $\vec{l}$ and $\vec{m}$. In the sigma mode of operation, i.e., when spin polarization is parallel to the y-axis, damping-like torque will try to align the weak magnetization $\vec{m}$ along the y-axis while the staggered magnetization $\vec{l}$ tries to align along the z-axis. Although the magnetic moments are already tilted towards +z-axis due to DMI, the tilt angle is very small. This is because DMI is weaker compared to exchange coupling D~0.01J [103]. Therefore, the inclination towards +z-axis can be ignored. Hence, in FiM, $\vec{m}$, will only have significant x and y component, i.e., $\vec{m}$=<m_x,m_y,0>. On the other hand, the staggered

magnetization can be written as $\vec{l}$=<l_x,0,l_z>. In polar co-ordinates staggered magnetization, $\vec{l}$, containing an angle of φ_1

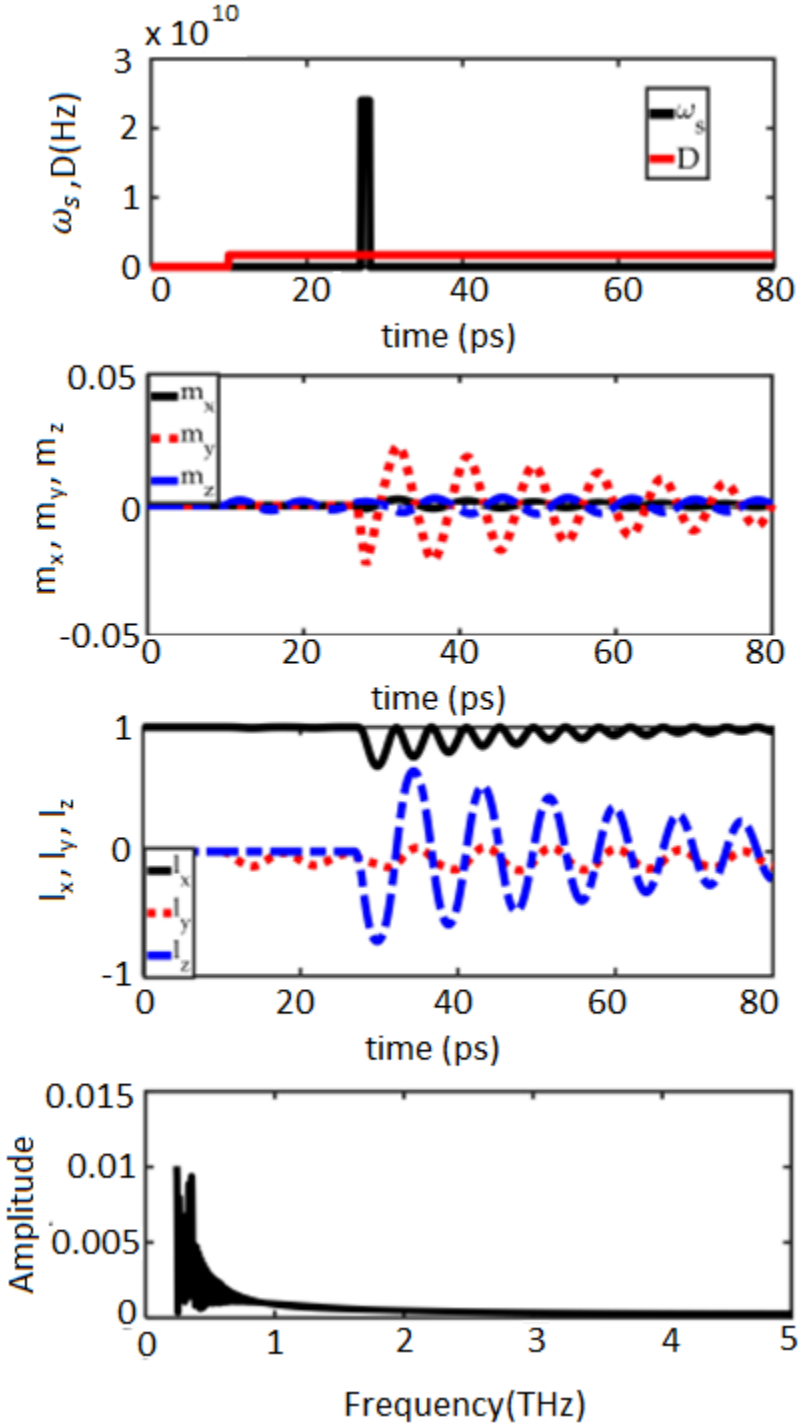

Fig. 4.5: Dynamics of staggered and weak magnetization in sigma mode. Note, m_y dominates the oscillation as expected in sigma mode of operation. The fast Fourier transformation (FFT) of l_z is also shown.

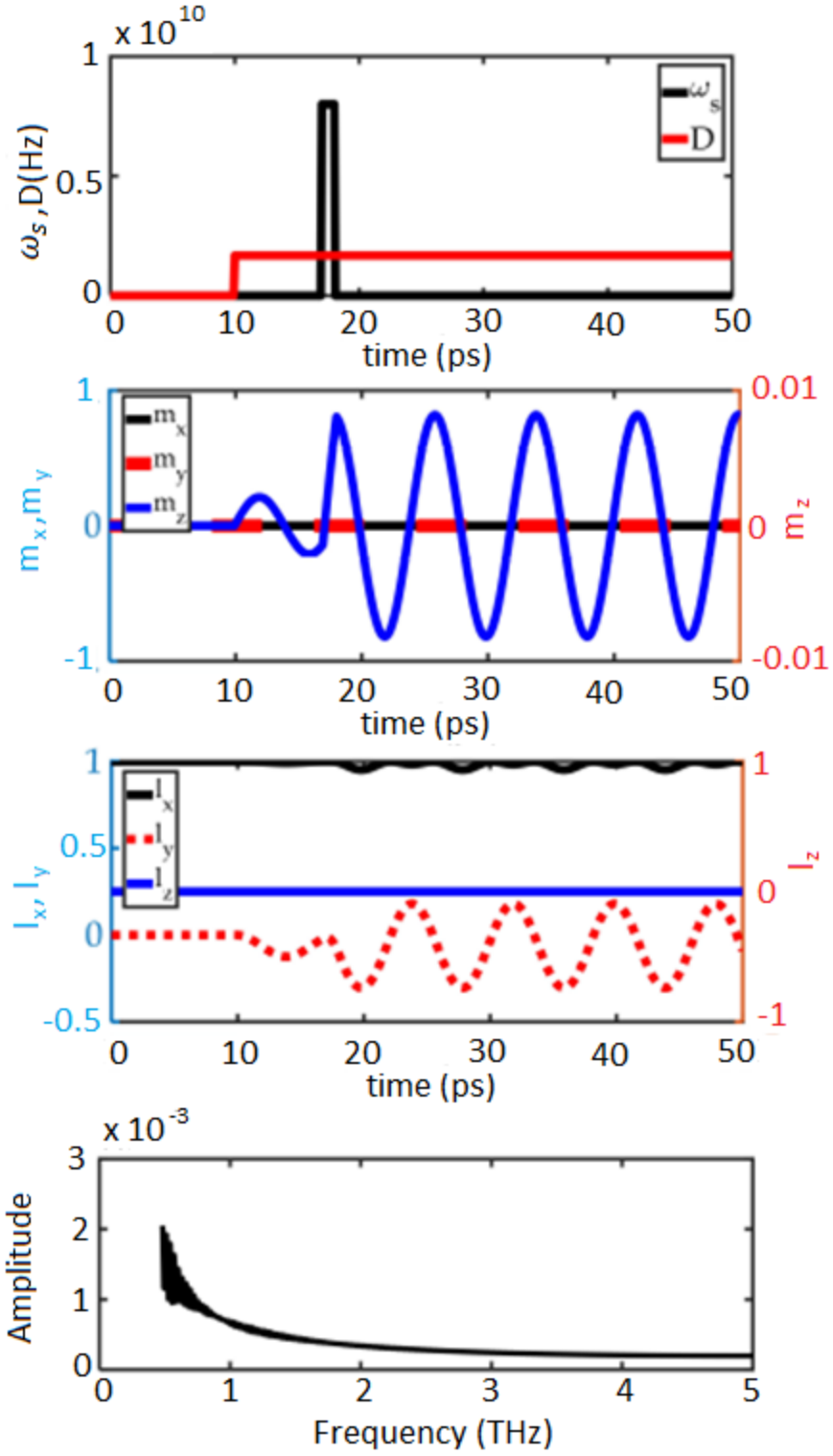

Fig. 4.6: Dynamics of staggered and weak magnetization in gamma mode. Note, m_z and l_y dominate the oscillation as expected in gamma mode of operation. The fast Fourier transformation (FFT) of m_z is also shown.

with the x-y plane (see Appendix C), is written as $\vec{l}$=<acosφ_1,0,asinφ_1> where $|\vec{l}|$=a and $m^2+l^2=1$. In FiM, we can show that (derivation in Appendix C)

$$\frac{d^2\varphi_1}{dt^2} - \left(\alpha a^2 + \frac{W_s p_y cosec^2\varphi_1}{2J - W_s p_y cot\varphi_1 + K_z}\right)\frac{d\varphi_1}{dt} + (K_x - K_z)(2J - W_s p_y cot\varphi_1 + K_z)a^2 \frac{sin2\varphi_1}{2} + W_s p_y\left(a^2 + \frac{W_f p_y cosec^2\varphi_1}{(2J - W_s p_y cot\varphi_1 + K_z)^2}\right) = 0 \quad (4.9)$$

Comparing with the differential equation of simple harmonic oscillator, the oscillation frequency can be written as, $\omega = \sqrt{(2J - W_s p_y cot\varphi_1 + K_z)(K_x - K_z)a^2}$. Note, oscillation frequency primarily depends on the magnitude of exchange coupling. The analytical equation yields the oscillation frequency to be 4.4 x 10^{11} Hz while FFT calculates the oscillation frequency to be 3.6 x 10^{11} Hz.

In the gamma mode of operation, i.e., when the injected current has spin polarization parallel to the z-axis, damping-like torque tries to incline the $\vec{m}$ towards -z-axis while $\vec{l}$ tries to align with y-axis. Therefore, the staggered magnetization and weak magnetization can be defined as $\vec{m}$=<m_x,0,m_z> and $\vec{l}$=<l_x,l_y,0>. It can be shown that the oscillation frequency of FiM in the gamma mode can be written as (derivation in Appendix C), $\omega = \sqrt{(2J - \frac{D_y}{a} sin\varphi_2 + K_x cos^2\varphi_2 - K_z)K_x a^2}$ where φ_2 is the angle between $\vec{l}$ and the x-y plane. The analytical equation yields the oscillation frequency to be 4.5 x 10^{11} Hz while FFT calculates the oscillation frequency to be 4.98 x 10^{11} Hz.

4.3 Effect of DMI on FiM Oscillation Frequency

In figure 4.7, the dependence of oscillation frequency on DMI is shown for gamma mode of oscillation in CoTb [108]. Typically DMI in the FiM/HM interface is measured to be on the order of 0.01J (measured at the CoTb/Pt interface) [108]. Nevertheless, theoretical papers [103] claim that DMI strength can be on the order of exchange coupling. The frequency vs normalized DMI curve in fig 4.7 can be fitted using the parabolic equation $f = a\sqrt{DMI} + C$. where a and C are constant fitting parameters. For CoTb, the fitting parameters are a = 3.0984$\sqrt{THz}$ and C = 0.45THz. It shows that oscillation frequency in FiM is a function of the square root of DMI at FiM/HM interface.

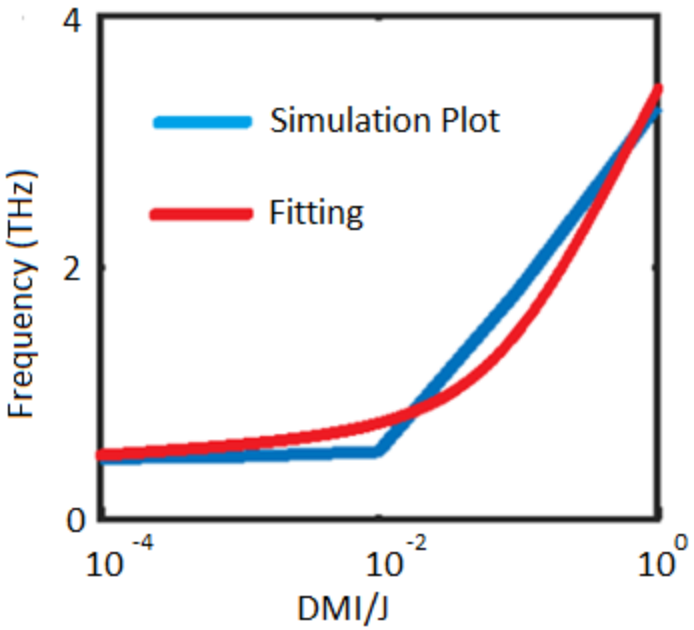

Fig. 4.7: DMI dependence of Gamma mode magnetization oscillation frequency in CoTb. The simulation parameters are taken from [108] (J=11.749 THz, K_x=26.9228 GHz, K_z=0, α = 0.002, DMI=0.11784 THz, W_s=0 GHz and W_f =0).

4.4 Magnetization Dynamics of Complex FiM

Complex ferrimagnet structures may have more than two magnetic moments in the sublattice like $Gd_3Fe_5O_{12}$ (fig. 4.8). In Gadolinium Iron Garnet, two Fe^{3+} ions are antiferromagnetically coupled with each other [113] (Fig. 4.8a). In a ferrimagnet, oppositely polarized magnetic moments and strongly exchange-coupled to each other while magnetic moments with iso-polarity are weakly exchange-coupled. The magnetism of Gd^{3+} ion depends on the temperature of the crystal lattice (fig. 4.8b and 4.8c) [112]. Exchange coupling between two Fe^{3+} ions (oppositely polarized), J_{m2m3}, is stronger than exchange coupling between Fe^{3+} ions and Gd^{3+} ion [112]. Moreover, exchange coupling between Gd^{3+} ion and two different Fe^{3+} ions (J_{m1m2} and J_{m3m1}) are also different from each other [113] (opposite polarization and iso-polarization). Note, the magnetic moment polarization directions of Gd^{3+} and Fe^{3+} ions are opposite below and above the compensation temperature. Nevertheless, the pairs of opposite and iso-polarized magnetic moments are identical and hence, the magnetization simulation framework is same for any temperature with small variation in parameters.

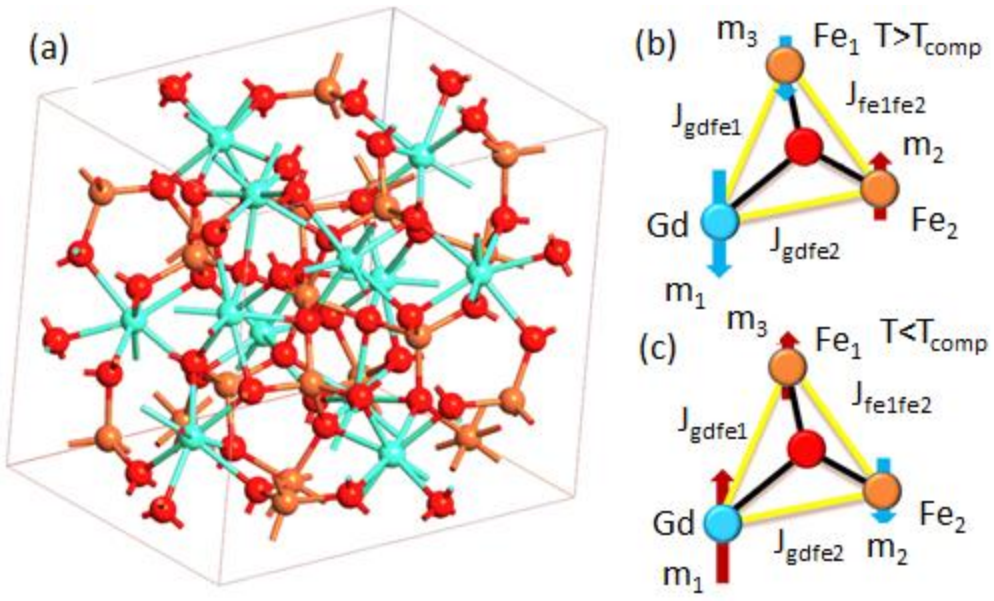

Fig. 4.8: (a) Schematic diagram of Gadolinium Iron Garnet crystal structure. (b) Magnetic moments in sublattice below the compensation temperature [113]. (c) Magnetic moments above compensation temperature.

In this case, the LLGS equations for the magnetic moments can be written as,

$$\frac{d\boldsymbol{m_1}}{dt} = \frac{J_{m3m1}}{1+\alpha^2}\,\boldsymbol{m_1}\times\boldsymbol{m_3} + \frac{\alpha J_{m3m1}}{1+\alpha^2}\,\boldsymbol{m_1}\times(\boldsymbol{m_1}\times\boldsymbol{m_3}) + \frac{J_{m1m2}}{1+\alpha^2}\,\boldsymbol{m_1}\times\boldsymbol{m_2} + \frac{\alpha J_{m1m2}}{1+\alpha^2}\,\boldsymbol{m_1}$$
$$\times(\boldsymbol{m_1}\times\boldsymbol{m_2}) + \frac{1}{1+\alpha^2}\,(\boldsymbol{m_2}+\boldsymbol{m_3})\times\boldsymbol{D_1} + \frac{\alpha}{1+\alpha^2}\,\boldsymbol{m_1}\times\big((\boldsymbol{m_2}+\boldsymbol{m_3})\times\boldsymbol{D_1}\big)$$
$$+ \frac{K_x m_{1x}}{1+\alpha^2}\,(\hat{x}\times\boldsymbol{m_1}) + \frac{\alpha K_x m_{1x}}{1+\alpha^2}\,(\hat{x}-m_{1x}\boldsymbol{m_1}) + \frac{K_z m_{1z}}{1+\alpha^2}\,(\hat{z}\times\boldsymbol{m_1})$$
$$+ \frac{\alpha K_z m_{1z}}{1+\alpha^2}\,(\hat{z}-m_{1z}\boldsymbol{m_1}) + \frac{W_s}{1+\alpha^2}\,\boldsymbol{m_1}\times(\boldsymbol{m_1}\times\boldsymbol{p}) - \frac{\alpha W_s}{1+\alpha^2}\,(\boldsymbol{m_1}\times\boldsymbol{p})$$
$$+ \frac{W_f}{1+\alpha^2}\,(\boldsymbol{m_1}\times\boldsymbol{p}) + \frac{\alpha W_f}{1+\alpha^2}\,\boldsymbol{m_1}$$
$$\times(\boldsymbol{m_1}\times\boldsymbol{p}) \qquad (4.10)$$

Note, the fundamental change in LLGS equation from the previous case is the addition of a couple of new terms for exchange coupling. The DMI vector $\vec{D}$ would also be different for each magnetic moment as each atom is at a different distance from the FiM/SHE metal interface. Rest of the equation is the same as the previous case. Similarly, the magnetization dynamics of $\overrightarrow{m_2}$ and $\overrightarrow{m_3}$ can be written (see Appendix D).

Note, field-like torque will be significant in this case due to asymmetry in the crystal structure. Weak and staggered magnetization dynamics can be evaluated as, $\vec{m} = \frac{\vec{m}_1+\vec{m}_2+\vec{m}_3}{3}$ and $\vec{l} = \frac{\vec{m}_1-\vec{m}_2+\vec{m}_3}{3}$. The magnetization dynamics diagram of Gadolinium Iron Garnet is shown in Appendix D. LLGS equation for more complex FiM crystals can be formed in a similar way.

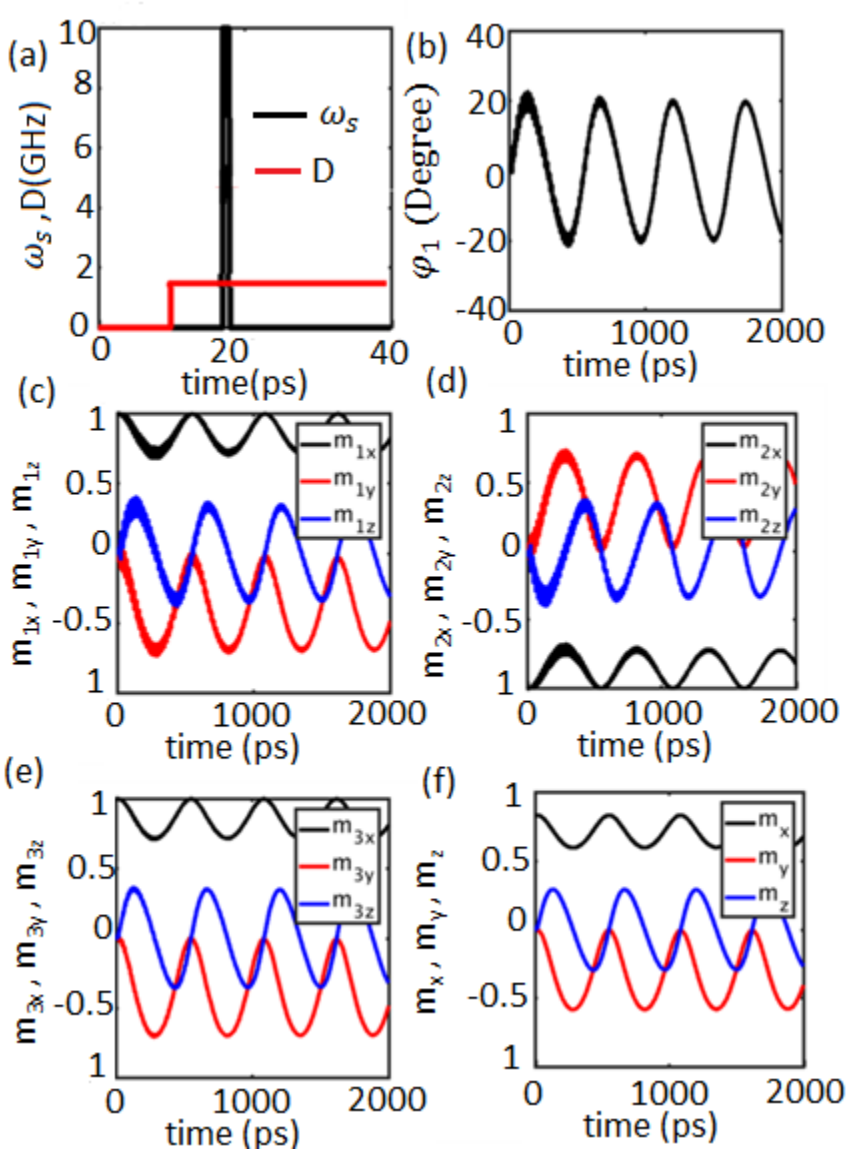

Fig. 4.9: Simulation of YIG magnetization dynamics. (a) The comparison of D_2 and spin current strength ($W_s=10^{10}$ Hz). The other simulation parameters are D_1 = 0.02536meV, D_2 = 0.001784meV, D_3 = 0.000896meV, k_x=5.2078 α=0.0003, W_f=0 [111]. (c),(d) and (e) Different components of magnetic moments in YIG sub lattice. (f) Components of resultant magnetization defined as, $\vec{m} = (\overrightarrow{m_1} + \overrightarrow{m_2} + \overrightarrow{m_3})/3$.

First principle calculation of individual exchange coupling between different pairs of magnetic moments in YIG is available in the literature [113]. We have taken the antiferromagnetic exchange coupling between Fe^{3+} ions to be 3.17meV, antiferromagnetic coupling between Y^{3+} and Fe^{3+} ions is to be 0.223eV and ferromagnetic coupling between Y^{3+} and Fe^{3+} ions to be 0.112eV [113]. Assuming individual DMIs to be equal to 0.008J, the magnetization dynamics simulation of YIG is shown in figure 4.9 which agrees well with the experimental measurements [109] [110]. The rest of the simulation parameters are listed in the description of fig. 4.9.

4.5 Conclusion

To conclude, we demonstrated the significance of the solitary effect of DMI on the magnetization of AFM and FiM. Our numerical simulation and analytical analysis revealed the fact that magnetization oscillation frequency in AFM and FiM primarily depends on the exchange coupling and interfacial DMI and is a very weak function of injected spin current density. It has been exhibited that the FL spin-transfer torques on AFM and FiM, ignored in previous works [99,106], can be quite significant. The overall magnetization dynamics of the FiM sublattice considering all of the major attributes have been proposed and analyzed. Finally, the magnetic structure of a complex FiM is investigated. FiM offers most of the favorable characteristics of AFM (high exchange coupling and DMI, faster switching and high oscillation frequency) and FM (net magnetization) and therefore can be a potential candidate in constructing spintronic devices like spin torque oscillator and magnetic memory.

4.6 Summary

Ferrimagnets (FiM) are divided into small domains comprising of oppositely polarized magnetic moments with weak anisotropy. FiM possesses a small net magnetization with strong exchange coupling energy. When FiM comes in contact with a material having strong spin-orbit coupling, like spin hall metal or topological insulator, the non-linear magnetic exchange interaction known as Dzyaloshinskii-Moriya interaction (DMI) becomes significant, especially at the interface. DMI interaction plays a crucial role in FiM magnetization dynamics. Moreover, spin-polarized current, injected into the FiM, introduces two different types of torques - namely

'field-like' (FL) torque and 'damping-like' (DL) torque. The combined effect of the inherent magnetism parameters and external magnetic perturbation yields exciting magnetization characteristics in FiM like fast switching and high-frequency oscillation. Moreover, FiM magnetization depends on the complexity and the symmetry properties of the FiM crystal structure.

5. FAST SWITCHING IN COTB BASED FERRIMAGNET TUNNEL JUNCTION

5.1 Magnetization Dynamics in CoTb

In a ferromagnet (FM), the magnetic moments precess around the switching axis before settling down due to damping force. Ferromagnets have slow switching speed (on the order of nanoseconds) [114,115] because of long precession time. Ferrimagnet (FiM), on the other hand, has strong exchange coupling among the oppositely polarized magnetic moments [116] (fig. 5.1(a), 5.1(b), 5.1(c)). Robust exchange coupling always tries to maintain the equilibrium 180^0 phase difference between the two oppositely polarized magnetic moments, $\overrightarrow{m_1}$ and $\overrightarrow{m_2}$, in FiM sublattice (fig.5.1(b)). Introduction of spin-polarized current from heavy spin Hall metal (SHE metal) can perturb the equilibrium magnetic configuration in FiM by exerting two types of SOT - field-like (FL) torque (green arrow in fig.5.1(d)) and damping-like (DL) torque (purple arrow in fig.5.1(d)) on the magnetic moments. If strong SOT can switch the magnetization direction of either $\overrightarrow{m_1}$ or $\overrightarrow{m_2}$, robust exchange coupling immediately switches the other one to maintain the equilibrium. Thus, $\overrightarrow{m_1}$ and $\overrightarrow{m_2}$ interchanges their magnetization direction. Since in equilibrium, $\overrightarrow{m_1}$ and $\overrightarrow{m_2}$ are 180^0 out of phase, exchange coupling does not allow them to oscillate for long around switching axis if the external magnetic perturbation (spin current flow) no longer exists. The phenomena of exchange coupled magnetization dynamics in FiM and antiferromagnet (AFM) is known as 'bulk torque'. Exchange coupling in thick quantum well like ferrimagnet slab depends on the slab thickness like the thickness dependence of exchange coupling in AFM [117]. Exchange coupling gradually increases with the increasing thickness of the FiM slab before getting saturated and hence, the torque between exchange-coupled oppositely polarized magnetic moments in FiM and AFM is called 'bulk torque'. Since the FiM exchange coupling is stronger than the FM damping force, the FiM switching time is lower than that of FM.

Internal exchange coupling plays a vital role in FiM magnetization dynamics. Exchange coupling is a long-range parameter [118] compared with the atomic dimension. In an FiM, the oppositely polarized magnetic moments are strongly exchange-coupled while unidirectional magnetic moments are weakly exchange-coupled.

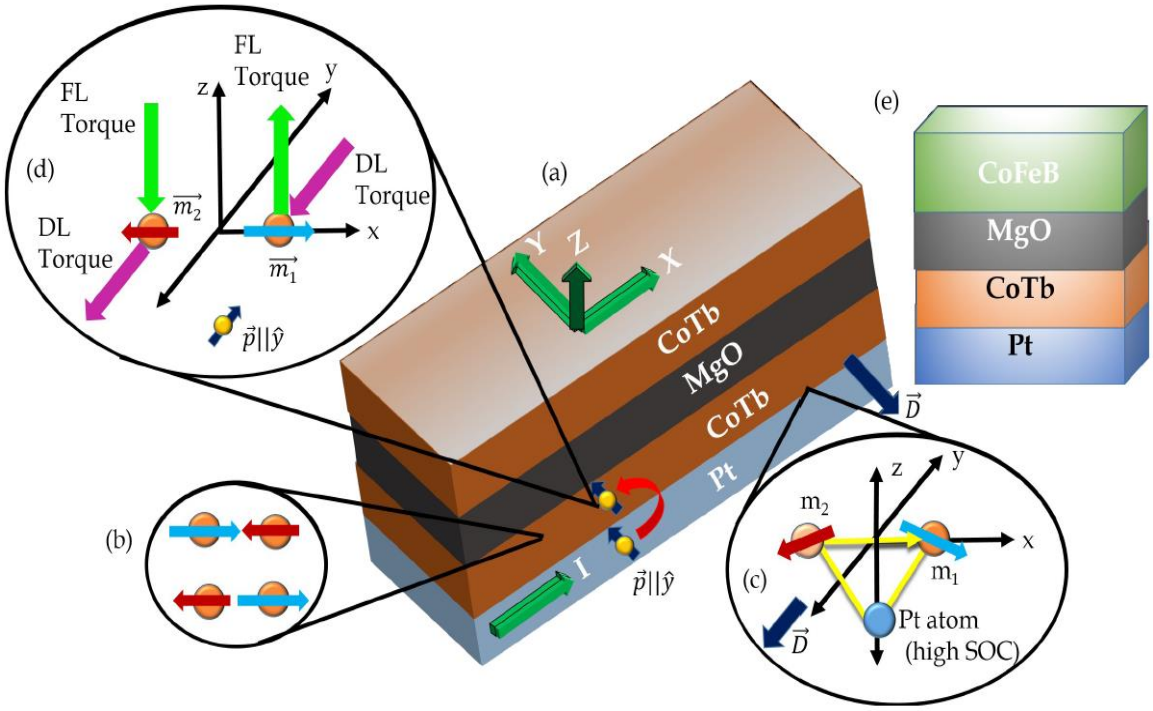

Fig. 5.1: (a) Proposed MTJ structures - CoTb/MgO/CoTb/Pt. Charge current is flowing along X-axis in Pt and spin current, polarized along Y-axis, is getting accumulated. Y-polarized spin current diffuses into CoTb slab (indicated by the red arrow). b) Unperturbed magnetic moments in CoTb. c) Direction (indigo arrow) and effect of DMI at CoTb/Pt interface. Strong DMI causes the interfacial magnetic moments of CoTb to incline a little bit towards -Z-axis. d) Directions of field-like (FL, green arrow) and damping-like (DL, purple arrow) torques exerted by Y-polarized spin current on CoTb magnetic moments. e) Proposed hybrid MTJ structure of CoFeB/MgO/CoTb/Pt.

Alloy made of transition metal (TM) and rear-earth (REM) metal shows excellent ferrimagnetic behavior. The exchange interaction between f and d electrons of REM and TM atoms causes the anti-parallel orientation of magnetic moments in the alloy [119]. CoTb is a newly found promising TM-RE ferrimagnetic alloy showing fast magnetization dynamics [119]. CoTb alloy needs to be thoroughly investigated to determine the range and value of inter-CoTb exchange coupling coefficients. An *ab-initio* approach, based on local spin density approximation (LSDA), to calculate exchange coupling between two moments in a magnetic material is presented in ref [120]. The same approach of spin-polarized relativistic Korringa-Kohn-Rostoker (KKR)) Green's function method [120] in conjunction with Heisenberg Hamiltonian [120] is used here to calculate the exchange coupling between the magnetic moments in CoTb layer. The simultaneous presence of strong exchange coupling and spin-

polarized current in FiM exhibits exciting magnetization dynamics which can be utilized in spin-based devices.

Source of spin-polarized current, Pt, underneath the CoTb (FiM), has strong spin-orbit coupling. A strong Dzyaloshinskii-Moriya interaction (DMI) is present at the CoTb/Pt interface which affects the magnetization dynamics of the CoTb interfacial magnetic moment [121, 122]. Strong DMI can tilt the interfacial magnetic moments by a small amount [122] as shown in figure 1d (red and blue arrow). The DMI tensor can be calculated by inspecting the antisymmetric components of the Heisenberg Hamiltonian [120]. We calculate of interfacial DMI by forming the interface crystal structure and constructing the interface Hamiltonian using the same *ab-initio* approach described above [115]. We took the interfacial DMI into account while calculating the magnetization dynamics of CoTb due to injection of spin-polarized current.

Spin-polarized current is injected in the free CoTb layer from the Pt underlayer. The spin-polarized current creates perturbation in the magnetic structure of CoTb and the magnetization dynamics of CoTb is modeled using the Landau-Lifshitz-Gilbert-Slonczewski (LLGS) [123] formalism. We model the magnetization dynamics of FiM devices driven by spin-polarized current from adjacent HM. We derive the DMI contribution to the magnetization dynamics of the FiM/HM interfacial magnetic moments. The switching time and corresponding power consumption are calculated and optimized by designing the thickness of the CoTb free layer. Note, increasing CoTb thickness decreases the switching time because the bulk torque in CoTb layer depends on the CoTb slab thickness. Nevertheless, thicker CoTb layer requires more current to switch.

Several experiments have been conducted on Heusler alloy (an FiM) based MTJ (Co_2MnSi/MgO/ Co_2MnSi) with MgO as a tunneling barrier [124-127] in which TMR is reported in a very wide range. Moreover, a drastic reduction in TMR is observed with increasing temperature [127]. The reason can be attributed to the rapid generation of magnons with increasing temperature [128] which reduces the MTJ antiparallel resistance. Co_2MnSi has three magnetic moments in the magnetic sublattice while CoTb has only two magnetic moments in the sublattice. Therefore, generation of magnons in CoTb with increasing temperature is less than that of Co_2MnSi. Our simulation shows that TMR variation in CoTb based MTJ is less temperature sensitive than Co_2MnSi based MTJ.

In fig.5.1, two possible configurations of FiM based MTJs are shown. The free layer of both the MTJs is $Co_{0.87}Tb_{0.13}$ [1119], which is a ferrimagnet with two oppositely polarized magnetic moments [119] in a sublattice. In one of the MTJs we use CoTb (FiM) as the fixed layer while in the other MTJ, CoFeB (FM) acts as the fixed layer (fig.5.1). MgO is used as the tunneling barrier for both the MTJs. We show that CoTb/MgO/CoTb MTJ has higher TMR than CoTb/MgO/CoFeB MTJ. In CoTb/MgO/CoTb MTJ, CoTb slabs of the same dimension as free and fixed layer result in coherent spin current tunneling which lowers the parallel magneto-resistance and increases TMR. A similar effect has been observed using Heusler alloy based MTJ [124]. On the other hand, incoherent spin tunneling between CoTb and CoFeB decreases the TMR in CoTb/MgO/CoFeB MTJ.

TMR ratio is an important figure of merit for MTJs. TMR is calculated using the NEGF formalism [129] for calculating the tunneling spin current. Note, we benchmark our simulation framework with published experimental and simulation results. We also analyze the thermal stability of the CoTb based and MTJ and show that due to strong exchange coupling and big volume, our proposed MTJ structure is relatively immune to thermal noise compared with FMTJ.

We simulate the magnetization dynamics of a ferrimagnet (CoTb) slab and show picosecond range switching. We also propose, design and analyze the performance of CoTb based MTJs for fast operation. We theoretically calculate the exchange coupling inside CoTb layer using spin-polarized relativistic KKR Green's function method. We show the way to calculate the interfacial DMI at the CoTb/Pt interface using an *ab-initio* method. The computed parameters are used to simulate and observe the magnetization dynamics of CoTb and optimize the switching characteristic and power consumption by designing proper CoTb thickness. NEGF formalism is used to calculate the TMR of the proposed MTJ. TMR ratio is increased by introducing coherent spin current tunneling between two identical CoTb layers acting as MTJ fixed and free layer. Finally, the thermal stability of the CoTb based MTJ is analyzed and relative performance comparison between our proposed MTJs and FM based MTJ is discussed.

5.2 Modeling and simulation of CoTb based FMTJ

Magnetization dynamics of ferrimagnet is significantly different from that of ferromagnet because of the oppositely polarized magnetic moments. Unlike ferromagnet, FiM magnetization is more dependent on the exchange coupling rather than anisotropy [121]. Moreover, in FiM, the

damping is less significant that FM [115]. The magnetization simulation of CoTb is done by dividing it into small sublattice grids. The magnetization of sublattice grids near the CoTb/Pt interface is simulated considering the interfacial DMI. After calculating the magnetization dynamics of CoTb slab, the tunneling magnetoresistance ratio (TMR) of CoTb based FMTJ is calculated using NEGF formalism. The simulation of CoTb based FMTJ has two major steps - calculation of CoTb based free layer magnetization dynamics and TMR of CoTb based FMTJ. First, the magnetization dynamics of the CoTb layer due to the injection of the spin current from the adjacent Pt layer (fig. 5.1) is simulated using the FiM LLGS formalism [123]. Exchange coupling in CoTb and DMI at the CoTb/Pt interface are calculated using KKR Green's function method.

5.2.1 *Ab-initio* Calculation of Exchange Coupling and DMI

The exchange coupling between two magnetic moments at position i and j, J_{ij} is calculated with the help of the scattering matrix. The scattering matrix is introduced in local spin density functional (LSDF) theory and the magnetic moments at position i and j are tilted by a small angle from their equilibrium position. The total energy difference between an equilibrium position and tilted configuration indicates the exchange coupling between the magnetic moments at position i and j. The formula is written as [120],

$$J_{ij} = \frac{1}{4\pi}\int Tr(t_{i\uparrow}^{-1} - t_{i\downarrow}^{-1})\hat{\tau}_{\uparrow}^{ij}(t_{j\uparrow}^{-1} - t_{j\downarrow}^{-1})\hat{\tau}_{\downarrow}^{ij}\,dE$$

$t_{i\uparrow}^{-1}$ and $t_{i\downarrow}^{-1}$ are inverse scattering matrices for up-spin and down-spin at site i, $t_{j\uparrow}^{-1}$ and $t_{j\downarrow}^{-1}$ are inverse scattering matrices for up-spin and down-spin at site j, E_F is the Fermi energy, $\hat{\tau}_{\uparrow}^{ij}$ and $\hat{\tau}_{\downarrow}^{ij}$ are the up-spin and down-spin scattering path operators respectively.

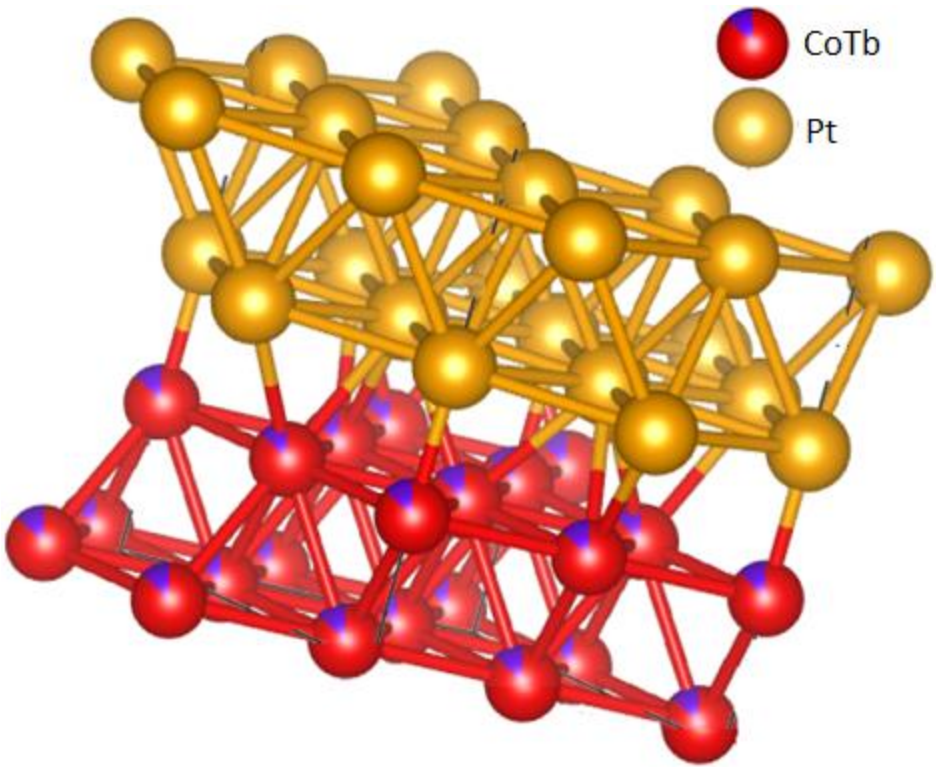

Fig. 5.2: Crystal structure of CoTb/Pt interface. Note, CoTb is an alloy with 87% Co and 13% of Tb. The alloy is constructed assuming a Cobalt lattice structure with hybrid atom containing 87% of Co and 13% Tb.

'Tr' indicates the trace over the orbital states. For cobalt, the trace is taken for 3d orbital while for Tb, the trace is calculated for 4f orbital. Inter-CoTb exchange coupling is a long-range parameter and hence, we use the 1nm calculation radius for exchange coupling calculation. Note, $Co_{0.87}Tb_{0.13}$ alloy is formed by building the standard Cobalt crystal structure. Then each Co atom is replaced by a hybrid atom containing 87% Co and 13%Tb (fig. 5.2) because electronic and magnetic properties of alloys can be calculated using the Coherent Potential Approximation (CPA) [130, 131].

The spin current is injected in CoTb from Pt underlayer. Pt has strong spin-orbit coupling and hence, CoTb magnetic moments feel strong DMI at the CoTb/Pt interface. CoTb/Pt interface DMI has not been theoretically studied before. We formed an artificial crystal structure at the interface and the lattice constant is assumed to be the average of the CoTb and Pt lattice constants. The strain at the interface is small (2.8%) and therefore, we have not considered any crystal deformation at the interface. In order to avoid any effect from quantum confinement, the artificial crystal structure is assumed to be periodic with two layers of Pt atoms and two layers of

CoTb atoms (fig. 5.2). Interfacial DMI is very short-ranged. Therefore, for interfacial DMI calculation, the calculation is performed over a short distance. Assuming a Pt atom to be center, the calculation radius is set to be 0.5nm. The spin-polarized relativistic Hamiltonian of the crystal is formed and compared with the Heisenberg Hamiltonian [132].

$$H_{ex} = -\sum_{i,j,i\neq j} J_{ij}\overrightarrow{m_i}.\overrightarrow{m_j}$$

$\overrightarrow{m_i}$ and $\overrightarrow{m_j}$ are the unit vectors along the magnetic moments at site i and j respectively. J_{ij} is the exchange coupling parameter between the magnetic moments at site i and j. The antisymmetric Components of the Hamiltonian represents the DMI at the interface.

Ab-initio calculation of exchange coupling parameter, J_{ex} inside CoTb layer and DMI, $\vec{D}$ at the CoTb/Pt interface is executed using SPRKKR [110] package. The interface between CoTb and Pt is formed using the package quantumwise [133-135]. The detail of exchange coupling and DMI calculation using spin polarization relativistic KKR Green's function method is discussed in [120]. *Ab-initio* exchange coupling and DMI simulation framework are bench-marked with published results as shown in fig.5.3.

5.2.2 Magnetization Dynamics in CoTb

Calculated J_{ex} and $\vec{D}$ are used in FiM magnetization simulation framework to determine the switching characteristics of the free CoTb layer in the FMTJ. In absence of external perturbation, two oppositely polarized magnetic moments, $\overrightarrow{m_1}$ and $\overrightarrow{m_2}$ in a FiM sublattice lies along the +x axis and -x-axis, respectively (fig. 1). FiM sublattice adjacent to strong spin-orbit coupling will be subject to DMI. DMI will tilt both the magnetic moments to -z-axis (fig. 1). Energy change in the sublattice due to DMI is expressed as, $\epsilon_{DMI} = \vec{D}.(\overrightarrow{m_1} \times \overrightarrow{m_2})$ [136]. $\vec{D}$ is the DMI vector which is pointing along the +y axis in this case (fig. 1b). Change in magnetization dynamics due to DMI alone is calculated from the derivative of ϵ_{DMI} with respect to the magnetic moment, i.e, $\frac{d\epsilon}{d\overrightarrow{m_1}}$ and $\frac{d\epsilon}{d\overrightarrow{m_2}}$ [137]. It can be shown that the DMI contribution to magnetization dynamics of, $\overrightarrow{m_1}$ and $\overrightarrow{m_2}$ is written as $\overrightarrow{m_2} \times \vec{D}$ and $\vec{D} \times \overrightarrow{m_1}$, respectively (derivation can be found in Appendix A).

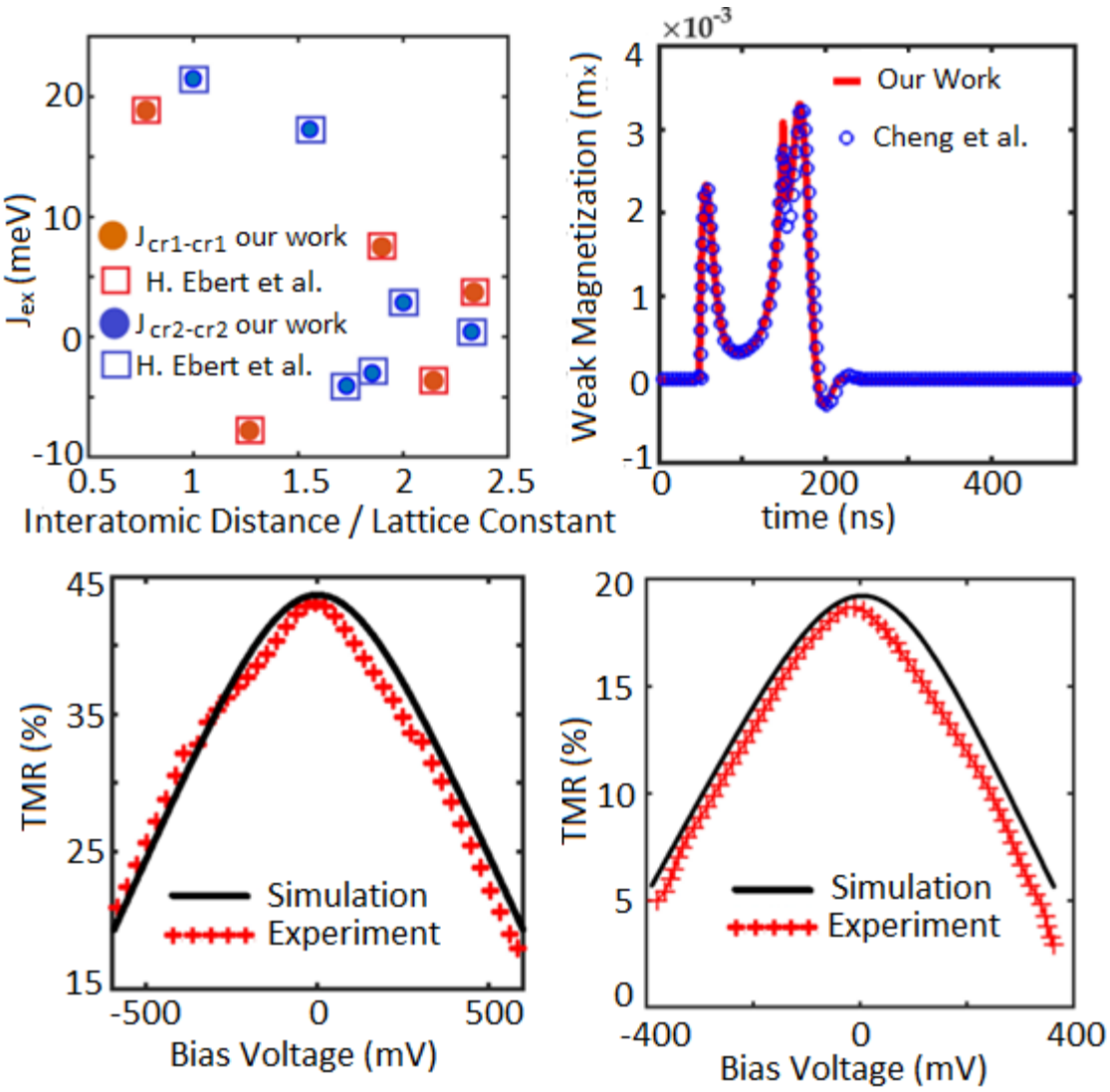

Fig. 5.3: Benchmarking of the simulation framework. (Top left) benchmarking *ab-initio* method of calculating exchange coupling with [120] for antiferromagnetic material CrSe, since, the magnetic structure of CrSe is similar to that of CoTb (top right) benchmarking magnetization dynamics simulation framework with simulation result from [138] for antiferromagnet NiO, benchmarking the NEGF formalism of calculating magneto-resistances and TMR ratio with experiments [124] for Heusler alloy based MTJs (bottom left) $Co_2MnSi/MgO/Co_2MnSi$ MTJ and (bottom right) $Co_2MnSi/MgO/CoFeB$ MTJ.

Therefore, before injecting the spin-polarized current, the magnetization dynamics can be defined by adding the DMI terms to the LLG [123] equation.

$$\frac{d\overrightarrow{m_1}}{dt} = J\overrightarrow{m_1} \times \overrightarrow{m_2} + \overrightarrow{m_2} \times \vec{D} + K_x m_{1x}\, \hat{\boldsymbol{x}} \times \overrightarrow{m_1} + K_z m_{1z}\, \hat{\boldsymbol{z}} \times \overrightarrow{m_1} + \alpha \overrightarrow{m_1} \times \frac{d\overrightarrow{m_1}}{dt} \quad (5.1)$$

$$\frac{d\overrightarrow{m_2}}{dt} = J\, \overrightarrow{m_2} \times \overrightarrow{m_1} + \overrightarrow{m_1} \times \vec{D} + K_x m_{2x}\, \hat{\boldsymbol{x}} \times \overrightarrow{m_2} + K_z m_{2z}\, \hat{\boldsymbol{z}} \times \overrightarrow{m_2} + \alpha \overrightarrow{m_2} \times \frac{d\overrightarrow{m_2}}{dt} \quad (5.2)$$

Here, J is the symmetric component of exchange coupling constant between $\overrightarrow{m_1}$ and $\overrightarrow{m_2}$, K_x and K_z are the in-plane and out-of-plane anisotropy constants, respectively and α is the Gilbert damping constant. The magnetization dynamics equations shown above are the nearest neighbor models. However, J usually is significant over long-range compared with atomic sublattice dimension [118]. Hence, the significant contributions from 'n' number of other neighbors can be included by adding the terms $\sum_{i=3}^{n} J_{1i}\overrightarrow{m_1} \times \overrightarrow{m_i}$ and $\sum_{j=3}^{n} J_{2j}\overrightarrow{m_2} \times \overrightarrow{m_j}$ in the first and second equation respectively.

Spin angular momentum transfer in FiM introduces the spin transfer torques on magnetic moments in sublattice. Spin polarization can be either parallel to y-axis (sigma mode) or z-axis (gamma mode) depending on the sign of spin hall angle of the underlayer SHE metal [121]. Fig 1 shows the directions of damping-like torque and field-like torque for different spin-polarized current. The damping-like torque is defined as $\overrightarrow{\tau_s} = W_s\overrightarrow{m_1} \times (\vec{p} \times \overrightarrow{m_1})$ [138] . $\vec{p}$ is the polarization vector and W_s is the strength of the damping like torque defined as $W_s = \frac{\xi\hbar\gamma J_s}{2M_0 Ve}$ [138]. Here ξ is the scattering efficiency, $\hbar$ is the reduced Plank's constant, γ is the gyromagnetic ratio, J_s is the spin-polarized current density. M_0 is defined as the saturation magnetization of the sub-lattice defined as $M_0 = \sqrt{m_1^2 + m_2^2}$. V refers to the volume of the sublattice and e is the electron charge. Field-like torque is expressed as $\overrightarrow{\tau_f} = W_f\overrightarrow{m_1} \times \vec{p}$ [139]. W_f is the strength of the FL torque defined as $W_f = \beta W_s$. β is the strength of the FL torque relative to DL torque. Injection of spin-polarized current yields the following magnetization dynamic equations for $\overrightarrow{m_1}$ and $\overrightarrow{m_2}$.

$$\frac{d\overrightarrow{m_1}}{dt} = J\overrightarrow{m_1} \times \overrightarrow{m_2} + \overrightarrow{m_2} \times \vec{D} + K_x m_{1x}\,\hat{\boldsymbol{x}} \times \overrightarrow{m_1} + K_z m_{1z}\,\hat{\boldsymbol{z}} \times \overrightarrow{m_1} + \alpha\overrightarrow{m_1} \times \frac{d\overrightarrow{m_1}}{dt} + W_s\,\overrightarrow{m_1} \times (\overrightarrow{m_1} \times \vec{p}) + W_f\overrightarrow{m_1} \times \vec{p} \quad (5.3)$$

$$\frac{d\overrightarrow{m_2}}{dt} = J\,\overrightarrow{m_2} \times \overrightarrow{m_1} + \overrightarrow{m_1} \times \vec{D} + K_x m_{2x}\,\hat{\boldsymbol{x}} \times \overrightarrow{m_2} + K_z m_{2z}\,\hat{\boldsymbol{z}} \times \overrightarrow{m_2} + \alpha\overrightarrow{m_2} \times \frac{d\overrightarrow{m_2}}{dt} + W_s\,\overrightarrow{m_2} \times (\overrightarrow{m_2} \times \vec{p}) + W_f\overrightarrow{m_2} \times \vec{p} \quad (5.4)$$

Algebraic manipulation of the LLGS equations will describe the complete magnetization dynamics of the two magnetic moments $\overrightarrow{m_1}$ and $\overrightarrow{m_2}$ inside FiM sublattice.

$$\frac{d\overrightarrow{m_1}}{dt} = \frac{J}{1+\alpha^2}\,\overrightarrow{m_1}\times\overrightarrow{m_2} + \frac{J\alpha}{1+\alpha^2}\,\overrightarrow{m_1}\times(\overrightarrow{m_1}\times\overrightarrow{m_2}) + \frac{1}{1+\alpha^2}\,\overrightarrow{m_2}\times\vec{D} + \frac{\alpha}{1+\alpha^2}\,\overrightarrow{m_1}$$
$$\times\left(\overrightarrow{m_2}\times\vec{D}\right) + \frac{K_x m_{1x}}{1+\alpha^2}\,\hat{\boldsymbol{x}}\times\overrightarrow{m_1} + \frac{\alpha K_x m_{1x}}{1+\alpha^2}\left(\hat{\boldsymbol{x}} - m_{1x}\overrightarrow{\boldsymbol{m_1}}\right) + \frac{K_z m_{1z}}{1+\alpha^2}\,\hat{\boldsymbol{z}}\times\overrightarrow{m_1}$$
$$+ \frac{\alpha K_z m_{1z}}{1+\alpha^2}\left(\hat{\boldsymbol{z}} - m_{1z}\overrightarrow{\boldsymbol{m_1}}\right) + \frac{W_s}{1+\alpha^2}\,\overrightarrow{m_1}\times(\overrightarrow{m_1}\times\vec{p}) - \frac{\alpha W_s}{1+\alpha^2}\,\overrightarrow{m_1}\times\vec{p}$$
$$+ \frac{W_f}{1+\alpha^2}\,\overrightarrow{m_1}\times\vec{p} + \frac{\alpha W_f}{1+\alpha^2}\,\overrightarrow{m_1}\times(\overrightarrow{m_1}\times\vec{p}) \qquad (5.5)$$

$$\frac{d\overrightarrow{m_2}}{dt} = \frac{J}{1+\alpha^2}\,\overrightarrow{m_2}\times\overrightarrow{m_1} + \frac{J\alpha}{1+\alpha^2}\,\overrightarrow{m_2}\times(\overrightarrow{m_2}\times\overrightarrow{m_1}) + \frac{1}{1+\alpha^2}\,\vec{D}\times\overrightarrow{m_1} + \frac{\alpha}{1+\alpha^2}\,\overrightarrow{m_2}$$
$$\times\left(\vec{D}\times\overrightarrow{m_1}\right) + \frac{K_x m_{2x}}{1+\alpha^2}\,\hat{\boldsymbol{x}}\times\overrightarrow{m_2} + \frac{\alpha K_x m_{2x}}{1+\alpha^2}\left(\hat{\boldsymbol{x}} - m_{2x}\overrightarrow{\boldsymbol{m_2}}\right) + \frac{K_z m_{2z}}{1+\alpha^2}\,\hat{\boldsymbol{z}}\times\overrightarrow{m_2}$$
$$+ \frac{\alpha K_z m_{2z}}{1+\alpha^2}\left(\hat{\boldsymbol{z}} - m_{2z}\overrightarrow{\boldsymbol{m_2}}\right) + \frac{W_s}{1+\alpha^2}\,\overrightarrow{m_2}\times(\overrightarrow{m_2}\times\vec{p}) - \frac{\alpha W_s}{1+\alpha^2}\,\overrightarrow{m_2}\times\vec{p}$$
$$+ \frac{W_f}{1+\alpha^2}\,\overrightarrow{m_2}\times\vec{p} + \frac{\alpha W_f}{1+\alpha^2}\,\overrightarrow{m_2}\times(\overrightarrow{m_2}\times\vec{p}) \qquad (5.6)$$

The weak and staggered magnetization order parameters can be defined as, $\vec{m} = \frac{\overrightarrow{m_1}+\overrightarrow{m_2}}{2}$ and $\vec{l} = \frac{\overrightarrow{m_1}-\overrightarrow{m_2}}{2}$ [121], respectively. The staggered magnetization, $\vec{l}$ can be written as,

$$\frac{d\vec{l}}{dt} = 2J\vec{l}\times\vec{m} + \vec{m}\times\vec{D} + K_x\,\hat{\boldsymbol{x}}\times\left(m_x\vec{l} + l_x\vec{m}\right) + K_z\,\hat{\boldsymbol{z}}\times\left(m_z\vec{l} + l_z\vec{m}\right) + \alpha\left(\vec{m}\times\frac{d\vec{l}}{dt} + \vec{l}\times\frac{d\vec{m}}{dt}\right)$$
$$+ W_s\left[\vec{l}\times(\vec{m}\times\vec{p}) + \vec{m}\times\left(\vec{l}\times\vec{p}\right)\right] + W_f\,\vec{l}\times\vec{p}$$

Similarly, the weak magnetization, $\vec{m}$ is written as,

$$\frac{d\vec{m}}{dt} = 2\vec{m}\times\vec{D} + K_x\,\hat{\boldsymbol{x}}\times\left(m_x\vec{m} + l_x\vec{l}\right) + K_z\,\hat{\boldsymbol{z}}\times\left(m_z\vec{m} + l_z\vec{l}\right) + \alpha\left(\vec{l}\times\frac{d\vec{l}}{dt} + \vec{m}\times\frac{d\vec{m}}{dt}\right)$$
$$+ W_s\left[\vec{l}\times\left(\vec{l}\times\vec{p}\right) + \vec{m}\times(\vec{m}\times\vec{p})\right] + W_f\,\vec{m}\times\vec{p}$$

Note, DMI is significant only at the CoTb/Pt interface and hence the DMI can be ignored for bulk FiM magnetization simulation. Also, field-like torque does not play a strong role in FiM magnetization dynamics [138]. Further discussion on FiM magnetization can be found in ref [122]. Therefore, we have also ignored the filed-like torque. The FiM LLGS simulation framework is benchmarked in fig. 5.3.

5.2.3 NEGF Calculation of TMR in CoTb Based FMTJ

After calculating the switching characteristics, an important figure of merit for MTJs, the TMR ratio, is determined using the NEGF [123] formalism of calculating the tunneling spin current. In the spin tunneling NEGF simulation framework, the fixed and free magnetic layers are considered to be the contacts and the MgO layer acts as the channel region. The Hamiltonians of the contacts and channel are formed using the effective mass approximation [115]. The major difference between the Hamiltonians of regular contact and magnetic contact is that the magnetic contact Hamiltonian contains the exchange splitting term between up-spin and downspin bands. By introducing proper tunneling barrier heights, we calculate the parallel and antiparallel magneto-resistance and TMR ratio. The spin tunneling NEGF formalism is discussed in detail in [129]. The TMR simulation framework is benchmarked with experimental results as shown in fig. 5.3. The NEGF simulation parameters for fig. 5.3 can be found in Appendix F.

5.3 Results and Discussion

In order to obtain optimum performance from the FiM based MTJ, some design issues need to be considered carefully. One of the major issues is the interface issue between FiM and tunneling oxide. There have been several experiments on Heusler alloy based FiM MTJ [124] in which researchers have reported TMR in a very wide range. The rough interface between complex Heusler alloy and MgO plays a vital role in the TMR variation. Also, the interface between heavy metal and FiM is important for efficient spin current injection.

MgO has halite cubic structure (space group $Fm\overline{3}n$)[140] and CoTb is also a member of the same space group[119]. Hence, CoTb does not create a rough interface with MgO. Moreover, we choose Pt as the heavy metal layer (fig. 5.1) since Pt has halite crystal structure similar to CoTb (same space group) [141] and the lattice constant of Pt (a=0.395nm)[141] is very close to that of Co (a=0.354nm)[142].

5.3.1 Thickness of Free CoTb and MgO Layer

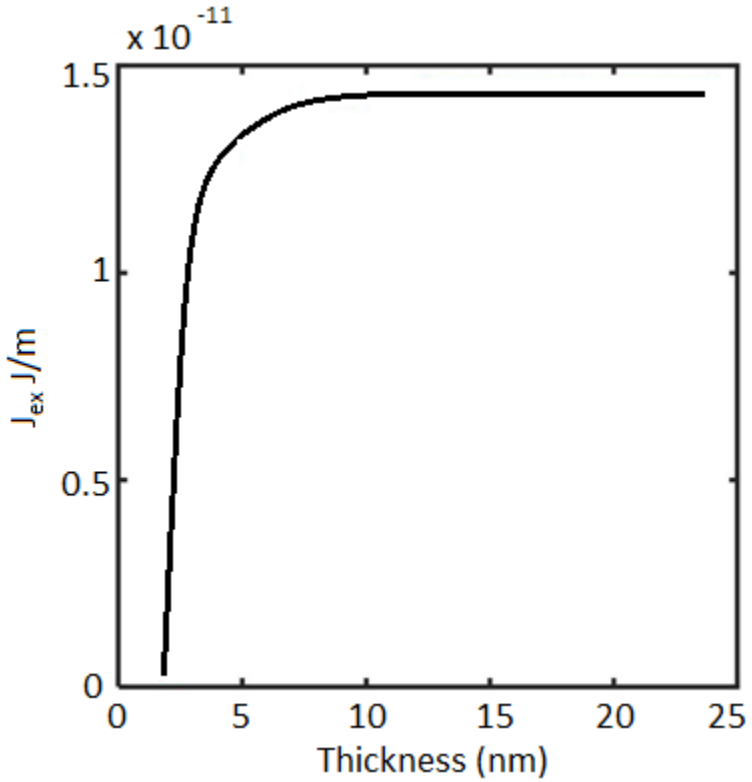

Fig. 5.4: Strength of J_{ex} in CoTb between nearest and oppositely polarized magnetic moments with respect to CoTb free layer thickness.

An important step in designing the FiM based MTJ is to determine the proper thickness of FiM layer to enable the maximum bulk torque and minimize the required switching power. In FiM, the exchange coupling gradually increases with the increasing thickness of FiM slab before getting saturated [117] and so does the bulk torque. Therefore, in order to utilize the maximum bulk torque for fast magnetization switching, the FiM slab has to be thick (~ 10-12 nm) [117]. Nevertheless, thick FiM layer needs a high spin current density for magnetization switching. Therefore, the choice of FiM slab thickness is critical to achieving optimum performance.

In fig.5.4 we have shown the strength of J_{ex} with respect to the thickness of FiM slab. Note, J_{ex} is a long-range parameter and in fig.5.4 we only considered the exchange coupling between oppositely polarized, nearest neighbor magnetic moments. The full range of J_{ex} for different thickness of FiM layer is shown in Appendix F. In order to get optimum performance, the thickness of CoTb free layer is set to be 10nm (from fig. 5.4). Note, the MgO tunneling barrier is

set to be 2nm thick to ensure a high TMR ratio [143]. The exchange coupling calculated for 10nm thick CoTb is used for FiM LLGS simulation.

5.3.2 Interfacial DMI Between CoTb and Pt

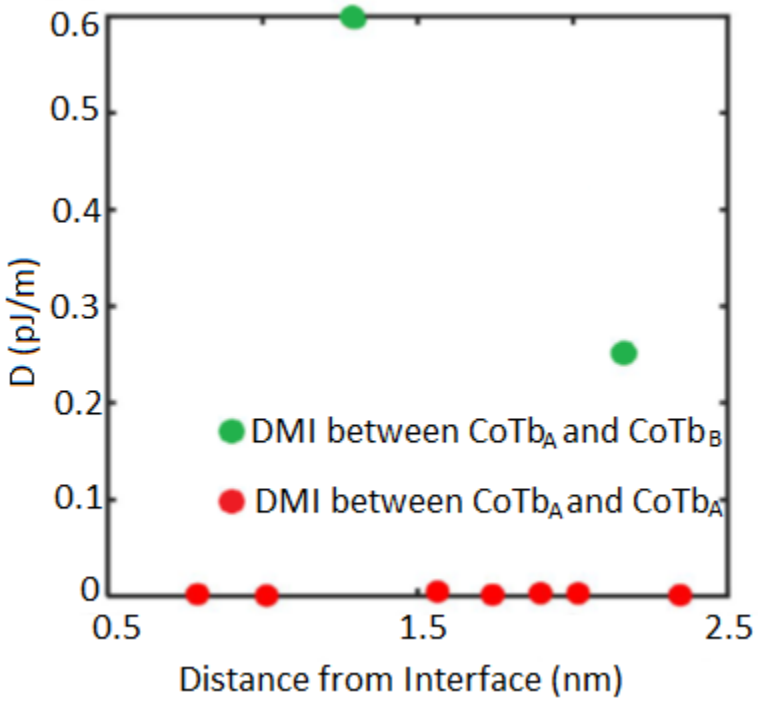

Fig. 5.5: Crystal structure of CoTb/Pt interface and KKR simulation result of DMI at the interface.

An important factor for determining the performance of FiM based MTJ is the interfacial DMI [121]. DMI acts as an external magnetic field and tilts the magnetic moments at CoTb/Pt interface. The lattice match between CoTb and Pt allows us to consider a relatively smooth interface between them. Note, the CoTb is grown along the z-axis with respect to Pt and hence, we only consider the z-component of the DMI as shown in fig. 5.5. Effect of DMI is only significant for a couple of CoTb atomic layers adjacent to the interface (fig. 5.5). Therefore, the magnetization dynamics of these two layers will be different than other atomic layers in CoTb. CoTb has a cubic structure with alternating CoTb hybrid atom holds the symmetry. Let us denote the atom positions with different symmetry as A and B ($CoTb_A$ and $CoTb_B$). The green dots in fig. 5.5 are the DMI between CoTb atoms at position A and B. The red dots are the DMI between CoTb atoms at site A and another similar site A. Fig. 5.5 indicates that the magnitude of interfacial DMI is almost an order less than inter-CoTb exchange coupling. According to the

classic DMI paper by Moriya, the DMI depends on the crystal symmetry [136]. If we consider the point bisecting line connecting two CoTb atoms to be the center of symmetry, then DMI is zero [136]. Many of the DMI vector components are zero due to the symmetry restrictions (DMI between $CoTb_A$-$CoTb_A$). Due to tilting of magnetic moments near the interface due to the presence of Pt atom, DMI between $CoTb_A$-$CoTb_A$ is not exactly zero but negligible compared with DMI between $CoTb_A$-$CoTb_B$.

5.3.3 Magnetization Dynamics Simulation with DMI and Switching Characteristics of CoTb Based FMTJ

In FiM, exchange coupling tries to maintain the equilibrium magnetization direction. In order to change the magnetization orientation, a strong torque has to be applied on the magnetic moments. Strong spin-polarized current can apply spin-transfer torque on FiM magnetic moments. Flow of charge current in the heavy spin Hall (SHE) metal generates spin-polarized current. In fig. 5.1, we inject a -Z-polarized spin current in the CoTb free layer from the adjacent Pt layer. The charge current to spin current conversion efficiency is measured using a figure of merit called spin hall angle [144] and Pt has a spin hall angle of 0.08 [134]. Spin current gets accumulated in Pt and diffuses into the CoTb layer. The spin-polarized current generates two different types of spin-transfer torque - field-like (FL) torque and damping like (DL) torque on the magnetic moments [139] in FiM. Field- like torque is significant in the skyrmions and domain wall-like structures [145]. CoTb has a simple and highly symmetric crystal structure and hence the only dominant spin-transfer torque will be the damping like torque. The magnetic moments inside CoTb are assumed to be arranged along X-axis (fig. 5.6) and -Z-polarized spin currents will generate DL torque along +Z-axis (fig. 5.1).

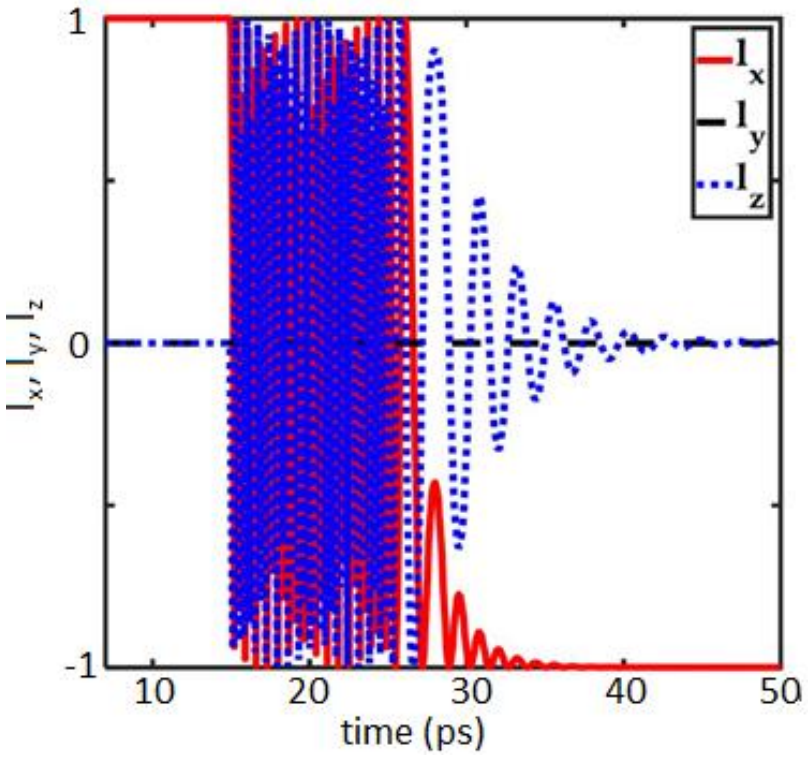

Fig. 5.6: Magnetization dynamics of the resultant magnetic field in the CoTb layer.

We have shown the dynamics of the different magnetization components of staggered magnetization $\vec{l}$ defined as, $\vec{l} = \frac{\overrightarrow{m_1} - \overrightarrow{m_2}}{2}$

The switching characteristic of staggered magnetization $\frac{\overrightarrow{m_1} - \overrightarrow{m_2}}{2}$ in 10nm CoTb layer is shown in fig.5.6. DL torque along Z-axis creates oscillation in the X and Z component of the magnetic moments (fig. 5.6). The staggered magnetization direction of CoTb switches in 23ps from +X to -X-direction while typical ferromagnet layer takes nano-seconds to switch [115]. Assuming the injection efficiency of spin current from Pt into CoTb to be 1, the charge current density required to switch the CoTb layer is calculated to be a 10ps pulse of 8.89×10^8A/cm^2 which is higher than the typical magnitude of the charge current to switch FM layers (10^6 - 10^7 A/cm^2 in FM based MTJs [115]). Simulation parameters are shown in TABLE 5.1. Note, in FiM, damping is very low [138] and hence we considered an arbitrary low damping constant.

Table 5.1. Parameters for magnetization dynamics simulation of CoFeB

Simulation Parameters	Value
Anisotropy constant along X-axis (J/m^3) [119]	7200
Anisotropy constant along Z-axis (J/m^3)	0
Exchange coupling (J/m)	1.4×10^{-11}
Gilbert damping factor, α	0.002
Spin current density (A/m^2)	2.4×10^{11}
DMI constant (J/m)	0.33×10^{-12}

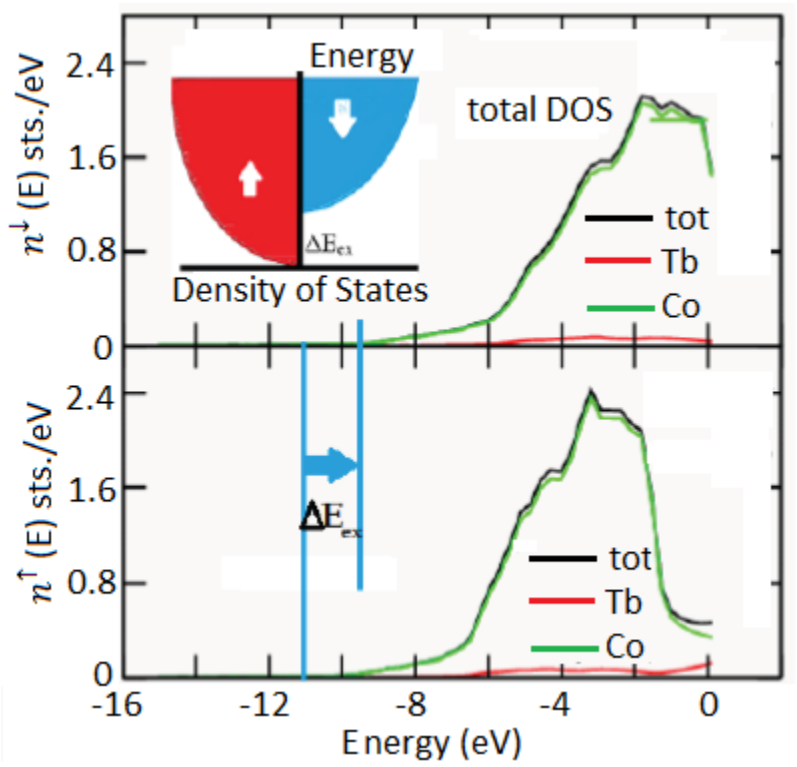

Fig. 5.7: (Inset) Schematic representation of the exchange splitting (ΔE_{ex}) which is the energy difference between spin-up and spin-down band in a magnetic material, (left) Spin resolved up-spin and downspin density of states in CoTb.

5.3.4 CoTb based FMTJ and Calculation of TMR

Except for switching characteristics, TMR is an important figure of merit of an MTJ. As stated earlier, we use NEGF formalism for determining the tunneling spin current to calculate the parallel (R_P) and antiparallel (R_{AP}) magneto-resistance of our proposed MTJs. Maximum TMR of CoTb/MgO/CoFeB is 38% while for CoTb/MgO/CoTb MTJ,

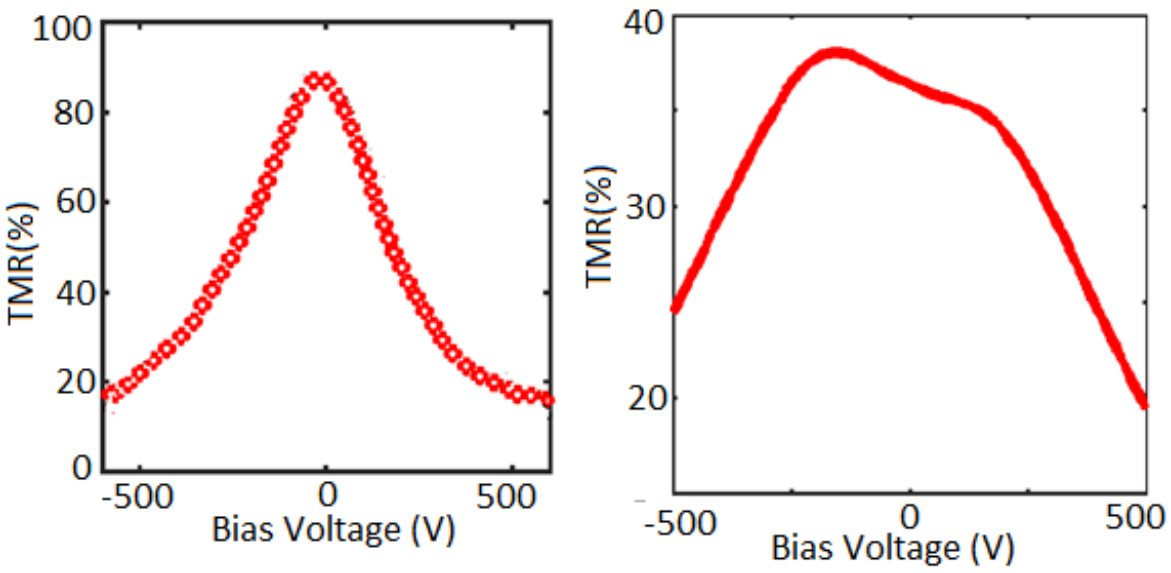

Fig. 5.8.: TMR in CoTb/MgO/CoTb MTJ (left) and CoTb/MgO/CoFeB MTJ (right).

the maximum TMR is 87% at room temperature. TMR is a function of exchange splitting in the spin-polarized band structure of the magnetic contacts. CoFeB has much bigger exchange splitting (2.25eV [146]) than that of CoTb (1.42eV) (fig. 5.7). Nevertheless, use of CoFeB as fixed layer and CoTb as free layer induces incoherence in spin current tunneling for parallel MTJ configuration. The difference in the density of states at different energy levels mainly causes the inelastic spin tunneling. In fig. 5.7 spin-resolved density of states for CoTb is shown. Inelastic spin tunneling causes the parallel resistance to go up resulting in lower TMR ($TMR = \frac{R_{AP}-R_p}{R_p}$). On the other hand, if the FMTJ free and fixed layers are both CoTb slab of the same dimension, spin current tunnel through the barrier MgO layer coherently, resulting in lower R_P. Therefore, CoTb/MgO/CoTb MTJ has higher TMR (fig. 5.8). Bandstructure analysis of CoTb yields an effective mass of $0.83m_0$ while the CoTb-MgO tunneling barrier height is found to be 2.1 eV. NEGF simulation for calculating the TMR is done using effective mass Hamiltonian as discussed in [129].

5.3.5 Thermal Stability

Thermal noise plays an important role in MTJ design. If the MTJ switching barrier is low, strong thermal noise can switch the magnetization of the free layer which is undesirable. The critical external magnetic field to switch the ferrimagnet magnetization direction is proportional

to the activation energy E_a of the ferrimagnet [147]. The activation energy in FiM is proportional to the exchange coupling and the volume $E_a \propto J_{ex}V$ [147]. Since ferrimagnet exchange coupling is very strong and the volume is big due to thick slab, CoTb based MTJ is relatively immune to thermal fluctuation compared with FM based MTJ and has a high retention time.

5.3.6 Memory Cell Design

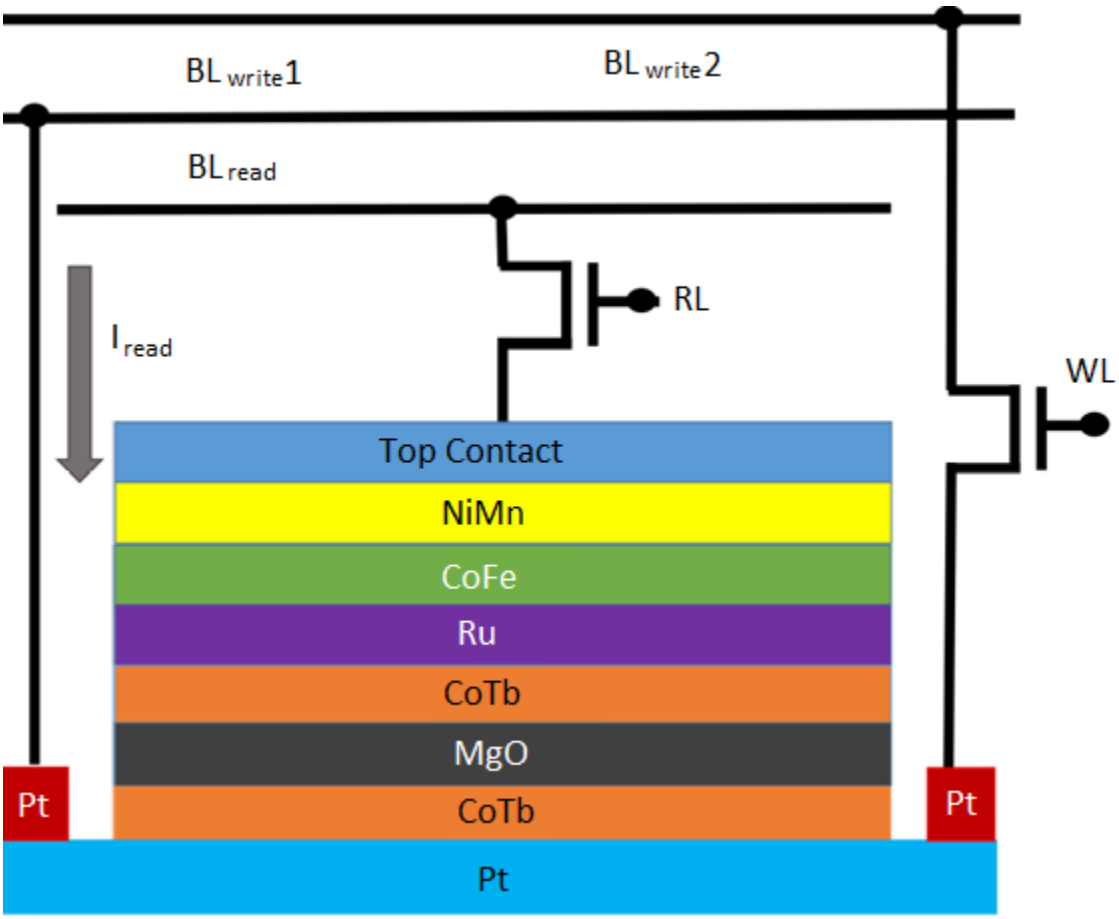

Fig. 5.9.: Diagram of the proposed memory cell

In Fig.5.9, we propose a memory cell using the CoTb based MTJ. The memory cell has three layers. The first layer is a CoTb based MTJ with Pt at the bottom for switching the free magnetic layer. The write current flows through the Pt underlayer and depending on the direction of the current, the free layer is expected to switch, leading to a change in resistance. The second layer is the antiferromagnetic (AFM) layer (Ni–Mn), which stabilizes the magnetization of the fixed magnet. The third layer comprising of ruthenium (Ru) and CoFe is called the synthetic AFM layer and it fixes the magnetization of the fixed magnetic layer by canceling the stray fields

around it [149]. In the proposed device, the CoFe, through nonmagnetic material Ru, is exchange coupled to the free magnetic layer [149]. In Fig.5.9, we also show the read and write circuitry. The top terminal is connected to read bit line BL_{read} via an access transistor controlled by a read line (RL). Read operation is performed by making the RL and BL_{read} high and BL_{write1} low. Two terminals at the two ends of the Pt are connected to two write lines via a pass transistor for allowing current flow in both directions. The pass transistor is controlled by the word line.

5.3.7 Comparison of Magnetic Memories with FM based MTJ and CoTb based MTJ

A major drawback of FM based MTJs is the relatively long switching time. Hence magnetic memories with FM based MTJ have large write time. Both experiments [146,149] and theoretical simulations exhibit nano-second range switching time for FM based MTJ. Nevertheless, CoTb based MTJ can be switched in 23ps (see TABLE 5.1). Assuming a CoFeB based MTJ as shown in [131], in order to achieve same switching speed, we need to apply $2.189 \times 10^{10} A/cm^2$ charge current through the bottom Pt layer which is 24.62x higher than CoTb based MTJ. Therefore, in case of iso-speed comparison, FMTJ is more energy-efficient than FM based MTJ. The simulation parameters for CoFeB based MTJ can be found in Appendix F.

Our theoretical study shows that our proposed CoTb based MTJ shows less temperature sensitivity (fig. 5.10) than FM or Heusler alloy based MTJ [146] due to the lower rate of magnon generation with increasing temperature. Also, CoTb based MTJ is thermally very stable and hence, CoTb based magnetic memory has longer retention time compared with FM based MTJ. However, the TMR ratio of CoTb based MTJ is 2-5x time lower than that of FM based MTJ [146]. Note, the exchange splitting between the spin-polarized

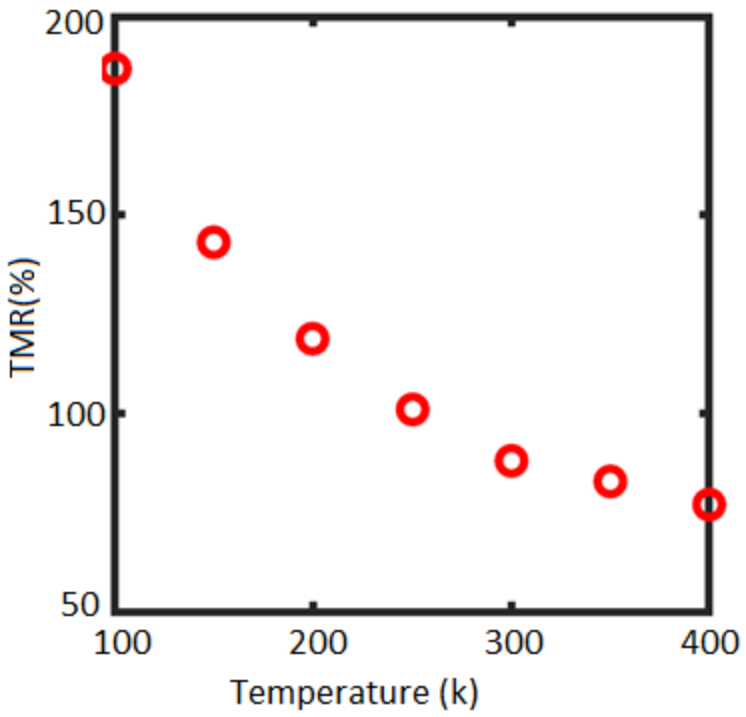

Fig. 5.10.: TMR variation with temperature in CoTb/MgO/CoTb MTJ.

bands in FiM is less than that of FM. Therefore, the difference between the magneto-resistance during parallel and antiparallel MTJ configuration is low in FiM based MTJ leading to low TMR ratio. It makes the read operation difficult. Also, the free layer of CoTb based MTJ is thick (10 nm) (discussed above) and hence, unlike FM based MTJ, critical switching current in FMTJ is high.

5.4 Conclusion

To conclude, we proposed FiM based MTJs - CoTB/MgO/CoFeB and CoTb /MgO/CoTb and our simulation demonstrated fast switching (on the order of ps range) in the MTJs. We showed lower power consumption in FMTJ for iso-high speed switching sacrificing TMR compared with typical FM based MTJs [146]. Moreover, our proposed FiM based MTJ has less interface issue and lower magnon generation rate with temperature resulting in stable performance. Tilting the magnetic moments in FiM prior to switching can reduce power consumption and make the device faster. Coupling of FiM with a strong antiferromagnet can tilt the magnetic moments inside FiM [121]. Further lowering of power consumption and improving the TMR can make

FiM MTJ a potential candidate for spin-based magnetic memories and other MTJ based applications.

5.5 Summary

A ferrimagnet (FiM) has small domains consisting of oppositely polarized and unequal magnetic moments. Oppositely polarized magnetic moments have strong exchange coupling between them resulting in robust torque in FiM called bulk torque. Due to the strong bulk torque, magnetic moments in FiM do not precess around switching axis for a long time unlike ferromagnets (FM) leading to faster switching speed compared to FM. In this chapter, we propose and model the switching of FiM (CoTb) with spin current injection from heavy spin Hall metal (SHE), such as Pt. We carry out *ab-initio* calculation of the Dzyaloshinskii-Moriya interaction (DMI) at the FiM(CoTb)/heavy metal(Pt) interface using spin-polarized relativistic Korringa-Kohn-Rostoker (KKR) Green's function method. We compute the exchange coupling among the magnetic moments inside the CoTb layer and model how the spin-orbit torque (SOT) along with the bulk torque can efficiently switch the FiM. Then we consider an FiM based magnetic tunnel junction (FMTJ) with SHE metal. We perform a comprehensive simulation and performance analysis of FiM(CoTb)/MgO/CoFeB and FiM(CoTb)/MgO/FiM(CoTb) FMTJs with Pt underlayer. Using non-equilibrium Green's function (NEGF) formalism, we calculate the tunneling magnetoresistance (TMR) of the proposed FMTJs at room temperature. Furthermore, the importance of thickness in CoTb magnetization dynamics is shown using our FiM magnetization simulation framework. We analyze and show that the CoTb based FMTJ has large switching energy barrier to ensure thermal stability. Finally, we show the performance comparison (TMR, write performance and power consumption) between our proposed FMTJs and FM based MTJ and our simulation exhibits that for picosecond range switching speed, FMTJ is ~25 times more energy-efficient than FM based MTJ.

6. RELIABILITY AND LIFETIME PREDICTION OF MTJ BASED ON BÜTTIKER PROBE BASED MODELING OF DIELECTRIC BREAKDOWN IN MGO TUNNELING LAYER

6.1 Quantum Transport Based Analysis for MTJ Dielectric Breakdown

In order to achieve better write efficiency in spin-transfer torque magnetic random access memory (STT-MRAM), researchers are fabricating MTJs with ~1nm thick MgO layer in between the fixed and the free ferromagnetic layers [153]. As a result, the voltage applied across these thin oxide layers can generate a tremendous amount of stress electric field (on the order of 10^8-10^9 V/m, fig. 6.1). Gradually traps start forming in the dielectric layer that eventually leading to the formation of percolation paths. When an electron is captured by a trap, the spin orientation of that electron is randomized [153] [154]. As a result, the spin filtering efficiency of the MTJ starts degrading over time, eventually causing functional failures. Over time, more traps get generated and when the traps line up, they form a breakdown path through the MgO dielectric layer.

Post-breakdown current-voltage (I-V) characteristic primarily depends on the type of dielectric breakdown. If the post-breakdown I-V characteristic is vastly different from its no-breakdown counterpart and follows Ohm's law [155], the dielectric is said to have experienced a hard breakdown. On the other hand, the soft dielectric breakdown is characterized by a power-law dependence between post-breakdown current and the corresponding voltage [155]. But in this case, the increase in post breakdown current at low voltage is smaller compared to corresponding hard breakdown current [155].

Over the past decade, a lot of research [155-161] focused on the breakdown characteristics/models of dielectric layers, especially for MOS devices. These models are mainly analytical in nature and can predict the breakdown behavior such as, post break down I-V characteristics and the time to failure. However, the analytical models are not sufficient to predict the spin current degradation through MTJ due to dielectric breakdown. This is because the ferromagnetic layers can be either in parallel or anti-parallel states and the tunneling ferromagnetic resistance varies with the corresponding magnetization orientation (fig. 6.2). Moreover, the spin tunneling current varies a lot depending on the angle of magnetization of the fixed and free layer in an MTJ (fig. 6.2). In addition, different ferromagnetic layers can have

different exchange coupling energy and different band structures that play a significant role in determining the post breakdown MTJ characteristics. Therefore, it is evident that for reliable spin-dependent current simulation, we need to explicitly consider both the up spin and the down spin band diagrams (fig. 6.1) and the density of states of both the ferromagnetic magnetic contacts and the channel dielectric.

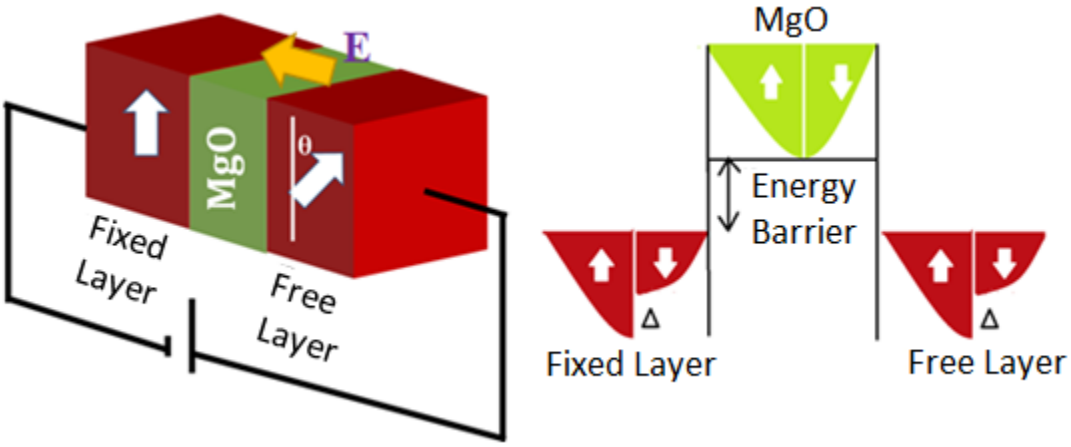

Fig. 6.1 Schematic band diagram of CoFeB-MgO-CoFeB MTJ for parallel configurations (left). Corresponding energy band diagram is shown on right.

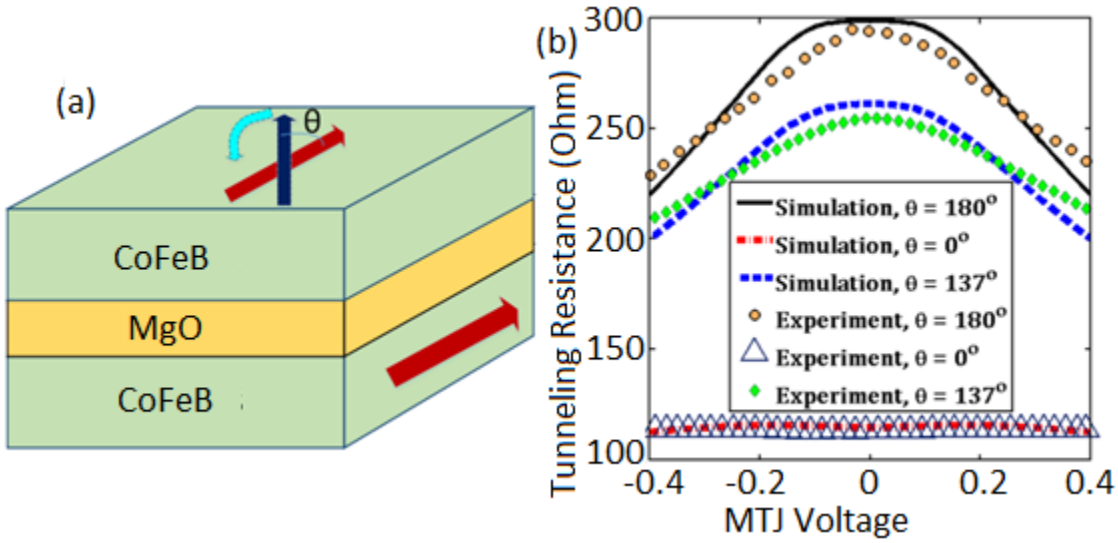

Fig. 6.2: (a). Schematic diagram showing the angle between the magnetization of the fixed and free layer in CoFeB/MgO/CoFeB MTJ. The angle is defined as θ. (b) Simulation data with our NEGF framework (without any defect or breakdown) and experimental data [3] on the variation of MTJ resistance with changing θ. Three values of θ (θ = 0^o, 137^o and 180^o) are considered here. (Root mean square value of error is less than 4%)

For modeling the post breakdown gate current-gate voltage characteristics, various theories have been proposed in the literature. They include variable range hopping (VRH) [159], inelastic macroscopic quantum tunneling [160], and quantum point contact (QPC) model [161]. In VRH theory, post soft breakdown current is modeled by an empirical equation $I_g = aV_g^b$ (because soft breakdown I_g-V_g characteristic follows the power-law), where, a and b are two empirical parameters depending on the type and the thickness of gate dielectric material. Soft breakdown spin current can also be modeled by such empirical equation. However, every time the material or the dimension of contact ferromagnet or channel dielectric are changed, one has to do a series of experiments to determine a and b. Even for fixed material and device dimensions, the relative magnetization orientation of the fixed and the free layer plays a large role in MTJ I-V characteristics. Inelastic macroscopic quantum tunneling method defines the tunneling resistance as $R_{ti}^{-1} = \frac{4\pi e^2}{\hbar}\left|T^i\right|\zeta_i\zeta_0$ [160]. Here T^i is the tunneling matrix and $\zeta_i \; and \; \zeta_0$ are the density of states in the electrodes. The gate tunneling current is defined as [160],

$$I_g(V_g) = \frac{2\pi e}{\hbar}\left(\prod_{i=1}^{N}\frac{R_Q}{4\pi^2 R_{ti}}\right)S^2\sum_{k=0}^{N-1}c_k^N(k_BT)^{2k}(eV_g)^{2(N-k)-1}$$

R_Q is the quantum resistance, N is the number of tunnel junctions and T is the temperature. The method cannot calculate the change MTJ current change due to dielectric breakdown because it does not consider spin up and down states separately. Also in the model, the breakdown current variation with temperature is modeled using a separate empirical relation $I_g(V_g) = \; aV_g^9 + bV_g^7T^2 + cV_g^5T^4 + d\,V_g^3T^6 + \; eV_gT^8$ where a, b, c, d and e are fitting parameters with T being the temperature. In our proposed NEGF based modeling, the effect of temperature is already built in the Fermi-Dirac distribution function (defined as $f = \frac{1}{1+exp^{E-E_F/kT}}$, E_F being the Fermi level). Hence, there is no need to model temperature variation separately. In the QPC model, the post breakdown current is modeled as [161],

$$I_g(V) = \frac{2e^2}{h}(V - V_0) + \frac{1}{\alpha}\ln\left[\frac{1+exp^{\alpha\{\phi(T)-\beta e(V-V_0)\}}}{1+exp^{\alpha\{\phi(T)+(1-\beta)e(V-V_0)\}}}\right]$$

α is fitting parameter depending on the shape of the energy barrier, V_0 is the voltage drop at the two electrodes, β is the fraction of voltage drop cross oxide and, ϕ, the barrier height is given by E_0-E_F, where E_0 is the bottom of first sub-band. The tunneling current is modeled using the

analytical equation. Note, however, it is not sufficient to model the spin-based tunneling current since it does not consider the spin-dependent density of states. Another drawback of the QPC model is that it projects the temperature dependence of post breakdown current using the analytical equation: $\phi(T) = \phi_0 + \xi T$, where ξ is an empirical fitting parameter. In our model, as stated earlier, we do not need to model temperature dependence using fitting parameters.

Analytical models do not account for spin-up and spin-down states separately. Hence, with the generation of traps, the tunneling current increases at the same rate for both the parallel and antiparallel MTJ configurations. As a result, the decrease in parallel tunneling magnetoresistance (R_P) over time is identical to the decrease in antiparallel magneto-resistance (R_{AP}). Therefore, the tunneling magneto-resistance (TMR = $(R_{AP} - R_P)/R_P$), will increase with the generation of new traps leading to a wrong conclusion. Note, models available in the literature are inadequate for reliability analysis of spin-current-based devices. Hence, we believe that quantum transport simulation considering the band diagrams of the contacts and channel is necessary for MTJ reliability analysis.

In this chapter, we propose a unified model for predicting the I-V characteristics of the dielectric layer due to the formation of traps at different positions and at different energy levels. In the next section, we discuss our simulation framework and show how Büttiker probe [150] can be used to model the traps. We show that our model can predict the behavior of the dielectric layer after both soft and hard breakdowns. We verified our model with the experimental results of post breakdown I-V characteristics of both conventional MOSFETs (with both single SiO_2 layer and HfSiON/SiO_2 multilayer as gate oxide) and MTJ. We also used NEGF formalism to calculate the spin current for both parallel and antiparallel states in order to determine the degradation of the tunneling magnetoresistance (TMR) due to the TDDB effect in MgO layer in MTJs. Finally, we have used the standard 3-D cell-based percolation model [157] to predict the MTJ lifetime.

6.2 Proposed Simulation Framework Using Büttiker Probe

In this section, we first discuss some of the major attributes of trap assisted tunneling. The capture cross-section of a trap in a particular dielectric depends on its position in the energy level [158]. A mid-bandgap trap has a relatively bigger capture cross-section than the ones near the conduction band edge or in the conduction band [162]. Researchers usually measure it

experimentally and we will use those experimentally measured values in our analyses. Another important thing to consider is the physical position of the trap. The physical position of a trap determines the distance that a carrier has to tunnel before being captured by the trap. Büttiker probe based NEGF model can be used to determine whether a trap is a surface trap or bulk trap by matching the post breakdown I-V characteristic.

In fig. 6.3. we have shown a schematic diagram of both the physical position and energy level of traps for an example dielectric. A major characteristic of trap assisted tunneling is the dephasing of the electron or hole when captured by a trap. Therefore, the tunneling probability and the dephasing of carrier need to be modeled simultaneously.

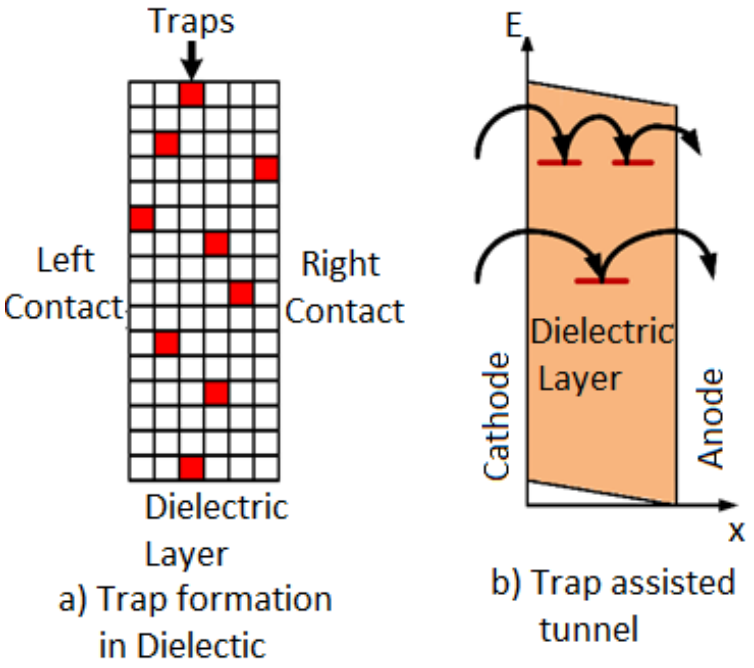

Fig. 6.3 Schematic diagram of trap position (a) Physical positions of trap (b) Energy level positions of traps.

6.2.1 Modeling Traps using Büttiker Probe

Büttiker probes are virtual probes that absorb the carriers, dephase them, and inject them back into the channel. Trap assisted tunneling can be modeled using these Büttiker probes by placing one probe at each of the trap location. Similar to the trap assisted tunneling, the carriers can tunnel from one contact to the probe and then from the probe to another contact. In addition, the carriers can also tunnel from one probe to another. A Büttiker probe's self-energy matrix can be written according to the corresponding trap's physical and energy level position and trap's

capture cross-section. Thus, a Büttiker probe can replicate the functionality of a trap.

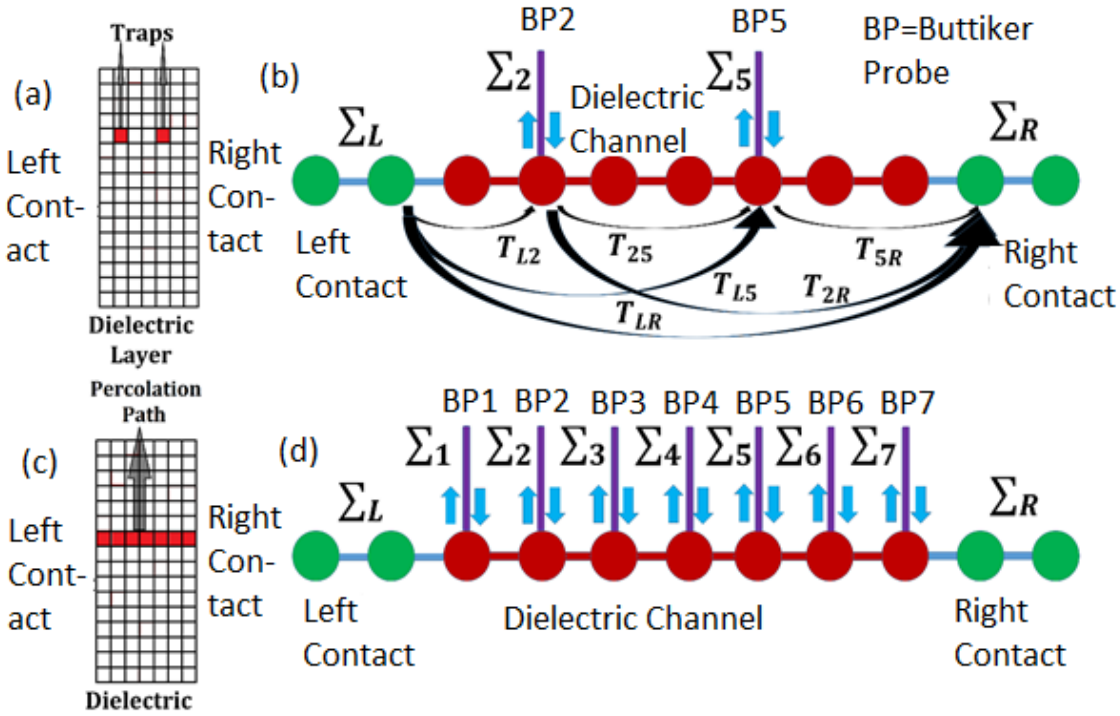

Fig. 6.4: Concept of Büttiker probe (BP). (a) Consider traps at grid position 2 and 5 (b) Modeling of trap assisted tunneling. Assuming traps are formed at grid position 2 and 5, we have attached Büttiker probes to those positions. All possible tunneling paths are shown with corresponding tunneling transmission probability (c) Formation of percolation path inside the dielectric (d) Modeling of percolation path. A virtual contact is attached to grid points where the trap is generated. These additional contacts are treated with a self-energy, like the real contacts.

Fig. 6.4 explains the concept of Büttiker probes. In addition to Büttiker probes, there are two more contacts (left and right contact) attached to the dielectric channel. In case of MTJ, the left and right contacts are the two ferromagnetic layers, i.e., the fixed layer and the free layer [163]. For MOSFETs, these two contacts are the top metal or polysilicon layer and the bottom channel or the substrate layer. For both cases, as the channel is an insulator, the electrons mainly tunnel through the dielectric layer from one contact to the other. Initially, we will describe the NEGF modeling of direct tunneling current. In order to do that we assumed that there are no pre-existing traps in the dielectric layer. After the application of a voltage across the dielectric layer, the Fermi functions at the left and the right contacts are $f_L(E)$ and $f_R(E)$, respectively. The current density can be written as [151] [164],

$$J = \frac{1}{q} \int G(E)\,(f_R - f_L)dE \tag{6.1}$$

Here, G(E) is the conductance and q is the electron charge. G(E) is defined in [112] [164] as G(E) = $\frac{q^2}{h}\,T(E)$, where T(E) is the transmission probability. The transmission probability depends on the retarded Green's function of the system and the self-energy matrices of the contacts. The retarded Green's function can be written as follows [151] [164],

$$\boldsymbol{G^R} = [\boldsymbol{EI} - \boldsymbol{H} - \boldsymbol{\Sigma_L} - \boldsymbol{\Sigma_R}]^{-1} \tag{6.2}$$

$\boldsymbol{\Sigma_L}\ and\ \boldsymbol{\Sigma}_R$ are the self-energy matrices of the left and the right contacts, respectively.

Therefore, the transmission probability between the left and the right contacts can be represented as [164]

$$T_{LR} = Trace\,[\boldsymbol{\Gamma_L G^R \Gamma_R G^A}] \tag{6.3}$$

$\boldsymbol{G^A}$ is the complex conjugate matrix of $\boldsymbol{G^R}$. Here $\boldsymbol{\Gamma_L}$ and $\boldsymbol{\Gamma_R}$ are two quantities defined as [164] $\boldsymbol{\Gamma_L} = i[\boldsymbol{\Sigma_L} - \boldsymbol{\Sigma_L^\dagger}]$ and $\boldsymbol{\Gamma_R} = i[\boldsymbol{\Sigma_R} - \boldsymbol{\Sigma_R^\dagger}]$. $\boldsymbol{\Sigma_L^\dagger}$ and $\boldsymbol{\Sigma_R^\dagger}$ are the complex conjugate matrices of $\boldsymbol{\Sigma_L}$ and $\boldsymbol{\Sigma_R}$, respectively. Γ is a matrix that physically represents how easily carriers get in or get out of a contact [127].

The concept of Büttiker probe is embedded into NEGF formalism to model the trap assisted tunneling. Let us assume that traps are formed at grid position 2 and 5 (fig. 6.4(a)). For modeling these two traps, we need to attach two Büttiker probes at those two grid points as shown in figure 6.4(b). These probes absorb carriers and inject them back to the channel. As a result, there is no net current through these probes i.e., the current conservation law is followed.

Note that the electrons have multiple paths for going from the left contact to the right contact. Electrons can be captured by the trap at grid point 2, then recaptured by the trap at grid point 5 and finally escape through the right contact (fig 6.4(b)). Also, electrons can tunnel from left contact to either trap at grid position 2 or grid position 5 and then tunnel to the right contact (fig 6.4(b)). Moreover, they can directly tunnel from left contact to the right contact. Let us consider the first trap assisted tunneling path. The corresponding tunneling transmission probabilities are T_{L2}, T_{25} and T_{5R} (fig 6.4(b)). These tunneling paths are in series connection with one another and the tunneling transmission probability is proportional to conductance. Therefore, the total tunneling transmission probability of the path, T_{L25R} can be written as,

$$\frac{1}{T_{L25R}} = \frac{1}{T_{L2}} + \frac{1}{T_{25}} + \frac{1}{T_{5R}} \tag{6.4}$$

Where, $T_{L2} = Trace\,[\mathbf{\Gamma_L G^R \Gamma_2 G^A}]$, $T_{25} = Trace\,[\mathbf{\Gamma_2 G^R \Gamma_5 G^A}]$ and $T_{5R} = Trace\,[\mathbf{\Gamma_5 G^R \Gamma_R G^A}]$ [151]. If $\mathbf{\Sigma_2}$ and $\mathbf{\Sigma_5}$ are the self-energy matrices of the Büttiker probes attached at grid positions 2 and 5, then $\mathbf{\Gamma_2} = i\left[\mathbf{\Sigma_2} - \mathbf{\Sigma_2^\dagger}\right]$ and $\mathbf{\Gamma_5} = i\left[\mathbf{\Sigma_5} - \mathbf{\Sigma_5^\dagger}\right]$. In the simple effective mass simulation, we have calculated the self-energy matrix of Büttiker probe as follows.

$$\mathbf{\Sigma_{Büttiker}} = \begin{bmatrix} \left(-t_{de} - qV_{eff}^{\alpha}\right)\exp(ika) & 0 \\ 0 & \left(-t_{de} - qV_{eff}^{\alpha}\right)\exp(ika) \end{bmatrix} \tag{6.5}$$

The corresponding $\Gamma_{\mathbf{Büttiker}}$ matrix can be defined as $\Gamma_{\mathbf{Büttiker}} = i[\mathbf{\Sigma_{Büttiker}} - \mathbf{\Sigma_{Büttiker}^\dagger}]$. Here a is the grid mesh size and t_{de} is defined as $t_{de} = \frac{\hbar^2}{2m_{de}}\,a^2$ where m_{de} is the electron effective mass in the dielectric. V_{eff} is the effective voltage at the trap position. When a voltage is applied across a dielectric layer the entire voltage can be assumed to appear and be uniformly distributed across that layer. Hence, the effective voltage at different trap positions is different. Effective voltage has a power factor α over it. The power factor appears because the current due to the soft breakdown of the dielectric layer exhibits power-law dependence on the corresponding voltage. Hence, for soft dielectric breakdown, α is greater than 1. However, when there is a hard breakdown α is equal to 1. Therefore, when a percolation path is formed, the type of breakdown needs to be determined first and the α factor is tuned accordingly. Also, the value of α depends on the dielectric material and the capture cross-section of the trap. For larger capture cross-section α is larger. Here one thing worth mentioning is that α is different from the voltage acceleration factor appearing in analytical equations for soft breakdown ($I \propto V_g^{\gamma}$, γ is called the voltage acceleration factor [165]). Therefore they may have a different value. In eqn. (6.5), k is the wave vector. It can be defined as,

$$k = \cos^{-1}\left(1 - \frac{E - qV_{eff}^{\alpha} + \xi i}{2t_{de}}\right) \tag{6.6}$$

ξ is a very small arbitrary energy. One thing worth mentioning is that except hard breakdown we should not add the self-energy matrices of Büttiker probes to the system Green's function. This is because Büttiker probes are artificial probes introduced for modeling. They are not part of the actual physical system. Hence, the introduction of Büttiker probes should not disturb the

system Green's function. But when there is a hard breakdown, the channel's transport characteristic is changed from tunneling to Ohmic conduction. Hence the system's Green's function is modified according to the following equation.

$$\boldsymbol{G^R = [EI - H - \Sigma_L - \Sigma_R - \Sigma_1 - \Sigma_2 - \cdots - \Sigma_n]^{-1}} \quad (6.7)$$

$\boldsymbol{\Sigma_1}$,$\boldsymbol{\Sigma_2}$,…,$\boldsymbol{\Sigma_n}$ are the self-energy matrices of the Büttiker probes attached along the channel.

From figure 6.4(b), let us consider other trap assisted tunneling paths. Electrons can be captured first by the trap at grid position 2 and then it can tunnel to the right contact. In this case, the tunneling transmission coefficient,

$$\frac{1}{T_{L2R}} = \frac{1}{\mathrm{T}_{L2}} + \frac{1}{T_{2R}} \quad (6.8)$$

Where, $T_{2R} = Trace\,[\boldsymbol{\Gamma_2 G^R \Gamma_R G^A}]$.

Similarly, as stated earlier, an electron can travel from left contact to the trap at grid position 5 and then to right contact (fig 6.4(b)). Hence, the tunneling transmission coefficient,

$$\frac{1}{T_{L5R}} = \frac{1}{\mathrm{T}_{L5}} + \frac{1}{T_{5R}} \quad (6.9)$$

Here, $T_{L5} = Trace\,[\boldsymbol{\Gamma_L G^R \Gamma_5 G^A}]$. Note, the electron can tunnel directly from left contact to right contact. Hence, there are a total of 4 paths for electrons to tunnel from left to right contact (fig 6.4(b)). As all these paths are parallel, the overall tunneling transmission coefficient,

$$T_{all} = T_{L25R} + T_{L2R} + T_{L5R} + T_{LR} \quad (6.10)$$

The total tunneling current can be expressed as,

$$J = \frac{q}{h} \int T_{all}\,(f_R - f_L)dE. \quad (6.11)$$

The Büttiker probe is used to model the percolation path (fig 6.4c). Post breakdown I-V characteristic can be modeled in the same way by attaching Büttiker probe to all the trap locations along the thickness (fig 6.4d). The carriers have many probable paths for trap assisted tunneling. All the tunneling probabilities are calculated as described earlier. Then they are added together to get the total transmission probability. In case of a MOS device, the channel region acts as the right contact (fig 6.4(c)). Therefore, the potential profile in the channel region should be carefully modeled and mapped into the system Hamiltonian. Especially if a drain voltage is

applied then the potential profile becomes asymmetric near the source and drain regions. In order to take that into consideration, we can divide the gate into small areas in which the potential profile can be assumed constant. The current through each of the small areas can be determined individually and integrated to get the total gate tunneling current. In addition, we need to consider the effect of flat band voltage and charge accumulation profile in the channel before and after inversion. If the dielectric layer consists of multiple oxide materials, potential profile in each of the materials needs to be determined and included in the Hamiltonian accordingly. Using a similar approach, we can determine the spin current in an MTJ before and after the breakdown. The spin current density between two successive lattice points is defined as, [166] [151]

$$J_s = \frac{2\pi}{i\hbar} \int Real[Trace(\boldsymbol{S}.(\boldsymbol{HG^n} - \boldsymbol{G^nH}))]\ dE. \qquad (6.12)$$

H is the system Hamiltonian and S is Pauli matrix. We need to determine the z-oriented spin current if we assume that both the fixed and free layers are pointing in the z-direction.

One important thing is that the magnetic contact self-energy contains the exchange splitting energy, Δ. But trap's electron capturing capability is independent of spin. Therefore, Büttiker probe self-energy matrix does not contain Δ.

6.3 Results and Discussion

In the dielectrics, stress-induced traps due to high electric field eventually lead to the formation of percolation paths. In this section, our proposed model is applied to calculate the stress-induced leakage current (SILC) due to the formation of multiple traps in HfSiON. It is followed by the calculation of soft breakdown (SBD) and hard breakdown (HBD) currents in SiO_2. The results are in close agreement with the experimental data. Then we consider the formation of percolation paths in MgO. We apply our simulation framework to calculate the post breakdown I-V characteristics and compare with experimental results. We have also calculated the TMR degradation in MTJ due to the formation of percolation paths in MgO. Finally, we have estimated the lifetime of the MTJ based on our calculation. Simulation parameters are shown in TABLE 6.1.

6.3.1 Stress-Induced Leakage Current

Amorphous dielectrics are being used extensively in modern electronic devices. Moreover, these dielectrics are thin and exposed to a very high electric field. Therefore, it is very important to analyze the effect of traps and point defects, both in the bulk and on the surface of these dielectrics. Traps can be either pre-existing or they can form over time due to stress (electric field stress or temperature stress). Here we first analyze the traps formed due to stress from the high electric field. We will show how to calculate the stress-induced trap density using Büttiker probe simulation by matching post-stress Ig-Vg characteristics. Then we will discuss the theory of calculating the pre-existing defect density using our simulation framework. We have initially considered high-k metal gate oxide (HKMG) transistor with a defect-free 1.8 nm HfSiON layer and 1 nm SiO2 interface layer (IL). First, we have matched the pre-stress I-V characteristic with experimental data from [168] (root mean square error < 5%). Simulation parameters are listed in table 6.1. In order to create stress-induced defects and observe SILC, constant voltage stress is applied to the dielectric stack for a very short time [168]. The dielectric layer is quite thick and free of pre-existing defects. Therefore, the application of a stress voltage for a very short time will generate only a few traps.

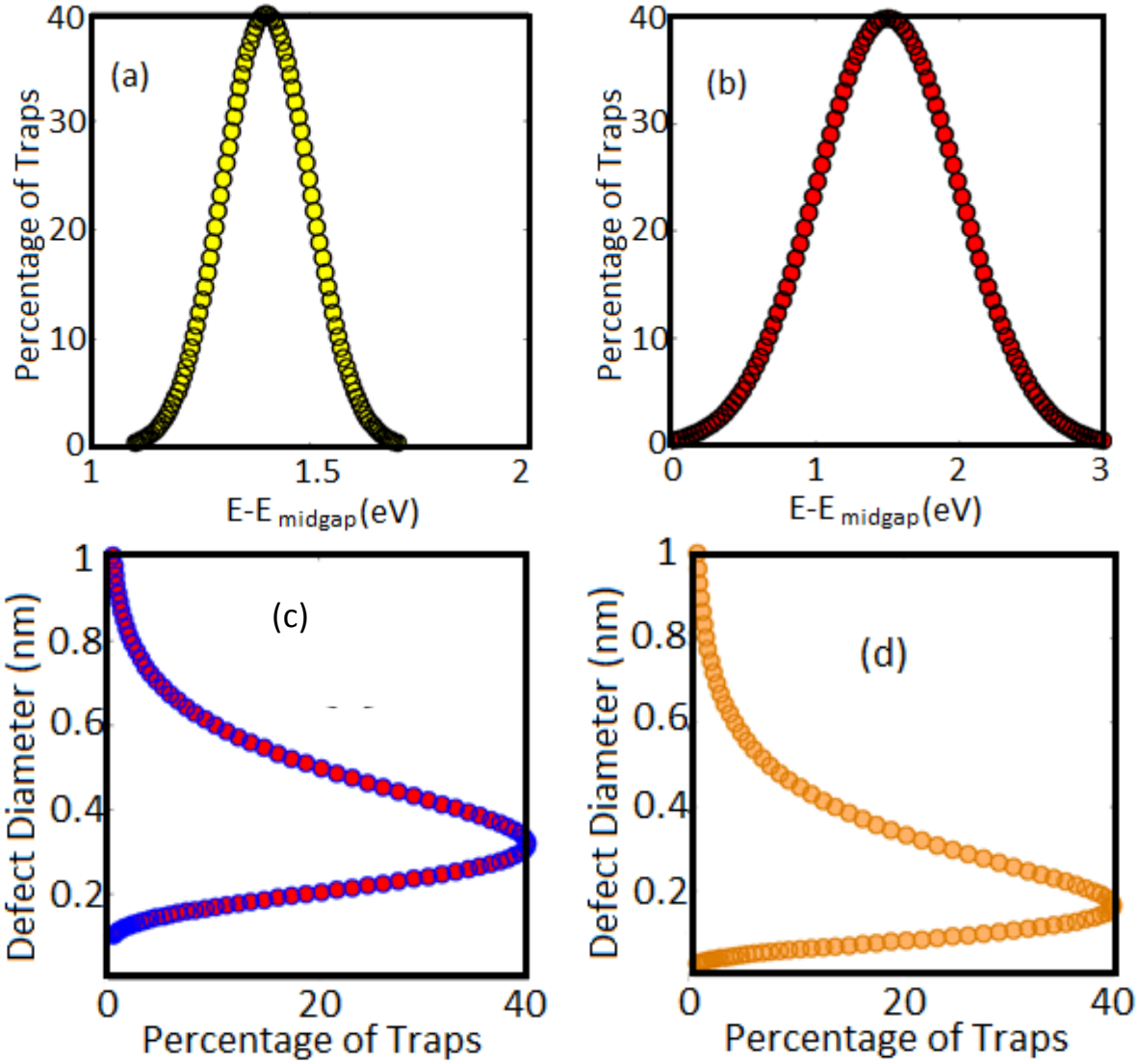

Fig. 6.5 Trap energy distribution of (a) HfSiON (similar to ref [25]) and (b) SiO_2 (similar to [26]). Corresponding defect diameter distribution of (a) HfSiON and (b) SiO_2

The work presented in [168] does not provide any information regarding the number of traps or their locations. The probability of stress-induced trap formation in a dielectric stack is higher at the interface of the two dielectrics [169]. Hence, in this case, we have assumed that the traps will form at the interface of HfSiON and SiO_2 layers. Regarding the energy level of the traps, we have considered the same distribution (fig. 6.5a, 6.5b) as shown in ref [169] [170].

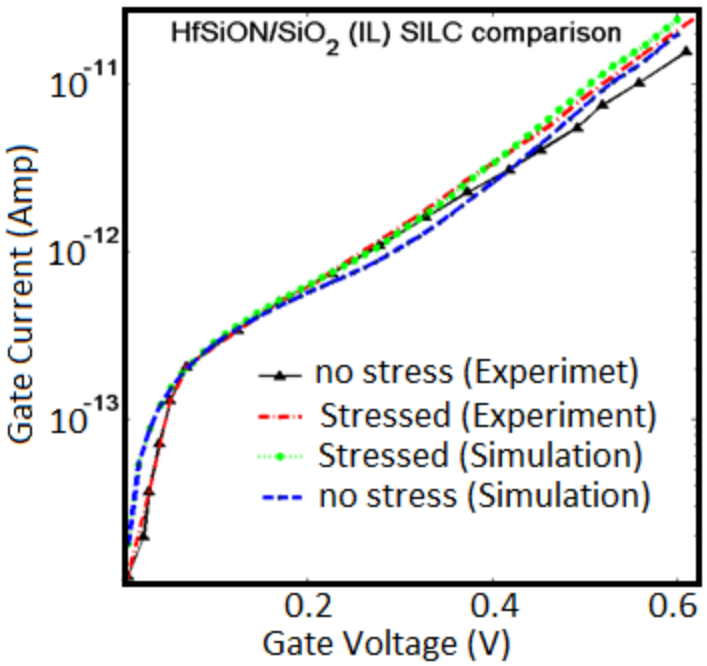

Fig. 6.6: Pre and post-stress-induced leakage current for 1.4 nm HfSiON and 0.8nm SiO_2 IL (both experiment [123] and simulation). The root mean square error is less than 5%.

The capture cross-section dimension of a trap depends on its energy level. The mid bandgap traps of HfSiON and SiO_2 layers have capture cross-section diameters of ~ 1nm [157] and 0.6nm [157], respectively. On the other hand, traps on the conduction band have zero capture cross-section area since they do not contribute to trap-assisted tunneling. In thin oxides, most of the traps have their energy level distributed near the conduction band [169] [170] (fig. 6.5). Therefore, in thin dielectric layers, the capture cross-sections of mid-gap traps to conduction band traps are assumed to decrease exponentially. The exponential function of decreasing capture cross-section diameter is modeled as d=exp(-a). Here d is the capture cross-section diameter of a trap and a is a fitting parameter which satisfies the previous statement. Depending on the energy level of a trap, the capture cross-section distribution can be found from the exponential function (Fig 6.5c and 6.5d). One Büttiker probe is placed at each trap positions to calculate the post-stress trap assisted tunneling. The number of Büttiker probes at the HfSiON/SiO2 interface and the acceleration factor α (in eqn. 6.6) are calibrated for the best match with the experimental data. The parameter, α depends on the capture cross-section diameter of the corresponding trap. α is bigger for the trap with a larger cross-section. For HfSiON, α is calibrated to be between 10 and 11 while for SiO_2, α is distributed between 1.5 to

1.9. We have found that for a trap density of $1.5x10^{19}/m^3$ at the HfSiON and SiO2 interface, the calculated SILC matches best with the experimental data (fig. 6.6). Thus, using the Büttiker probe method, we can determine the stress-induced trap density.

The pre-existing defect density in the oxide layer can be determined in a similar way. Pre-stress defect-free I-V characteristic for a different sample of $HfSiON/SiO_2$ dielectric stack (same or different dimension) can be determined from the same NEGF simulation framework. Let us assume that experimentally observed current is larger than the simulation value at all voltages for the new device. The extra current is coming from pre-existing trap assisted tunneling. For introducing the trap assisted tunneling into the NEGF simulation framework, we need to include one Büttiker probe at each defect position. The number, positions and self-energies (i.e., the value of α) of these probes are calibrated in the simulation framework for matching the experimental I-V characteristics. From the number of Büttiker probe needed in simulation for matching the pre-stress I_V characteristics, we can calculate the pre-existing defect density.

6.3.2 SiO_2 Soft Breakdown

It has been experimentally observed that the SBD in dielectrics is characteristically different from the HBD [155]. In case of soft dielectric breakdown, the post breakdown current shows comparatively smaller increment from the pre-breakdown value and follows a power law. The soft breakdown can be modeled with our proposed Büttiker probe by attaching probes to all grid points along the breakdown path (fig. 6.4d). The shape of the breakdown path (how many traps line up to form the percolation path) can be determined by the percolation theory. The energy levels of the traps are assumed to have Gaussian distribution from the conduction band edge to 3 eV inside the bandgap (fig. 6.5b) [170]. If we tune the power factor α in equation (6.5), we can get excellent matching of post breakdown I-V characteristics. Here, one thing worth mentioning is that the power factor α depends on the capture cross-section of the defects. As mentioned earlier, the capture cross-section depends on the energy level of the traps. Traps at the percolation path can form at different energy levels. Therefore, α can be different for different Büttiker probes.

In ref [161], the post soft breakdown I-V characteristic in a MOS capacitor ($Poly\text{-}Si/SiO_2/Si$ system) has been experimentally demonstrated. While benchmarking the simulation, we have observed that most of the traps have the power factor $\alpha = 1.7$. Few traps have α near 1.5 and

these traps can be assumed to be close to the conduction band (fig 6.5b). These traps have a lower capture cross-section and contribute less towards tunneling. While few other traps have α near 1.9 and these traps can be assumed to sit a bit deeper (close to mid-bandgap) in energy diagram. These traps have a bigger capture cross-section and contribute more towards tunneling. Applying these values of α, we have seen an excellent match between our simulation result and the experimental observation (shown in fig 6.7a). Simulation parameters are listed in table 6.1.

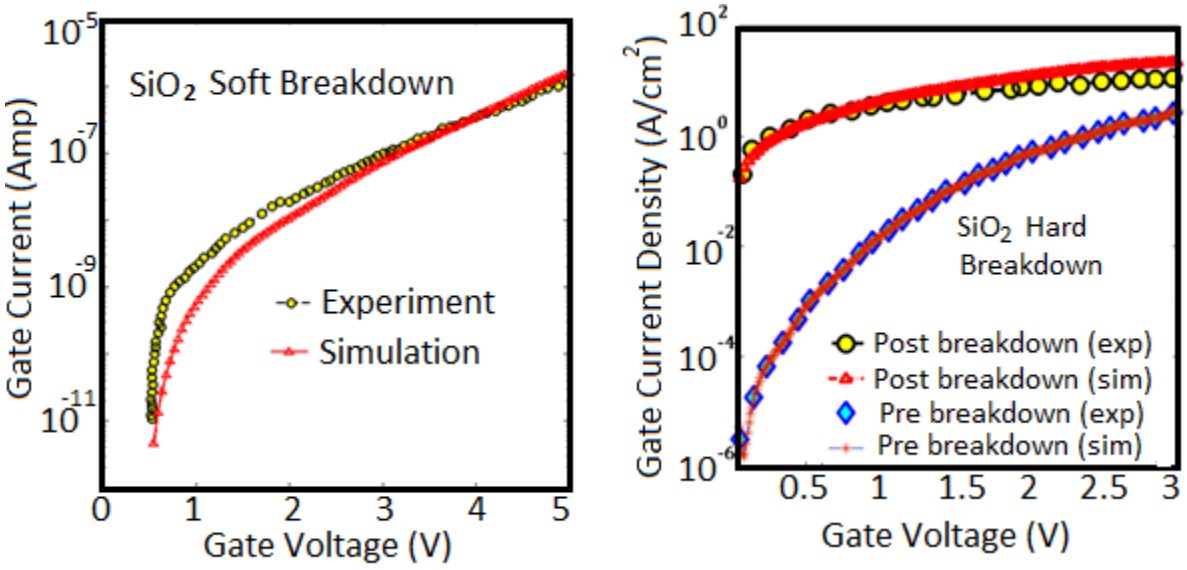

Fig. 6.7: (a). Post soft breakdown current for 1.7 nm SiO_2 (both experiment [161] and simulation). Root mean square of error is 11.76% (b). Post hard breakdown current for 2.2 nm SiO_2 (both experiment [171] and simulation). Root mean square of error is ~13%.

6.3.3 SiO_2 Hard Breakdown

Hard breakdowns mainly occur in thick dielectrics [155] because of the high gate voltage. It can also happen in thin dielectrics if the electric field stress is very high. A hard breakdown can be easily separated from a soft breakdown by the huge change in post-breakdown (PBD) current and the Ohmic nature of the PBD I-V characteristics (the power factor $\alpha = 1$). In this case, the system's retarded Green's function will be constructed according to eqn. 7. In ref [171], post hard breakdown I-V characteristic is shown for a MOS capacitor with 2.2nm thick SiO_2. In figure 6.7(b), we have shown both the experimental and simulation data before and after the hard breakdown (simulation parameters are listed in Table 6.1). It is evident that after the hard breakdown, the gate leakage current increases by several orders of magnitude but the increase of current with voltage is almost linear.

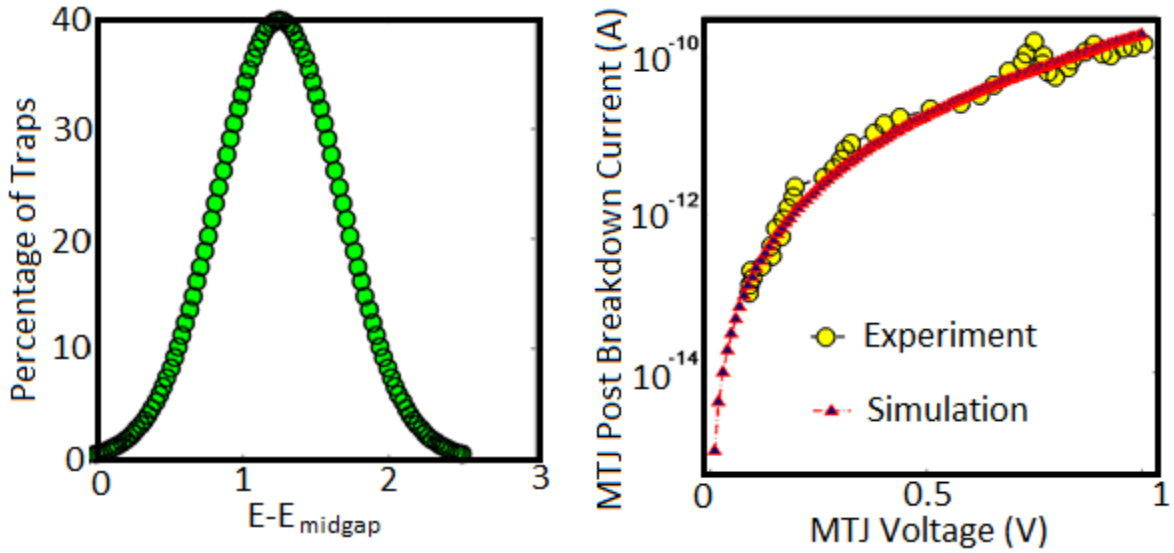

Fig. 6.8: (a) Trap energy distribution of MgO (b)Post soft breakdown current-voltage characteristics in MTJ from experiment [173] and from our simulation framework (root mean square error is less than 2%).

6.3.4 MgO Soft Breakdown

MgO is a mid-κ dielectric with a low Weibull slope [172]. It has gained popularity due to its excellent spin current filtering capacity. Hence it has become the prime choice for fabricating MTJ. In [173], a post soft breakdown I-V characteristic of 1nm thick MgO in an MTJ is reported. The MTJ stack is comprised of CoFeB/MgO/CoFeB. It was observed in [130] that the SILC activation energy of MgO (0.37eV) is quite high (compared with HfO_2 [174]). Therefore, although the bulk trap has a large capture cross-section (~ 0.9 nm [175]), in a very thin MgO layer, the trap energy levels are distributed near the conduction band edge. As a result, the trap capturing cross-section will be much smaller than the bulk value like other dielectrics. Considering the fact, we have calibrated the post-soft breakdown I-V characteristics with the experiment [173]. Most of the traps have the power factor α to be equal to 9. Traps energy level distribution is again assumed to be Gaussian, distributed from the bottom of conduction band to 2.5eV inside the bandgap. Most of the traps are assumed to be at an energy level of 1.25 eV. Very few traps near the conduction band have α to be around 8.5. Few traps deep inside the bandgap have α to be around 9.5.

Breakdown in the MgO layer has a significant impact on MTJ characteristics. Due to breakdown, the %TMR decreases significantly. This is because the parallel tunneling magnetoresistance (R_P) is mainly dominated by the exchange splitting energy, Δ of the magnetic contacts (shown in fig. 6.1). For parallel configuration, huge exchange splitting allows the

majority of spin to tunnel easily through the energy barrier created by the MgO layer. The formation of a percolation path does not affect the process significantly. Hence, R_p does not change significantly due to breakdown. But for the antiparallel configuration, the exchange splitting energy opposes spin tunneling. Therefore, a percolation path significantly decreases the antiparallel tunneling magnetoresistance (R_{AP}). In figure 6.9(a) we have shown the pre and post-breakdown parallel and antiparallel tunneling magnetoresistance (R_p and R_{AP} respectively) of a CoFeB-MgO-CoFeB MTJ with 1nm thick MgO layer (same structure as shown in [152]). Also, the corresponding degradation in TMR is shown in figure 6.9(b). We can observe that R_{AP} decreases at a much faster rate than R_P.

The reason for %TMR degradation after a breakdown can be attributed to the spin-independent nature of the dielectric traps [153][154]. Traps inside the MgO layer helps tunneling irrespective of electron spin. When an electron is captured by a trap, the spin properties get randomized. The spin-wave function of an electron in a trap can be represented as,

$$|\psi_s\rangle = a_{z+}|u_{z+}\rangle + a_{z-}|d_{z-}\rangle \tag{6.13}$$

Here $a_{z+}a_{z+}^*$, $a_{z-}a_{z-}^*$, $|u_{z+}\rangle$ and $|d_{z+}\rangle$ represents the spin polarization probability and spin basis vector (spinors) along +z and -z-axis, respectively. These two spinors can represent spin pointing at any direction.

Table 6.1. Parameters used in Büttiker probe simulation

Parameter Name	Value
Grid mesh size	0.1 nm
CoFeB effective mass (m_{FM}/m_0)	0.8 [176]
CoFeB-MgO barrier height	0.77 eV [176]
CoFeB-MgO Fermi level	2.25 eV [176]
CoFeB exchange splitting energy	2.15 eV [176]
MgO tunneling effective mass (m_{FM}/m_0)	0.18 [176]
Weibull slope of MgO (β)	0.6 [174]
MgO voltage acceleration factor (γ)	25.6 [174]
TiN work function	4.4 eV [177]

Table 6.1 continued

TiN effective mass (m_{TIN}/m_0)	1.1 [178]
Si effective mass	0.26
Si electron affinity	4.05 eV
Temperature	300 k
HfSiON tunneling effective mass	0.03 [179]
HfSiON bandgap	5.32 eV [179]
HfSiON electron affinity	2.95 eV [179]
TiN-HfSiON barrier height	1.45 eV
SiO_2 tunneling effective mass	0.42 [180]
SiO_2 electron affinity	0.95 eV [181]
Si-SiO_2 barrier height	3.1 eV [182]
SiO_2 bandgap	9 eV

In a trap, it can be assumed that these two probabilities are equal i.e., $a_{z+}a_{z+}^* = a_{z-}a_{z-}^*$. Therefore, the spin filtering efficiency of the MgO layer is expected to go down after the formation of traps and percolation paths. Fig. 6.9 (b) shows the TMR degradation of an MTJ operating at different voltages. If the MTJ operates at 1mA (V~0.6V), we observe that the TMR goes down by about 25% after one soft breakdown. Therefore, 3 to 4 soft breakdowns in the MgO layer can cause functional failure of the MTJ.

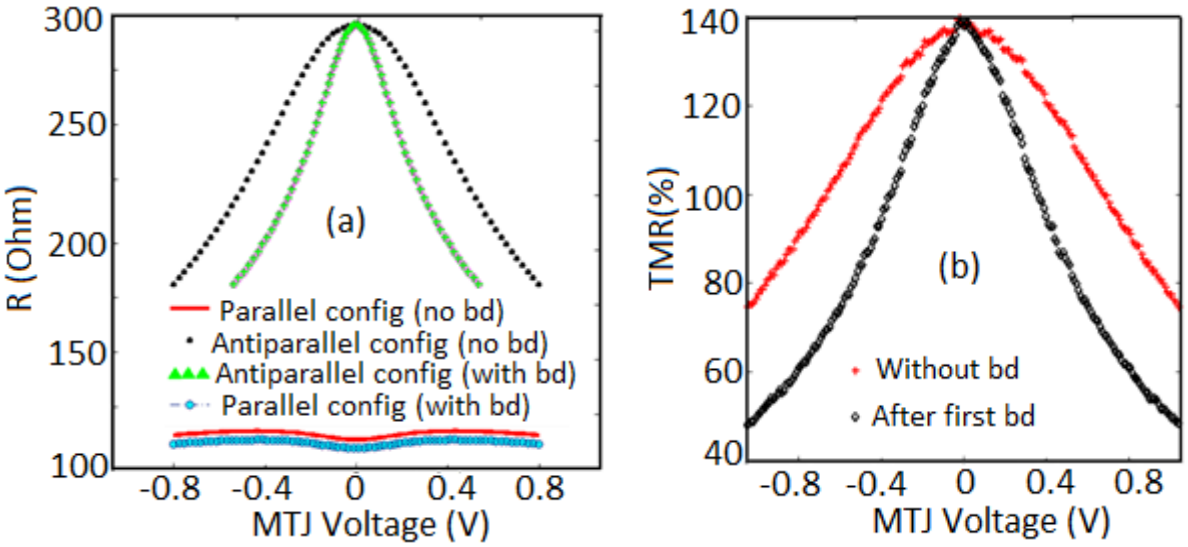

Fig. 6.9: (a): Simulation data for pre and post breakdown (bd) parallel and antiparallel resistance (R_p and R_{AP}) in MTJ (device dimension can be found in [152]) (b) Change in %TMR before and after breakdown (simulation data).

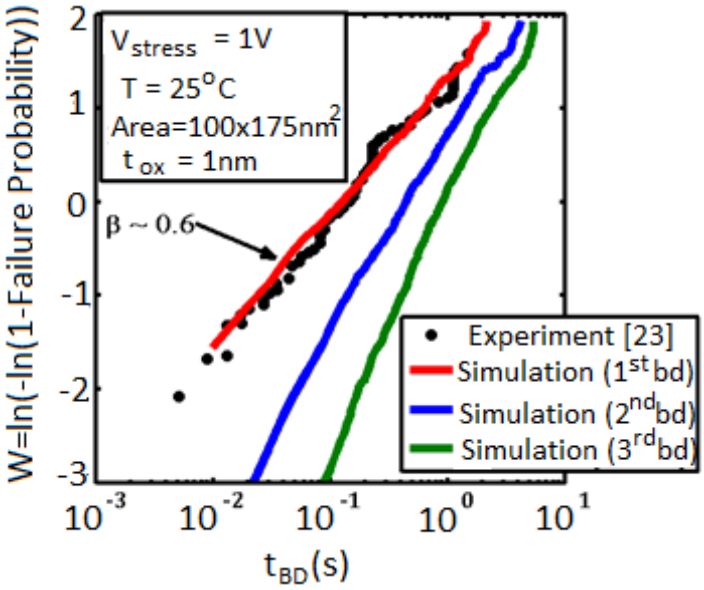

Fig. 6.10: Weibull plot of MgO for 1st and 3rd breakdown. 1st breakdown data is calibrated with experiment [174] using percolation model and based on the calibrated data, Weibull plot for 3rd breakdown is plotted at a stress voltage of 1V.

In order to estimate the MTJ lifetime, we have implemented a 3-D cell-based percolation model [157] and calibrated the Weibull distribution after the 1st breakdown with experimental data [174]. The simulation is done using 1000 sample MTJs. Then the Weibull plot for 3rd SBD is drawn (fig. 6.10) using data from the percolation model. We can see that 1% of the MTJs suffer

3rd SBD after 0.03s for a stress voltage of 1V. As the MgO area in [130] is different from our simulation, we need to do area scaling using standard area scaling formulation [156].

After area scaling, we have found that 1% of the 1000 MTJ samples have 3rd SBD after 0.0631s at stress voltage of 1V. For determining the device lifetime at operating voltage, we need to do voltage scaling. For voltage scaling, we have used the following equation [156],

$$V_{op} = V_{acc} - log_{10}(\frac{t_{op}}{t_{acc}})/\gamma \quad (6.14)$$

Here, γ is the voltage acceleration factor (value is listed in Table 6.1). We can see that at operating voltage of 0.6V, 1% MTJs in 1000 sample MTJs will have 3rd soft breakdown in almost 24 years. Therefore, we can draw the conclusion that MgO based MTJs have comparatively much longer lifetime than standard CMOS devices.

6.4 Conclusion

In this chapter, we have presented a Büttiker probe based post breakdown current model for dielectric materials. The proposed method is flexible, can be applied to a wide range of dielectric materials, and has shown excellent potential for TDDB analysis. The simulation framework shows good match with experimental data for any type, shape and size of the dielectric. In addition, it has the flexibility to model traps formed at any position. It is a physics-based, close to the atomistic simulation model, yet does not consume much computational resources. Most importantly, it can predict spin current and TMR degradation in MTJs that cannot be done with conventional TDDB models.

6.5 Summary

Dielectric layers are gradually being downscaled in different electronic devices like MOSFETs and magnetic tunnel junctions (MTJ) with shrinking device sizes. As a result, the time-dependent dielectric breakdown has become a major issue in such devices. In this chapter, we propose a generalized way of modeling the stress-induced leakage current (SILC) and post-breakdown current (PBC) due to time-dependent wear-out of the dielectric layer. We model the traps formed in the dielectric layer using Büttiker probe and incorporate the Büttiker probe self-energies in standard self-consistent non-equilibrium Green's function formalism in order to

determine SILC and PBC. In addition, we have shown the impact of the breakdown in the dielectric layer on the spin current and spin filtering characteristics of an MTJ. The proposed model is generic in nature. It can be extended from MTJs and conventional CMOS technology to any other devices with any type of single and multiple layers of dielectric material(s).

7. CONCLUSION

7.1 Conclusion and Summary

Switching of free layer magnet, i.e., the writing operation is the slowest and the most 'power-hungry' operation in magnetic tunnel junction (MTJ). Spin transfer torque (STT) based current-driven switching technique offers relatively lower switching power consumption compared to the field-driven MTJ switching. Switching of STT-MTJ requires a single external magnetic field perpendicular to the spin-transfer torque and magnetization axis of the free layer. In STT-MTJ, the read current and write current flow in the same direction causing reliability issue called 'destructive read failure'. STT-MTJ is also difficult to scale down. Large writing voltage also exposes the tunneling barrier to a high electric field which may cause dielectric breakdown. In order to solve the issues, spin-orbit torque (SOT) based current-driven MTJ has been proposed. SOT_MTJ is a three terminal device with separate read and write paths. Hence, SOT-MTJ is more reliable and easily scalable. In SOT-MTJ, spin-transfer torque is applied on MTJ free layer magnet by injecting spin-polarized current. One of the major bottlenecks of SOT-MTJ is the inefficiency in charge current to spin current conversion. Heavy spin Hall metals (HM), like Pt, β-W etc are primarily used to generate spin current from charge current. In heavy spin Hall metals, strong spin-orbit coupling separates the electrons with different spins. Nevertheless, the charge to spin current conversion efficiency is low in HMs. On the other hand, topological insulator not only has better conversion efficiency than any other material available till date but also can generate both in-plane and out-of-plane spin currents due to strong Rashba effect. Therefore, use of topological insulator as spin injector eliminates the necessity of using an external magnetic field to switch the MTJ free layer because the simultaneous presence of in-plane and out-of-plane spin-torques breaks the magnetization symmetry in MTJ free layer. Nevertheless, topological insulator has low conductance and hence, a large amount of current shunts through the top ferromagnet free layer introducing a major source of power loss. To minimize the loss, we decided to replace the high conductance ferromagnet metallic free layer with comparatively low conductance ferromagnet insulator. It degrades the spin conversion efficiency of topological insulator (TI) to some extent due to rough surface state but reduces the power loss.

To further minimize the MTJ write-operation power, we explored the option of using topological semi-metal as the spin injector. Topological semi-metal has lower charge to spin current conversion efficiency than TI. But the simulation shows that it has better spin Hall angle than heavy spin Hall metals (HM). Furthermore, the topological semimetal has higher electrical conductivity than TI which results in low shunting current loss. Our simulation showed that the use of topological semi-metal significantly reduces the MTJ switching power compared with HMs and TI as a spin injector.

Slow switching speed is another significant drawback of ferromagnet MTJ. Ferromagnets have long switching time due to precession movement of magnetic moments around the switching axis before getting settled down due to damping. On the other hand, ferrimagnets have faster switching speed because of high exchange coupling between oppositely polarized magnetic moments. Hence, in the presence of large enough spin-transfer torque, the magnetic moments rotate and settle down quickly along the switching axis. First, we tried to formulate the proper magnetization dynamics formalism of ferrimagnet. When ferrimagnet devices come in contact with the material of high spin-orbit coupling, interfacial DMI interaction becomes prominent. We derived the DMI contribution to FiM magnetization dynamics and proposed the simulation framework for analyzing the magnetization of FiM. We analyzed the performance of a ferrimagnet (CoTb) based MTJ (CoTb/MgO/CoTb/Pt). We calculated the exchange coupling in CoTb using *ab-initio* calculation and found that exchange coupling in CoTb is a thickness-dependent parameter. We also calculated the DMI at the CoTb/Pt interface using KKR Green's function method and simulated the magnetization dynamics of the MTJ free layer. We found that CoTb based MTJ has picosecond range switching speed and good thermal stability. However, due to the thick CoTb free layer, the critical switching current is higher. Also, due to lower exchange splitting between the spin-dependent density of states, the TMR in CoTb based MTJ is lower compared with ferromagnet MTJ.

MTJs are fabricated with thin tunneling MgO layer (1-1.5 nm) in order to reduce the overall operational power consumption. Thin crystalline MgO layer is exposed to a high electric field during MTJ operation, making it vulnerable to time-dependent dielectric breakdown. We proposed Büttiker probe based spin-dependent quantum transport simulation for TDDB analysis in MTJ. We calculated the effect of trap generation and breakdown path formation in the MgO layer on the overall MTJ performance. We found that in the CoFeB-MgO(1nm)-CoFeB MTJ,

TMR starts degrading with the trap generation and breakdown path formation. After the third soft breakdown in the MgO layer, MTJ goes out of order. The Weibull plot analysis showed that it takes around 24 years for 1% MTJ (in a sample of 1000 MTJs) to become non-functional under an operating voltage of 0.6V and room temperature. The result will vary for different MgO thicknesses and operating conditions.

APPENDIX A. DERIVATION OF DMI

DMI interaction plays a vital role in antiferromagnet and ferrimagnet magnetization dynamics. DMI can create oscillation in the magnetic domains of AFM and FiM even in the absence of the spin-polarized current.

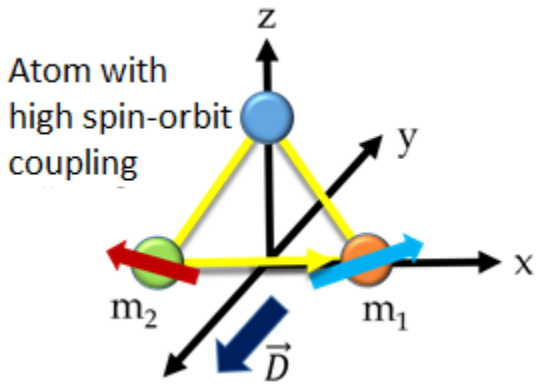

Fig. A.1: Schematic diagram of DMI between FiM sub-lattice and adjacent atom with high spin-orbit coupling. Due to DMI, magnetic moments inside FiM sub-lattice are tilted towards +z-axis.

In fig.A.1, the magnetic easy axis of FiM crystal is considered to be parallel to the x-axis and the hard axis is parallel to the z-axis. Therefore, in a sub-lattice, two magnetic moments of unequal magnitude are lying along the +x axis and the -x-axis. A material with high spin-orbit coupling, like SHE metal or TI, is grown on top of the FiM crystal along the +z axis. The proximity of SHE metal or TI atoms to the FiM sub-lattices introduces a strong DMI effect between them. The energy associated with DMI is written as [80],

$$\epsilon = \vec{D}.(\overrightarrow{m_1} \times \overrightarrow{m_2})$$

Here $\vec{D}$ is the DMI vector along -y-axis, $\overrightarrow{m_1}$ and $\overrightarrow{m_2}$ are the two magnetic moments in the FiM crystal sub-lattice. $\vec{D}, \overrightarrow{m_1}$ and $\overrightarrow{m_2}$ can be written as,

$$\vec{D} = D_x\hat{x} + D_y\hat{y} + D_z\hat{z}$$

$$\overrightarrow{m_1} = m_{1x}\hat{x} + m_{1y}\hat{y} + m_{1z}\hat{z}$$

$$\overrightarrow{m_2} = m_{2x}\hat{x} + m_{2y}\hat{y} + m_{2z}\hat{z}$$

Hence the expression of the energy becomes,

$$\epsilon = D_x\left(m_{1y}m_{2z} - m_{2y}m_{1z}\right) + D_y(m_{1z}m_{2x} - m_{2z}m_{1x}) + D_z\left(m_{1x}m_{2y} - m_{2x}m_{1y}\right)$$

Change in the magnetization of $\overrightarrow{m_1}$ due to DMI is determined from the change in energy with respect to $\overrightarrow{m_1}$ i.e., $\frac{d\epsilon}{d\overrightarrow{m_1}} = \frac{d\epsilon}{dm_{1x}}\hat{x} + \frac{d\epsilon}{dm_{1y}}\hat{y} + \frac{d\epsilon}{dm_{1z}}\hat{z}$. It can be shown that,

$$\frac{d\epsilon}{dm_{1x}} = -D_y m_{2z} + D_z m_{2y}$$

$$\frac{d\epsilon}{dm_{1y}} = D_x m_{2z} - D_z m_{2x}$$

$$\frac{d\epsilon}{dm_{1z}} = -D_x m_{2y} + D_y m_{2x}$$

Hence the change in magnetization of $\overrightarrow{m_1}$ due to solitary effect of DMI can be written as,

$$\frac{d\epsilon}{d\overrightarrow{m_1}} = \left(-D_y m_{2z} + D_z m_{2y}\right)\hat{x} + \left(D_x m_{2z} - D_z m_{2x}\right)\hat{y} + \left(-D_x m_{2y} + D_y m_{2x}\right)\hat{z}$$

Close inspection of the terms reveals that,

$$\frac{d\epsilon}{d\overrightarrow{m_1}} = \overrightarrow{m_2} \times \vec{D}$$

Similarly, change in magnetization of $\overrightarrow{m_2}$ due to the solitary effect of DMI can be written as,

$$\frac{d\epsilon}{d\overrightarrow{m_2}} = \vec{D} \times \overrightarrow{m_1}$$

Note, both $\overrightarrow{m_2} \times \vec{D}$ and $\vec{D} \times \overrightarrow{m_1}$ points to the +z axis. Therefore, DMI will try to tilt the magnetic moments along the hard axis.

APPENDIX B. DERIVATION OF ANALYTICAL EQUATION OF OSCILLATION FREQUENCY OF AFM

I. Sigma Mode

In Sigma mode of operation, the injected spin-polarized current is parallel to the +y axis. In AFM crystal sub-lattice, the magnetic moments cancel each other. Therefore, the weak magnetization field can be written as $\vec{m} = m_y\hat{y}$ (detail explanation can be found in the main text) while the staggered magnetization can be expressed as $\vec{l} = l_x\hat{x} + l_z\hat{z}$. The staggered magnetization is written as (from the main text),

$$\frac{d\vec{l}}{dt} = 2J\,(\vec{l} \times \vec{m}) + (\vec{m} \times \vec{D}) + K_x(\hat{x} \times (m_x\,\vec{l} + l_x\,\vec{m})) + K_z(\hat{z} \times (m_z\,\vec{l} + l_z\,\vec{m})) +$$
$$\alpha\left(\vec{m} \times \frac{d\vec{l}}{dt} + \vec{l} \times \frac{d\vec{m}}{dt}\right) + W_s\left(\vec{m} \times (\vec{l} \times \vec{p}) + \vec{l} \times (\vec{m} \times \vec{p})\right) + W_f(\vec{l} \times \vec{p})$$

Taking cross multiplication on both sides by $\vec{l}$ yields,

$$\frac{d\vec{l}}{dt} \times \vec{l} = 2J\,(\vec{l} \times \vec{m}) \times \vec{l} + (\vec{m} \times \vec{D}) \times \vec{l} + K_x(\hat{x} \times (m_x\,\vec{l} + l_x\,\vec{m})) \times \vec{l} + K_z(\hat{z} \times (m_z$$
$$\vec{l} + l_z\,\vec{m})) \times \vec{l} + \alpha\left(\vec{m} \times \frac{d\vec{l}}{dt} + \vec{l} \times \frac{d\vec{m}}{dt}\right) \times \vec{l} + W_s\left(\vec{m} \times (\vec{l} \times \vec{p}) + \vec{l} \times (\vec{m} \times \vec{p})\right) \times \vec{l} +$$
$$W_f(\vec{l} \times \vec{p}) \times \vec{l} \qquad \text{(B.1)}$$

Algebraic manipulation (shown below) of the terms produces the expression of $\vec{m}$ in terms if $\vec{l}$ and $\frac{d\vec{l}}{dt}$. Constraints used for the derivation of oscillation frequency for sigma mode of operation are,

$$\vec{l}\,.\vec{m} = 0$$
$$m^2 + l^2 = 1$$
$|\vec{m}| << |\vec{l}|$ and hence $l^2 \sim 1$
$$\vec{l}.\frac{d\vec{l}}{dt} = 0$$
$$\vec{m} \times \vec{p} = 0$$
$$\vec{m} \times \vec{D} = 0$$

Considering individual terms of eqn. B.1 sequentially,

$$2J\ (\vec{l}\ \times\ \vec{m}) \times \vec{l} = -2J\ \vec{l} \times (\vec{l}\ \times\ \vec{m})$$

$$= -2J\ [\vec{l}(\vec{l}\ .\vec{m}) - \vec{m}(\vec{l}\ .\vec{l})] = 2J\vec{m}\ (l_x^2 + l_z^2)$$

$$\left(\vec{m}\ \times\ \vec{D}\right) \times \vec{l} = 0$$

$$K_x\left(\hat{x}\ \times (m_x\ \vec{l} + l_x\ \vec{m})\right) \times \vec{l} =\ K_x l_x(\hat{x}\ \times \vec{m}) \times \vec{l}$$

$$= -K_x l_x \vec{l} \times (\hat{x}\ \times \vec{m}) = -K_x l_x(\hat{x}\ (\vec{l}\ .\vec{m}) - \vec{m}(\vec{l}\ .\hat{x}\ )) = K_x l_x^2 \vec{m}$$

$$K_z\left(\hat{z}\ \times (m_z\ \vec{l} + l_z\ \vec{m})\right) \times \vec{l} =\ K_z(\hat{z}\ \times\ l_z\ \vec{m}) \times \vec{l}$$

$$= -K_z l_z\left(\hat{z}\ (\vec{l}\ .\vec{m}) - \vec{m}(\vec{l}\ .\hat{z}\ )\right) =\ K_z l_z^2 \vec{m}$$

The higher order damping terms $\vec{m}\ \times \frac{d\vec{l}}{dt}\ and\ \vec{l}\ \times \frac{d\vec{m}}{dt}$ are ignored.

$$W_s\ \left(\vec{m}\ \times (\vec{l} \times \vec{p}) + \vec{l}\ \times (\vec{m} \times \vec{p})\right) \times \vec{l} =\ W_s\ \left(\vec{m}\ \times (\vec{l} \times \vec{p})\right) \times \vec{l}$$

$$=\ W_s\ \left(\vec{l}\ (\vec{p}\ .\vec{m}) - \vec{p}(\vec{l}\ .\vec{m}\ )\right) \times \vec{l} =\ W_s\ \left(\vec{l}\ (\vec{p}\ .\vec{m})\right) \times \vec{l} = 0$$

$$W_f(\vec{l} \times \vec{p}) \times \vec{l} =\ -W_f\left(\vec{l}(\vec{l}.\vec{p}) - \vec{p}(\vec{l}.\vec{l})\right) =\ W_f\vec{p}\ (l_x^2 + l_z^2)$$

Hence eqn. 1 yields,

$$\frac{d\vec{l}}{dt} \times \vec{l} = 2J\vec{m}\ (l_x^2 + l_z^2) + K_x l_x^2 \vec{m} +\ K_z l_z^2 \vec{m} +\ W_f\vec{p}\ (l_x^2 + l_z^2)$$

The weak magnetization can be expressed as,

$$\vec{m} = \frac{1}{2J + K_x l_x^2 + K_z l_z^2}\left(\frac{d\vec{l}}{dt} \times \vec{l} - W_f\vec{p}\ \right)$$

In AFM, J >>K_x and J >> K_z. Therefore,

$$\vec{m} = \frac{1}{2J}\left(\frac{d\vec{l}}{dt} \times \vec{l} - W_f\vec{p}\ \right)$$

It agrees well with ref [72].

Differentiating both sides,

$$\frac{d\vec{m}}{dt} = \frac{1}{2J}\left(\frac{d^2\vec{l}}{dt^2} \times \vec{l} + \frac{d\vec{l}}{dt} \times \frac{d\vec{l}}{dt} - W_f \frac{d\vec{p}}{dt}\right) = \frac{1}{2J}\left(\frac{d^2\vec{l}}{dt^2} \times \vec{l}\right)$$

Substituting in eqn. 4.5 of main text yields,

$$\frac{1}{2J}\left(\frac{d^2\vec{l}}{dt^2} \times \vec{l}\right) = \vec{D} \times \vec{l} + K_x l_x \hat{x} \times \vec{l} + K_z l_z \hat{z} \times \vec{l} + \alpha\left(\vec{l} \times \frac{d\vec{l}}{dt}\right) + W_s\left(\vec{l} \times \left(\vec{l} \times \vec{p}\right)\right) \qquad (B.2)$$

The staggered magnetization $\vec{l}$ contains an angle φ_1 with x-y plane and in polar coordinate, $\vec{l}$ can be written as, $\vec{l} = < cos\varphi_1, 0, sin\varphi_1 >$ (as stated in the main text). Therefore, $\frac{d\vec{l}}{dt} = < -sin\varphi_1 \frac{d\varphi}{dt}, 0, cos\varphi_1 \frac{d\varphi}{dt} > and$

$\frac{d^2\vec{l}}{dt^2} = < -sin\varphi_1 \frac{d^2\varphi_1}{dt^2} - cos\varphi_1 \left(\frac{d\varphi_1}{dt}\right)^2, 0, cos\varphi_1 \frac{d^2\varphi_1}{dt^2} - sin\varphi_1 \left(\frac{d\varphi_1}{dt}\right)^2 >.$

Considering only the y components, eqn. B.2 can be written as,

$$\frac{1}{2J}\frac{d^2\varphi_1}{dt^2} = \frac{K_x - K_z}{2} sin2\varphi_1 + \alpha\frac{d\varphi_1}{dt} + W_s p_y \qquad (B.3)$$

Comparing eqn. B.3 with second order differential equation of simple harmonic oscillator, the oscillation frequency can be expressed as,

$$\omega = \sqrt{2J(K_x - K_z)}$$

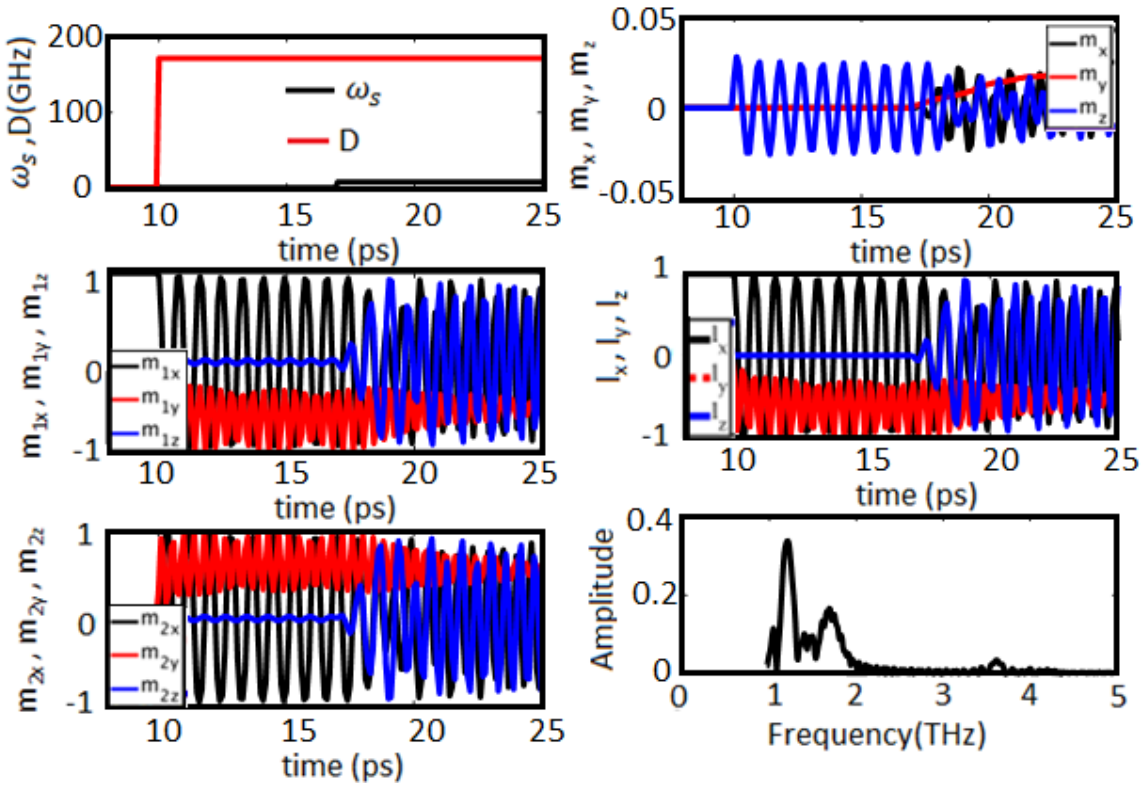

Fig. B.1: Micromagnetic simulation results for antiferromagnet ReFeO3 in sigma mode. Simulation parameters are taken from ref [74] (J_{m1m2} = 172.2 THz, DMI = 0.001* J, W_s = 8GHz, K_x = 6.2812 GHz, $\alpha = 0$, K_z = 0 and W_f = 0).

The analytical equation of oscillation frequency in gamma mode agrees well with ref [74]. In figure 2, atomistic micromagnetic simulation of ReFeo3 in sigma mode is displayed. As explained earlier, AFM and FiM shows similar pattern in response to external magnetic perturbation. Note, the oscillation frequency of AFM is much higher than that of FiM. This is because AFM has much larger exchange coupling than FiM. Also at the interface of AFM and material with high spin orbit coupling, the DMI is high. High DMI introduces z-component in the magnetic moments. Introduction of z-component initiates very high exchange coupling torque along y component and big oscillation can be seen in y and x component.

Interesting result is obtained from the Fourier transformation of the oscillations. The oscillation frequency of y component is higher than oscillation frequency of x component and hence both peaks are shown in FFT diagram.

The fast Fourier transformation of the oscillation pattern shows that the oscillation frequency (x component) is 1.2109×10^{12} Hz while the analytical expression $\omega = \sqrt{2J(K_x - K_z)}$ yields the oscillation frequency to be 1.47×10^{12} Hz.

II. Gamma Mode

In Gamma mode of operation, the injected spin polarized current is parallel to +z axis. In AFM crystal sub-lattice, the magnetic moments cancel each other. Therefore, the weak magnetization field can be written as $\vec{m} = m_z \hat{z}$ (detail explanation can be found in main text) while the staggered magnetization can be expressed as $\vec{l} = l_x \hat{x} + l_y \hat{y}$. The staggered magnetization is written as (from main text),

$$\frac{d\vec{l}}{dt} = 2J\,(\vec{l} \times \vec{m}) + (\vec{m} \times \vec{D}) + K_x(\hat{x} \times (m_x \vec{l} + l_x \vec{m})) + K_z(\hat{z} \times (m_z \vec{l} + l_z \vec{m})) + \alpha \left(\vec{m} \times \frac{d\vec{l}}{dt} + \vec{l} \times \frac{d\vec{m}}{dt}\right) + W_s \left(\vec{m} \times (\vec{l} \times \vec{p}) + \vec{l} \times (\vec{m} \times \vec{p})\right) + W_f(\vec{l} \times \vec{p})$$

Taking cross multiplication on both sides by $\vec{l}$ yields,

$$\frac{d\vec{l}}{dt} \times \vec{l} = 2J\,(\vec{l} \times \vec{m}) \times \vec{l} + (\vec{m} \times \vec{D}) \times \vec{l} + K_x(\hat{x} \times (m_x \vec{l} + l_x \vec{m})) \times \vec{l} + K_z(\hat{z} \times (m_z \vec{l} + l_z \vec{m})) \times \vec{l} + \alpha \left(\vec{m} \times \frac{d\vec{l}}{dt} + \vec{l} \times \frac{d\vec{m}}{dt}\right) \times \vec{l} + W_s \left(\vec{m} \times (\vec{l} \times \vec{p}) + \vec{l} \times (\vec{m} \times \vec{p})\right) \times \vec{l} + W_f(\vec{l} \times \vec{p}) \times \vec{l} \quad \text{(B.4)}$$

Algebraic manipulation (shown below) of the terms produces the expression of $\vec{m}$ in terms if $\vec{l}$ and $\frac{d\vec{l}}{dt}$. Constraints used for the derivation of oscillation frequency for sigma mode of operation are,

$$\vec{l} \cdot \vec{m} = 0$$

$$m^2 + l^2 = 1$$

$|\vec{m}| << |\vec{l}|$ and hence $l^2 \sim 1$

$$\vec{l} \cdot \frac{d\vec{l}}{dt} = 0$$

$$\vec{m} \times \vec{p} = 0$$

$$\vec{l} \cdot \vec{p} = 0$$

Considering individual terms of eqn. B.4 sequentially,

$$2J\,(\vec{l}\times\vec{m})\times\vec{l} = -2J\,\vec{l}\times(\vec{l}\times\vec{m})$$

$$= -2J\,[\vec{l}(\vec{l}\,.\vec{m}) - \vec{m}(\vec{l}\,.\vec{l})] = 2J\vec{m}\,l^2$$

$$\left(\vec{m}\times\vec{D}\right)\times\vec{l} = -\vec{m}l_yD_y$$

$$K_x\left(\hat{x}\times(m_x\,\vec{l}+l_x\,\vec{m})\right)\times\vec{l} = K_xl_x(\hat{x}\times\vec{m})\times\vec{l}$$

$$= -K_xl_x\vec{l}\times(\hat{x}\times\vec{m}) = -K_xl_x(\hat{x}\,(\vec{l}\,.\vec{m}) - \vec{m}(\vec{l}\,.\hat{x}\,)) = K_xl_x^2\vec{m}$$

$$K_z\left(\hat{z}\times(m_z\,\vec{l}+l_z\,\vec{m})\right)\times\vec{l} = K_z(\hat{z}\times m_z\,\vec{l})\times\vec{l}$$

$$= -K_zm_z\left(\hat{z}\,(\vec{l}\,.\vec{l}) - l(\vec{l}\,.\hat{z}\,)\right) = -K_zl^2\vec{m}$$

The higher order damping terms $\vec{m}\times\frac{d\vec{l}}{dt}$ and $\vec{l}\times\frac{d\vec{m}}{dt}$ are ignored.

$$W_s\left(\vec{m}\times(\vec{l}\times\vec{p}) + \vec{l}\times(\vec{m}\times\vec{p})\right)\times\vec{l} = W_s\left(\vec{m}\times(\vec{l}\times\vec{p})\right)\times\vec{l}$$

$$= W_s\left(\vec{l}\,(\vec{p}\,.\vec{m}) - \vec{p}(\vec{l}\,.\vec{m}\,)\right)\times\vec{l} = W_s\left(\vec{l}\,(\vec{p}\,.\vec{m})\right)\times\vec{l} = 0$$

$$W_f(\vec{l}\times\vec{p})\times\vec{l} = -W_f\left(\vec{l}(\vec{l}.\vec{p}) - \vec{p}(\vec{l}.\vec{l})\right) = W_f\vec{p}\,l^2$$

Hence eqn. B.4 yields,

$$\frac{d\vec{l}}{dt}\times\vec{l} = 2J\vec{m}\,l^2 - \vec{m}l_yD_y + K_xl_x^2\vec{m} + -K_zl^2\vec{m} + W_f\vec{p}\,l^2$$

The weak magnetization can be expressed as,

$$\vec{m} = \frac{1}{2J - l_yD_y + K_xl_x^2 + K_z}\left(\frac{d\vec{l}}{dt}\times\vec{l} - W_f\vec{p}\,\right)$$

In AFM, J >>K_x and J >> K_z. Therefore,

$$\vec{m} = \frac{1}{2J - l_yD_y}\left(\frac{d\vec{l}}{dt}\times\vec{l} - W_f\vec{p}\,\right)$$

The staggered magnetization $\vec{l}$ contains an angle φ_2 with x-y plane and in polar coordinate, $\vec{l}$ can be written as, $\vec{l} = < cos\varphi_2, sin\varphi_2, 0 >$ (as stated in the main text). Therefore, $\frac{d\vec{l}}{dt} = < -sin\varphi_2 \frac{d\varphi_2}{dt}, cos\varphi_2 \frac{d\varphi_2}{dt}, 0 > and$

$\frac{d^2\vec{l}}{dt^2} = < -sin\varphi_2 \frac{d^2\varphi_2}{dt^2} - cos\varphi_2 \left(\frac{d\varphi_2}{dt}\right)^2, cos\varphi_2 \frac{d^2\varphi_2}{dt^2} - sin\varphi_2 \left(\frac{d\varphi_2}{dt}\right)^2, 0 >$..Substituting in eqn. () yields,

$$\vec{m} = \frac{1}{2J - sin\varphi_2 \, D_y} \left(\frac{d\varphi_2}{dt}\hat{z} - W_f \vec{p}\,\right)$$

Differentiating both sides yields,

$$\frac{dm_z}{dt} = \frac{1}{2J - D_y sin\varphi_2} \frac{d^2\varphi_2}{dt^2} - \frac{D_y cos\varphi_2}{(2J - D_y sin\varphi_2)^2} \frac{d\varphi_2}{dt} - \frac{D_y cos\varphi_2}{(2J - D_y sin\varphi_2)^2} W_f p_z$$

Cancelling the null terms, eqn. B.5 can be rewritten as,

$$\frac{d\vec{m}}{dt} = \vec{D} \times \vec{l} + K_x l_x \hat{x} \times \vec{l} + K_z m_z \hat{z} \times \vec{l} + \alpha \left(\vec{l} \times \frac{d\vec{l}}{dt}\right) + W_s \left(\vec{l} \times \left(\vec{l} \times \vec{p}\right)\right) \qquad (B.5)$$

Considering only the z components, eqn. B.5 can be written as,

$$\frac{1}{2J - D_y sin\varphi_2} \frac{d^2\varphi_2}{dt^2} - \frac{D_y cos\varphi_2}{(2J - D_y sin\varphi_2)^2} \frac{d\varphi_2}{dt} - \frac{D_y cos\varphi_2}{(2J - D_y sin\varphi_2)^2} W_f p_z = -D_y cos\varphi_2 + K_x \, cos\varphi_2 sin\varphi_2 + \alpha \frac{d\varphi_2}{dt} + W_s p_z \qquad (B.6)$$

Eqn B.4 can be rewritten as,

$$\frac{d^2\varphi_2}{dt^2} - \left(\alpha + \frac{D_y cos\varphi_2}{(2J - D_y sin\varphi_2)^2}\right)\left(2J - D_y sin\varphi_2\right)\frac{d\varphi_2}{dt} - W_s p_z \left(2J - D_y sin\varphi_2\right) - \frac{D_y cos\varphi_2}{2J - D_y sin\varphi_2} W_f p_z + 2JD_y cos\varphi_2 - (D_y^2 + 2JK_x)\frac{sin2\varphi_2}{2} + K_x D_y sin^2\varphi_2 cos\varphi_2 = 0 \qquad (B.7)$$

Comparing eqn. B.7 with second order differential equation of simple harmonic oscillator, the oscillation frequency can be expressed as,

$$\omega = \sqrt{D_y^2 + 2JK_x}$$

The fast Fourier transformation of the oscillation pattern shows that the oscillation frequency is 1.1621×10^{12} Hz while the analytical expression $\omega = \sqrt{D_y^2 + 2JK_x}$ yields the oscillation frequency to be 1.4809×10^{12} Hz.

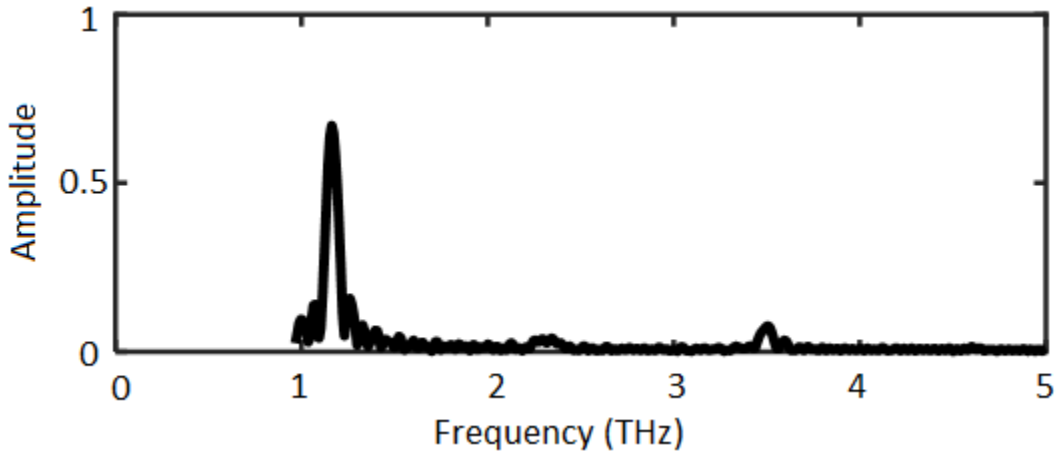

Fig. B.2 : The fast Fourier transformation of oscillation of l_x. Simulation parameters are same as fig. 2

APPENDIX C. DERIVATION OF ANALYTICAL EQUATION OF OSCILLATION FREQUENCY OF FiM

I. Sigma Mode

In Sigma mode of operation, the injected spin polarized current is parallel to +y axis. In FiM crystal sub-lattice the magnetic moments do not cancel each other. Therefore, the weak and staggered magnetization in this case can be written as,

$$\vec{m} = < m_x, m_y, 0 > \text{ and } \vec{l} = < l_x, 0, l_z >$$

The constraints in sigma mode of operation for FiM are,

$$m^2 + l^2 = 1$$

$$\vec{l}.\frac{d\vec{l}}{dt} = 0$$

$$\vec{m}.\frac{d\vec{m}}{dt} = 0$$

$$\vec{l}.\vec{p} = 0$$

$$\vec{l}.\vec{D} = 0$$

The staggered magnetization is written as (from main text),

$$\frac{d\vec{l}}{dt} = 2J\,(\vec{l} \times \vec{m}) + (\vec{m} \times \vec{D}) + K_x(\hat{x} \times (m_x\,\vec{l} + l_x\,\vec{m})) + K_z(\hat{z} \times (m_z\,\vec{l} + l_z\,\vec{m})) +$$

$$\alpha\left(\vec{m} \times \frac{d\vec{l}}{dt} + \vec{l} \times \frac{d\vec{m}}{dt}\right) + W_s\left(\vec{m} \times (\vec{l} \times \vec{p}) + \vec{l} \times (\vec{m} \times \vec{p})\right) + W_f(\vec{l} \times \vec{p})$$

Taking cross multiplication on both sides by $\vec{l}$ yields,

$$\frac{d\vec{l}}{dt} \times \vec{l} = 2J\,(\vec{l} \times \vec{m}) \times \vec{l} + (\vec{m} \times \vec{D}) \times \vec{l} + K_x(\hat{x} \times (m_x\,\vec{l} + l_x\,\vec{m})) \times \vec{l} + K_z(\hat{z} \times (m_z\,\vec{l} + l_z\,\vec{m})) \times \vec{l} + \alpha\left(\vec{m} \times \frac{d\vec{l}}{dt} + \vec{l} \times \frac{d\vec{m}}{dt}\right) \times \vec{l} + W_s\left(\vec{m} \times (\vec{l} \times \vec{p}) + \vec{l} \times (\vec{m} \times \vec{p})\right) \times \vec{l} + W_f(\vec{l} \times \vec{p}) \times \vec{l}$$

Algebraic manipulation of each term is shown below,

$$2J\left(\vec{l} \times \vec{m}\right) \times \vec{l} = -2J\,\vec{l} \times \left(\vec{l} \times \vec{m}\right)$$

$$= -2J\vec{l}\left(\vec{l}\,.\vec{m}\right) + 2J\vec{m} \times \left(\vec{l}\,.\vec{l}\right) = -2J\vec{l}(l_x m_x) + 2J\vec{m}l^2$$

$$\left(\vec{m} \times \vec{D}\right) \times \vec{l} = -\vec{l} \times \left(\vec{m} \times \vec{D}\right) = -\vec{m}\left(\vec{l}.\vec{D}\right) + \vec{D}\left(\vec{l}.\vec{m}\right) = \vec{D}(l_x m_x)$$

$$K_x\left(\hat{x} \times (m_x \vec{l} + l_x \vec{m})\right) \times \vec{l} = K_x\left(-m_x l_z^2 \hat{x} + m_y l_x^2 \hat{y} + m_x l_z l_x \hat{z}\right)$$

$$K_z\left(\hat{z} \times (m_z \vec{l} + l_z \vec{m})\right) \times \vec{l} = K_z(l_z^2 \vec{m} - m_x l_z l_x \hat{z})$$

$$W_s\left(\vec{m} \times \left(\vec{l} \times \vec{p}\right) + \vec{l} \times (\vec{m} \times \vec{p})\right) \times \vec{l} = -2W_s(l_x m_x)\left(\left(l_z p_y\right)\hat{x} - \left(l_x p_y\right)\hat{z}\right)$$

$$W_f\left(\vec{l} \times \vec{p}\right) \times \vec{l} = W_f l^2 \vec{p}$$

Hence, ignoring the higher order damping terms,

$$\frac{d\vec{l}}{dt} \times \vec{l} = -2J\vec{l}(l_x m_x) + 2J\vec{m}l^2 + \vec{D}(l_x m_x) + K_x\left(-m_x l_z^2 \hat{x} + m_y l_x^2 \hat{y} + m_x l_z l_x \hat{z}\right)$$
$$+ K_z(l_z^2 \vec{m} - m_x l_z l_x \hat{z}) - 2W_s(l_x m_x)\left(\left(l_z p_y\right)\hat{x} - \left(l_x p_y\right)\hat{z}\right) + W_f l^2 \vec{p} \qquad \text{(C.8)}$$

The derivative of staggered magnetization can be defined as, $\frac{d\vec{l}}{dt} = < \frac{dl_x}{dx}, 0, \frac{dl_z}{dx} >$. Therefore, $\frac{d\vec{l}}{dt} \times \vec{l}$ only contains y component. Equating the y components of the vector eqn. C.9 on both sides yields,

$$\frac{d\vec{l}}{dt} \times \vec{l} = 2Jm_y l^2 \hat{y} + \vec{D}(l_x m_x) + K_x m_y l_x^2 \hat{y} + K_z l_z^2 m_y \hat{y} + W_f l^2 \vec{p} \qquad \text{(C.9)}$$

Taking dot product on both side of eqn. C.4 by $\vec{l}$ yields (ignoring the higher order damping terms),

$$\frac{d\vec{l}}{dt}.\vec{l} = 0 = 2J\left(\vec{l} \times \vec{m}\right).\vec{l} + \left(\vec{m} \times \vec{D}\right).\vec{l} + K_x(\hat{x} \times (m_x \vec{l} + l_x \vec{m})).\vec{l} + K_z(\hat{z} \times (m_z \vec{l} + l_z \vec{m})).\vec{l} + W_s\left(\vec{m} \times \left(\vec{l} \times \vec{p}\right) + \vec{l} \times (\vec{m} \times \vec{p})\right).\vec{l} + W_f\left(\vec{l} \times \vec{p}\right).\vec{l}$$

Algebraic manipulation of each term of this equation are shown below.

$$\left(\vec{l} \times \vec{m}\right).\vec{l} = 0$$

$$\left(\vec{m} \times \vec{D}\right).\vec{l} = m_x l_z D_y$$

$$\left(\hat{x} \times \vec{l}\right).\vec{l} = 0$$

$$(\hat{x} \times \vec{m}).\vec{l} = m_y l_z$$

$$(\hat{z} \times \vec{l}).\vec{l} = 0$$

$$(\hat{z} \times \vec{m}).\vec{l} = -m_y l_x$$

$$\left(\vec{m} \times (\vec{l} \times \vec{p})\right).\vec{l} = m_y p_y l^2$$

$$\left(\vec{l} \times (\vec{m} \times \vec{p})\right).\vec{l} = 0$$

$$(\vec{l} \times \vec{p}).\vec{l} = 0$$

Therefore,

$$m_x l_z D_y + K_x m_y l_z l_x - K_z m_y l_z l_x + W_s m_y p_y l^2 = 0 \qquad \text{(C.10)}$$

The weak magnetization component along x axis can be written as,

$$m_x = \frac{-(K_x m_y l_z l_x - K_z m_y l_z l_x + W_s m_y p_y l^2)}{l_z D_y} \qquad (C.11)$$

Substituting in equation C.10 yields,

$$\left|\frac{d\vec{l}}{dt} \times \vec{l}\right| = 2Jm_y l^2 - \frac{l_x}{l_z}\left(K_x m_y l_z l_x - K_z m_y l_z l_x + W_s m_y p_y l^2\right) + K_x m_y l_x^2 + K_z l_z^2 m_y + W_f l^2 p_y$$

The weak magnetization component along y axis can be written as,

$$m_y = \frac{\left|\frac{d\vec{l}}{dt} \times \vec{l}\right| - W_f l^2 p_y}{2Jl^2 - \frac{l_x}{l_z}\left(K_x l_z l_x - K_z l_z l_x + W_s p_y l^2\right) + K_x l_x^2 + K_z l_z^2}$$

Simplifying,

$$m_y = \frac{\left|\frac{d\vec{l}}{dt} \times \vec{l}\right| - W_f l^2 p_y}{2Jl^2 - \frac{l_x}{l_z} W_s p_y l^2 + K_z l^2} \qquad (C.12)$$

Considering only y components in eqn. C.9 yield

$$\frac{d\overrightarrow{m_y}}{dt} = (K_z - K_x) l_x l_z \hat{y} + \alpha \vec{l} \times \frac{d\vec{l}}{dt} - W_s l^2 p_y \hat{y} - W_s m_x^2 p_y \hat{y} \qquad (C.13)$$

The staggered magnetization $\vec{l}$ contains an angle φ_1 with x-y plane and in polar coordinate, $\vec{l}$ can be written as, $\vec{l} = < a\cos\varphi_1, 0, a\sin\varphi_1 >$ (as stated in the main text). Therefore, $\frac{d\vec{l}}{dt} = < -a\sin\varphi_1 \frac{d\varphi_1}{dt}, 0, a\cos\varphi_1 \frac{d\varphi_1}{dt} > and$

$\frac{d^2\vec{l}}{dt^2} = < -asin\varphi_1 \frac{d^2\varphi_1}{dt^2} - acos\varphi_1 \left(\frac{d\varphi_1}{dt}\right)^2, 0, acos\varphi_1 \frac{d^2\varphi_1}{dt^2} - asin\varphi_1 \left(\frac{d\varphi_1}{dt}\right)^2 >$

Algebraic manipulation of different terms are shown below.

$$\frac{d\vec{l}}{dt} \times \vec{l} = a^2 \frac{d\varphi_1}{dt} \hat{y}$$

Therefore,

$$m_y = \frac{a^2 \frac{d\varphi_1}{dt} - W_f a^2 p_y}{2Ja^2 - W_s p_y a^2 cot\varphi_1 + K_z a^2}$$

Differentiating both sides with respect to t yields,

$\frac{dm_y}{dt}\left(2Ja^2 - W_s p_y a^2 cot\varphi_1 + K_z a^2\right) + \frac{a^2\frac{d\varphi_1}{dt} - W_f a^2 p_y}{2Ja^2 - W_s p_y a^2 cot\varphi_1 + K_z a^2} W_s p_y a^2 cosec^2\varphi_1 = a^2 \frac{d^2\varphi_1}{dt^2}$

Cancelling a^2 terms on both sides yields,

$\frac{dm_y}{dt}\left(2J - W_s p_y cot\varphi_1 + K_z\right) + \frac{\frac{d\varphi_1}{dt} - W_f p_y}{2J - W_s p_y cot\varphi_1 + K_z} W_s p_y cosec^2\varphi_1 = \frac{d^2\varphi_1}{dt^2}$

Therefore,

$$\frac{dm_y}{dt} = \frac{1}{2J - W_s p_y cot\varphi_1 + K_z} \frac{d^2\varphi_1}{dt^2} - \frac{\frac{d\varphi_1}{dt} - W_f p_y}{(2J - W_s p_y cot\varphi_1 + K_z)^2} W_s p_y cosec^2\varphi_1 \qquad \text{(C.14)}$$

Equating both sides of eqn. C.13 and C.14,

$(K_z - K_x)a^2 sin\varphi_1 cos\varphi_1 + \alpha a^2 \frac{d\varphi_1}{dt} - W_s a^2 p_y - W_s m_x^2 p_y = \frac{1}{2J - W_s p_y cot\varphi_1 + K_z} \frac{d^2\varphi_1}{dt^2} -$

$\frac{\frac{d\varphi_1}{dt} - W_f p_y}{(2J - W_s p_y cot\varphi_1 + K_z)^2} W_s p_y cosec^2\varphi_1$

We can safely assume that $a^2 \gg m_x^2$. Therefore, $W_s p_y (a^2 + m_x^2) \sim W_s a^2 p_y$. The second order differential equation of staggered magnetization can be written as,

$$\frac{d^2\varphi_1}{dt^2} - \left(\alpha a^2 + \frac{W_s p_y cosec^2\varphi_1}{2J - W_s p_y cot\varphi_1 + K_z}\right)\frac{d\varphi_1}{dt} + (K_x - K_z)(2J - W_s p_y cot\varphi_1 + K_z)a^2 \frac{sin2\varphi_1}{2}$$
$$+ W_s p_y (a^2 + \frac{W_f p_y cosec^2\varphi_1}{(2J - W_s p_y cot\varphi_1 + K_z)^2}) = 0$$

Comparing with the equation of harmonic oscillator, the oscillation frequency can be written as,

$$\omega = \sqrt{(K_x - K_z)(2J - W_s p_y cot\varphi_1 + K_z)a^2}$$

The value of 'a' depends on the ratio of magnetic moments in the crystal sub-lattice. In antiferromagnet, this ratio is 1. In case of oscillating pattern, the angle φ_1 can be assumed to be the average value.

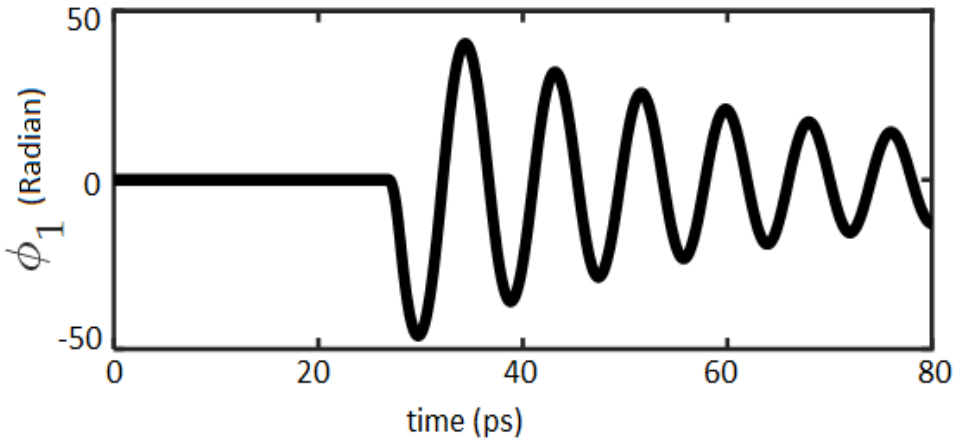

Fig. C.1. : Oscillation pattern of φ_1, considering the ratio of magnetic moment of Co and Tb, a ~ 0.56.

II. Gamma Mode

In Gamma mode of operation, the injected spin polarized current is parallel to +z axis. In FiM crystal sub-lattice the magnetic moments do not cancel each other. Therefore, the weak and staggered magnetization in this case can be written as

$$\vec{m} = < m_x, 0, m_z > \text{ and } \vec{l} = < l_x, l_y, 0 >$$

The constraints in sigma mode of operation for FiM are,

$$m^2 + l^2 = 1$$

$$\vec{l}.\frac{d\vec{l}}{dt} = 0$$

$$\vec{m}.\frac{d\vec{m}}{dt} = 0$$

$$\vec{l}.\vec{p} = 0$$

$$\vec{m}.\vec{D} = 0$$

$$l^2 \gg m_x^2$$

The staggered magnetization is written as (from main text),

$$\frac{d\vec{l}}{dt} = 2J\,(\vec{l} \times \vec{m}) + (\vec{m} \times \vec{D}) + K_x(\hat{x} \times (m_x\,\vec{l} + l_x\,\vec{m})) + K_z(\hat{z} \times (m_z\,\vec{l} + l_z\,\vec{m})) + \alpha\left(\vec{m} \times \frac{d\vec{l}}{dt} + \vec{l} \times \frac{d\vec{m}}{dt}\right) + W_s\left(\vec{m} \times (\vec{l} \times \vec{p}) + \vec{l} \times (\vec{m} \times \vec{p})\right) + W_f(\vec{l} \times \vec{p})$$

Taking cross multiplication on both sides by $\vec{l}$ yields,

$$\frac{d\vec{l}}{dt} \times \vec{l} = 2J\,(\vec{l} \times \vec{m}) \times \vec{l} + (\vec{m} \times \vec{D}) \times \vec{l} + K_x(\hat{x} \times (m_x\,\vec{l} + l_x\,\vec{m})) \times \vec{l} + K_z(\hat{z} \times (m_z\,\vec{l} + l_z\,\vec{m})) \times \vec{l} + \alpha\left(\vec{m} \times \frac{d\vec{l}}{dt} + \vec{l} \times \frac{d\vec{m}}{dt}\right) \times \vec{l} + W_s\left(\vec{m} \times (\vec{l} \times \vec{p}) + \vec{l} \times (\vec{m} \times \vec{p})\right) \times \vec{l} + W_f(\vec{l} \times \vec{p}) \times \vec{l}$$

Algebraic manipulation of each term is shown below,

$$2J\left(\vec{l} \times \vec{m}\right) \times \vec{l} = -2J\,\vec{l} \times \left(\vec{l} \times \vec{m}\right)$$
$$= -2J\vec{l}\left(\vec{l}\,.\vec{m}\right) + 2J\vec{m} \times \left(\vec{l}\,.\vec{l}\right) = -2J\vec{l}(l_x m_x) + 2J\vec{m}l^2$$

$$\left(\vec{m} \times \vec{D}\right) \times \vec{l} = -\vec{l} \times \left(\vec{m} \times \vec{D}\right) = -\vec{m}\left(\vec{l}.\vec{D}\right) + \vec{D}\left(\vec{l}.\vec{m}\right) = -\vec{m}\left(l_y D_y\right) + \vec{D}(l_x m_x)$$

$$K_x\left(\hat{x} \times (m_x\,\vec{l} + l_x\,\vec{m})\right) \times \vec{l} = K_x\left(-m_x l_y^2 \hat{x} + m_x l_x l_y \hat{y} + m_z l_x^2 \hat{z}\right)$$

$$K_z\left(\hat{z} \times (m_z\,\vec{l} + l_z\,\vec{m})\right) \times \vec{l} = -K_z m_z l^2 \hat{z}$$

$$W_s\left(\vec{m}\times(\vec{l}\times\vec{p})+\vec{l}\times(\vec{m}\times\vec{p})\right)\times\vec{l}=2W_s m_x l_x l_y p_y\hat{x}-2W_s m_x p_y l_x^2\hat{y}$$

$$W_f(\vec{l}\times\vec{p})\times\vec{l}=W_f p_z l^2\hat{z}$$

Hence, ignoring the higher order damping terms,

$$\frac{d\vec{l}}{dt}\times\vec{l}=-2J\vec{l}(l_x m_x)+2J\vec{m}l^2-\vec{m}(l_y D_y)+\vec{D}(l_x m_x)+K_x\left(-m_x l_y^2\hat{x}+m_x l_x l_y\hat{y}+m_z l_x^2\hat{z}\right)-K_z m_z l^2\hat{z}+2W_s m_x l_x l_y p_y\hat{x}-2W_s m_x p_y l_x^2\hat{y}+W_f p_z l^2\hat{z} \quad \text{(C.15)}$$

The derivative of staggered magnetization can be defined as, $\frac{d\vec{l}}{dt}=<\frac{dl_x}{dx},0,\frac{dl_z}{dx}>$. Therefore, $\frac{d\vec{l}}{dt}\times\vec{l}$ only contains z component. Equating the y components of the vector eqn. C.15 on both sides yields,

$$\frac{d\vec{l}}{dt}\times\vec{l}=2Jm_z l^2\hat{z}-m_z l_y D_y\hat{z}+K_x m_z l_x^2\hat{z}-K_z m_z l^2\hat{z}+W_f p_z l^2\hat{z} \quad \text{(C.16)}$$

Therefore,

$$m_z=\frac{\left|\frac{d\vec{l}}{dt}\times\vec{l}\right|-W_f p_z l^2}{2Jl^2-l_y D_y+K_x l_x^2-K_z l^2}$$

Equating z component of eqn. C.4 of main article on both side,

$$\frac{d\vec{m_z}}{dt}=-l_x D_y\hat{z}+K_x l_x l_z\hat{z}+\alpha\vec{l}\times\frac{d\vec{l}}{dt}-W_s l^2 p_z\hat{y} \quad \text{(C.17)}$$

The staggered magnetization $\vec{l}$ contains an angle φ_2 with x-y plane and in polar coordinate, $\vec{l}$ can be written as, $\vec{l}=<acos\varphi_2,asin\varphi_2,0>$ (as stated in the main text). Therefore, $\frac{d\vec{l}}{dt}=<-asin\varphi_2\frac{d\varphi_2}{dt},acos\varphi_2\frac{d\varphi_2}{dt},0>$ and

$\frac{d^2\vec{l}}{dt^2}=<-asin\varphi_2\frac{d^2\varphi_2}{dt^2}-acos\varphi_2\left(\frac{d\varphi_2}{dt}\right)^2,acos\varphi_2\frac{d^2\varphi_2}{dt^2}-asin\varphi_2\left(\frac{d\varphi_2}{dt}\right)^2,0>$

Algebraic manipulation of different terms is shown below.

$$\frac{d\vec{l}}{dt} \times \vec{l} = -a^2 \frac{d\varphi_2}{dt} \hat{z}$$

Therefore,

$$m_z = \frac{-a^2 \frac{d\varphi_2}{dt} - W_f a^2 p_z}{2Ja^2 - D_y a sin\varphi_2 + K_x a^2 cos^2\varphi_2 - K_z a^2}$$

Differentiating both sides with respect to t yields,

$$\frac{dm_z}{dt}\left(2Ja^2 - D_y a sin\varphi_2 + K_x a^2 cos^2\varphi_2 - K_z a^2\right) +$$

$$\frac{-a^2\frac{d\varphi_2}{dt} - W_f a^2 p_z}{2Ja^2 - D_y a sin\varphi_2 + K_x a^2 cos^2\varphi_2 - K_z a^2}\left(-D_y a cos\varphi_2 \frac{d\varphi_2}{dt} - K_x a^2 sin2\varphi_2 \frac{d\varphi_2}{dt}\right) = -a^2 \frac{d^2\varphi_2}{dt^2}$$

Cancelling a^2 terms on both sides yields,

$$\frac{dm_z}{dt}\left(2J - \frac{D_y}{a} sin\varphi_2 + K_x cos^2\varphi_2 - K_z\right) + \frac{-\frac{d\varphi_2}{dt} - W_f p_z}{2J - \frac{D_y}{a} sin\varphi_2 + K_x cos^2\varphi_2 - K_z}\left(-\frac{D_y}{a} cos\varphi_2 \frac{d\varphi_2}{dt} -\right.$$

$$\left. K_x sin2\varphi_2 \frac{d\varphi_2}{dt}\right) = -\frac{d^2\varphi_2}{dt^2}$$

Therefore,

$$\frac{dm_z}{dt} =$$

$$\frac{-1}{2J - \frac{D_y}{a} sin\varphi_2 + K_x cos^2\varphi_2 - K_z} \frac{d^2\varphi_2}{dt^2} - \frac{\frac{d\varphi_2}{dt} + W_f p_z}{\left(2J - \frac{D_y}{a} sin\varphi_2 + K_x cos^2\varphi_2 - K_z\right)^2}\left(\frac{D_y}{a} cos\varphi_2 \frac{d\varphi_2}{dt} + K_x sin2\varphi_2 \frac{d\varphi_2}{dt}\right)$$

(C.18)

Equating both sides of eqn. C.17 and C.18,

$$-a cos\varphi_2 D_y + K_x a^2 sin\varphi_2 cos\varphi_2 + \alpha a^2 \frac{d\varphi_2}{dt} - W_s a^2 p_z = \frac{-1}{2J - \frac{D_y}{a} sin\varphi_2 + K_x cos^2\varphi_2 - K_z} \frac{d^2\varphi_2}{dt^2} -$$

$$\frac{\frac{d\varphi_2}{dt} + W_f p_z}{\left(2J - \frac{D_y}{a} sin\varphi_2 + K_x cos^2\varphi_2 - K_z\right)^2}\left(\frac{D_y}{a} cos\varphi_2 + K_x sin2\varphi_2\right) \frac{d\varphi_2}{dt}$$

The second order differential equation of staggered magnetization can be written as,

$$\frac{d^2\varphi_2}{dt^2} + \left[\frac{\frac{d\varphi_2}{dt} + W_f p_z}{2J - \frac{D_y}{a}sin\varphi_2 + K_x cos^2\varphi_2 - K_z}\left(\frac{D_y}{a}cos\varphi_2 + K_x sin2\varphi_2\right)\right.$$
$$\left. + \alpha a^2\left(2J - \frac{D_y}{a}sin\varphi_2 + K_x cos^2\varphi_2 - K_z\right)\right]\frac{d\varphi_2}{dt}$$
$$+ K_x(2J - \frac{D_y}{a}sin\varphi_2 + K_x cos^2\varphi_2 - K_z)a^2\frac{sin2\varphi_1}{2}$$
$$- \left(acos\varphi_2 D_y + W_s a^2 p_z\right)\left(2J - \frac{D_y}{a}sin\varphi_2 + K_x cos^2\varphi_2 - K_z\right) = 0$$

Comparing with the equation of harmonic oscillator the oscillation frequency can be written as,

$$\omega = \sqrt{K_x(2J - \frac{D_y}{a}sin\varphi_2 + K_x cos^2\varphi_2 - K_z)a^2}$$

Considering the ration of magnetic moment of Co and Tb, a ~ 0.56.

APPENDIX D. MAGNETIZATION DYNAMICS OF COMPLEX FIM

Magnetization dynamics of complex ferrimagnet such as Gadolinium Iron Garnett (GIG) is discussed in the main article. The magnetization of magnetic moment $\overrightarrow{m_2}$ and $\overrightarrow{m_3}$ can be written as follows,

$$\frac{d\overrightarrow{m_2}}{dt} = \frac{J_{m1m2}}{1+\alpha^2}\,\overrightarrow{m_2} \times \overrightarrow{m_1} + \frac{\alpha J_{m1m2}}{1+\alpha^2}\,\overrightarrow{m_2} \times (\overrightarrow{m_2} \times \overrightarrow{m_1}) + \frac{J_{m2m3}}{1+\alpha^2}\,\overrightarrow{m_2} \times \overrightarrow{m_3} + \frac{\alpha J_{m2m3}}{1+\alpha^2}\,\overrightarrow{m_2}$$
$$\times (\overrightarrow{m_2} \times \overrightarrow{m_3}) + \frac{1}{1+\alpha^2}\,\overrightarrow{D_2} \times (\overrightarrow{m_3} + \overrightarrow{m_1}) + \frac{\alpha}{1+\alpha^2}\,\overrightarrow{m_2} \times \left(\overrightarrow{D_2} \times (\overrightarrow{m_3} + \overrightarrow{m_1})\right)$$
$$+ \frac{K_x m_{2x}}{1+\alpha^2}\,(\hat{x} \times \overrightarrow{m_2}) + \frac{\alpha K_x m_{2x}}{1+\alpha^2}\,(\hat{x} - m_{2x}\overrightarrow{m_2}) + \frac{K_z m_{2z}}{1+\alpha^2}\,(\hat{z} \times \overrightarrow{m_2})$$
$$+ \frac{\alpha K_z m_{2z}}{1+\alpha^2}\,(\hat{z} - m_{2z}\overrightarrow{m_2}) + \frac{W_s}{1+\alpha^2}\,\overrightarrow{m_2} \times (\overrightarrow{m_2} \times \vec{p}) - \frac{\alpha W_s}{1+\alpha^2}\,(\overrightarrow{m_2} \times \vec{p})$$
$$+ \frac{W_f}{1+\alpha^2}\,(\overrightarrow{m_2} \times \vec{p}) + \frac{\alpha W_f}{1+\alpha^2}\,\overrightarrow{m_2} \times (\overrightarrow{m_2} \times \vec{p})$$

$$\frac{d\overrightarrow{m_3}}{dt} = \frac{J_{m3m1}}{1+\alpha^2}\,\overrightarrow{m_3} \times \overrightarrow{m_1} + \frac{\alpha J_{m3m1}}{1+\alpha^2}\,\overrightarrow{m_3} \times (\overrightarrow{m_3} \times \overrightarrow{m_1}) + \frac{J_{m2m3}}{1+\alpha^2}\,\overrightarrow{m_3} \times \overrightarrow{m_2} + \frac{\alpha J_{m2m3}}{1+\alpha^2}\,\overrightarrow{m_3}$$
$$\times (\overrightarrow{m_3} \times \overrightarrow{m_2}) + \frac{1}{1+\alpha^2}\,(\overrightarrow{m_1} + \overrightarrow{m_2}) \times \overrightarrow{D_3} + \frac{\alpha}{1+\alpha^2}\,\overrightarrow{m_3}$$
$$\times \left((\overrightarrow{m_1} + \overrightarrow{m_2}) \times \overrightarrow{D_3}\right) + \frac{K_x m_{3x}}{1+\alpha^2}\,(\hat{x} \times \overrightarrow{m_3}) + \frac{\alpha K_x m_{3x}}{1+\alpha^2}\,(\hat{x} - m_{3x}\overrightarrow{m_3})$$
$$+ \frac{K_z m_{3z}}{1+\alpha^2}\,\hat{z} \times \overrightarrow{m_3} + \frac{\alpha K_z m_{3z}}{1+\alpha^2}\,(\hat{z} - m_{3z}\overrightarrow{m_3}) + \frac{W_s}{1+\alpha^2}\,\overrightarrow{m_3} \times (\overrightarrow{m_3} \times \vec{p})$$
$$- \frac{\alpha W_s}{1+\alpha^2}\,(\overrightarrow{m_3} \times \vec{p}) + \frac{W_f}{1+\alpha^2}\,(\overrightarrow{m_3} \times \vec{p}) + \frac{\alpha W_f}{1+\alpha^2}\,\overrightarrow{m_3} \times (\overrightarrow{m_3} \times \vec{p})$$

GIG has one strong antiferromagnet coupling and two weaker ferromagnet coupling in a sub-lattice as shown in the main article. The resultant magnetic moment oscillation frequency in complex ferrimagnet is therefore lower than that of antiferromagnet.

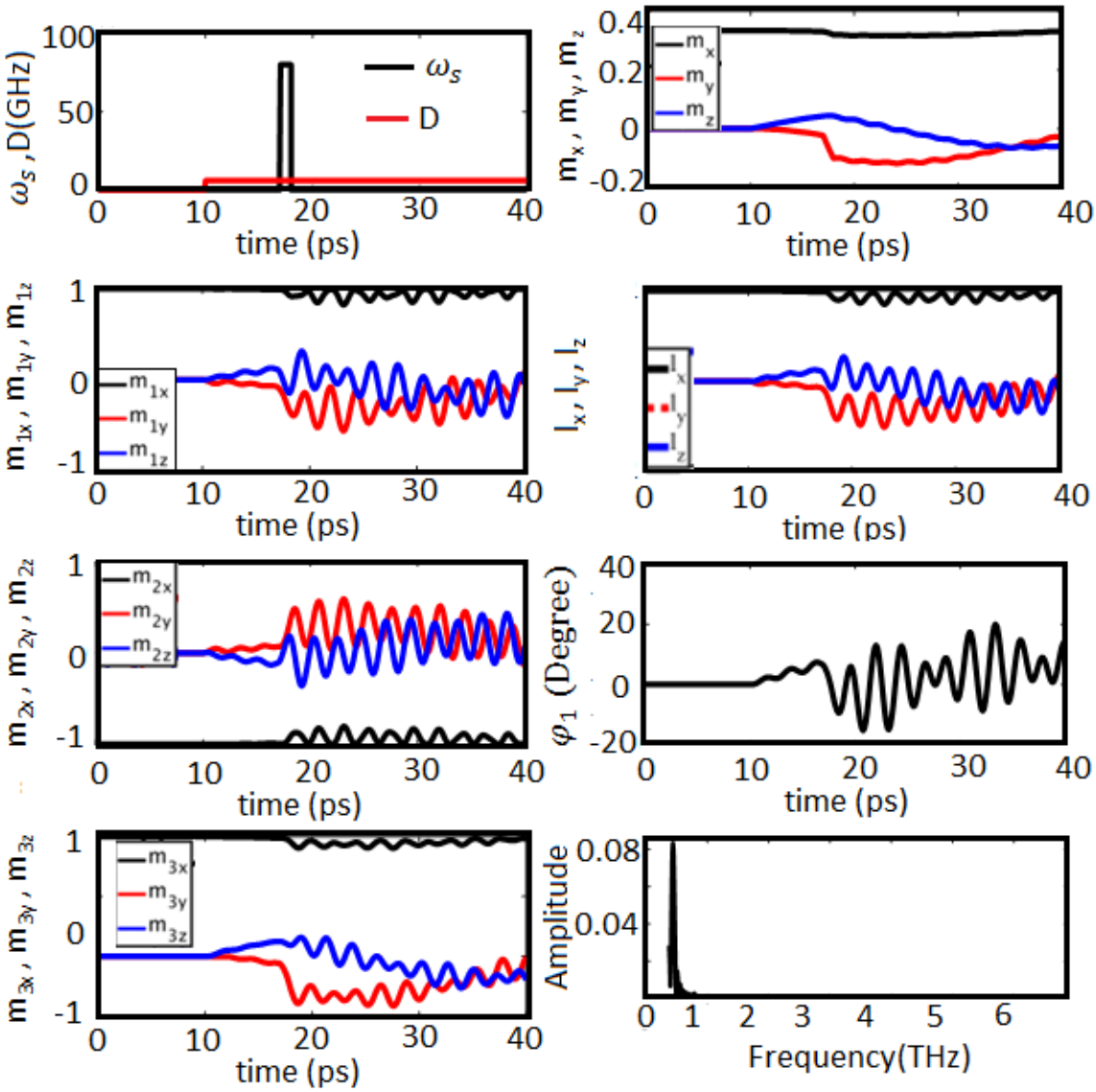

Fig. D.1 : Micromagnetic simulation results for antiferromagnet Gadolinium Iron Garnett (GIG) in sigma mode. Simulation parameters are taken from ref [79] (J_{m1m2} = 5.9941 THz, J_{m2m3} = 1.197 THz, J_{m3m1} = 2.3939 THz, DMI_1 = 0.01* $J_{m1m2,}$ DMI_2 = 0.01* $J_{m2m3,}$ DMI_3 = 0.01* $J_{m3m1,}$ W_s = 80GHz, K_x = 49.383 GHz, $\alpha = 0$, K_z = 0 and W_f = 0).

Close inspection of the oscillation patterns confirms our claim that although the spin current density is bigger than DMI, it has little influence on the oscillation frequency. Rather introduction of spin polarized current increases the oscillation amplitude. Also, the oscillation frequency (4.425 x 10^{11} Hz) is lower than that of AFM because of smaller exchange coupling and DMI but higher than FM.

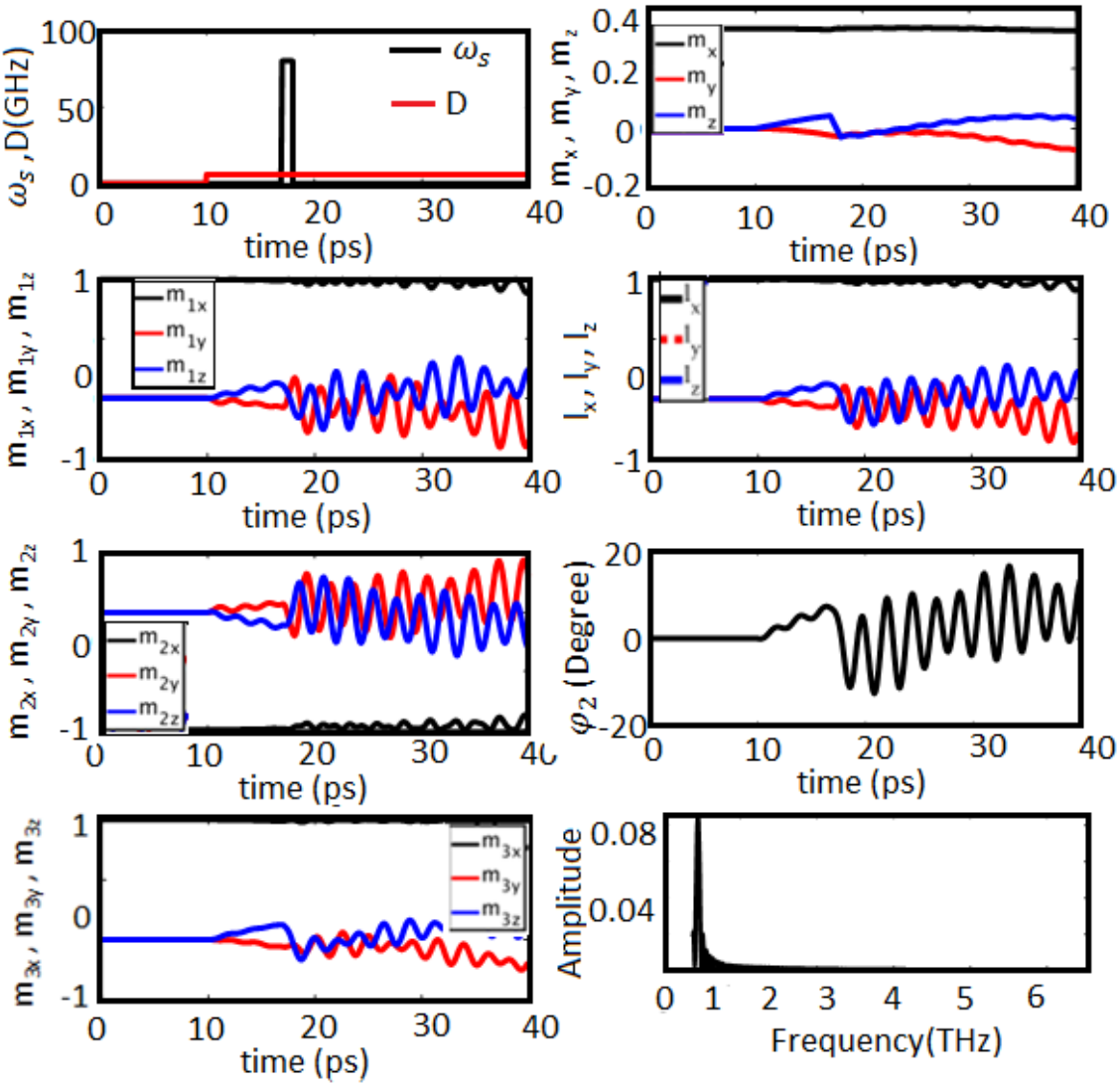

Fig. D.2: Micromagnetic simulation results for antiferromagnet Gadolinium Iron Garnett (GIG) in gamma mode. Simulation parameters are same as figure 5. The oscillation frequency is 4.5 x 10^{11} Hz.

APPENDIX E. DERIVATION OF PAULI SPIN MATRICES FOR 3 SPIN SYSTEM

An electron spin can be in two states – up-spin and downspin. In a three spin system, there can be total eight spin combinations. Therefore, there can be total eight Eigen-states in three spin system. We can denoting the up-spin states of first, second and third electrons by α_1, α_2 and α_3 and downspin states of first, second and third electrons by β_1, β_2 and β_3 respectively. The possible spin states can be defined as,

Electron 1	Electron 2	Electron 3	Denoted as
1/2	1/2	1/2	$\alpha_1\alpha_2\alpha_3$
1/2	1/2	-1/2	$\alpha_1\alpha_2\beta_3$
1/2	-1/2	1/2	$\alpha_1\beta_2\alpha_3$
-1/2	1/2	1/2	$\beta_1\alpha_2\alpha_3$
1/2	-1/2	-1/2	$\alpha_1\beta_2\beta_3$
-1/2	1/2	-1/2	$\beta_1\alpha_2\beta_3$
-1/2	-1/2	1/2	$\beta_1\beta_2\alpha_3$
-1/2	-1/2	-1/2	$\beta_1\beta_2\beta_3$

The Eigen-states for three spin systems can be defined as,

$$\alpha_1\alpha_2\alpha_3 = \begin{bmatrix}1\\0\\0\\0\\0\\0\\0\\0\end{bmatrix}, \alpha_1\alpha_2\beta_3 = \begin{bmatrix}0\\1\\0\\0\\0\\0\\0\\0\end{bmatrix}, \alpha_1\beta_2\alpha_3 = \begin{bmatrix}0\\0\\1\\0\\0\\0\\0\\0\end{bmatrix}, \beta_1\alpha_2\alpha_3 = \begin{bmatrix}0\\0\\0\\1\\0\\0\\0\\0\end{bmatrix},$$

$$\alpha_1\beta_2\beta_3 = \begin{bmatrix}0\\0\\0\\0\\1\\0\\0\\0\end{bmatrix}, \beta_1\alpha_2\beta_3 = \begin{bmatrix}0\\0\\0\\0\\0\\1\\0\\0\end{bmatrix},$$

$$\beta_1\beta_2\alpha_3 = \begin{bmatrix}0\\0\\0\\0\\0\\0\\1\\0\end{bmatrix}, \beta_1\beta_2\beta_3 = \begin{bmatrix}0\\0\\0\\0\\0\\0\\0\\1\end{bmatrix}$$

These vectors are the unit vector in the space of interest. If the spins of three electrons is denoted as $\overrightarrow{\sigma_1}, \overrightarrow{\sigma_2}\ and\ \overrightarrow{\sigma_3}$, the overall spin of the system can be written as,

$$\vec{\Sigma} = (\overrightarrow{\sigma_1} + \overrightarrow{\sigma_2}) + \overrightarrow{\sigma_3} \qquad \text{(E.1)}$$

The overall spin system can have x, y and z component which can be denoted as $\Sigma_x,\ \Sigma_y\ and\ \Sigma_z$. In other word, these three components are the Pauli spin matrices in three electron system. If we can determine the effect of these Pauli spin matrices on the eigenvectors, we can calculate these matrices.

Let us first consider the effect of Σ_x on the eigenvector $\alpha_1\alpha_2\alpha_3$.

$$\Sigma_x\alpha_1\alpha_2\alpha_3 = \Sigma_x \begin{bmatrix}1\\0\\0\\0\\0\\0\\0\\0\end{bmatrix} \qquad \text{(E.2)}$$

Again Σ_x can be denoted from equation (E.1) as,

$$\Sigma_x = (\sigma_{1x} + \sigma_{2x}) + \sigma_{3x}$$

Therefore, $\Sigma_x\alpha_1\alpha_2\alpha_3$ can be modified as,

$$\Sigma_x\alpha_1\alpha_2\alpha_3 = [(\sigma_{1x} + \sigma_{2x}) + \sigma_{3x}]\alpha_1\alpha_2\alpha_3 = \alpha_3\ (\sigma_{1x} + \sigma_{2x})\alpha_1\alpha_2 + \alpha_1\alpha_2\sigma_{3x}\alpha_3$$

Rearranging the terms using the basic properties of spin matrices we get,

$$\Sigma_x\alpha_1\alpha_2\alpha_3 = \alpha_2\alpha_3\sigma_{1x}\alpha_1 + \alpha_1\alpha_3\sigma_{2x}\alpha_2 + \alpha_1\alpha_2\sigma_{3x}\alpha_3 \qquad \text{(E.3)}$$

From the one spin Pauli spin matrix system, if we consider the eigenvectors as $\alpha = \begin{bmatrix}1\\0\end{bmatrix}$ and $\beta = \begin{bmatrix}0\\1\end{bmatrix}$ and the Pauli spin matrices as, $\sigma_x = \begin{bmatrix}0 & 1\\1 & 0\end{bmatrix}$, $\sigma_y = \begin{bmatrix}0 & -i\\i & 0\end{bmatrix}$ and $\sigma_z = \begin{bmatrix}1 & 0\\0 & -1\end{bmatrix}$, then the following operations yield,

$$\sigma_x\alpha = \begin{bmatrix}0 & 1\\1 & 0\end{bmatrix}\begin{bmatrix}1\\0\end{bmatrix} = \begin{bmatrix}0\\1\end{bmatrix} = \beta$$

$$\sigma_y\alpha = \begin{bmatrix}0 & -i\\i & 0\end{bmatrix}\begin{bmatrix}1\\0\end{bmatrix} = \begin{bmatrix}0\\i\end{bmatrix} = i\beta$$

$$\sigma_z\alpha = \begin{bmatrix}1 & 0\\ 0 & -1\end{bmatrix}\begin{bmatrix}1\\0\end{bmatrix} = \begin{bmatrix}1\\0\end{bmatrix} = \alpha$$

$$\sigma_x\beta = \begin{bmatrix}0 & 1\\ 1 & 0\end{bmatrix}\begin{bmatrix}0\\1\end{bmatrix} = \begin{bmatrix}1\\0\end{bmatrix} = \alpha$$

$$\sigma_y\beta = \begin{bmatrix}0 & -i\\ i & 0\end{bmatrix}\begin{bmatrix}0\\1\end{bmatrix} = \begin{bmatrix}-i\\0\end{bmatrix} = -i\alpha$$

$$\sigma_z\beta = \begin{bmatrix}1 & 0\\ 0 & -1\end{bmatrix}\begin{bmatrix}0\\1\end{bmatrix} = \begin{bmatrix}0\\-1\end{bmatrix} = -\beta$$

In equation (E.3), we can write $\sigma_{1x}\alpha_1 = \beta_1$, $\sigma_{2x}\alpha_2 = \beta_2$ and $\sigma_{3x}\alpha_3 = \beta_3$ and therefore, equation E.3 can be rewritten as,

$$\Sigma_x\alpha_1\alpha_2\alpha_3 = \beta_1\alpha_2\alpha_3 + \alpha_1\beta_2\alpha_3 + \alpha_1\alpha_2\beta_3$$

We can also write this equation as the summation of eigenvector 1D matrices as,

$$\Sigma_x\alpha_1\alpha_2\alpha_3 = \begin{bmatrix}0\\0\\0\\1\\0\\0\\0\\0\end{bmatrix} + \begin{bmatrix}0\\0\\1\\0\\0\\0\\0\\0\end{bmatrix} + \begin{bmatrix}0\\1\\0\\0\\0\\0\\0\\0\end{bmatrix}$$

Therefore the first row and column of x component of Pauli spin matrices can be written as,

$$\Sigma_x = \begin{bmatrix}0 & 1 & 1 & 1 & 0 & 0 & 0 & 0\\ 1 & ? & ? & ? & ? & ? & ? & ?\\ 1 & ? & ? & ? & ? & ? & ? & ?\\ 1 & ? & ? & ? & ? & ? & ? & ?\\ 0 & ? & ? & ? & ? & ? & ? & ?\\ 0 & ? & ? & ? & ? & ? & ? & ?\\ 0 & ? & ? & ? & ? & ? & ? & ?\\ 0 & ? & ? & ? & ? & ? & ? & ?\end{bmatrix}$$

Now let us consider the effect of Σ_x on the eigenvector $\alpha_1\alpha_2\beta_3$.

$$\Sigma_x\alpha_1\alpha_2\beta_3 = \Sigma_x\begin{bmatrix}0\\1\\0\\0\\0\\0\\0\\0\end{bmatrix} \qquad \text{(E.4)}$$

$\Sigma_x\alpha_1\alpha_2\beta_3$ can be modified as,

$$\Sigma_x\alpha_1\alpha_2\beta_3 = [(\sigma_{1x} + \sigma_{2x}) + \sigma_{3x}]\alpha_1\alpha_2\beta_3 = \beta_3\,(\sigma_{1x} + \sigma_{2x})\alpha_1\alpha_2 + \alpha_1\alpha_2\sigma_{3x}\beta_3$$

Rearranging the terms using the basic properties of spin matrices we get,

$$\Sigma_x\alpha_1\alpha_2\beta_3 = \alpha_2\beta_3\sigma_{1x}\alpha_1 + \alpha_1\beta_3\sigma_{2x}\alpha_2 + \alpha_1\alpha_2\sigma_{3x}\beta_3 = \beta_1\alpha_2\beta_3 + \alpha_1\beta_2\beta_3 + \alpha_1\alpha_2\alpha_3$$

(E.5)

We can also write this equation as the summation of eigenvector 1D matrices as,

$$\Sigma_x\alpha_1\alpha_2\alpha_3 = \begin{bmatrix}0\\0\\0\\0\\0\\1\\0\\0\end{bmatrix} + \begin{bmatrix}0\\0\\0\\0\\1\\0\\0\\0\end{bmatrix} + \begin{bmatrix}1\\0\\0\\0\\0\\0\\0\\0\end{bmatrix}$$

Therefore the x component of Pauli spin matrices can be updated as,

$$\Sigma_x = \begin{bmatrix}0 & 1 & 1 & 1 & 0 & 0 & 0 & 0\\ 1 & 0 & 0 & 0 & 1 & 1 & 0 & 0\\ 1 & 0 & ? & ? & ? & ? & ? & ?\\ 1 & 0 & ? & ? & ? & ? & ? & ?\\ 0 & 1 & ? & ? & ? & ? & ? & ?\\ 0 & 1 & ? & ? & ? & ? & ? & ?\\ 0 & 0 & ? & ? & ? & ? & ? & ?\\ 0 & 0 & ? & ? & ? & ? & ? & ?\end{bmatrix}$$

Now let us consider the effect of Σ_x on the eigenvector $\alpha_1\beta_2\alpha_3$.

$$\Sigma_x\alpha_1\beta_2\alpha_3 = \Sigma_x\begin{bmatrix}0\\0\\1\\0\\0\\0\\0\\0\end{bmatrix} \qquad \text{(E.6)}$$

$\Sigma_x\alpha_1\beta_2\alpha_3$ can be modified as,

$$\Sigma_x\alpha_1\beta_2\alpha_3 = [(\sigma_{1x} + \sigma_{2x}) + \sigma_{3x}]\alpha_1\beta_2\alpha_3 = \alpha_3\,(\sigma_{1x} + \sigma_{2x})\alpha_1\beta_2 + \alpha_1\beta_2\sigma_{3x}\alpha_3$$

Rearranging the terms using the basic properties of spin matrices we get,

$$\Sigma_x\alpha_1\beta_2\alpha_3 = \alpha_3\beta_2\sigma_{1x}\alpha_1 + \alpha_3\alpha_1\sigma_{2x}\beta_2 + \alpha_1\beta_2\sigma_{3x}\alpha_3 = \beta_1\beta_2\alpha_3 + \alpha_1\alpha_2\alpha_3 + \alpha_1\beta_2\beta_3$$

(E.7)

We can also write this equation as the summation of eigenvector 1D matrices as,

$$\Sigma_x\alpha_1\alpha_2\alpha_3 = \begin{bmatrix}0\\0\\0\\0\\1\\0\\0\\0\end{bmatrix} + \begin{bmatrix}0\\0\\0\\0\\0\\0\\1\\0\end{bmatrix} + \begin{bmatrix}1\\0\\0\\0\\0\\0\\0\\0\end{bmatrix}$$

Therefore the x component of Pauli spin matrices can be updated as,

$$\Sigma_x = \begin{bmatrix}0 & 1 & 1 & 1 & 0 & 0 & 0 & 0\\ 1 & 0 & 0 & 0 & 1 & 1 & 0 & 0\\ 1 & 0 & 0 & 0 & 1 & 0 & 1 & 0\\ 1 & 0 & 0 & ? & ? & ? & ? & ?\\ 0 & 1 & 1 & ? & ? & ? & ? & ?\\ 0 & 1 & 0 & ? & ? & ? & ? & ?\\ 0 & 0 & 1 & ? & ? & ? & ? & ?\\ 0 & 0 & 0 & ? & ? & ? & ? & ?\end{bmatrix}$$

Now let us consider the effect of Σ_x on the eigenvector $\beta_1\alpha_2\alpha_3$.

$$\Sigma_x\beta_1\alpha_2\alpha_3 = \Sigma_x \begin{bmatrix}0\\0\\0\\1\\0\\0\\0\\0\end{bmatrix} \qquad \text{(E.8)}$$

$\Sigma_x\beta_1\alpha_2\alpha_3$ can be modified as,

$$\Sigma_x\beta_1\alpha_2\alpha_3 = [(\sigma_{1x} + \sigma_{2x}) + \sigma_{3x}]\beta_1\alpha_2\alpha_3 = \alpha_3\,(\sigma_{1x} + \sigma_{2x})\beta_1\alpha_2 + \beta_1\alpha_2\sigma_{3x}\alpha_3$$

Rearranging the terms using the basic properties of spin matrices we get,

$$\Sigma_x\beta_1\alpha_2\alpha_3 = \alpha_3\alpha_2\sigma_{1x}\beta_1 + \alpha_3\beta_1\sigma_{2x}\alpha_2 + \beta_1\alpha_2\sigma_{3x}\alpha_3 = \alpha_1\alpha_2\alpha_3 + \beta_1\beta_2\alpha_3 + \beta_1\alpha_2\beta_3 \qquad \text{(E.9)}$$

We can also write this equation as the summation of eigenvector 1D matrices as

$$\Sigma_x\alpha_1\alpha_2\alpha_3 = \begin{bmatrix}0\\0\\0\\0\\1\\0\\0\\0\end{bmatrix} + \begin{bmatrix}0\\0\\0\\0\\0\\0\\1\\0\end{bmatrix} + \begin{bmatrix}1\\0\\0\\0\\0\\0\\0\\0\end{bmatrix}$$

Therefore the x component of Pauli spin matrices can be updated as,

$$\Sigma_x = \begin{bmatrix} 0 & 1 & 1 & 1 & 0 & 0 & 0 & 0 \\ 1 & 0 & 0 & 0 & 1 & 1 & 0 & 0 \\ 1 & 0 & 0 & 0 & 1 & 0 & 1 & 0 \\ 1 & 0 & 0 & 0 & 0 & 1 & 1 & 0 \\ 0 & 1 & 1 & 0 & ? & ? & ? & ? \\ 0 & 1 & 0 & 1 & ? & ? & ? & ? \\ 0 & 0 & 1 & 1 & ? & ? & ? & ? \\ 0 & 0 & 0 & 0 & ? & ? & ? & ? \end{bmatrix}$$

Now let us consider the effect of Σ_x on the eigenvector $\alpha_1\beta_2\beta_3$.

$$\Sigma_x\alpha_1\beta_2\beta_3 = \Sigma_x \begin{bmatrix} 0 \\ 0 \\ 0 \\ 0 \\ 1 \\ 0 \\ 0 \\ 0 \end{bmatrix} \qquad \text{(E.10)}$$

$\Sigma_x\alpha_1\beta_2\beta_3$ can be modified as,

$$\Sigma_x\alpha_1\beta_2\beta_3 = [(\sigma_{1x} + \sigma_{2x}) + \sigma_{3x}]\alpha_1\beta_2\beta_3 = \beta_3\,(\sigma_{1x} + \sigma_{2x})\alpha_1\beta_2 + \alpha_1\beta_2\sigma_{3x}\beta_3$$

Rearranging the terms using the basic properties of spin matrices we get,

$$\Sigma_x\alpha_1\beta_2\beta_3 = \beta_2\beta_3\sigma_{1x}\alpha_1 + \alpha_1\beta_2\sigma_{2x}\beta_2 + \alpha_1\beta_2\sigma_{3x}\beta_3 = \beta_1\beta_2\beta_3 + \alpha_1\alpha_2\beta_3 + \alpha_1\beta_2\alpha_3 \qquad \text{(E.11)}$$

We can also write this equation as the summation of eigenvector 1D matrices as,

$$\Sigma_x\alpha_1\alpha_2\alpha_3 = \begin{bmatrix} 0 \\ 0 \\ 0 \\ 0 \\ 0 \\ 0 \\ 0 \\ 1 \end{bmatrix} + \begin{bmatrix} 0 \\ 1 \\ 0 \\ 0 \\ 0 \\ 0 \\ 0 \\ 0 \end{bmatrix} + \begin{bmatrix} 0 \\ 0 \\ 1 \\ 0 \\ 0 \\ 0 \\ 0 \\ 0 \end{bmatrix}$$

Therefore the x component of Pauli spin matrices can be updated as,

$$\Sigma_x = \begin{bmatrix} 0 & 1 & 1 & 1 & 0 & 0 & 0 & 0 \\ 1 & 0 & 0 & 0 & 1 & 1 & 0 & 0 \\ 1 & 0 & 0 & 0 & 1 & 0 & 1 & 0 \\ 1 & 0 & 0 & 0 & 0 & 1 & 1 & 0 \\ 0 & 1 & 1 & 0 & 0 & 0 & 0 & 1 \\ 0 & 1 & 0 & 1 & 0 & ? & ? & ? \\ 0 & 0 & 1 & 1 & 0 & ? & ? & ? \\ 0 & 0 & 0 & 0 & 1 & ? & ? & ? \end{bmatrix}$$

Now let us consider the effect of Σ_x on the eigenvector $\beta_1\alpha_2\beta_3$.

$$\Sigma_x \beta_1 \alpha_2 \beta_3 = \Sigma_x \begin{bmatrix} 0 \\ 0 \\ 0 \\ 0 \\ 1 \\ 0 \\ 0 \\ 0 \end{bmatrix} \quad \text{(E.12)}$$

$\Sigma_x \beta_1 \alpha_2 \beta_3$ can be modified as,

$$\Sigma_x \beta_1 \alpha_2 \beta_3 = [(\sigma_{1x} + \sigma_{2x}) + \sigma_{3x}] \beta_1 \alpha_2 \beta_3 = \beta_3 \, (\sigma_{1x} + \sigma_{2x}) \beta_1 \alpha_2 + \beta_1 \alpha_2 \sigma_{3x} \beta_3$$

Rearranging the terms using the basic properties of spin matrices we get,

$$\Sigma_x \beta_1 \alpha_2 \beta_3 = \alpha_2 \beta_3 \sigma_{1x} \beta_1 + \beta_1 \beta_3 \sigma_{2x} \alpha_2 + \beta_1 \alpha_2 \sigma_{3x} \beta_3 = \alpha_1 \alpha_2 \beta_3 + \beta_1 \beta_2 \beta_3 + \beta_1 \alpha_2 \alpha_3 \quad \text{(E.13)}$$

We can also write this equation as the summation of eigenvector 1D matrices as,

$$\Sigma_x \alpha_1 \alpha_2 \alpha_3 = \begin{bmatrix} 0 \\ 1 \\ 0 \\ 0 \\ 0 \\ 0 \\ 0 \\ 0 \end{bmatrix} + \begin{bmatrix} 0 \\ 0 \\ 0 \\ 1 \\ 0 \\ 0 \\ 0 \\ 0 \end{bmatrix} + \begin{bmatrix} 0 \\ 0 \\ 0 \\ 0 \\ 0 \\ 0 \\ 0 \\ 1 \end{bmatrix}$$

Therefore the x component of Pauli spin matrices can be updated as,

$$\Sigma_x = \begin{bmatrix} 0 & 1 & 1 & 1 & 0 & 0 & 0 & 0 \\ 1 & 0 & 0 & 0 & 1 & 1 & 0 & 0 \\ 1 & 0 & 0 & 0 & 1 & 0 & 1 & 0 \\ 1 & 0 & 0 & 0 & 0 & 1 & 1 & 0 \\ 0 & 1 & 1 & 0 & 0 & 0 & 0 & 1 \\ 0 & 1 & 0 & 1 & 0 & 0 & 0 & 1 \\ 0 & 0 & 1 & 1 & 0 & 0 & ? & ? \\ 0 & 0 & 0 & 0 & 1 & 1 & ? & ? \end{bmatrix}$$

Now let us consider the effect of Σ_x on the eigenvector $\beta_1 \beta_2 \alpha_3$,

$$\Sigma_x \beta_1 \beta_2 \alpha_3 = \Sigma_x \begin{bmatrix} 0 \\ 0 \\ 0 \\ 0 \\ 1 \\ 0 \\ 0 \\ 0 \end{bmatrix} \quad \text{(E.14)}$$

$\Sigma_x \beta_1 \beta_2 \alpha_3$ can be modified as,

$$\Sigma_x \beta_1 \beta_2 \alpha_3 = [(\sigma_{1x} + \sigma_{2x}) + \sigma_{3x}] \beta_1 \beta_2 \alpha_3 = \alpha_3 \, (\sigma_{1x} + \sigma_{2x}) \beta_1 \beta_2 + \beta_1 \beta_2 \sigma_{3x} \alpha_3$$

Rearranging the terms using the basic properties of spin matrices we get,

$$\Sigma_x\beta_1\alpha_2\beta_3 = \beta_2\alpha_3\sigma_{1x}\beta_1 + \beta_1\alpha_3\sigma_{2x}\beta_2 + \beta_1\beta_2\sigma_{3x}\alpha_3 = \alpha_1\beta_2\alpha_3 + \beta_1\beta_2\beta_3 + \beta_1\alpha_2\alpha_3 \quad \text{(E.15)}$$

We can also write this equation as the summation of eigenvector 1D matrices as,

$$\Sigma_x\alpha_1\alpha_2\alpha_3 = \begin{bmatrix}0\\0\\1\\0\\0\\0\\0\\0\end{bmatrix} + \begin{bmatrix}0\\0\\0\\1\\0\\0\\0\\0\end{bmatrix} + \begin{bmatrix}0\\0\\0\\0\\0\\0\\0\\1\end{bmatrix}$$

Therefore the x component of Pauli spin matrices can be updated as,

$$\Sigma_x = \begin{bmatrix}0&1&1&1&0&0&0&0\\1&0&0&0&1&1&0&0\\1&0&0&0&1&0&1&0\\1&0&0&0&0&1&1&0\\0&1&1&0&0&0&0&1\\0&1&0&1&0&0&0&1\\0&0&1&1&0&0&0&1\\0&0&0&0&1&1&1&?\end{bmatrix}$$

Finally, let us consider the effect of Σ_x on the eigenvector $\beta_1\beta_2\beta_3$

$$\Sigma_x\beta_1\beta_2\beta_3 = \Sigma_x\begin{bmatrix}0\\0\\0\\0\\1\\0\\0\\0\end{bmatrix} \quad \text{(E.16)}$$

$\Sigma_x\beta_1\beta_2\beta_3$ can be modified as,

$$\Sigma_x\beta_1\beta_2\beta_3 = [(\sigma_{1x} + \sigma_{2x}) + \sigma_{3x}]\beta_1\beta_2\beta_3 = \beta_3\,(\sigma_{1x} + \sigma_{2x})\beta_1\beta_2 + \beta_1\beta_2\sigma_{3x}\beta_3$$

Rearranging the terms using the basic properties of spin matrices we get,

$$\Sigma_x\beta_1\beta_2\beta_3 = \beta_2\beta_3\sigma_{1x}\beta_1 + \beta_1\beta_3\sigma_{2x}\beta_2 + \beta_1\beta_2\sigma_{3x}\beta_3 = \alpha_1\beta_2\beta_3 + \beta_1\alpha_2\beta_3 + \beta_1\beta_2\alpha_3 \quad \text{(E.17)}$$

We can also write this equation as the summation of eigenvector 1D matrices as,

$$\Sigma_x \alpha_1 \alpha_2 \alpha_3 = \begin{bmatrix} 0 \\ 0 \\ 0 \\ 0 \\ 1 \\ 0 \\ 0 \\ 0 \end{bmatrix} + \begin{bmatrix} 0 \\ 0 \\ 0 \\ 0 \\ 0 \\ 1 \\ 0 \\ 0 \end{bmatrix} + \begin{bmatrix} 0 \\ 0 \\ 0 \\ 0 \\ 0 \\ 0 \\ 1 \\ 0 \end{bmatrix}$$

Therefore the x component of Pauli spin matrices can be updated as,

$$\Sigma_x = \begin{bmatrix} 0 & 1 & 1 & 1 & 0 & 0 & 0 & 0 \\ 1 & 0 & 0 & 0 & 1 & 1 & 0 & 0 \\ 1 & 0 & 0 & 0 & 1 & 0 & 1 & 0 \\ 1 & 0 & 0 & 0 & 0 & 1 & 1 & 0 \\ 0 & 1 & 1 & 0 & 0 & 0 & 0 & 1 \\ 0 & 1 & 0 & 1 & 0 & 0 & 0 & 1 \\ 0 & 0 & 1 & 1 & 0 & 0 & 0 & 1 \\ 0 & 0 & 0 & 0 & 1 & 1 & 1 & 0 \end{bmatrix}$$

Similarly, we can show that,

$$\Sigma_y = \begin{bmatrix} 0 & -i & -i & -i & 0 & 0 & 0 & 0 \\ i & 0 & 0 & 0 & -i & -i & 0 & 0 \\ i & 0 & 0 & 0 & -i & 0 & -i & 0 \\ i & 0 & 0 & 0 & 0 & -i & -i & 0 \\ 0 & i & i & 0 & 0 & 0 & 0 & -i \\ 0 & i & 0 & i & 0 & 0 & 0 & -i \\ 0 & 0 & i & i & 0 & 0 & 0 & -i \\ 0 & 0 & 0 & 0 & i & i & i & 0 \end{bmatrix} \text{ and } \Sigma_z = \begin{bmatrix} 3 & 0 & 0 & 0 & 0 & 0 & 0 & 0 \\ 0 & 1 & 0 & 0 & 0 & 0 & 0 & 0 \\ 0 & 0 & 1 & 0 & 0 & 0 & 0 & 0 \\ 0 & 0 & 0 & 1 & 0 & 0 & 0 & 0 \\ 0 & 0 & 0 & 0 & -1 & 0 & 0 & 0 \\ 0 & 0 & 0 & 0 & 0 & -1 & 0 & 0 \\ 0 & 0 & 0 & 0 & 0 & 0 & -1 & 0 \\ 0 & 0 & 0 & 0 & 0 & 0 & 0 & -3 \end{bmatrix}$$

APPENDIX F. ELABORATED FIGURE OF COTB FREE LAYER SWITCHING CHARACTERISTICS

In figure F.1, a 10 ps pulse of 8.89×10^8 A/cm^2 current is applied. As a result, the magnetization direction of CoTb is switched. Initially the resultant magnetization was along +x axis. After the application of current pulse the magnetization is switched to –x axis as shown by the magnetization dynamics of staggered magnetization, represented by the red curve in second figure). Figure F.1 shows the angle φ_1, which measures the x component orientation of the staggered magnetization, defined as,

$$\varphi_1 = \cos^{-1} \frac{l_x}{\sqrt{l_x^2 + l_y^2 + l_z^2}}$$

Considering 99% deviation from the initial state as newly switched state, it can be calculated from the figure of φ_1 that the switching is completed after 23ps.

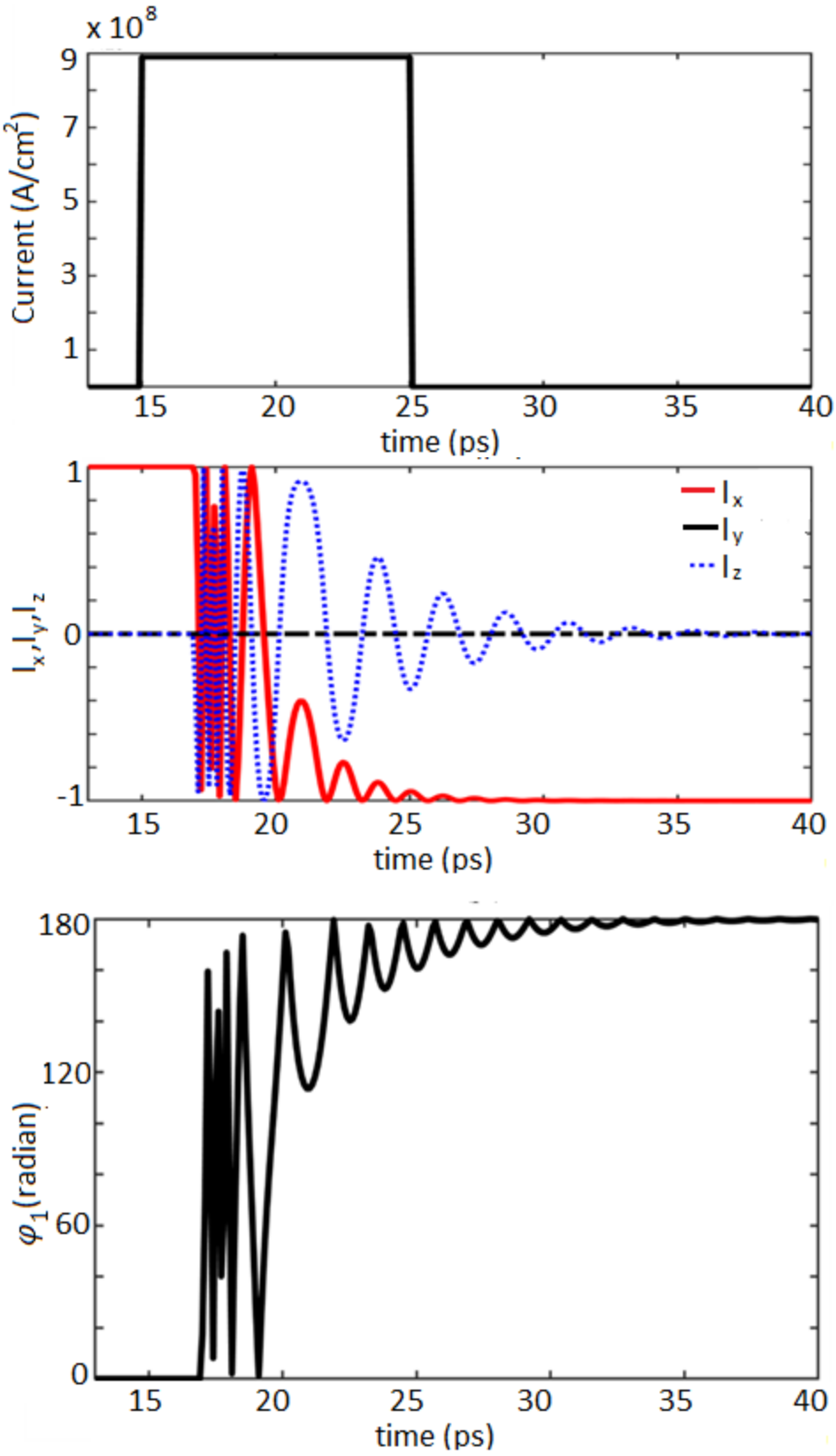

Fig. F.1 : Elaborated figure showing the switching of CoTb free layer due to the injection of spin polarized current.

REFERENCES

[1] J. M. Rabaey, A. P. Chandrakasan, and B. Nikolic, Digital integrated circuits: a design perspective. Pearson Education, 2003.

[2] S. Borkar and A. A. Chien, “The future of microprocessors,” Communications of the ACM, vol. 54, no. 5, p. 67, May 2017.

[3] N. A. Kurd, S. Bhamidipati, C. Mozak, J. L. Miller, P.Mosalikanti, T.M.Wilson, A. M. El-Husseini, M. Neidengard, R. E. Aly, M. Nemani, M. Chowdhury, and R. Kumar, “A Family of 32 nm IA Processors,” IEEE Journal of Solid-State Circuits, vol. 46, no. 1, pp. 119–130, Jan. 2011.

[4] R. J. Riedlinger, R. Bhatia, L. Biro, B. Bowhill, E. Fetzer, P. Gronowski, and T. Grutkowski, “A 32nm 3.1 billion transistor 12-wide-issue Itanium processor for mission-critical servers,” in 2011 IEEE International Solid-State Circuits Conference. IEEE,Feb.2011,pp.84–86.

[5] T. Fischer, S. Arekapudi, E. Busta, C. Dietz, M. Golden, S. Hilker, A. Horiuchi, K. A. Hurd, D. Johnson, H. McIntyre, S. Naffziger, J. Vinh, J. White, and K.Wilcox, “Design solutions for the Bulldozer 32nm SOI 2-core processor module in an 8-core CPU,” in 2011 IEEE International Solid-State Circuits Conference. IEEE, Feb. 2011, pp. 78–80.

[6] S. Narenda, L. C. Fujino, and K. C. Smith, “Through the Looking Glass Continued (III): Update to Trends in Solid-State Circuits and Systems from ISSCC 2014 [ISSCC Trends],” IEEE Solid-State Circuits Magazine, vol. 6, no. 1, pp. 49–53, 2014.

[7] P. C. Chetan and P. K. Dahiya, "Different leakage power reduction techniques in SRAM Circuits: A State-of-the-art Review", International Research Journal of Engineering and Technology, vol. 04, issue 07, July, 2017.

[8] 2011. [Online]. Available: http://www.isscc.org/doc/2011/2011\ Trends.pdf

[9] K. C. Smith, A. Wang, and L. C. Fujino, “Through the Looking Glass Part 2 of 2: Trend Tracking for ISSCC 2013 [ISSCC Trends],” IEEE Solid-State Circuits Magazine, vol. 5, no. 2, pp. 33–43, Jan. 2013.

[10] R. Keller, D. Kramer, and J.-P. Weiss, Facing the multicore-challenge: aspects of new paradigms and technologies in parallel computing. NewYork,NY,USA: Springer, 2010.

[11] 2010. [Online]. Available: http://www.itrs.net/Links/2010ITRS/2010Update/ ToPost/ERD\ ERM\ 2010FINALReportMemoryAssessment\ ITRS.pdf

[12] Y. Huai, “Spin-transfer torque MRAM (STT-MRAM): challenges and prospects,” AAPPS Bulletin, vol. 18, no. 6, pp. 33–40, 2008.

[13] Staff, bit-tech. Intel Sandy Bridge Review. bit-tech at <http://www.bit-tech.net/hardware/cpus/2011/01/03/intel-sandy-bridge-review/1>.

[14] Why SSDs Are Awesome: An SSD Primer | Samsung SSD.

[15] Null, L., Null, P. S. U. L. & Lobur, J. The Essentials of Computer Organization and Architecture. (Jones & Bartlett Publishers, 2014).

[16] S. Yuasa, T. Nagahama, A. Fukushima, Y. Suzuki, and K. Ando, “Giant roomtemperature magnetoresistance in single-crystal Fe/MgO/Fe magnetic tunnel junctions.” Nature materials, vol. 3, no. 12, pp. 868–71, Dec. 2004..

[17] D. D. Sayeef Salahuddin and S. Datta, “Spin transfer torque as a nonconservative pseudo-field,” 2008.

[18] Akerman, J. APPLIED PHYSICS: Toward a Universal Memory. Science 308, 508–510 (2005).

[19] Chappert, C., Fert, A. & Van Dau, F. N. The emergence of spin electronics in data storage. Nat. Mater. 6, 813–823 (2007).

[20] Tehrani, S. et al. Progress and outlook for MRAM technology. IEEE Trans. Magn. 35, 2814–2819 (1999).

[21] Park, W., Song, I.-H., Park, S. & Kim, T. Technology of MRAM (Magneto-resistive Random Acces Memory) Using MTJ(Magnetic Tunnel Junction) Cell. J. Semicond. Technol. Sci. 2, (2002).

[22] Slonczewski, J. C. Conductance and exchange coupling of two ferromagnets separated by a tunneling barrier. Phys. Rev. B 39, 6995–7002 (1989).

[23] Ralph, D. C. & Stiles, M. D. Spin transfer torques. J. Magn. Magn. Mater. 320, 1190–1216 (2008).

[24] Slonczewski, J. C. Current-driven excitation of magnetic multilayers. J. Magn. Magn. Mater. 159, L1–L7 (1996).

[25] Berger, L. Emission of spin waves by a magnetic multilayer traversed by a current. Phys. Rev. B 54, 9353–9358 (1996).

[26] Katine, J., Albert, F., Buhrman, R., Myers, E. & Ralph, D. Current-Driven Magnetization Reversal and Spin-Wave Excitations in Co /Cu /Co Pillars. Phys. Rev. Lett. 84, 3149–3152 (2000).

[27] Huai, Y., Albert, F., Nguyen, P., Pakala, M. & Valet, T. Observation of spin-transfer switching in deep submicron-sized and low-resistance magnetic tunnel junctions. Appl. Phys. Lett. 84, 3118–3120 (2004).

[28] Fuchs, G. D. et al. Spin-transfer effects in nanoscale magnetic tunnel junctions. Appl. Phys. Lett. 85, 1205–1207 (2004).

[29] Everspin ships first ST-MRAM memory with 500X performance of flash. Computerworld (2012).

[30] J. H. on O. & Pm, 2014 at 4:32. Everspin teams up with GlobalFoundries to build commercial MRAM. ExtremeTech.

[31] Editorial, "Memory with a spin", Nature Nanotechnology 10, 185 (2015).

[32] Liu, L. et al. "Spin-torque switching with the giant spin Hall effect of tantalum",. Science 336, 555–558 (2012).

[33] Zhao, Prenat (Eds.), "Spintronics-based Computing", Sprin. (2015), p 145

[34] T. Brozek (Ed.), "Micro and Nanoelectronics:Emerging Device Challenges and Solutions", CRC Press (2014), p222-223.

[35] A. R. Mellnik, et al., "Spin-transfer torque generated by a topological insulator," Nature 511, 449 (2014).

[36] Alex Ryckman Mellnik, Ph.D. dissertation, Cornell University, (2015).

[37] Liu C-X, et al., "Model Hamiltonian for topological insulators," Phys. Rev. B 82 045122, (2010).

[38] H. Zhang et al., "Topological insulators in Bi2Se3, Bi2Te3 and Sb2Te3 with a single Dirac cone on the surface," Nat. Phys. 5, 438 (2009).

[39] Edelstein, "Spin polarization of conduction electrons induced by electric current in two-dimensional asymmetric electron systems," S. S. Comm.73, 233–235 (1990).

[40] Fan, et al., "Magnetization switching through giant spin-orbit torque in a magnetically doped topological insulator heterostructure," N. Mat., 13, 699–704 (2014).

[41] S. Hong, et al. "Modeling potentiometric measurements in topological insulators including parallel channels," Phys. Rev. B. 86, 085131 (2012).

[42] Y. Lu and J. Guo, "Quantum simulation of topological insulator based spin transfer torque device," Appl. Phys. Lett., vol. 102, p. 073106, (2013).

[43] P. Yu, M. Cardona, Fundamentals of Semiconductors: Physics and Materials Properties, 3rd ed., (Springer. Section 2.6, 2005) p. 68.

[44] Chang , C . Z . et al., “Growth of quantum well films of topological insulator Bi2Se3 on insulating substrate,” SPIN 1, 21 – 25 (2011).

[45] Li, Y.Y. et al. “Intrinsic Topological Insulator Bi2Te3 Thin Films on Si and Their Thickness Limit”, Adv. Mater. 22, 4002 (2010).

[46] G. Wang, et al., “Atomically Smooth Ultrathin Films of Topological Insulator Sb2Te3,” Nano Res. 3, 874 (2010).

[47] C. L. Kane and E. J. Mele, “Z2 Topological Order and the Quantum Spin Hall Effect,” Phys. Rev. Lett. 95, 146802 (2005).

[48] Rui Yu et al. “Quantized Anomalous Hall Effect in Magnetic Topological Insulators,” Science 329, 61 (2010).

[49] T. Yokoyama, et al. “Theoretical study of the dynamics of magnetization on the topological surface,” Phys. Rev. B 81, 241410 (2010).

[50] Z. Jiang,. et al.,” A comparative transport study of Bi2Se3 and Bi2Se3/yttrium iron garnet”, Appl. Phys. Lett. 104, 222409 (2014).

[51] Sinova,et al.,”Universal Intrinsic Spin Hall Effect”, PRL. 92, 126603

[52] S. Narishige, et al., “Crystal Structure and Magnetic Properties of Permalloy Films Sputtered by Mixed,” IEEE Trans. Magn. 28, 990 (1992).

[53] J.M. Luttinger, “The Effect of a Magnetic Field on Electrons in a Periodic Potential,” Phys. Rev. B 84 (1951) 814.

[54] S. Datta, Quantum Transport, 2nd ed., (Cambridge Uni. Press (2005)).

[55] C. Augustine, et al., “Numerical Analysis of Typical STT-MTJ Stacks for 1T-1R Memory Arrays,” IEEE Tran. on Elec. Dev., Vol. 58, No. 12, (2011).

[56] J.C. Slonczewski, “Current-driven excitation of magnetic multilayers”, Journal of Magnetism and Magnetic Materials, 159 (1996), L1-L7.

[57] A. Manchon, et al.,” Spin transfer torque with spin diffusion in magnetic tunnel junctions”, Phys. Rev. B 86, 060404 (2012).

[58] H. Kurebayashi et al., “An antidamping spin–orbit torque originating from the Berry curvature”, Nat. Nanotechnol. 9, 211 (2014).

[59] D. D. Tang and Y.J. Lee, Magnetic Memory: Fundamentals and Technology, 1st edn., (Cambridge University Press, New York, 2010) p. 109.

[60] Y. Jiang, et al., “Landau Quantization and the Thickness Limit of Topological Insulator Thin Films of Sb2Te3,” P.R.L. 108, 016401 (2012).

[61] A. Vansteenkiste et al., “The design and verification of MuMax3,” AIP Adv. 4, 107133 (2014).

[62] Jinghua Guo (Ed.),“X-Rays in Nanoscience: Spectroscopy, Spectromicroscopy and Scattering Techniques,” (Wiley, New York, 2010) p. 71.

[63] Hertel, R., “Thickness dependence of the magnetization structures of thin permalloy rectangles”, Z. Metallkd. 93, 957–962. (2002).

[64] W. Stoecklein, et al., “Ferromagnetic resonance studies of exchange-biased Permalloy thin films”, Phys. Rev. B 38, 6847(1988)

[65] D. T. Edmonds and R. G. Petersen, “Effective Exchange Constant in Yttrium Iron Garnet”,Phys. Rev. Lett. 2 (1959) 499.

[66] C. Hahn, et al., “Comparative measurements of inverse spin Hall effects and magnetoresistance in YIG/Pt and YIG/Ta”, PRB. 87, 174417 (2013).

[67] S.O.Demokritov, A.N.Slavin (Eds.), “Magnoics : From Fundamentals to Applications,” (Springer, Verlag Berlin Heidelberg, 2013) p. 129-143.[68]

[68] Y. Lu et al., "Topological-insulator-based non-volatile memory cell: A quantum device simulation," IEDM Tech. Dig., 26.4.1 (2012)

[69] X. Fong, Y. Kim, K. Yogendra, D. Fan, A. Sengupta,A. Raghunathan, and K. Roy, IEEE Transactions on Computer-Aided Design of Integrated Circuits and Systems 35, 1 (2016)..

[70] L. Liu, C.-F. Pai, Y. Li, H. W. Tseng, D. C. Ralph, and R. A. Buhrman, Science 336, 555 (2012).

[71] A. K. Reza, X. Fong, Z. A. Azim, and K. Roy, IEEE Trans. Electron Devices 63, 1359 (2016).

[72] A. R. Mellnik, J. S. Lee, A. Richardella, J. L. Grab, P. J.Mintun, M. H. Fischer, A. Vaezi, A. Manchon, E.-A.Kim, N. Samarth, and D. C. Ralph, Nature511, 449451(2014).

[73] T. Yokoyama, J. Zang, and N. Nagaosa, Phys. Rev. B81, 241410 (2010).

[74] Z. Jiang, F. Katmis, C. Tang, P. Wei, J. S. Moodera and J. Shi, Applied Physics Letters104, 222409 (2014).

[75] H. Zhang, C. X. Liu, X. L. Qi, X. Dai, and S. C. Fang,Z. Zhang, Nature Physics5, 438442 (2009).

[76] J. Xiong, S. K. Kushwaha, T. Liang, J. W. Krizan, M. Hirschberger, W. Wang,

R. J. Cava, and N. P. Ong,Science 350, 413 (2015).

[77] Z. K. Liu, B. Zhou, Y. Zhang, Z. J. Wang, H. M. Weng,D. Prabhakaran, S.-K. Mo, Z. X. Shen, Z. Fang, X. Dai,Z. Hussain, and Y. L. Chen, Science343, 864 (2014).

[78] S.-Y. Xu, C. Liu, S. K. Kushwaha, R. Sankar, J. W.Krizan, I. Belopolski, M. Neupane, G. Bian, N. Ali-doust, T.-R. Chang, H.-T. Jeng, C.-Y. Huang, W.-F.Tsai, H. Lin, P. P. Shibayev, F.-C. Chou, R. J. Cava,and M. Z. Hasan, Science347, 294 (2015).

[79] Z. Wang, Y. Sun, X.-Q. Chen, C. Franchini, G. Xu,H. Weng, X. Dai, and Z. Fang, Phys. Rev. B85, 195320(2012).

[80] J. P. Perdew, J. A. Chevary, S. H. Vosko, K. A. Jackson,M. R. Pederson, D. J. Singh, and C. Fiolhais, Phys. Rev.B46, 6671 (1992).

[81] D. Datta, B. Behin-Aein, S. Datta, and S. Salahuddin,IEEE Transaction on Nanotechnology11, 261 (2011).

[82] H. J. Monkhorst and J. D. Pack, Phys. Rev. B13, 5188(1976).

[83] E. R. Davidson and D. Feller, Chemical Reviews86, 681(1986).

[84] Atomistix ToolKit with virtual nanolab, version 2018.6,QuantumWise A/S (www.quantumwise.com)

[85] A. P. Mackenzie and Y. Maeno, Rev. Mod. Phys.75, 657(2003),

[86] S. Datta, Lessons from Nanoelectron-ics,2nd ed. (WorldScientific,2018) https://www.worldscientific.com/doi/pdf/10.1142/10440.

[87] J. Xiong, S. Kushwaha, J. Krizan, T. Liang, R. J. Cava,and N. P. Ong, Europhys. Lett. 114, 27002 (2016).114,27002 (2016).

[88] C. Liu, J. Hellerstedt, M. T. Edmonds, and M. S. Fuhrer, Phys. Rev. B96, 235412 (2017)..

[89] X.-G. Zhang and W. H. Butler, Phys. Rev. B70, 172407 (2004).

[90] S. Ikeda, J. Hayakawa, Y. Ashizawa, Y. M. Lee, K. Miura,H. Hasegawa, M. Tsunoda, F. Matsukura, and H. Ohno,Applied Physics Letters93, 082508 (2008).

[91] P. Khalili Amiri, Z. M. Zeng, J. Langer, H. Zhao, G. Row-lands, Y.-J. Chen, I. N. Krivorotov, J.-P. Wang, H. W.Jiang, J. A. Katine, Y. Huai, K. Galatsis, and K. L.Wang, Applied Physics Letters98, 112507 (2011).

[92] A. Brataas, A. D. Kent, and H. Ohno, Nature Materials11, 372381 (2012).

[93] A. Sengupta, Z. Al Azim, X. Fong,and K. Roy, Applied Physics Letters 106,093704(2015),https://doi.org/10.1063/1.4914111.

[94] J. C. Slonczewski, J. Magn. Magn. Mater.159, L1 (1996).

[95] A. Vansteenkiste, J. Leliaert, M. Dvornik, M. Helsen,F. Garcia-Sanchez, and B. Van Waeyenberge, AIP Adv.4, 107133 (2014).

[96] M. Pajda, J. Kudrnovsky, I. Turek, V. Drchal, and P. Bruno, Phys. Rev. B 64, 174402 (2001)

[97] A. K. Reza and K. Roy, IEEE Trans. Electron Devices 66, 1599 (2019).

[98] T. Jungwirth, X. Marti, P. Wadley and J. Wunderlich, "Antiferromagnetic spintronics," Nature Nanotechnol., vol. 11, pp. 231–241, Mar. 2016, DOI: 10.1038/nnano.2016.18

[99] R. Cheng, M. W. Daniels, J. G. Zhu and D. Xiao, "Ultrafast switching of antiferromagnets via spin-transfer torque," Phys. Rev. B, Condens. Matter, vol. 91, p. 064423, Feb. 2015, DOI: 10.1103/PhysRevB.91.064423

[100] T. Shiino, S. H. Oh, P. M. Haney, S. W. Lee, G. Go, B. G. Park and K. J. Lee, "Antiferromagnetic Domain Wall Motion Driven by Spin-Orbit Torques," Phys. Rev. Lett. Vol. 91, p. 064423. Aug. 2015, DOI: 10.1103/PhysRevLett.117.087203

[101] A. K. Reza, X. Fong, Z. A. Azim and K. Roy, "Modeling and Evaluation of Topological Insulator/Ferromagnet Heterostructure-Based Memory," IEEE Trans. Electron Devices, vol. 63, no. 3, Mar. 2016, DOI: 10.1109/TED.2016.2520941

[102] A. D. Kent and D. C. Worledge, "A new spin on magnetic memories," Nature Nanotechnol., vol. 10, no. 3, pp. 187–191, Mar. 2015, DOI: 10.1038/nnano.2015.24

[103] T. H. Kim, P. Grnberg, S. H. Han and B. Cho, "Ultrafast spin dynamics and switching via spin transfer torque in antiferromagnets with weak ferromagnetism," Sci. Rep. 6, 35077, 2016, DOI: 10.1038/srep35077

[104] P. H. Jang, K. Song, S. J. Lee, S. W. Lee and K. J. Lee, "Detrimental effect of interfacial Dzyaloshinskii-Moriya interaction on perpendicular spin-transfer-torque magnetic random access memory," Appl. Phys. Lett. 107, 202401 (2015); doi: 10.1063/1.4936089

[105] J. C. Slonczewski, "Current-driven excitation of magnetic multilayers,"J. Magn. Mater., vol. 159, pp. L1-L7, 1996. DOI: 10.1016/0304-8853(96)00062-5

[106] K. M. D. Hals, Y. Tserkovnyak and A. Brataas, "Phenomenology of Current-Induced Dynamics in Antiferromagnets," Phys. Rev. Lett. vol 106, p. 107206, Mar. 2011, DOI: 10.1103/PhysRevLett.106.107206

[107] E. Martinez, S. Emori, N. Perez, L. Torres, and G. S. D. Beach, "Current-driven dynamics of Dzyaloshinskii domain walls in the presence of in-plane fields: Full micromagnetic and one-dimensional analysis," J. Appl. Phys. Vol. 115, p. 213909, 2014, DOI: 10.1063/1.4881778

[108] J. Finley and L. Liu, "Spin-Orbit-Torque Efficiency in Compensated Ferrimagnetic Cobalt-Terbium Alloys," Phys. Rev. Applied. Vol 6, p. 054001, 2016, DOI: 10.1103/PhysRevApplied.6.054001

[109] M. Evelt, C. Safranski, M. Aldosary, V. E. Demidov, I. Barsukov, A. P. Nosov, A. B. Rinkevich, K. Sobotkiewich, X. Li, J. Shi, I. N. Krivorotov & S. O. Demokritov, "Spin Hall-induced auto-oscillations in ultrathin YIG grown on Pt," Scientific Reportsvolume 8, Article number: 1269 (2018)

[110] S. Emori, A. Matyushov, H. M. Jeon, C. J. Babroski, T. Nan, A. M. Belkessam, J. G. Jones, M. E. McConney, G. J. Brown, B. M. Howe, N. X. Sun, "Spin-orbit torque and spin pumping in YIG/Pt with interfacial insertion layers," Appl. Phys. Lett. 112, 182406 (2018)

[111] T. Moriya, "Anisotropic superexchange interaction and weak ferromagnetism," Physical Review 120, 91 (1960), DOI: 10.1103/PhysRev.120.91

[112] M. Pajda, J. Kudrnovsky, I. Turek, V. Drchal, and P. Bruno, "Ab initio calculations of exchange interactions, spin-wave stiffness constants, and Curie temperatures of Fe, Co, and Ni," Phys. Rev. B, Vol. 64, p. 174402, 2001, DOI: 10.1103/PhysRevB.64.174402

[113] Li-Shan Xie, Guang-Xi Jin, Lixin He, Gerrit E. W. Bauer, Joseph Barker, and Ke Xia, "First-principles study of exchange interactions of yttrium iron garnet", Phys. Rev. B 95, 014423.

[114] Editorial, Nat. Nanotechnol. 10, 185 (2015).

[115] A. K. Reza, X. Fong, Z. A. Azim, and K. Roy, IEEE Trans. Electron Devices 63, 1359 (2016).

[116] N. Spaldin, Magnetic Materials Fundamentals and Applications, 2nd ed. (Cambridge University Press, Cambridge, 2010), p. 113..

[117] T. Ambrose and C. L. Chien, J. Appl. Phys. 83, 6822 (1998).

[118] M. Pajda, J. Kudrnovsky, I. Turek, V. Drchal, and P. Bruno, Phys. Rev. B 64, 174402 (2001)..

[119] J. Finley and L. Liu, Phys. Rev. Lett. 6, 054001 (2016).

[120] H. Ebert and S. Mankovsky, Phys. Rev. B 79, 045209 (2009).

[121] T. H. Kim, P. Grunberg, S. H. Han, and B. Cho, Sci. Rep. 6, 35077 (2016).

[122] A. K. Reza and K. Roy, IEEE Trans. Electron Devices 66, 1599 (2019).

[123] J. C. Slonczewski, J. Magn. Magn. Mater. 159, L1 (1996).

[124] J. Zhang, T. Phung, A. Pushp, Y. Ferrante, J. Jeong, C. Rettner, B. P. Hughes, S.-H. Yang, Y. Jiang, and S. S. P. Parkin, Appl. Phys. Lett. 110, 172403 (2017).

[125] Z. Wen, H. Sukegawa, S. Kasai, K. Inomata, and S. Mitani, Phys. Rev. Appl. 2,

[126] 024009 (2014).

[127] L. Bainsla, K. Z. Suzuki, M. Tsujikawa, H. Tsuchiura, M. Shirai, and S. Mizukami, Appl. Phys. Lett. 112, 052403 (2018).

[128] B. Hu, K. Moges, Y. Honda, H.-X. Liu, T. Uemura, M. Yamamoto, J.-I. Inoue, and M. Shirai, Phys. Rev. B 94, 094428 (2016).

[129] P. Buczek, A. Ernst, P. Bruno, and L. M. Sandratskii, Phys. Rev. Lett. 102, 247206 (2009).

[130] S. Datta, Quantum Transport: Atom to Transistor (Cambridge University Press, 2005).

[131] P. Soven, Phys. Rev. 156, 809 (1967).

[132] G. M. Stocks, W. M. Temmerman, and B. L. Gyorffy, Phys. Rev. Lett. 41, 339 (1978).

[133] G. S. Joyce, Phys. Rev. 155, 478 (1967).

[134] QuantumWise A/S, see www.quantumwise.com for "Atomistix toolkit version 2017.2.".

[135] M. Brandbyge, J.-L. Mozos, P. Ordejón, J. Taylor, and K. Stokbro, Phys. Rev. B 65, 165401 (2002).

[136] J. M. Soler, E. Artacho, J. D. Gale, A. Garca, J. Junquera, P. Ordejn, and D. Snchez-Portal, J. Phys. Condens. Matter 14, 2745 (2002).

[137] T. Moriya, Phys. Rev. 120, 91 (1960).

[138] E. Martinez, S. Emori, N. Perez, L. Torres, and G. S. D. Beach, J. Appl. Phys. 115, 213909 (2014).

[139] R. Cheng, M. W. Daniels, J. G. Zhu, and D. Xiao, Phys. Rev. B 91, 064423 (2015).

[140] MgO Crystal Structure, Datasheet from "Pauling file multinaries edition—2012" in

SpringerMaterials (Springer, Berlin, 2016).

[141] Pt Crystal Structure, Datasheet from "Pauling file multinaries edition—2012" in SpringerMaterials (Springer, Berlin, 2016).

[142] Co Crystal Structure, Datasheet from "Pauling file multinaries edition—2012" in SpringerMaterials (Springer, Berlin, 2016).

[143] S. Yuasa, T. Nagahama, A. Fukushima, Y. Suzuki, and K. Ando, Nat. Mater. 3, 868–871 (2004).

[144] A. R. Mellnik, J. S. Lee, A. Richardella, J. L. Grab, P. J. Mintun, M. H. Fischer, A. Vaezi, A. Manchon, E.-A. Kim, N. Samarth, and D. C. Ralph, Nature 511, 449–451 (2014).

[145] T. Shiino, S. H. Oh, P. M. Haney, S. W. Lee, G. Go, B. G. Park, and K. J. Lee, Phys. Rev. Lett. 117, 087203 (2016).

[146] H. Kubota, A. Fukushima, K. Yakushiji, T. Nagahama, S. Yuasa, K. Ando, H. Maehara, Y. Nagamine, K. Tsunekawa, D. D. Djayaprawira, N. Watanabe, and Y. Suzuki, Nat. Phys. 4, 37–41 (2008)

[147] Y. Huai, AAPPS Bull. 18, 33 (2008).

[148] D. D. Tang and Y.-J. Lee, Magnetic Memory: Fundamentals and Technology (Cambridge University Press, 2010).

[149] J. Hayakawa, S. Ikeda, Y. Lee, R. Sasaki, F. Matsukura, T. Meguro, H. Takahashi, and H. Ohno, in 2006 IEEE International Magnetics Conference (INTERMAG) (IEEE, 2006), p. 6.

[150] M. Büttiker, "Four-terminal phase-coherent conductance," Phys. Rev. Lett., vol. 57, pp. 1761–1764, Oct. 1986

[151] S. Datta, Quantum Transport, 2nd ed. Cambridge, U.K.: Cambridge Univ. Press, 2005

[152] H. Kubota et al., "Quantitative measurement of voltage dependence of spin-transfer torque in MgO-based magnetic tunnel junctions," Nature Phys., vol. 4, no. 1, pp. 37–41, 2008.

[153] F. Chevy, K. W. Madison, V. Bretin, and J. Dalibard, Trapped Particles and Fundamental Physics. Berlin, Germany: Springer, 2002, p. 92

[154] Z. Sun and Q. Gu, "Spontaneous separation of large-spin Fermi gas in the harmonic trap: A density functional study," Sci. Rep., vol. 6, Aug. 2016, Art. no. 31776.

[155] M. A. Alam, B. E. Weir, and P. J. Silverman, "A study of soft and hard breakdown—Part I: Analysis of statistical percolation conductance," IEEE Trans. Electron Devices,

vol. 49, no. 2, pp. 232–238, Feb. 2002

[156] M. A. Alam, B. E. Weir, and P. J. Silverman, "A study of soft and hard breakdown—Part II: Principles of area, thickness, and voltage scaling," IEEE Trans. Electron Devices, vol. 49, no. 2, pp. 239–246, Feb. 2002.

[157] T. Nigam, A. Kerber, and P. Peumans, "Accurate model for timedependent dielectric breakdown of high-k metal gate stacks," in Proc. IEEE IRPS, Apr. 2009, pp. 523–530.

[158] M. Masuduzzaman, A. E. Islam, and M. A. Alam, "Exploring the capability of multifrequency charge pumping in resolving location and energy levels of traps within dielectric," IEEE Trans. Electron Devices, vol. 55, no. 12, pp. 3421–3431, Dec. 2008.

[159] K. Okada, H. Kubo, A. Ishinaga, and K. Yoneda, "A new prediction method for oxide lifetime and its application to study dielectric breakdown mechanism," in Dig. Symp. VLSI Technol., 1998, pp. 158–159.

[160] T. Nigam, S. Martin, and D. Abusch-Magder, "Temperature dependence and conduction mechanism after analog soft breakdown," in Proc. Int. Rel. Phys. Symp., 2003, pp. 417–423.

[161] A. Cester, L. Bandiera, J. Sune, L. Boschiero, G. Ghidini, and A. Paccagnella, "A novel approach to quantum point contact for post soft breakdown conduction," in IEDM Tech. Dig., 2001, pp. 305–308.

[162] R. P. Vedula, S. Palit, M. A. Alam, and A. Strachan, "Role of atomic variability in dielectric charging: A first-principles-based multiscale modeling study," Phys. Rev. B, Condens. Matter, vol. 88, no. 20, p. 205204, 2013.

[163] M. Jullière, "Tunneling between ferromagnetic films," Phys. Lett. A, vol. 54, no. 3, pp. 225–226, Sep. 1975.

[164] S. Datta, Lessons From Nanoelectronics: A New Perspective on Transport. Singapore: World Scientific, 2012.

[165] L. A. Escobar and W. Q. Meeker, "A review of accelerated test models," Statist. Sci., vol. 21, no. 4, pp. 552–577, 2006.

[166] A. K. Reza, X. Fong, Z. A. Azim, and K. Roy, "Modeling and evaluation of topological insulator/ferromagnet heterostructure-based memory," IEEE Trans. Electron Devices, vol. 63, no. 3, pp. 1359–1367, Mar. 2016.

[167] R. O'Connor et al., "SILC defect generation spectroscopy in HfSiON using constant voltage stress and substrate hot electron injection," in Proc. IEEE IRPS, Apr./May 2008, pp. 324–329

[168] K. S. Yew, D. S. Ang, and G. Bersuker, "Bimodal Weibull distribution of metal/high-κ gate stack TDDB—Insights by scanning tunneling microscopy," IEEE Electron.

Device Lett., vol. 33, no. 2, pp. 146–148, Feb. 2012.

[169] M. Duan et al., “Insight into electron traps and their energy distribution under positive bias temperature stress and hot carrier aging,” IEEE Trans. Electron Devices, vol. 63, no. 9, pp. 3642–3648, Sep. 2016.

[170] N. L. Anderson, R. P. Vedula, P. A. Schultz, R. M. Van Ginhoven, and A. Strachan, “Defect level distributions and atomic relaxations induced by charge trapping in amorphous silica,” Appl. Phys. Lett., vol. 100, no. 17, p. 172908, 2012.

[171] K. Komiya and Y. Omura, “Aspects of hard breakdown characteristics in a 2.2-nm-thick SiO2 film,” J. Semicond. Technol. Sci., vol. 2, no. 3, pp. 164–169, Sep. 2002.

[172] R. O’Connor, G. Hughes, P. Casey, and S. B. Newcomb, “Degradation and breakdown characteristics of thin MgO dielectric layers,” J. Appl. Phys., vol. 107, no. 2, p. 024501, 2010.

[173] C. Yoshida, M. Kurasawa, Y. M. Lee, K. Tsunoda, M. Aoki, and Y. Sugiyama, “A study of dielectric breakdown mechanism in CoFeB/MgO/CoFeB magnetic tunnel junction,” in Proc. Int. Rel. Phys. Symp. (IRPS), Montreal, QC, Canada, 2009, pp. 139–142.

[174] C. Yoshida and T. Sugii, “Reliability study of magnetic tunnel junction with naturally oxidized MgO barrier,” in Proc. IEEE IRPS, Apr. 2012, pp. 2A.3.1–2A.3.5.

[175] J. Yang et al., “Intrinsic correlation between PBTI and TDDB degradations in nMOS HK/MG dielectrics,” in Proc. IEEE Int. Rel. Phys. Symp. (IRPS), Apr. 2012, pp. 5D.4.1–5D.4.7.

[176] D. Datta, B. Behin-Aein, S. Datta, and S. Salahuddin, “Voltage asymmetry of spin-transfer torques,” IEEE Trans. Nanotechnol., vol. 11, no. 2, pp. 261–272, Mar. 2012.

[177] L. P. B. Lima, H. F. W. Dekkers, J. G. Lisoni, J. A. Diniz, S. Van Elshocht, and S. De Gendt, “Metal gate work function tuning by Al incorporation in TiN,” J. Appl. Phys., vol. 115, no. 7, p. 074504, Feb. 2014.

[178] J. S. Chawla, X. Y. Zhang, and D. Gall, “Effective electron mean free path in TiN(001),” J. Appl. Phys., vol. 113, no. 6, p. 063704, 2013.

[179] M.-J. Chen and C.-Y. Hsu, “Evidence for a very small tunneling effective mass (0.03 m0) in MOSFET high-k (HfSiON) gate dielectrics,” IEEE Electron Device Lett., vol. 33, no. 4, pp. 468–470, Apr. 2012.

[180] B. Brar, G. D. Wilk, and A. C. Seabaugh, “Direct extraction of the electron tunneling effective mass in ultrathin SiO2,” Appl. Phys. Lett., vol. 69, no. 18, pp. 2728–2730, Oct. 1996.

[181] Y.-C. Yeo, T.-J. King, and C. Hu, “Metal-dielectric band alignment and its implications for metal gate complementary metaloxide-semiconductor technology,” J. Appl. Phys., vol. 92, no. 12, pp. 7266–7271, 2002.

[182] A. Hadjadj, O. Simonetti, T. Maurel, G. Salace, and C. Petit, “Si–SiO2 barrier height and its temperature dependence in metal-oxidesemiconductor structures with ultrathin gate oxide,” Appl. Phys. Lett., vol. 80, no. 18, pp. 3334–3336, 2002

VITA

Ahmed Kamal Reza received the B.S. degree from the Department of Electrical and Electronic Engineering, Bangladesh University of Engineering and Technology, Dhaka, Bangladesh, in 2011. He is currently pursuing the Ph.D. degree in micro and nano electronics with the Electrical and Computer Engineering Department, Purdue University, West Lafayette, IN, USA.

He is mainly involved in device modeling and simulation, and spin-based memory design and optimization.